The Dissertation Committee for Stephanie Sue Adkins Certifies that this is the approved version of the following dissertation:

Carbon Dioxide and Water Emulsion Stability and Rheology with Nonionic Hydrocarbon Surfactants or Particles

Committee:

Keith Johnston, Supervisor

Quoc Nguyen

Isaac Sanchez

Gary Rochelle

Peter Rossky

Carbon Dioxide and Water Emulsion Stability and Rheology with Nonionic Hydrocarbon Surfactants or Particles

by

Stephanie Sue Adkins, B.S. Ch.E.

Dissertation

Presented to the Faculty of the Graduate School of

The University of Texas at Austin

in Partial Fulfillment

of the Requirements

for the Degree of

Doctor of Philosophy

The University of Texas at Austin

May, 2009

Dedication

To my family and friends for their love and support.

Acknowledgements

I would like to thank the graduate students and professors who have worked with me on this research including my committee. In addition, I would like to give thanks to Xi Chen, Andrea Miller, Mehul Patel, Jasmine Tam, Gaurav Gupta, Griffen Smith, Jasper Dickson, Michal Matteucci, John Keagy, Li Ma, Enza Torino, and all the undergraduates I have worked with. Thanks again to Dr. Quoc Nguyen and Dr. Aaron Sanders (at Dow) for all the discussions on this project.

Carbon Dioxide and Water Emulsion Stability and Rheology using Nonionic Surfactants or Particles

Publication No._____

Stephanie Sue Adkins, PhD

The University of Texas at Austin, 2008

Supervisor: Keith Johnston

For the first time the interfacial properties of nonionic hydrocarbon surfactants at both the air-water and CO_2-water interfaces are investigated in terms of surfactant structure to determine the changes in surfactant efficiency (negative of the logarithm of the surfactant concentration to create a surface pressure of 20 mN/m). At the air-water interface, linear surfactant tails are more efficient due to the higher packing ability of the straight chains in the dense surfactant monolayer. However, at the CO_2-water interface, surfactant adsorption is small and tails can be solvated. Thus, branching which increases both tail solvation and tail hydrophobicity also enlarges the hard disk area of the surfactant to ultimately increase the efficiency of the surfactant at the CO_2-water interface.

CO_2-in-water concentrated emulsions (foams) are studied over short and long times to evaluate the foam stability as a function of both surfactant structure and foam conditions using *in-situ* optical microscopy. The surface pressure measured at the CO_2-water interface is correlated with the short time stability of coalescing foams with very

small cell sizes (under 0.4 μm in diameter). Long time stability of bubbles to coalescence is shown under a variety of conditions. The rheology of these bulk CO_2-in-water foams under high-pressure conditions are also evaluated through measurements of the pressure drop over a capillary tube. Viscosities in excess of 200 cP are measured, an increase of over 1000 time that of pure CO_2 (0.09 cP at 24 ˚C and 2000 psia). The viscosity of the C/W foams are found to correlate with bubble size, continuous phase viscosity, shear rate, and interfacial tension.

Hydrophobic silica particles adsorbed at the interface are also used to stabilize water-in-CO_2 emulsions as an alternative to surfactant stabilizers. The difficulties of tail solvation associated with many hydrocarbon surfactants in CO_2 can be removed by using particles instead of surfactant. A porous cross-linked shell is formed about the hydrophilic (colloidal and fumed) silica to render the particles CO_2-philic and the cross-linking removes ligand tails from the particle surface.

Table of Contents

List of Tables

List of Figures

Chapter 1: Introduction

Carbon dioxide (CO_2) is a non-toxic, non-flammable, and recyclable solvent that is an environmentally friendly alternative to organic solvents. The critical point of CO_2 is 31.1 °C and 1070 psia, which is highly accessible for many applications. At conditions above the critical point, the CO_2 become super critical with properties intermediate of a gas and liquid. The tunable properties (density, viscosity, and diffusivity) of the super critical fluid with temperature and/or pressure add another dimension of control compared to traditional solvents. Colloidal dispersions[1] including emulsions,[2-5] metal nanocrystals,[6-12] polymer latexes,[13] and inorganic silica[14-18] dispersions have been reported in CO_2 for applications such as photoresist drying,[19,20] metal extraction,[21] nanoparticle synthesis,[6,7,10,12,22] enzymatic catalysis,[23] and dry cleaning.[24]

Mixtures of water and CO_2, the two most abundant solvents on earth, have been investigated in the form of micellar solutions, microemulsions (< 10 nm drops),[25-31] miniemulsions (< 500 nm drops),[32-34] and macroemulsions (> 500 nm drops).[2,4,35-37] Microemulsions are thermodynamically stable and optically transparent. Macroemulsions, which are turbid, are not thermodynamically stable and must be

kinetically stabilized against flocculation, coalescence, and gravitational settling. Miniemulsions exist in the droplet size range between microemulsions and macroemulsions.

Surfactant tails are often poorly solvated by CO_2 leading to poor stability of CO_2 and water emulsions. The low cohesive energy density and weak van der Waals forces, characterized by a low polarizability per unit volume and low dielectric constant (1.0-1.6), can lead to a lower solvation strength, especially for hydrocarbon tails.[38] Tail solvation is improved with low molecular weight surfactants,[39] or "stubby" hydrocarbon surfactants with little tail overlap[34,40-42] and a low free volume at the CO_2-water interface.[41,43] For polymeric stabilizers where solvation is weaker, it is usually necessary to choose monomers with low cohesive energy densities, for example siloxanes, trisiloxanes, fluoroalkanes, fluoroethers, and fluoroacrylates.[2,33,34,44-48] The high cost of fluorinated surfactants make hydrocarbon surfactants much more attractive, examples of which are poly(ether carbonate) copolymers[49] and peracetylated sugars[50] that have high CO_2 solubility. Commercial hydrocarbon surfactants, such as Dynol 604[51] and poly-(ethylene glycol) 2,6,8-trimethyl-4-nonyl ether (TMN 6)[52], have also been employed for CO_2-water emulsions.

1.1 ENHANCED OIL RECOVERY

The initial primary recovery of crude oil from ground reservoirs typically leaves approximately 90% of the original oil in the reservoir. Primary recovery involves allowing the natural pressure of the reservoir or gravity transport oil into the wellbore (drilled hole), wherein pumps (or other lift technology) bring that oil to the surface.

Secondary recovery methods generally use water or gas injection to drive the oil towards the wellbore. Secondary recovery methods can produce 20-40% of the original oil in the reservoir, leaving a large amount of un-produced crude oil.[53] Enhanced oil recovery (EOR) is the next phase in the life of the oil reservoir. EOR methods include thermal recovery where heat is introduced to reduce the viscosity of the oil, gas injection (including natural gas, nitrogen, and carbon dioxide gases), and chemical injection where polymers or surfactants are introduced in the reservoir.

EOR with CO_2 injection (or flooding) was first attempted in 1972 in Texas and has successfully been utilized in the Permian Basin (Western Texas to Eastern New Mexico). Naturally occurring CO_2 taken directly from the ground can be used for the gas flooding, or CO_2 that is produced during industrial processes (such as natural gas processing and hydrogen plants) can be captured and used. Reducing the amount of CO_2 (a green house gas) emissions through capture and redirection to the ground is one key benefit of CO_2 flooding. Another major advantage of using CO_2 is that it is miscible[54,55] in all proportions with the lighter hydrocarbon components of the crude oil (up to 14 carbons depending on the system pressure) and partially miscible with heavier hydrocarbons.[56] Upon contact, some of the CO_2 dissolves in the crude oil thereby reducing the viscosity of the oil and allowing it to flow more easily towards the producer well. Currently, EOR with CO_2 has spread through out the middle of the United States, Pennsylvania, and Alaska to a limited extent. Next generation technologies for CO_2 EOR could double the efficiency of domestic oil recovery according to reports to the Department of Energy (DOE) Office of Fossil Energy in February 2006. In addition to EOR, CO_2 sequestration in the ground can occur after the crude oil is removed.[57]

However, EOR by CO_2 injection is often plagued with inefficient oil recovery.[58,59] The low viscosity of CO_2 (0.01-0.1 cP) leads to a high CO_2 mobility (the ratio of

effective rock permeability to CO_2 viscosity) relative to other reservoir fluids (water and oils). Thus, an unfavorable mobility ratio occurs causing fingering of the CO_2 through the oil. In addition, gravity override takes place due to the lower density of CO_2 relative to the other fluids in the reservoir. Heterogeneity of the reservoir can produce layers of varying porosity and permeability, thus the CO_2 can channel (preferentially flood) through high permeability layers and can result in early break-through of CO_2.[60] A reduced amount of oil is recovered from the reservoir, plus higher CO_2 handling and recycling costs result.

Therefore, mobility control of the CO_2 is of great importance for improving CO_2 EOR. The mobility of the CO_2 can be reduced with the formation of viscous concentrated CO_2-in-water (C/W) emulsions. High internal phase emulsions (greater the 74% dispersed phase by volume) of CO_2 are also known as C/W foams or concentrated emulsions. As with traditional air-in-water foams the viscosity of the foam is greater than the viscosity of the dispersed phase due to the continuous network of the water phase through out the foam structure.

Foam in porous media is of the form of gas dispersed in a continuous liquid phase where some gas flow paths are made discontinuous with liquid lamella.[59-61] As the liquid lamella move through a pore, they flow first through a diverging and then a converging type channel.[62] The mobility of the gas is mainly determined by the foam texture (number of foam lamella) in the porous media. During flow in porous media, the foam is constantly generating new bubbles. The generation of lamella in the pores occurs by the mechanisms of snap-off, lamella division, and leave-behind. However, lamella destruction also occurs by bubble during foam flow in porous media. The relative rates of foam generation and destruction determine whether the mobility of the dispersed phase is controlled through out the entire reservoir.

Kovscek and Bertin showed that *in-situ* foam generation in sandstone (a porous media) could be used to reduce the mobility of Nitrogen gas.[63] In addition, the flow of the injected fluid was diverted to the low permeability portion of the heterogeneous sandstone using a parallel core setup due to the nearly independent establishment of the foam texture and gas mobility in the cores. As the mobility of the CO_2 phase can vary with the heterogeneity of the reservoir, the problems that plague CO_2 flooding can be diminished. Furthermore, the CO_2 is still able to contact and be solvated by the crude oil with the use of C/W foams thereby retaining the main advantage of CO_2 floods. Asghari and Khalil investigated the effect of operation parameters on the mobility of C/W foams in porous media (crushed carbonate pack) where the commercial surfactant Chase CD 1045 was the most effective surfactant tested.[64] In addition, an increase in temperature and a reduction in pressure was found to lower C/W foam mobilities, although the addition of salt had little effect on the foam mobility.

1.2 FOAM STABILITY

For EOR with C/W foam, the foam is injected (or created) in the ground and remains there for weeks to months. Therefore, foam stability is required for these long time periods, where the rate of foam destruction cannot be greater than that of bubble formation in order to prevent a huge reduction in the number of lamella over time. The loss of surfactant to the reservoir rock or other reservoir fluids is one factor that acts to destabilize the foam lamella as it flows through out the reservoir. Drainage of the water in the foam lamella can also reduce the stability of the foam. Coalescence (lamella rupture) and Ostwald ripening occur to reduce the number of lamella and increase the average

bubble size over time. Ostwald ripening occurs with the diffusion of the dispersed phase (CO_2) from smaller bubbles to larger ones as the polydispersity of the foam is the driving force. Coalescence in the form of spinodal decomposition occurs when surfactant at the interface cannot repel neighboring bubbles, making the foam unstable.[65-68] With the appropriate stabilizers in the lamella, the foam can reach a metastable state, however coalescence can still occur due to the formation and growth of thermally activated holes in the lamella.[67,69,70]

In the presence of oil, foam lamella can also be destroyed. There are four basic configurations when oil is present in a foam.[71] The emulsified oil drop can stay in the water lamella or plateau borders (where three bubbles meet) without interaction with the water-CO_2 interface. If the drop interacts with the CO_2-water interface, it can form a pseudo-emulsion film where a thin liquid film separates the oil drop from the gas phase. If the pseudo-emulsion film breaks, an oil lens can form at the CO_2-water interface. Finally, the oil lens can spread at the CO_2-water interface creating an oily layer. In addition, a large oil lens may connect the two CO_2-water interfaces of the lamella creating an oil bridge.[72] Most antifoaming mechanisms include the oil bridge as the reason for the lamella breakage.

Kuhlman et al. investigated the effect of light oil on CO_2 foams where microvisual cell experiments showed that light oil spread at the CO_2-water interface due to the low interfacial tension between the oil and CO_2.[73] As the foam flowed, the light hydrocarbons were stripped away increasing the interfacial tension and stopping the spreading of the oil. Spreading oil does not necessarily break the foam; however foam has increased cell size when oil spreads at the interface. The stability of the water-oil lamella determines the stability of the foam with spreading oil. Yang and Reed[74] also studied mobility control using CO_2 foams when decane was co-injected where increasing

the amount of decane increased the mobility across the core starting with only 3% decane. The differential pressure across the core decreased to half the oil-free value when 9% decane was injected. Therefore, small amounts of light oil can be effect in increasing the mobility of the foam. This is not altogether damaging to EOR, as the flow of light oil should not be hindered by the foam. Thus, breaking of the foam in the reservoir where light oil is present is likely, however stability is necessary when the light oil has been removed in the swept regions of the reservoir.

1.3 OBJECTIVES

The primary objective of this dissertation is to examine the stabilization of emulsions with water and liquid or super-critical CO_2. The majority of the work is dedicated to investigating novel nonionic hydrocarbon surfactant structures at the CO_2-water interface and the resulting C/W foams formed. The initial work focuses on studying the surfactants at both the air-water and CO_2-water interfaces through surface pressure (interfacial tension) measurements as a function of the surfactant head and tail structure. A high-pressure captive bubble technique is used to determine the interfacial tension at the CO_2-water interface. The differences between the air-water and CO_2-water interfaces are determined as well as the most effective surfactant structures for each system. The stability of C/W foams with the nonionic surfactants is investigated next over both short and long time periods to determine the effect of the different surfactant tail structures and variation of foam conditions, respectively. *In-situ* optical microscopy allows the foam to be photographed and analyzed over set time periods ranging from a fraction of a second to hours. The rheology of the bulk C/W foams stabilized with the hydrocarbon surfactants

are also examined in terms of the pressure drop measured over a capillary tube. The effect of system conditions (including temperature, quality, and salinity) and texture on the apparent viscosity of the bulk C/W foams are studied. Finally, solid particles are examined as an alternative stabilizer to surfactants for CO_2-water emulsions. In this case, the hydrophilic silica particles are tailored by cross-linking a CO_2-philic polymer on the particle surface to form a shell. These particles stabilize water-in-CO_2 emulsions without the difficulties of tail solvation, which can occur with surfactants, thus increasing the utility of CO_2 under a variety of conditions.

1.4 DISSERTATION OUTLINE

Chapter 2 compares the interfacial properties of nonionic hydrocarbon surfactants at the air-water and CO_2-water interface. For the first time, the effect of surfactant structure is investigated in terms of surfactant efficiency (negative of the logarithm of the surfactant concentration to create a surface pressure of 20 mN/m) at both interfaces to demonstrate the differences between the hydrophobic phases. At the air-water interface, linear surfactant tails are more efficient than branched surfactants of the same carbon number due to the higher packing ability of the straight chains in the dense surfactant monolayer. However, at the CO_2-water interface, surfactant adsorption is small and tails can be solvated. Thus, branching which increases both tail solvation and tail hydrophobicity also enlarges the hard disk area of the surfactant to ultimately increase the efficiency of the surfactant. Xi Chen conducted many of the interfacial experiments with CO_2.

In Chapter 3 the stability of the CO_2-in-water foams is evaluate over short and long times as a function of surfactant structure and foam conditions using *in-situ* optical microscopy. The surface pressure measured at the CO_2-water interface is correlated with the short time stability of coalescing foams with very small cell sizes (under 0.4 μm in diameter). Long time stability of bubbles (over 0.9 μm in diameter) to coalescence is shown under a variety of conditions for several surfactants, even surfactants with a high distribution towards CO_2. The mechanisms leading to coalescence in oil-water and air-water systems are discussed and compared with the CO_2-water foams. Ostwald ripening occurs in the CO_2-water foams under all conditions due to the polydispersity of the bubble sizes in the foams.

The rheology of the bulk CO_2-in-water foams under high-pressure conditions are evaluated in Chapter 4 through measurements of the pressure drop over a capillary tube. The relationship between the shear stress and shear rate are modeled as either Newtonian or Power-law fluids. In some cases, a combination behavior is shown. Viscosities in excess of 200 cP are measured, an increase of over 1000 time that of pure CO_2 (0.09 cP at 24 ˚C and 2000 psia). Both shear-thinning and shear-thickening behavior is measured and correlated with changes to foam texture. The viscosity of the C/W foams are found to correlate with bubble size, continuous phase viscosity, shear rate, and interfacial tension as other air-water foams and oil-water emulsions have been shown to associate.

In Chapter 5, hydrophobic silica particles adsorbed at the interface are used to stabilize water-in-CO_2 emulsions for the first time. A porous cross-linked shell is formed about the hydrophilic (colloidal and fumed) silica to render the particles CO_2-philic resulting in average water drops as low as 7.5 μm. Ostwald ripening and coalescence were not visible in the emulsions for 7 days, although settling did occur (due to the equal amounts of each phase). CO_2-philic particles offer a new route to highly stable water-in-

CO_2 emulsions, with particle energies of attachment on the order of 10^6 kT, even at densities as low as 0.78 g/ml. The use of particles for stabilizing colloids as an alternative to surfactants removes the difficulties of tail solvation associated with surfactants in CO_2.

Supplementary material is included in Appendices A, B, and C with additional figures and tables. Appendix D presents the investigation of stable colloidal dispersions of a lipase-perfluoropolyether complex in liquid and supercritical CO_2. The protein complex was studied using high-pressure dynamic light scattering. The aggregation that occurs between the protein complex molecules illustrates the difficulties of ligand tail solvation in CO_2.

Chapter 2: Effect of Branching on the Interfacial Properties of Nonionic Hydrocarbon Surfactants at the Air-Water and Carbon Dioxide-Water Interfaces

The interfacial tensions, surface pressures, and adsorption of nonionic hydrocarbon surfactants at the air-water (A-W) and carbon dioxide-water (C-W) interfaces were investigated systematically as a function of the EO (ethylene oxide unit) length and tail structure. Major differences in the properties are explained in terms of the driving force for surfactant adsorption, tail solvation, area per surfactant molecule, and surfactant packing. As the surfactant architecture is varied, the changes in tail-tail interactions, steric effects, areas occupied by the surfactant at the interface, and tail hydrophobicity are shown to strongly influence the interfacial properties, including the surfactant efficiency (the concentration to produce 20 mN/m interfacial tension reduction). For linear surfactants at the A-W interface, high efficiencies result from dense monolayers produced by the high interfacial tension driving force for adsorption and strong tail-tail interactions. At the C-W interface, where a low interfacial tension leads to a much lower surfactant adsorption, the contact between the phases is much greater. Branching or increasing the number of tail chains increase the hydrophobicity, tail solvation, and adsorption of the surfactant. Furthermore, the area occupied by the surfactant increases with branching, number of tails, and number of EO monomers in the head group, to reduce contact of the phases. These factors produce greater efficiencies for branched and double-tail surfactants at the C-W interface, as well as surfactants with longer EO head groups.

2.1 INTRODUCTION

Carbon dioxide and water are two of the most abundant resources on earth. Carbon dioxide (CO_2) is an environmentally benign, non-toxic, non-flammable, and recyclable solvent with an accessible critical point of 31.1 °C and 1070 psia. The tunable solvation strength of CO_2 with temperature and pressure has a large effect on bulk and interfacial properties.[75] Because of the weak van der Waals forces of CO_2, characterized by a low polarizability per unit volume and low dielectric constant (1.0-1.6), the structure of steric stabilizers are different than in the case of water and oils.[38] Dispersions of CO_2 and water have been investigated in the form of micellar solutions, microemulsions (< 10 nm),[25-31] miniemulsions (< 500 nm),[32-34] and macroemulsions (> 500 nm).[2,4,35-37] They have been investigated for various applications in industry such as emulsion templating,[76,77] nanoparticle synthesis,[12] photoresist drying,[19] dry cleaning, enzymatic catalysis,[23] and enhanced oil recovery (EOR).[59] In EOR with CO_2, the formation of foams can increase the viscosity of the gas by 100 to 1000 fold and thus decrease the mobility of CO_2 (ratio of the effective permeability of the fluid to its viscosity)[56,59] to improve the sweep efficiency markedly. However, the effects of surfactant structure on the formation and stability for CO_2-in-water (C/W) foams (also called emulsions) are often based on studies of air-in-water (A/W) foams at atmospheric conditions.

The molecular architecture of a surfactant for a CO_2 foam is expected to be fundamentally different from that for a foam with a nearly ideal gas such as nitrogen. The molecular interactions between the surfactant tail and CO_2 phase, as a function of pressure, can have a large effect on the surfactant partitioning between the CO_2 and water phases,[78] the interfacial tension,[79] adsorption of the surfactant at the interface,[79,80] and

thus the structure of the surfactant monolayer.[81-83] Since an ideal gas does not dissolve surfactants or interact with surfactant tails, CO_2 foams require a new dimension in understanding. Philips et al. found that rheological data generated for nitrogen foams was not sufficient to describe the same system with CO_2 foams.[84] Thus, fundamental interfacial studies are needed to differentiate the effects of surfactant structure at the CO_2-water (C-W) versus air-water (A-W) interfaces.

Another important distinction between C/W and A/W foams is the marked difference in the interfacial tension (γ_o) for the C-W versus air-water A-W interface (without surfactant). The surface tension of water is 72 mN/m; however, γ_o for C-W ranges from 20-30 mN/m, depending on temperature and pressure. Rosen found that the saturated adsorption of surfactant at the O-W interface increased as γ_o between the two phases increased.[85] Therefore because of the smaller γ_o for the C-W versus A-W interface, there is a smaller driving force for surfactant to adsorb at the C-W interface to further lower the interfacial tension. Thus, the area per surfactant molecule (A_m) at the C-W interface is often much larger than that at the A-W interface as shown experimentally[86,87] and by molecular dynamics simulations.[81]

The interfacial behavior of surfactants at the C-W interface, particularly for conditions most relevant to W/C microemulsions, has already been studied.[4,37,43,78,79,82,83,87-89] The most effective surfactants for microemulsions initially required fluorocarbons or siloxane surfactant tails to achieve ultra-low interfacial tension (γ) values which were of paramount importance in these systems.[90-93] It was discovered experimentally and with molecular simulation that "stubby" hydrocarbon surfactants with branched and methylated tails blocked interactions of water and CO_2, and thus lowered γ to favor formation of W/C microemulsions.[36,42,43,79] For C/W emulsions and foams, the

ultra low γ for microemulsions are not necessary; however, the surfactant must stabilize the thin aqueous films between the discrete CO_2 domains.

The objective of this work is to compare surface pressures (π) and surfactant adsorption of nonionic hydrocarbon surfactants with various tail architectures and head group lengths at the A-W and C-W interfaces. Major differences in the properties are explained in terms of the driving force for surfactant adsorption, tail solvation, area per surfactant molecule (A_m), and surfactant packing. As the head and tail structures of the surfactant are varied, the changes in tail-tail interactions, steric effects, area occupied by the surfactant at the interface, and tail hydrophobicity are shown to have a large affect on the interfacial properties, including the surfactant efficiency (pC20, which is the concentration to produce a 20 mN/m γ reduction). Profound differences in behavior at the A-W versus C-W interfaces are observed upon the formation of branched tails and double tails that have not been explored previously. This understanding of interfacial properties is highly relevant for designing surfactants for stable C/W emulsions and foams for uses including enhanced oil recovery.

2.2 THEORY

Two key thermodynamic properties that influence C-W emulsions and foams are the hydrophilic-CO_2-philic balance (HCB) and the surface equation of state. The phase behavior and curvature of a surfactant monolayer, and thus the resulting emulsion, can be manipulated by varying a formulation variable, such as the hydrophilic-lipophilic balance (HLB) of the surfactant, salinity, and temperature.[94,95] An analogous hydrophilic-CO_2-

philic balance (HCB) has been defined and characterized for high pressure C-W systems.[42,96]

$$1/HCB = \frac{A_{TC} - A_{TT} - A_{CC}}{A_{HW} - A_{HH} - A_{WW}} \quad [1]$$

where A_{ij} is the interaction energy for the various interactions between CO_2 (C), the surfactant tail (T), water (W), and the surfactant head (H). For a CO_2-philic surfactant, where 1/HCB > 1, the surfactant partitions more towards the CO_2 phase and bends about water, forming a W/C emulsion, as shown in Figure 2.1.[94,97] When 1/HCB < 1, the surfactant prefers the aqueous phase and the interface is concave with respect to CO_2, resulting in a C/W emulsion.[3,80,98] The emulsion undergoes a phase inversion at the balanced state when HCB = 1, where the surfactant exhibits an equal affinity for both phases[99] and the interfacial tension (γ) is a minimum (Figure 2.1).[37,82,100-102]

As the interfacial tension of the bare C-W interface (γ_o) varies with the system conditions the effect of the surfactant on the interface is better described by the surface pressure (π). π is defined as the difference between γ_o and γ with surfactant present. The adsorption (molar surface density, Γ) of the surfactant monolayer is obtained from the Gibbs adsorption equation below the CMC (critical micelle concentration):

$$\Gamma = -\frac{1}{RT}\left(\frac{\partial \gamma}{\partial \ln C_{surf}}\right)_{T,P} \quad [2]$$

where C_{surf} is the surfactant concentration, R is the gas constant, and T is the temperature. The area occupied by each surfactant molecule in the monolayer (A_m) is given by

$$A_m = \frac{1}{N_A \Gamma} \quad [3]$$

where N_A is Avogadro's number. The surface pressure at the CMC, π_{cmc}, is known as the effectiveness of the surfactant.[103,104] The efficiency of the surfactant, pC20, is calculated

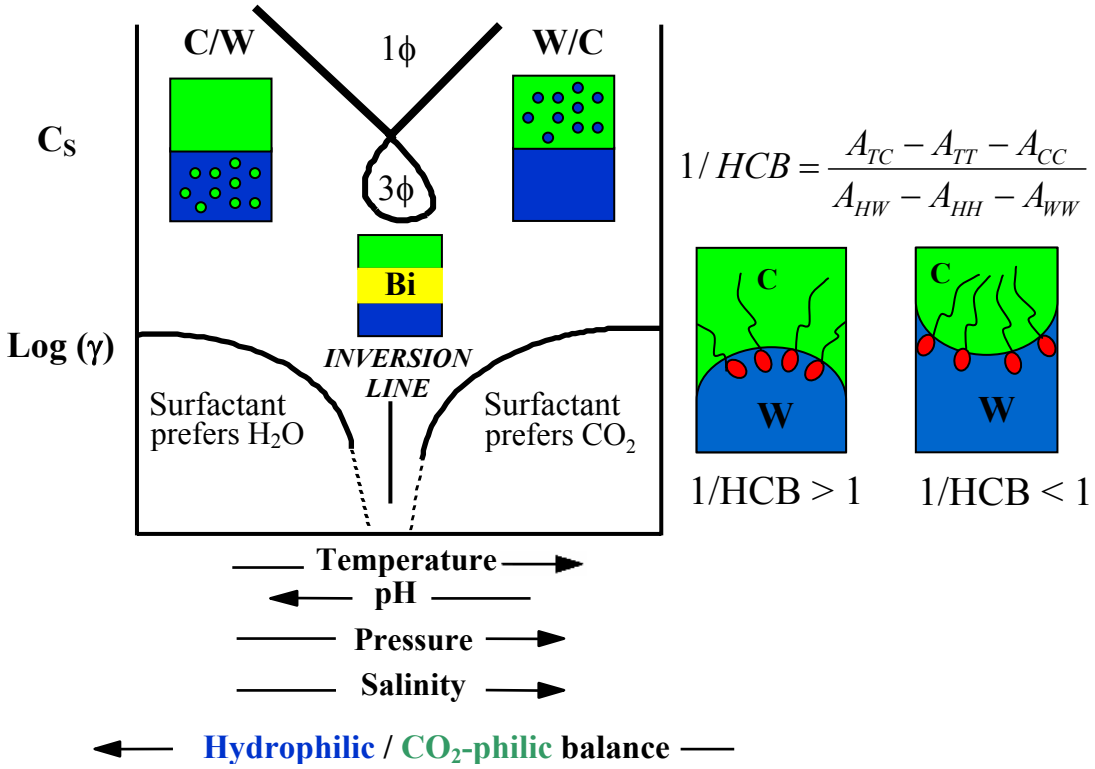

Figure 2.1: Schematic representation of the effect of formulation variables on the phase behavior and interfacial tension of a ternary water-CO_2-nonionic surfactant system.

using the surfactant concentration (C_{20} in units of M) necessary to produce a π of 20 mN/m and is defined as

$$pC20 = -\log(C_{20}) \quad [4]$$

where C_{20} is calculated from a linear fit of the π-log(C) plot below the CMC. The nearest π points to 20 mN/m are used if the plot is non-linear.[85,104]

2.2.1 Surface Equation of State

A surface equation of state (SEOS) can be used to describe π. For a nonionic surfactant the SEOS may be expressed as a "hard-disk" reference term (HD) for the head group and a perturbation term [105]

$$\pi = \pi_{HD} + (\pi_o + \pi_{el}) \quad [5]$$

where π_o is the solvent-tail interaction term, and π_{el} describes electrostatic interactions on the aqueous side of the interface. According to Flory-Krigbaum theory[106]

$$\pi_o = \frac{\alpha_a kT(1-2\chi)v_t^2}{2v_o m^{1/2}\alpha l}\frac{1}{A_m{}^2} \quad [6]$$

$$\chi = v_o(\delta_o - \delta_t)^2 / kT \quad [7]$$

where $\alpha_a = \pi^{1/2}/6$, v_o is the molar volume of the solvent (CO_2 for C/W foam), v_t is the volume of the tail, m is the degree of polymerization, l is the length of a tail segment, χ is the Flory interaction parameter, k is the Boltzmann constant, and $\alpha = 1$. The solubility parameters for the solvent and surfactant tail are δ_o and δ_t, respectively. If $\chi = ½$, then $\pi_o = 0$. In cases where CO_2 is an effective solvent for the tails, $\chi < ½$, and attractive forces favor interpenetration (mixing) of solvent and surfactant tails resulting in an increase A_m for a given π_o. Likewise, π_o increases for a given A_m. The weak solvation of surfactant tails by CO_2, as a result of its low cohesive energy density, leads to unusually large χ

values relative to oils.[87] The smaller molar volume of CO_2 relative to hydrocarbon oils contributes to π_o.

2.3 EXPERIMENTAL METHODS

2.3.1 Materials

Sodium chloride (GR, EM Science), calcium chloride dihydrate (Certified A.C.S, Fisher) and magnesium chloride hexahydrate (Enzyme Grade, Fisher) were used as received. The surfactants 2-ethyl-hexanol-poly(propylene oxide)$_5$-b-poly(ethylene oxide)$_m$ (denoted 2EH-PO_5-EO_m) where m = 9, 11, or 15, 2-ethyl-hexanol-b-poly(ethylene oxide)$_{11.8}$ (denoted 2EH-$EO_{11.8}$), 1-hexanol-poly(propylene oxide)$_5$-b-poly(ethylene oxide)$_{15}$ (denoted 1Hex-PO_5-EO_{15}), lauric acid-b-poly(ethylene oxide)$_{12}$ (denoted LA-EO_{12}), and dioctyl-glycerin-b-poly(ethylene oxide)$_{12}$ (denoted DOG-EO_{12}) were gifts from Dow and used without any further purification. Figure 2.2 contains the structures of these surfactants. The subscripts denote the average number of repeat units per molecule based on the relative mass during synthesis. Research-grade carbon dioxide was passed through an oxygen trap (Oxyclear Model RGP-31-300, Labclear, Oakland, CA) prior to use. Brine was made of deionized (DI) water (Nanopure II, Barnstead, Dubuque, IA), with 2% NaCl, 0.5% $CaCl_2$ and 0.1% $MgCl_2$ w/w (by weight) in water. Concentrations by volume are denoted v/v.

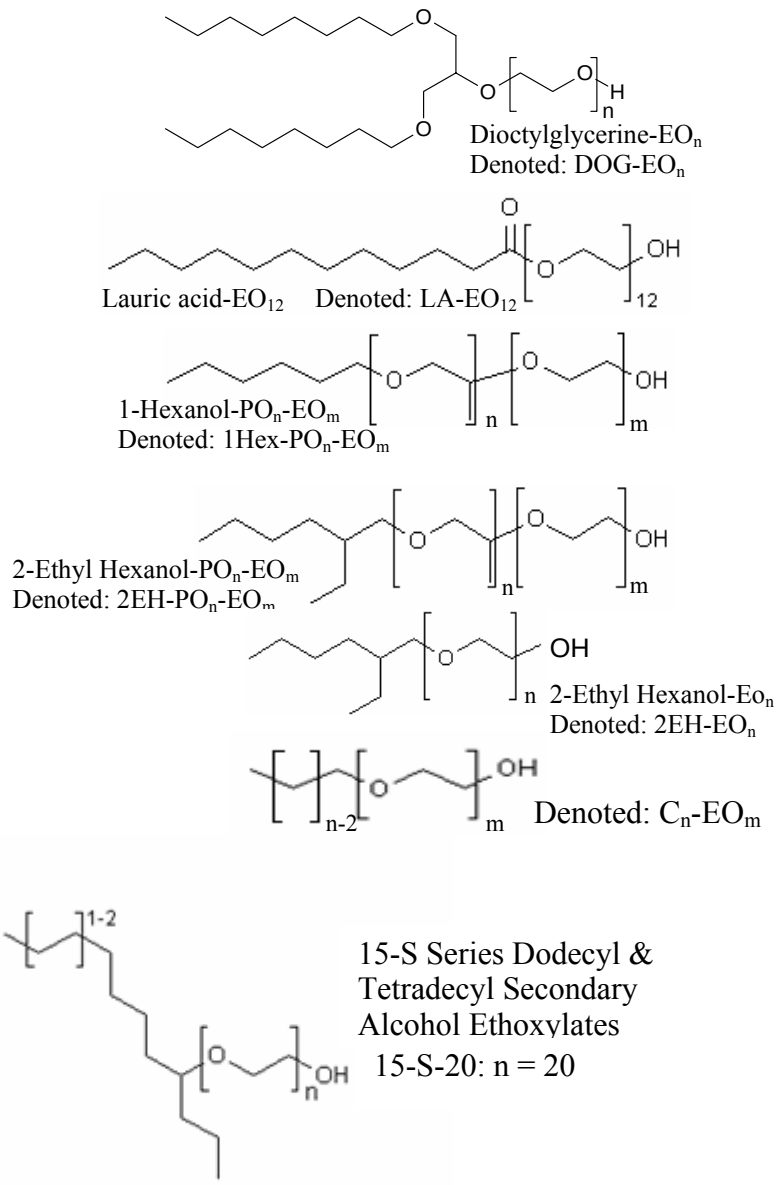

Figure 2.2: Schematic of surfactant structures and naming schemes.

2.3.2 Cloud Point Temperature

The cloud point temperature of the aqueous surfactant solution was measured in a water bath equipped with a temperature controller.[107] The surfactant concentration was 1.0% v/v in water for all samples. The error in the cloud point temperature was ± 1 °C.

2.3.3 Interfacial Tension Measurement

The interfacial tension between CO_2 and aqueous surfactant solutions is determined from axisymmetric drop shape analysis of a captive bubble[108] as previously reported.[107] Briefly, a CO_2 bubble is captured by a glass stage inserted from the top of the view cell chamber, which is filled with surfactant solution. The illuminated bubble is recorded with the digital camera and the profiles were then analyzed through a computer program imbedded in a software package CAM200 (KSV Ltd., Finland) according to the Laplace equation and the interfacial tension was recorded.

The interfacial tension measurements in this study were obtained by averaging at least 10 measurements that were acquired every 10 seconds. Measurements were conducted 2 minutes after a new drop was formed at the lowest density for a given temperature and then the density was increased. A near equilibrium value was assured by examining the standard deviation of the measurements for every condition. When the standard deviation became less than 2% of the mean value, the averaged interfacial tension was assumed to be the equilibrium value. The surface tension of air-aqueous surfactant solutions is measured using the pendant drop method using the same analysis method as the captive bubble.[82]

2.4 RESULTS

2.4.1 Air-Water Interfacial Properties

The properties of several nonionic surfactants at the A-W interface are presented in Table 2.1 at 24 ºC. The CMC, cloud point temperature, and HLB of the surfactants are also included in Table 2.1. The CMC is calculated from the break in the slope of the log(concentration)-γ plot, an example of which can be seen in Figures 2.3 and 2.4 for 15-S-20 and 2EH-PO_5-EO_9, respectively. For 1Hex-PO_5-EO_{15}, the slope of the points closest to the CMC was used.

The surface tension of the surfactant at the CMC, γ_{cmc}, is calculated by averaging at least three measurements conducted at different concentrations above the CMC. The most effective surfactant (highest π_{cmc}) is DOG-EO_{12} with a value of 46.9 mN/m, and the least effective surfactant at the air-water interface is 15-S-20 with a π_{cmc} of only 34.7 mN/m. The surfactants with the highest pC20 values have linear tails. The least efficient (low pC20) surfactants are 1Hex-PO_5-EO_{15} and 2EH-$EO_{11.8}$ with pC20 values of only 3.4-3.5. The –pC20 is labeled in Figures 2.3 and 2.4. The A_m values were determined from equation 3. The surfactant with the lowest measured A_m and thus the largest surfactant adsorption is DOG-EO_{12} with 27 A^2 per molecule. 1Hex -PO_5-EO_{15} has the largest A_m with 100 A^2 per molecule. For comparison between surfactants, one PO unit is estimated to equal about 0.77 CH_2 groups at a surface pressure of 20 mN/m for A-W.[109] For example, an additional 3.85 carbons is added to the 8 carbons of the 2EH-PO_5-EO_{11} tail giving the equivalent of nearly 12 carbons for this surfactant, the same as for LA-EO_{12}.

Table 2.1: Interfacial properties of nonionic surfactants at the A-W interface at 24 ˚C where γ_o is 72.5 mN/m. The data for C_{16}-EO_{15}, C_{16}-EO_{12}, and C_{12}-EO_{12} are from referenced sources as marked. $^{\alpha}$ indicates interpolation of the data for C_{16}-EO_{10} and C_{16}-EO_{15} from Zhang et al.[110]

Surfactants	**Cloud Point (°C)**	**HLB**	**CMC in Water (*10^{-5} M)**	**CMC in Water (% w/w)**	**γ_{cmc} (mN/m)**	**A_m (A^2/molecule)**	**π_{cmc} (mN/m)**	**pC20**
2EH-PO_5-EO_9	61	13.6	394	0.28	27.6	79	44.9	4.5
2EH-PO_5-EO_{15}	>80	15.6	263	0.28	31.9	82	40.6	4.3
1Hex-PO_5-EO_{15}	>80	16.5	1440	1.47	31.6	100	40.9	3.5
C_{16}-EO_{15}[110]		13.5	0.9	0.0008	37.5	43	35.0	5.6
C_{16}-EO_{12} $^{\alpha}$[110]		12.7	1.26	0.0007	36.4	41	36.1	5.5
C_{12}-EO_{12}[111]		14.5	12.5	9e-5	38.3	78	34.2	5.3
LA-EO_{12}	56	15.2	286	0.21	30	62	42.5	4.1
DOG-EO_{12}	46	13.9	17.3	0.015	25.6	30	46.9	4.5
2EH-PO_5-EO_{11}	71	14.4	213	0.19	28.7	69	43.8	4.4
2EH-$EO_{11.8}$	>80	16.2	1570	1.0	31.5	74	41.0	3.4
15-S-20	>100	16.5	64.8	0.067	38.1	68	34.7	4.2

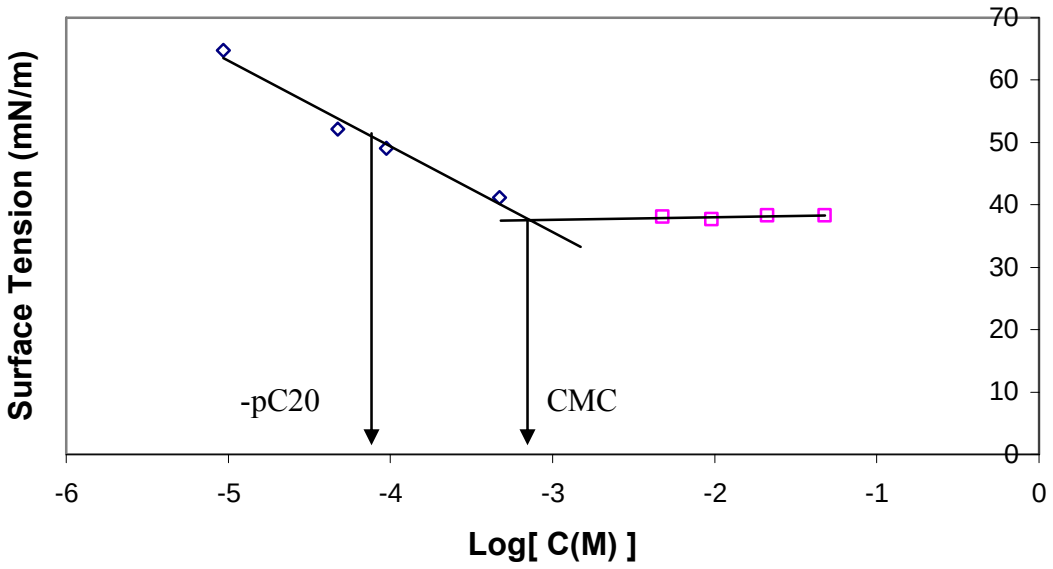

Figure 2.3: The surface tension for 15-S-20 at the air-water interface is plotted as a function of the logarithm of surfactant concentration with labeled CMC and -pC20.

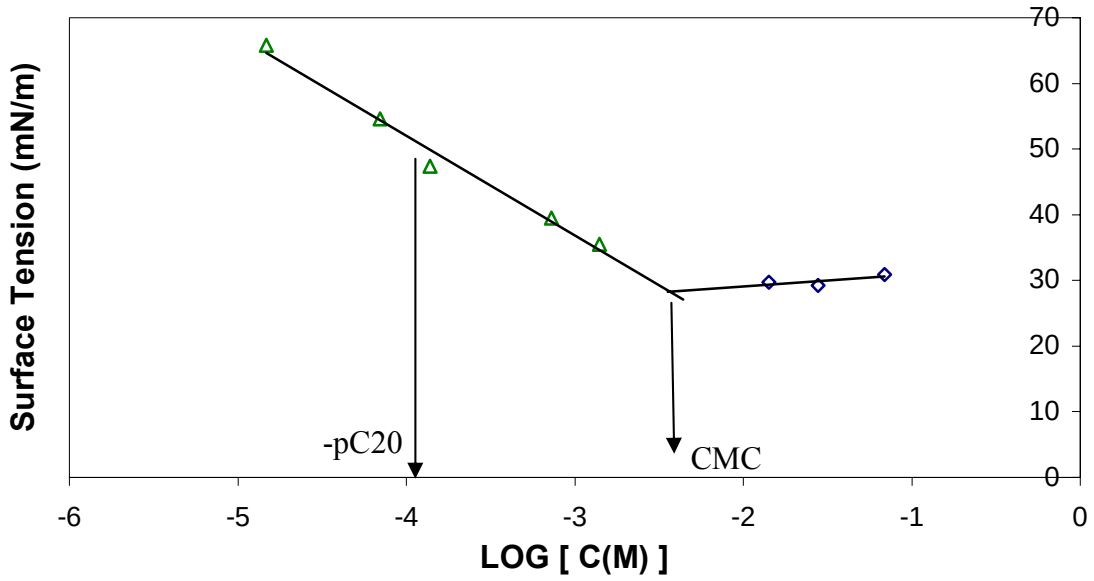

Figure 2.4: The surface tension for LA-EO_{12} at the air-water interface is plotted as a function of the logarithm of surfactant concentration with labeled CMC and -pC20.

2.4.2 CO_2-Water Interfacial Properties

The properties of the nonionic surfactants at the C-W interface are summarized in Table 2.2 at 2000 psia and 24-60 ºC. The C-W γ of the surfactant solutions containing 0.01% w/w surfactant in the water are included in the table at 24 ºC, along with the corresponding π. As the γ_o for C-W depends on the system temperature and pressure, π is the proper way to compare different conditions to understand the role of the solvation forces on the head and tail groups of the surfactant. Values of γ_o were calculated based on the regression function model presented by Hebach et al.[112] for (densities of CO_2) $\rho_{CO2} <$ 0.915 g/ml. For $\rho_{CO2} >$ 0.915 g/ml, γ_o was interpolated by linearly fitting their experimental values at 24 °C, consequently there is a discontinuity in π at this density. Table 2.2 also includes pC20 and A_m measurements for several surfactants at 24-60 ˚C. The γ, π, pC20, and A_m of these surfactants at various conditions of CO_2 density, temperature, and concentration as well as CMC values for C-W systems are included in Appendix A.

Figure 2.5 presents γ of the C-W system as a function of the log of concentration at 60 ˚C and 2000-4000 psia for 1Hex-PO_5-EO_{15}. Figure 2.6 presents the C-W π as a function of CO_2 density for 0.01% w/w 2EH-PO_5-EO_9, 2EH-PO_5-EO_{15}, DOG-EO_{12}, and 1Hex-PO_5-EO_{15} at 24 ºC. In addition, the C-W π is presented as a function of density for 0.01% w/w DOG-EO_{12} at 24-40 ˚C in Figure 2.7 and 0.1% w/w 2EH-PO_5-EO_{15} at 24-70 ºC in Figure 2.8. In both cases, an increase in temperature at constant ρ_{CO2} results in an increase in π as seen at approximately 0.75 g/ml. From 0.3-0.65 g/ml in Figures 2.7 and 2.8, an increase in ρ_{CO2} does not produce a significant change in π at constant temperature. However, from densities above 0.65 g/ml, π is reduced with an increase in the density.

Table 2.2: The interfacial properties of nonionic surfactants at the C-W interface at 2000 psia and 24 ˚C (except as labeled). The γ_o of the C-W interface at 24 ˚C and 2000 psia is 27.7 mN/m. The γ and π are measured at 0.01% w/w surfactant. * indicates the pC20 are estimated from the 0.01% w/w γ data.

Surfactants	**CMC at A-W (% w/w)**	**γ (mN/m)**	**π (mN/m)**	**A_m (A^2/molecule)**	**pC20 24 ºC**	**pC20 40 ºC**	**pC20 60 ºC**
2EH-PO_5-EO_9	0.28	7.5	20.2	219	3.9	4.2	4.5
2EH-PO_5-EO_{15}	0.28	5.6	22.1	233	4.4	5.2	5.2
1Hex-PO_5-EO_{15}	1.47	8.5	19.2	339	3.7	4.4	5.5
DOG-EO_{12}	0.015	4.1	23.6	-	5.1	5.7	-
LA-EO_{12}	0.21	7.9	19.8	-	3.8*	-	-
2EH-$EO_{11.8}$	0.99	12.8	14.9	-	-	-	-
2EH-PO_5-EO_{11}	0.42	7.6	20.1	-	4.0*	-	-

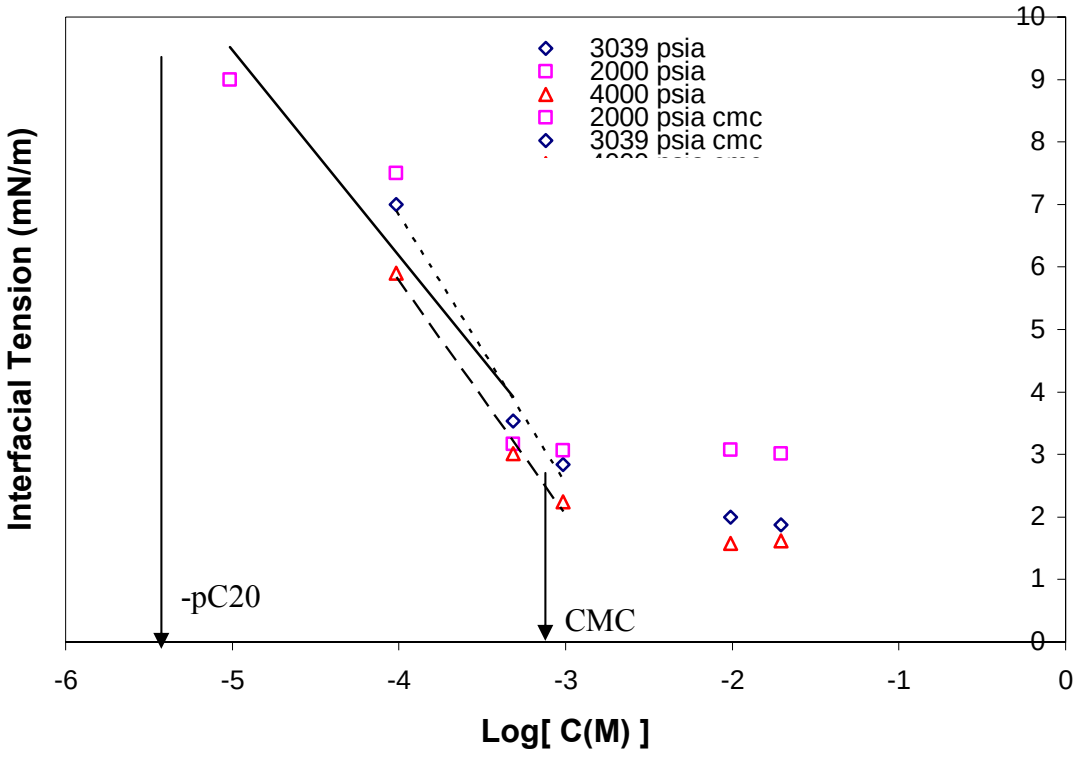

Figure 2.5: The interfacial tension of 1Hex-PO_5-EO_{15} at the C-W interface is plotted as a function of the logarithm of concentration at 60 ˚C and 2000-4000 psia. The –pC20 and CMC are labeled for 2000 psia and 60 ˚C.

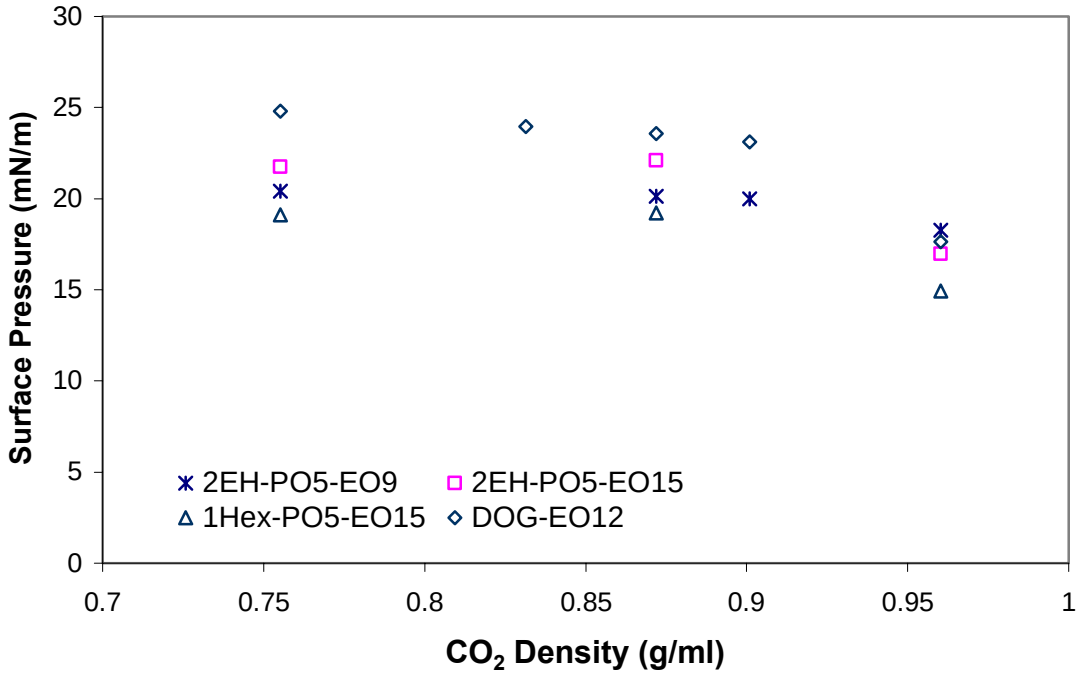

Figure 2.6: The C-W π is plotted as a function of CO_2 density at 24 ˚C and 2000 psia. 0.01% w/w surfactant is used for 2EH-PO_5-EO_9, 2EH-PO_5-EO_{15}, 1Hex-PO_5-EO_{15}, and DOG-EO_{12} in the plot.

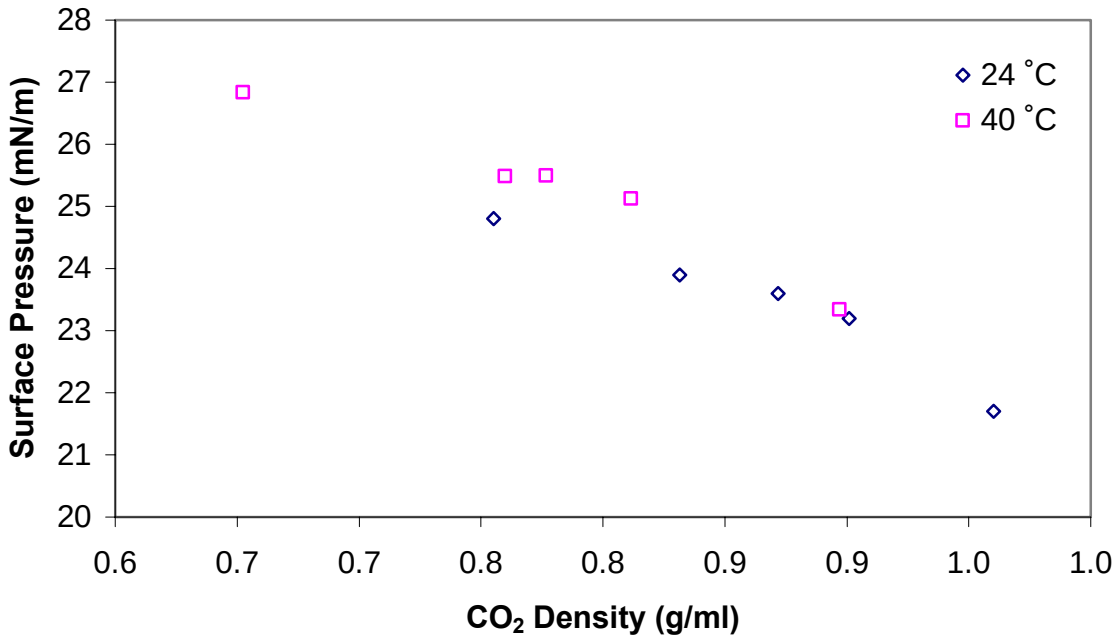

Figure 2.7: The C-W π is plotted as a function of density for 0.01% w/w DOG-EO_{12} at 24-40 ˚C.

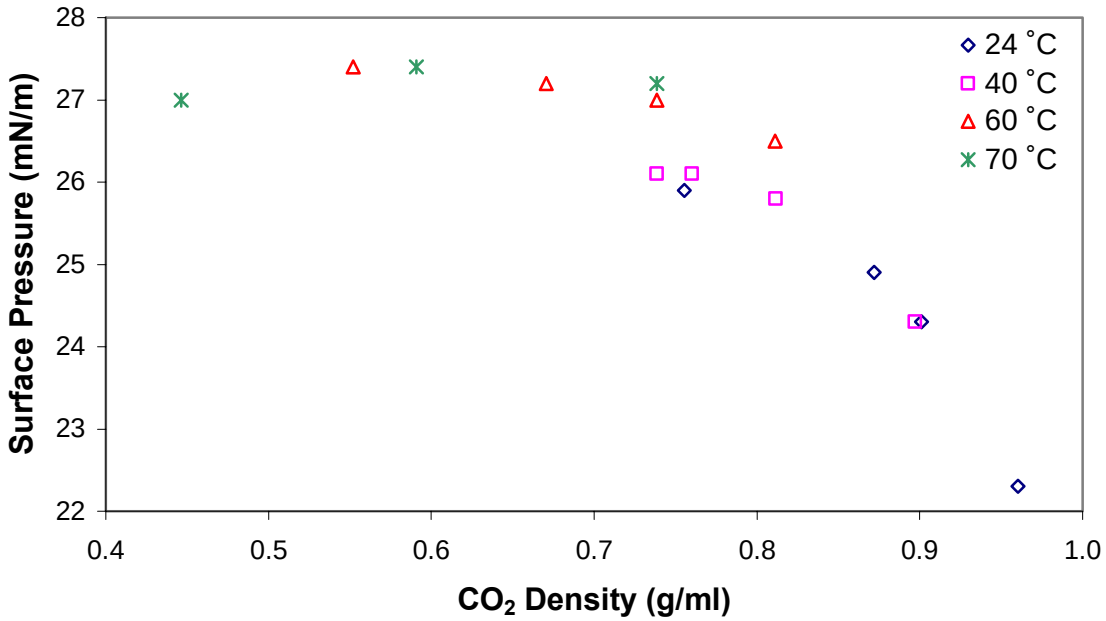

Figure 2.8: The C-W π for 0.1% w/w 2EH-PO_5-EO_{15} is plotted as a function of CO_2 density at 24-70 ˚C.

2.5 DISCUSSION

A summary for this discussion of the differences between the properties of various types of surfactants at the A-W versus C-W interfaces is presented in Table 2.3. The high γ_o value of the binary A-W interface, 72 mN/m, creates a greater initial driving force for surfactant Γ compared with the lower γ_o for C-W (20-30 mN/m).[85] The higher free energy penalty of the W-A interface has the potential to produce a higher level of adsorption to lower the free energy. The ability of CO_2 to solvate the tails, which is not available for air, also affects Γ. The combination of these factors leads to A_m values that are larger at the C-W interface. Figure 2.9 presents schematics of the structure of surfactant monolayers adsorbed at the A-W and C-W interfaces for various tail architectures that will be discussed throughout the discussion section. The surfactant heads are represented as ovals and the carbon chains of the tails are represented by the wavy lines. Monolayer geometries are shown for linear, branched, and double-chain tails at both the A-W and C-W interfaces.

2.5.1 Effect of Tail Structure at the A-W Interface

At the A-W interface, the high γ_o that favors high adsorption and strong tail-tail interactions lead to low A_m values, or equivalently a high surface concentration in the surfactant monolayer as depicted in Figure 2.9.[113] From Table 2.1, the measured A_m values range from 30-100 A^2 per molecule. As the length of the tail is increased at the A-W interface, tail-tail interactions are enhanced and as a consequence surfactant adsorption is improved. In addition, increasing the surfactant tail length increases the efficiency

Table 2.3: Summary of the A-W and C-W interfacial properties for nonionic surfactants with either a linear (*l*), branched or double-chain tail, and increase in the number of EO head groups.

	Air-Water	**CO_2-Water**
γ_o	**72 mN/m**	**20-30 mN/m**
Linear Tail:		
T-T Interactions	Strong with high packing: no tail solvation	Fairly strong: screened by CO_2 solvation and large A_m
$\Gamma = 1/A_m$	High: high γ_o and strong T-T interactions	Low: small γ_o and high CO_2 penetration
pC20	High: high Γ, increases linearly with tail length	Low: low Γ and limited tail solvation
π_{cmc}	High: high Γ	Lower than A-W: lower γ_o
Contact of Phases	Low: high T-T interactions	High: high A_m and CO_2 penetration
Branched or Double-chain Tail:		
T-T Interactions	Weaker than *l*: lower packing	Weaker than *l*: lower packing and greater tail solvation
$\Gamma = 1/A_m$	Lower than *l*: weaker T-T interactions (but greater hydrophobicity can increase Γ)	Higher than *l*: greater tail solvation and greater hydrophobicity
pC20	Lower than *l* with equal number of C's: lower packing Higher than *l* with equal tail length: greater hydrophobicity increases Γ	Higher than *l*: greater A_{HD} and greater tail solvation
π_{cmc}	Higher than *l*: higher CMC increases adsorption	Unknown
Contact of Phases	Lower than *l* at equal surf. conc.: greater A_{HD}	Lower than *l*: greater A_{HD} and greater tail solvation
EO Length (Head Size):		
$\Gamma = 1/A_m$	Equal	Equal
pC20	Equal	Higher with more EO: A_{HD} increases
Contact of Phases	Same	Lower with more EO: A_{HD} increases

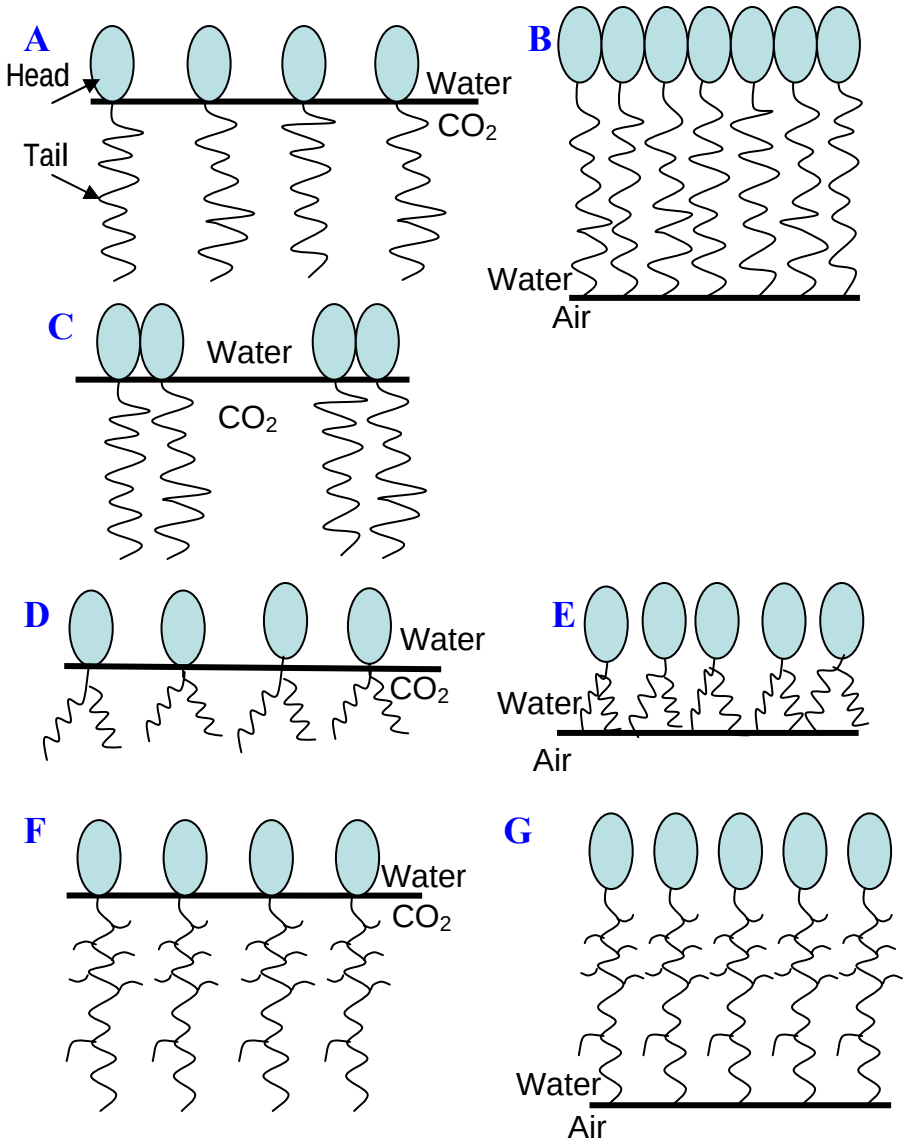

Figure 2.9: Schematic showing adsorption of nonionic surfactant molecules adsorbed at the A-W (B, E, and G) and C-W (A, C, D, F) interfaces with either a linear (A, B, and C), branched (F and G), or double-chain tail (D and E). The nonionic structure is labeled in A, and the phases are each labeled.

(pC20) of the surfactant at the A-W interface linearly due to the greater hydrophobicity of the tail (Table 2.1). The π_{cmc} increases with length as well for nonionic surfactants, for a given mole ratio of EO units.[85]

The efficiencies of the surfactants, pC20, at the A-W interface (Table 2.1) may be used to characterize adsorption and packing at the A-W interface, before it is fully saturated. Varadaraj et al. investigated the effect of branching on the pC20 value at the A-W interface and found that branched tails were more efficient than linear tails of the same length; however they are less efficient than linear tails of the same carbon number.[104] The situation is similar for our surfactants. Steric repulsion between methylated and branched surfactant tails decrease tail-tail interactions and the surfactant adsorption at the interface[114] as depicted in Figure 2.9. Consequently, the pC20 values for branched surfactants are smaller relative to linear surfactants with the same number of carbons in the tail.

A double-chain tail structure, such as that for DOG-EO_{12}, has been shown to be more efficient (higher pC20) than the corresponding linear tail of the same carbon number, however the surfactants had ionic ethylene oxy sulfate heads which were repulsive.[103] The additional area between neighboring ionic heads will affect the surfactant performance, thus the larger double-chain tail surfactant had a higher pC20. For the nonionic surfactants investigated here, the pC20 of DOG-EO_{12} is lower relative to C_{16}-EO_{12}. The double-chain tail disrupts the monolayer packing thus lowering the pC20, similar to the effect of tail branching. Because of the lack of repulsion between the EO heads, the effect of the tails is more pronounced.

The lowest pC20 values are for 2EH-$EO_{11.8}$ and 1Hex-PO_5-EO_{15}, which have the equivalency of 8 and 10 carbons, respectively. The low hydrophobicity of the tails for these surfactants cannot balance the strong hydrophilicity of the larger heads, as seen in

the extremely high CMC values. A high concentration of surfactant is required before the hydrophobic effect of the tails leads to the formation of micelles, indicating the preference of the molecules for the water phase versus the A-W interface. In summary, the unbalanced nature of the heads versus tails in these surfactants causes low adsorption of these surfactants at the A-W interface and low pC20 values.

2.5.2 Effect of Tail Structure at the C-W Interface

The interfacial properties are quite different at the C-W versus A-W interface, as shown in the summary in Table 2.3. At the C-W interface, solvation of tails by CO_2 molecules screen tail-tail interactions leading to larger A_m values relative to A-W.[113] Similar findings have been shown for the oil-water interface compared with the A-W interface. Aveyard et al. confirmed larger A_m values for $C_{12}EO_1$ and $C_{12}EO_2$ (mono- and dioxyethylene dodecyl ethers) at the heptane-water interface relative to the air-water interface.[115]

As shown in Table 2.2, the A_m values at the C/W interface are typically 3 times larger than at the A/W interface due to the low driving force for surfactant adsorption (γ_o) and a greater penetration of small CO_2 molecules into the tail region of the surfactant monolayer.[85] These factors result in larger interfacial contact of the two phases for C-W relative to A-W.[116] Packing of surfactant molecules at the C-W interface is also much less important due to the large A_m values.

The pC20 and π values for 0.01 % w/w surfactant at the C-W interface may be used to determine surfactant adsorption (Table 2.2). As expected, the small tail of 2EH-$EO_{11.8}$ does not balance the large head resulting in low surfactant adsorption (Figure 2.1) and consequently the lowest π. For the C-W interface greater tail solvation increases surfactant adsorption resulting in greater blocking of interfacial area as depicted in Figure

2.9, which raises π. The solubility of methylated and branched surfactants of the Tergitol TMN family (nonionic ethoxylates) in CO_2 were much greater than those of corresponding linear surfactants as measured by a lower cloud point pressure and a greater surfactant Γ at the C-W interface by Ryoo et al.[42] Branching of the tail or addition of PO units increases the hydrophobicity of the tail compared to a linear tail of the same length.[117] It also raises the relative solvation of the tail by CO_2[103,118] thus decreasing tail-tail interactions which lowers χ and increases π (equations 6 and 7). PO has a higher solubility in CO_2 relative to EO and CH_2 due to a low cohesive energy density, favorable interactions with the quadrupole moment of CO_2, and weaker self-association.[36,46,119-121] Additionally, pendent CH_3 groups have a lower cohesive energy density than CH_2 groups and favor solvation by CO_2.[80] The more favorable solvation for DOG-EO_{12} tail leads to a lower χ, higher Γ, and greater π values than the linear LA-EO_{12} as well as all of the other 12 EO surfactants listed at 0.01% w/w surfactant in water.

In addition to influencing solvation (through π_o of equation 6), branching or PO addition to the tail cause the molecule to occupy a larger area, *that is*, with a lower fractional free volume[41,43] at the interface than for a linear tail (Figure 2.9). This occupied area is essentially A_{HD}. The increase in A_{HD} also raises π. Previously, the measured area per alkyl chain in the adsorption layer was proven to be greater for a double-chain tail than the corresponding single-chain tail at the W-O interface.[109] Rekvig et al. also found that a double-chain tail blocks more interfacial area than a linear tail for the same interfacial concentration of surfactant through simulations.[122] A larger A_{HD} is responsible for the decrease in interfacial contact of oil and water, or alternatively CO_2 and water, which lowers γ.[85,109,113,123,124] This effect of branching on A_{HD}[36,42,43,79] and thus pC20 may be seen for the branched 2EH-PO_5-EO_{15} versus 1-Hex-PO_5-EO_{15} at the C-W interface (Table 2.2). The increase in A_{HD} is pronounced for DOG-EO_{12} as the two chains of the

tail may independently spread out at the interface occupying a large area[103] and leading to the highest pC20 value in Table 2.2 at 24 ˚C. The additional tail solvation from the weaker tail-tail interactions also help to increase the pC20 value of DOG-EO_{12}.

Variation in the solvation of surfactant tails can also occur with changes in the density of CO_2. An increase in the density of the CO_2 increases the solvation of the hydrocarbon tails, as well as γ_o. Thus, it is more meaningful to examine density effects on π rather than γ (Figures 2.6-2.8). At all conditions, a drop in π occurs as the density of CO_2 is raised, with a larger change occurring at higher densities. As the density of CO_2 is increased, the tail-CO_2 interactions become more favorable, as described by the SEOS (equations 6 and 7) and χ decreases. The lower χ value by itself would increase π at a constant A_m. In contrast, the experimental π decreases, which is most likely due to an increase in A_m. The drop in γ_o with density reduces the driving force for adsorption and raises A_m. Although there is a high degree of error in the A_m measurements, a slight increase at higher densities is seen for all of the surfactants except 2EH-PO_5-EO_9.[107] In addition, from equation 6, if $\chi < 0.5$, then π_o is a positive contribution to π and the larger A_m would ultimately lower π.

The difference in interfacial properties for the A-W and C-W interfaces is substantial. Branching improves solvation, favors adsorption and raises π for the C-W interface whereas, for the A-W interface it decreases packing and raises A_m which lowers π. Thus, it is not obvious that one may infer the behavior at C-W interfaces from easily measured data at A-W interfaces at atmospheric pressure. However, such a correlation may be possible in some instances. Eastoe et al. found a correlation between γ_{cmc} of a given surfactant at the A-W interface and its performance in W-C microemulsions as measured by the phase transition pressure (P_{trans}) for a range of homologous anionic

fluorocarbon surfactants.[125] The trend in γ_{cmc} did not entirely match the P_{trans} results, or correlate with the relative changes.

2.5.3 Effect of Temperature

An increase in the thermal energy of the system can have a major effect on the interactions of a surfactant with both water and CO_2. This behavior has been investigated by optical microscopy,[35] turbidimetry,[18,126,127] SANS, [128,129] and Monte Carlo simulations.[130] When the density is held constant, the C-W γ_o decreases slightly as the temperature is elevated up to 70 ^oC. For nonionic EO surfactants, a rise in temperature leads to dehydration of the EO groups[32] until finally they are no longer hydrophilic and the surfactant precipitates from the water at the cloud point. Therefore, increasing the temperature of the system at constant CO_2 density pushes the balance of these surfactants away from the water and more towards CO_2 (Figure 2.1).[32] As the EO groups are dehydrated and the surfactant is closer to the balanced point, adsorption is expected to increase.

The changes in surfactant performance with this change in balanced state are exemplified by 1Hex-PO_5-EO_{15} and 2EH-PO_5-EO_{15}. The 1Hex-PO_5-EO_{15} tail is less CO_2-philic than 2EH-PO_5-EO_{15} as a result of fewer branches. This shift away from the interface towards water produces a lower π. As the temperature is raised from 24 to 40 $^{\circ}C$, 1Hex-PO_5-EO_{15} moves from water to the interface, and the pC20 increases from 3.5 to 4.4 at 2000 psia, respectively.

In addition to the temperature driven change in EO hydration of the head groups, enhanced solvation of the tail groups by CO_2 can also occur. Greater CO_2 solvation of poly(1,1-dihydroperfluoroctyl methacrylate)-b-poly(ethylene oxide) tails as indicated by less flocculation of W/C miniemulsions droplets was found at higher temperatures.[127]

Greater extension and solvation of polymer brushes in CO_2 as well as end-grafted polymers on silica has also occurred with an increase in temperature.[126,128] As Figures 2.7 and 2.8 illustrate, π increases slightly with temperature elevation when the nonionic surfactants DOG-EO_{12} and 2EH-PO_5-EO_{15} are present, respectively, due to the greater tail solvation.

2.5.4 Effect of Head Size

For single-tail nonionic surfactants at the A-W interface, an increase in hydrophilicity with the number of EO groups increases the CMC and A_m. Schick et al. found an increase in A_m from 55 to 77 A^2 per molecule when the number of EO groups was increased from 7 to 12 with a single *n*-dodecanol tail.[131] Here the larger head group occupied more space than the linear tail and raised A_m (see Figure 2.9). For a branched tail, A_m did not increases with the EO length[132] since A_{HD} of the branched tail was greater than that of the EO groups.[132] We found the same behavior for the series of surfactants 2EH-PO_5-EO_m, where m = 9, 11 and 15 in Table 2.1, where the A_m was the about the same for all three. A highly flexible PO segment will occupy much more area than a more rigid alkane tail. In addition, the ethyl branch will raise the tail area. The combination of these effects causes the tail to be more dominant than the EO head in influencing A_m. The similar A_m values produce about the same pC20 values.

For the C-W interface, the A_m is also relatively constant for m = 9 and 15 for the 2EH-PO_5-EO_m surfactants (Table 2.2). Like the A-W interface, the A_m was dominated by the larger area of the tail versus the head. However, unlike the case for the A-W interface, the pC20 increased with an increase in the number of EO groups (9 to 15) at the C-W interface (Table 2.2) at all temperatures. With the larger A_m values at the C-W interface, the interfacial area occupied by the surfactant molecule to block contact between water

and CO_2 is very important.[43] The additional EO units of 2EH-PO_5-EO_{15}, which have a moderate solubility in CO_2,[46] are capable of increasing the area occupied by the surfactant molecule. In addition, the greater hydrophilicity and higher cloud point temperature of 2EH-PO_5-EO_{15} allow the surfactant to remain more interfacially active as the temperature is raised, relative to 2EH-PO_5-EO_9 (as shown in Table 2.2 in terms of π and pC20).[109] As a consequence of the tail solvation that occurs at the C-W interface, changes in the number of EO groups lead to different results than in the case of the A-W interface. Whereas the identical A_m values result in equal pC20 values for the A-W interface, pC20 and π are increased at the C-W interface with a greater number of EO units.

2.6 CONCLUSIONS

The interfacial tensions of nonionic hydrocarbon surfactants at the A-W and C-W interfaces were investigated systematically as a function of the EO length and tail structure. For linear surfactants at the A-W interface, high efficiencies (pC20) result from dense monolayers produced by the high γ_o driving force for adsorption and strong tail-tail interactions. The dense monolayers reduce contact between the phases. For a given carbon number, branched or double-tails lower the packing ability, reduce attractive tail-tail interactions, and thus lower efficiencies.

At the C-W interface where a low γ_o creates a low driving force for adsorption, A_m and thus the contact between the phases is greater, relative to the A-W interface. Thus, the steric repulsion term in the surface equation of state is much less important, and instead, the tail solvation plays the major role. The tail solvation increases with branching

or double tails from a closer balance between tail-tail versus CO_2-CO_2 interactions (smaller and more favorable χ). This increase in solvation, as well as the increase in surfactant hydrophobicity, both raise the adsorption. Furthermore, the increase in occupied area of the surfactant with branching raises A_{HD} and reduces contact of the water and CO_2 phases. These factors produce greater efficiencies (pC20s) for branched tails, and in our case, the highest efficiencies with a double tail (Table 2.2). The area occupied by the surfactant can also be increased by adding EO groups to the head, given the moderate solubility of EO in CO_2. As a consequence the efficiency of 2EH-PO_5-EO_{15} is greater than that of 2EH-PO_5-EO_9, although at the A-W interface the efficiencies are equal.

Despite the differences in γ_o, tail solvation, and surfactant adsorption at the C-W and A-W interfaces, pC20 values above 5 were achieved in each case for the best surfactants. For the A-W interface at constant carbon number, this required linear surfactants for high packing to block the two phases. In contrast, for the C-W interface where adsorption is much lower, a double-tailed surfactant was the most efficient as a consequence of tail solvation and a larger occupied area. This fundamental understanding of interfacial properties, and the profound differences at A-W and C-W interfaces, will be very useful for designing surfactants for C/W foams in a variety of applications including enhanced oil recovery.

Chapter 3: Morphology and Stability of Carbon Dioxide-in-Water Foams with Nonionic Hydrocarbon Surfactants

The stabilities of high-pressure carbon dioxide-in-water (C/W) foams formed with branched nonionic hydrocarbon surfactants were investigated by *in-situ* optical microscopy. Over two dozen hydrocarbon surfactants were shown to stabilize C/W foams with Sauter mean bubble diameters as low as 1-2 microns. Coalescence of the C/W foam bubbles was rare for bubbles larger than about 0.5 μm over a 60-hour period. In addition, Ostwald ripening became very slow after 60 hours. By better blocking of the CO_2 and water phases with branched and double-tail surfactants, the interfacial tension deceases, the surface pressure increases, and the C/W foams become highly stable. For branched surfactants, the stabilities were markedly lower for air/water foams and decane-water emulsions. The greater stability of the C/W foams to coalescence may be attributed to a smaller capillary pressure, lower drainage rates, and a sufficient surface pressure and thus dilational modulus, plus small film sizes, to hinder spatial and surface density fluctuations that lead to coalescence. Unexpectedly, the foams were stable even when the surfactant favored the CO_2 phase over the water phase, in violation of Bancroft's rule. This unusual behavior is influenced by the low drainage rate, which makes Marangoni stabilization of less consequence, and the strong tendency of emerging holes in the lamella to close as a result of surfactant tail flocculation in CO_2. The high distribution coefficient towards CO_2 versus water is of significant practical interest for mobility control in CO_2 sequestration and enhanced oil recovery by foam formation.

3.1 INTRODUCTION

Emulsions and foams of carbon dioxide and water, the two most plentiful solvents on earth are of interest in a wide range of applications in green chemical processing, materials science, microelectronics and biotechnology.[133] Carbon dioxide may be injected into reservoirs for sequestration and/or for enhanced oil recovery (EOR).[134] Carbon dioxide (CO_2) is miscible[54,55] in all proportions with the lighter hydrocarbon components of the crude oil (up to 14 carbons depending on the system pressure) and partially miscible with heavier hydrocarbons[56] which facilitates the oil recovery process. Rossen et al. reviewed mobility control in EOR with CO_2 foams.[59] CO_2 is an environmentally benign, non-toxic, non-flammable, and recyclable solvent that is in many cases available or produced near oil reservoirs. Given its accessible critical point of 31.1 ˚C and 1070 psia, sufficient solvent strength of CO_2 can be reached under many reservoir conditions.

The design of surfactants for the stabilization of the continuous aqueous films in a C/W foam is still in its infancy.[59,80] An important distinction between C/W and A/W foams is the marked difference in γ_o (without surfactant present) for the CO_2-water (C-W) (20 to 30 mN/m) versus the air-water (A-W) interface (72 mN/m). The smaller γ_o for the C-W interface leads to a smaller driving force for surfactant adsorption to further reduce the interfacial tension.[85] Therefore, the area per surfactant molecule (A_m) at the C-W interface is often much larger than that at the A-W interface as shown experimentally[86,87] and by molecular dynamics simulations.[81] Most studies of surfactants at the C-W interface have focused on W/C microemulsions.[37,43,78,79,82,83,88,135-137] In most cases, fluorocarbon or siloxane surfactant tails were required to achieve sufficiently low γ values and reduce interdroplet interactions.[91,138-140] However, “stubby” hydrocarbon

surfactants with branched and methylated tails blocked the interfacial contact of water and CO_2 to lower γ enough for W/C microemulsions.[36,42,43,79] For C/W foams with much lower specific surface areas than microemulsions, the surfactant requirements are much less stringent. Consequently, γ may be much higher and strong attraction between tails on two approaching water droplets are now no longer limiting.

CO_2 foams have been previously studied by da Rocha et al.[98] where nonionic block copolymer stabilizers were explored for C/W emulsions with up to 70% v/v (by volume) CO_2 with stability against coalescence and flocculation for greater than 48 hours. In addition, Dhanuka et al.[80] studied the hydrocarbon surfactant commercially known as Tergitol TMN 6 by Dow (90% poly (ethylene glycol) 2,6,8-trimethyl-4-nonyl ether and 10% water w/w, by weight) as a stabilizer for 50-90% v/v CO_2 emulsions. Cell sizes of less than 10 μm were observed along with stability in excess of 24 hours for a 90% v/v C/W foam.

For foams, the stabilities of the lamellae play a key role in the macroscopic stability. The destabilization of foam over time occurs via multiple mechanisms including drainage of the liquid in the lamella, coalescence of neighboring bubbles (lamella rupture), and Ostwald ripening. Coalescence in the form of spinodal decomposition occurs when the attractive van der Waals forces between neighboring bubbles overcome the repulsive forces in the foam lamella.[65-68] With the appropriate stabilizers in the lamella, the foam can reach a metastable state where coalescence can occur due to the formation and growth of holes in the lamella[67,69,70] or drainage of the lamella.[141-143] Spatial and surface density fluctuations[144] can be responsible for the formation of these holes and can also induce spinodal decomposition.[66] The combined effects of thermodynamic and rheological properties on the stability of emulsions of oil and water are well-known to be highly complex and only partially understood.[66,142,145] For C/W

foams, we are not aware of any studies that have reported each of the key properties: foam texture (at the micron length scale), foam stability, interfacial properties, and foam viscosity.

The objectives of this study are to demonstrate that viscous C/W foams (emulsions) may be formed with over two dozen branched nonionic hydrocarbon surfactants, and to evaluate various factors that influence foam stabilities, particularly foam texture, phase behavior and recent measurements of interfacial properties at the C-W interface.[146] These properties include γ, π, and the surfactant efficiency, pC20, which is the concentration to produce 20 mN/m drop in interfacial tension. Foams with greater than 90% v/v CO_2 were characterized by *in-situ* optical microscopy over time periods from seconds to days for a cell path length of only 25 μm.[80] The viscosity, bubble size, and polydispersity are examined versus surfactant structure over a range in concentration, shear rate, temperature, salinity, and foam quality to characterize the ageing mechanisms: drainage, coalescence, and Ostwald ripening. Stable foams are reported even for surfactants that favor the dispersed CO_2 phase over the continuous water phase.

For surfactants with branched tails, the stabilities of C/W foams are compared with much less stable A/W foams and O/W emulsions. The behavior is described in terms of cloud point temperature, surface pressure, Laplace pressure, and surfactant efficiency. As the distribution coefficient of the surfactant is shifted from hydrophilic to CO_2-philic with temperature, the C/W foam stabilities changed very little in violation of Bancroft's rule. We attribute this unusual behavior to viscous stresses transmitted through each phase during emulsion formation, slow film drainage, and reduced hole formation and growth. Further studies will be required to offer a more complete understanding. The measurement and understanding of foam stability and viscosity are useful for the design of surfactants for CO_2 foam in enhanced oil recovery. In EOR, the surfactants in this

study that are CO_2 soluble and favor CO_2 over water may be used to improve injectivity and mobility control in order to increase oil recovery.

3.2 EXPERIMENTAL METHODS

3.2.1 Materials

Sodium chloride (GR, EM Science), calcium chloride dihydrate (Certified A.C.S, Fisher) and magnesium chloride hexahydrate (Enzyme Grade, Fisher) were used as received. The surfactants (structures and naming schemes presented in Figure 3.1) were gifts from Dow and used without any further purification. The subscripts denote the average number of repeat units per molecule based on the relative mass during synthesis. Research-grade carbon dioxide was passed through an oxygen trap (Oxyclear Model RGP-31-300, Labclear, Oakland, CA) prior to use. Brine was made of deionized (DI) water (Nanopure II, Barnstead, Dubuque, IA), with 2% NaCl, 0.5% $CaCl_2$ and 0.1% $MgCl_2$ w/w in water (by weight). The symbol v/v means by volume in the aqueous phase for surfactants unless otherwise stated.

3.2.2 Cloud Point Temperature

The cloud point temperature of the aqueous surfactant solution was measured in a water bath equipped with a temperature controller. The surfactant concentration was 1.0% v/v in water for all samples. The error in the cloud point temperature was ± 1 ˚C. The cloud point temperature in brine included 2% NaCl, 0.5% $CaCl_2$, and 0.1% $MgCl_2$ w/w in the water.

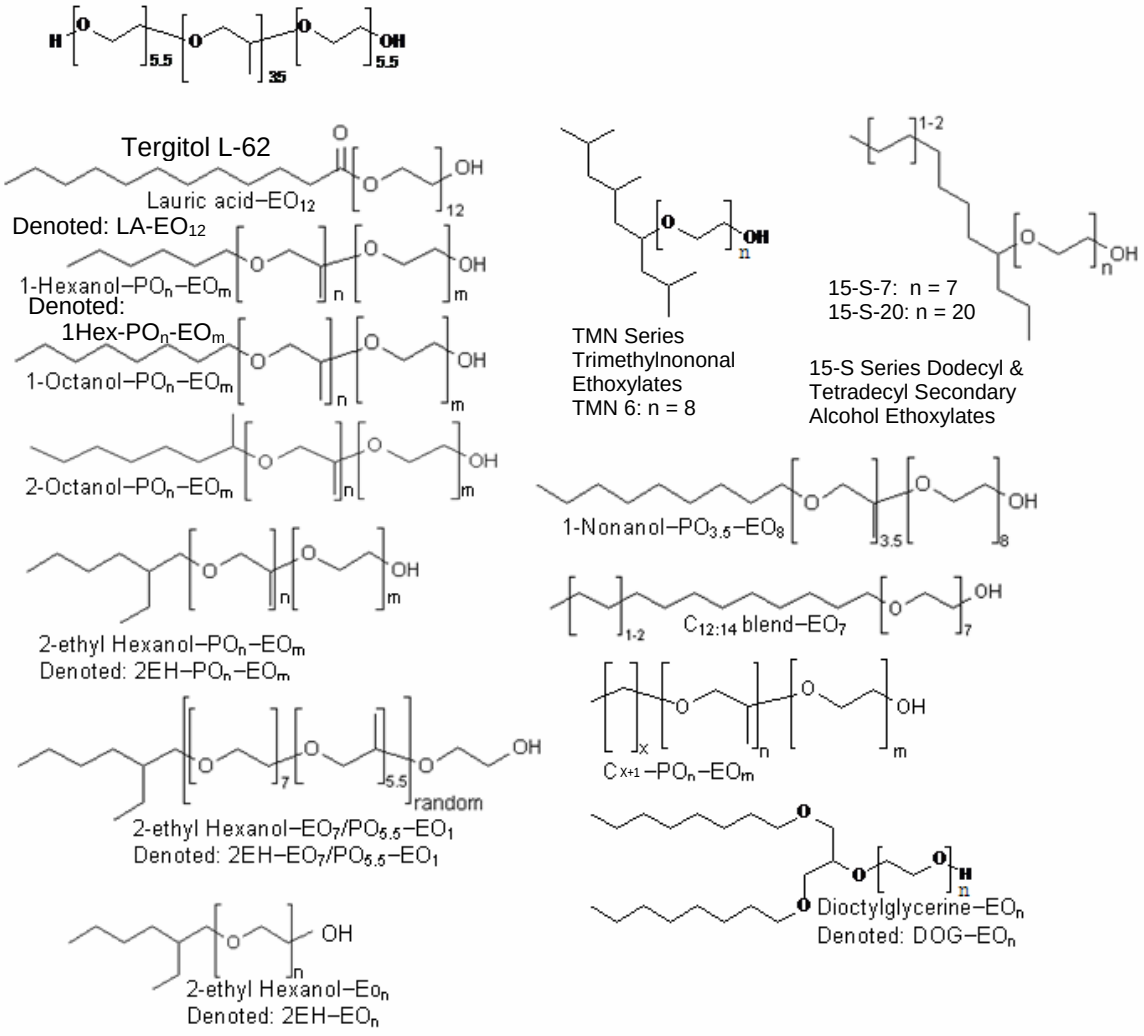

Figure 3.1: Schematics and naming scheme of surfactants.

3.2.3 Interfacial Tension Measurement

The interfacial tension between CO_2 and aqueous surfactant solutions is determined from axisymmetric drop shape analysis of a captive bubble[108] as previously reported.[107] The surface pressure (π) is the difference between γ_o (no surfactant) and γ (with surfactant). The efficiency of a surfactant (pC20) is calculated as the –log of the surfactant concentration (in units of M) to produce a π of 20 mN/m as determined from the –log(concentration)-π plots. The error in pC20 is ± 0.2.

3.2.4 Partitioning of Surfactant into CO_2

The detailed procedure to measure the equilibrium partitioning of the surfactant between the CO_2 and water phases has been previously published.[107] Briefly, a sample of CO_2 upper phase is taken from a C-W-surfactant system and the concentration of surfactant in the sample solution was determined by pendant-drop surface tension measurement below the CMC based on a calibration made for known surfactant concentrations.

3.2.5 C/W Foam Formation and Apparent Viscosity

The apparatus to measure foam viscosity is depicted in Figure 3.2. An Isco syringe pump (model 260D) with a series D pump controller and an HPLC dual head pump (LDC/Milton Roy consta Metric III) were used to inject the CO_2 and aqueous surfactant solution, respectively, at set flow rates. The mixture of CO_2 and surfactant solution entered a sand pack with hydrophilic pores for foam generation. The sand pack was either 10.2 cm long, 0.386 cm inner diameter tube packed with pre-washed 20-40

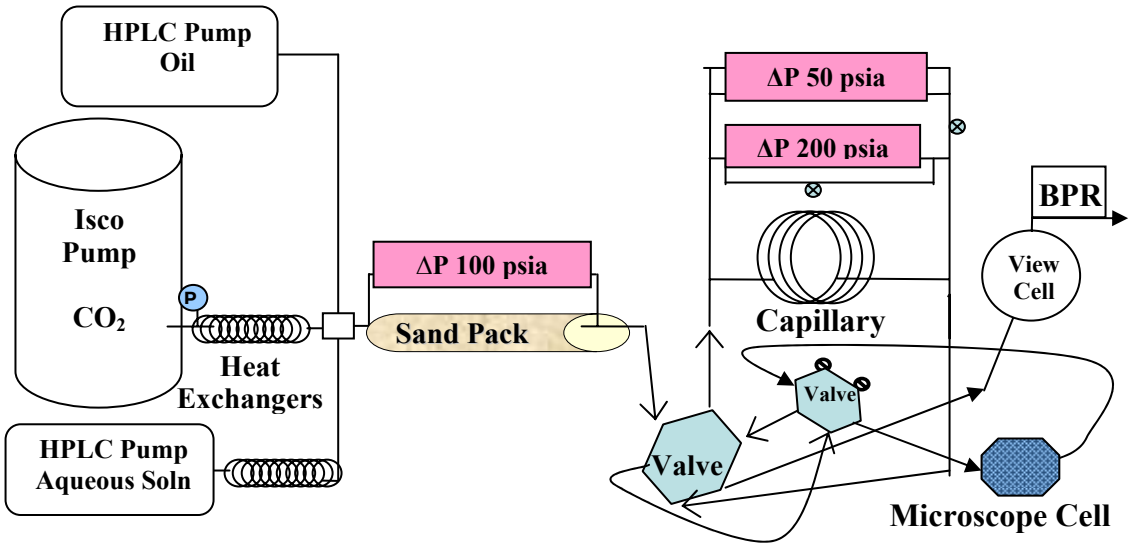

Figure 3.2: Schematic of equipment used for foam viscosity and bubble size measurements. BPR means the back pressure regulator. The sand pack is used as the foam generator. The pressure transducers are represented by a circle with a P in the middle.

Mesh non-spherical sand (420-840 μm in diameter) that gives 50 μm pores or a 12.1 cm long, 0.76 cm inner diameter tube packed with non-spherical sand of 125 μm diameter that gives 10 μm pores. Only for the short time (1-2 min) stability of highly sheared foams (total foam flow rates of 12-15 ml/min reported in Table 3.2) a sand pack with 10 um pores was used in which the length was extended to 14.7 cm long. Appendix B includes information on foam generation in porous media and the equations for estimating pore size in sand packs. Sand was held in place by wire screens affixed to tubing ends. The sand pack for the TMN 6 experiments used packed cotton at the tubing ends instead of the wire screens. Sand packs were rinsed with a few hundred ml of ethanol and several liters of DI water until the effluent was surfactant-free. Then surfactant pre-adsorption was accomplished by running a sufficient volume of surfactant solution (20-50 mL) thru the sand pack. In certain experiments, a differential pressure meter was used to measure the pressure drop across the sand pack using a 100-psia diaphragm.

The foam generated in the sand pack flowed through a six-port valve (Valco Instruments, model C6W) followed by a capillary (0.0762 cm inner diameter, 195 cm long). Either a high-range or a low-range differential pressure meter (Validyne model CD23) measured the differential pressure (ΔP) across the capillary. The high-range pressure meter contained either a 100 or 250-psia diaphragm, while the low-ranged pressure meter contained either a 20 or 50-psia diaphragm. An average ΔP was obtained by averaging the values recorded over at least 2 minutes while the foam was flowing at approximately steady state, with ΔP varying less than 15% of the mean value.

The effluent of the capillary flowed through a second six-port valve (Valco Instruments, model C6W) into a stainless steel cylindrical visual cell with two sapphire windows (0.4 cm path length and 1.8 cm diameter) where macroscopic visual

observations of the bulk flowing foam were made. Finally the foam flowed through the heated (> 40 ˚C with a water bath) back-pressure regulator (BPR) (Swagelok model SS-4R3A adjustable relief valve with either a R3A-E spring for 2250-3000 psia back pressure setting or a R3A-F spring for 3000-4000 psia) where CO_2 expanded to atmospheric conditions and the surfactant solution was captured for disposal. The system pressure reported was the pressure at the BPR. The BPR was adjusted to set the system pressure. The temperature of the entire apparatus was maintained at ± 0.2 ˚C by use of a water bath equipped with one or more temperature controllers (Julabo, Inc.).

The apparent viscosity of a bulk foam (η_{foam}) is calculated from the known shear rate ($\dot{\gamma}$) and measured pressure difference (ΔP) across the capillary with a length (L) of 195 cm. The shear stress (τ) and shear rate are calculated from $\Delta P R_{cap}/L$ and the velocity gradient (U/R_{cap}), respectively. The average velocity, U, is determined from the total volumetric flow rate of the foam (the sum of the flow rates for the two phases, Q_{total}) divided by the cross sectional area of the capillary tube. An additional geometric scaling term, $\lambda = 0.5$, is used to calculate the apparent foam viscosity

$$\eta_{foam} = \frac{\tau}{\dot{\gamma}} = \frac{\left(\frac{\Delta P \cdot R_{cap}}{L}\right)}{\left(\frac{U}{R_{cap}}\right)} \lambda = \frac{\lambda R_{cap}^{\,2} \Delta P}{LU} \qquad [1]$$

where R_{cap} is the capillary tube radius (0.0381 cm).

3.2.6 C/W Foam Microscopy and Stability

The *in-situ* characterization of bubble sizes and size distributions of the C/W foam was measured by diverting foam flow after the sand pack or capillary tube to a high-pressure microscopy cell[4] with the two six-port injection valves. One valve determined the sampling point for the foam and the second controlled flow through the microscopy

cell. The microscopy cell was mounted on a microscope (Nikon Eclipse ME600). The sapphire windows (Swiss Jewel Company, W6.36, 0.635 cm diameter and 0.229 cm thickness) were separated with foil spacers creating a path length of approximately 25 μm.[80]

When flow through the cell was stopped, microscopy images were captured via a Photometrics CoolSNAP CF CCD camera connected to a computer. Foam was flowed through the microscopy cell for several cell volumes prior to image recording to ensure the foam photographed had not aged significantly. The CCD camera was programmed to take photos at set time intervals (from < 1 s to several hrs) to provide stability measurements over time. The temperature of the microscope cell and tubing was controlled by electrical heating tape (thermolyne briskheat flexible electric tape, Barnstead/thermolyne) wrapped around the microscopy cell and tubing and thermostated using a temperature controller (Omega CN7600, Omega) at the same temperature as the water bath.

The images were analyzed with ImageJ software by setting the scale using microscopy standards, adjusting the threshold value of the image, and using the measure particles function. In most cases bubble areas with a circularity of 0.60 or greater were obtained and thus converted to spherical radii. Size distribution parameters and average radii were then calculated using the formulas below. The minimum bubble size that could be measured had a diameter of 0.4 μm at 50x magnification, 0.88 μm at 20x magnification, and 1.8 μm at 10x magnification; bubbles smaller than these values could not be detected with the microscope and were not sized.

To determine average bubble sizes for a given shear rate, 6-9 microscope images at each condition were analyzed, corresponding to at least several hundred bubbles and

up to 10,000 bubbles. The Sauter mean diameter of a given foam, D_{sm}, and the polydispersity U_{poly} are calculated as follows

$$D_{sm} = \frac{\sum_i D_i^3}{\sum_i D_i^2} \quad [2]$$

$$U_{poly} = \frac{1}{D_{med}} \frac{\sum_i D_i^3 \left| D_{med} - D_i \right|}{\sum_i D_i^3} \quad [3]$$

where D_i is the diameter of a foam bubble and D_{med} is the median bubble diameter of the foam. Number average diameters, D_{avg}, can also be calculated from the D_i values.

Stability of the foam is measured by photographing a given foam over known time increments. For the short time (1-2 min) stability of highly sheared foams (total foam flow rates of 12-15 ml/min with sand pack of 14.7 cm long, 0.76 cm inner diameter tube packed with non-spherical sand of 125 μm diameter in Table 3.2), a magnification of 50x was used and only the changes in the bubbles in the top layer were measured (reported in Table 3.2). The high flow rate of the foam is varied to produce nearly all small (< 0.4 μm) bubbles. When formed, the foam is trapped in the microscopy cell. Initially, the foam is photographed every 1 sec for 2 minutes starting immediately after flow was stopped. After collection of the foam photographs, the stack of images is converted using the last images with the largest sizes to determine the threshold values for the stack. A circularity of about 0.3 is used. The bubbles greater than 0.4 μm in diameter are measured from the foam photos for every 5 seconds to track size changes over time. Then the polydispersity (equation 3), total volume of the bubbles (sum of volumes of all the measured bubbles), and D_{sm} (equation 2) are calculated for each of these times. Plots are made of these properties over time and *dv/dt* is determined as the slope of the measured volume as a function of time (Table 3.2). For the stability of larger bubble sizes over longer times, a single layer of bubbles on the order of 1 to 100 μm was

trapped in the microscopy cell and measured over various times. The images are analyzed using the appropriate microscopy scale and circularity (generally 0.5-0.6) at known times.

3.2.7 Oil-in-Water and Air-in-Water Systems

For oil-water tests, systems containing 90% v/v decane and 10% v/v aqueous solution containing 1% v/v surfactant in DI water were formed in a 20 mL vial and sonicated a the maximum pulse for 20 minutes. Observations occurred after sonication.

The A/W foams are formed by blowing compressed air canisters through a 12 gauge needle affixed to the outlet straw into an aqueous surfactant solution. The aqueous surfactant solution filled 10% v/v of the vial volume with 1% v/v surfactant in DI water and a 90% v/v air foam was formed by filling the remaining volume of the vial container.

3.3 RESULTS

The measured cloud point temperatures of the surfactants in water and brine and the calculated HLB (hydrophilic-lipophilic balance) values (using the method of Guo[147]) are presented in Table 3.1. The measured apparent viscosities (calculated using the measured ΔP in equation 1) of the bulk C/W foams (η_{foam}) in a capillary tube at varying temperatures are also presented in Table 3.1 with the initial D_{sm} (equation 2) of the foam bubbles. The majority of the foams contained a quality of 90% v/v CO_2 and the foams were stabilized with 1% v/v surfactant (in the aqueous phase) at approximately 2000 psia. The foams were generated with the 50 μm pore sand pack and at a total foam flow rate

Table 3.1: Surfactant properties, bulk foam apparent viscosities, and initial D_{sm} are listed (at Q_{total} of 6 ml/min, 2000 psia, 90% v/v CO_2, and 1% v/v surfactant where the coarse sand pack with 50 μm pores was used). $^{\delta}$ indicates 87% v/v CO_2, $^{\varepsilon}$ indicates 88% v/v CO_2, $^{\Psi}$ indicates Q_{total} of 4 ml/min, ^{a} indicates 0.5% v/v surfactant, $^{\beta}$ indicates 1% v/v TMN 6, and $^{\Theta}$ indicates No foam with 1% v/v TMN 6 24 ˚C.

	Cloud Point (ºC)		HLB	Phase Change (˚C)	Foam (with Water) at Q_{total} of 6 ml/min							
					24 ˚C		40 ˚C		60 ˚C		70 ˚C	
Surfactant	**Water**	**Brine**			η_{foam} (cP)	D_{sm} (μm)	η_{foam} (cP)	D_{sm} (μm)	η_{foam} (cP)	D_{sm} (μm)	η_{foam} (cP)	D_{sm} (μm)
L62	(32)	27	8.8		130$^{\Psi}$	33	No foam		No foam			
TMN 6 (5 %)$^{\Theta}$	(36)$^{\beta}$	31$^{\beta}$	12.9		74	18	18$^{\varepsilon}$	27	No foam			
15-S-7	(37)	32	12.5		45	51	17	46	No foam			
15-S-20	(>100)		16.5		141	21	94	26	53	34	51	19
Lutensol XP70	58		-		16	90	17	42	7	Slugs	-	
$C_{8\text{-}14}$-$PO_{2.5}$-EO_7 [a]	60		12.1		38	65	22	50	No foam			
TM NP-9	(54)		(12.9)		140	20	40	18	No foam			
LA-EO_{12}	56		15.2		14	61	-		No foam			
1Hex-PO_5-EO_9	49		14.6		31	106	73	55	No foam			
1Hex-PO_5-EO_{11}	64		15.4		49	66	94	29	35	46	No foam	
1Hex-PO_5-EO_{13}	78		16		36	63	90	24	49	35	No foam	
1Hex-PO_5-EO_{15}	> 80		16.5		46	80	87	25	55	37	59	52
1-Octanol-$PO_{4.5}$-EO_8	58		13.4		35	57	No foam		-			
1-Octanol-$PO_{4.5}$-EO_{12}	59		14.9		9	41	No foam		-			
1-Nonanol-$PO_{3.5}$-EO_8	58		13.2		110	43	76	42	No foam			
C_{13}-$PO_{1.5}$-EO_6	34		10.8		31	52	-		No foam			
C_{11}-PO_2-EO_7	50	42	12.2		79	53	61	46	No foam			
$C_{12\text{-}14}$-EO_7	52		12.1		No foam		-		-			
C_9-PO_4-EO_8	56		13		156	34	99	18	No foam			
2-Octanol-PO_9-EO_9	45	36	12.4	40-60 ppt	140	47	86	40	No foam			
2EH-PO_2-EO_4	< 24		11.2		10	63	No foam		No foam			
2EH-PO_3-EO_3	< 24		9.7		No foam		-		-			
2EH-PO_5-EO_8	54	40	13.2		88	39	41	50	No foam			
2EH-PO_9-EO_9	40	34	12.4	40-60 ppt	145	27	78	47	No foam			
2EH-PO_{12}-EO_{11}	39	32	12.3	24-40 III	135	20	55	47	No foam			
2EH-PO_5-EO_9	60	54	13.6	40-60 ppt	125	27	101	28	26	61	No foam	
2EH-PO_5-EO_{11}	71		14.4		190	13	96	46	50	40	No foam	
2EH-PO_5-EO_{13}	> 80		15.1		137	14	100	18	49	41	No foam	
2EH-PO_5-EO_{15}	> 80		15.6		153	22	140	26	57	35	53	38
2EH-EO_5	< 24		12.8		19	26	2$^{\delta}$	48	No foam			
2EH-$EO_{11.8}$	> 80		16.2		60	39	49	28	43	25	40	35
DOG-EO_{12}	46	38	13.9	40-60 ppt	116	30	74	48	24	-	No foam	

(Q_{total}) of 6 ml/min. A large number of surfactant structures were able to form the C/W foams. Forming the C/W foams is less challenging than forming the inverse system, a W/C concentrated emulsion.[148]

Decane-water systems with 1% v/v of 2EH-PO_5-EO_9 or 2EH-PO_5-EO_{15} in the aqueous phase formed W/O systems with 90% v/v decane at 24 ˚C. White emulsions are formed with sonification, however immediately after sonification is stopped, the white water droplets begin settling to the bottom of the vial and the turbidity of the oil phase is reduced. Although both of the surfactants are hydrophilic and water soluble, the inverse W/O emulsion is formed due to the small amount of water in the system and the instability of the O/W emulsion. The interfacial tension of decane and water in the presence of 1% w/w 2EH-PO_5-EO_9 in the water phase using a captive decane droplet was measured at 2.5 mN/m. The interfacial tension of 1% w/w 2EH-PO_5-EO_{15} at the decane-water interface was 3 mN/m.

A/W foams with 90% v/v air can be formed with either 1% v/v of 2EH-PO_5-EO_9 or 2EH-PO_5-EO_{15} in the aqueous phase. The bubbles formed can be seen with the naked eye and are in the mm size range. However, the bubbles at the top of the vial start coalescing immediately after formation and over half of the foam volume disappears in less than 1.5 minutes.

3.3.1 Cloud Point Temperature

As the temperature of the C/W foam is increased close to the cloud point temperature of the surfactant, rapid changes in stability occur. The precipitation of the surfactant from the water phase into a separate surfactant-rich phase at the cloud point greatly reduces the stability of the foam lamella. Consequently, the maximum temperature where a foam can be generated depends highly on the cloud point of the

aqueous solution. Furthermore, the presence of salts typically makes the surfactants less soluble and depresses the cloud point (Table 3.1). Bonfillon-Colin and Langevin attribute the rupture of foam films at the cloud point to bridging of the foam films by droplets of the surfactant-rich phase.[149] It is believed that when spreading of a thin film of the surfactant-rich phase occurs, it will enhance this bridging in a manner similar to that of spreading oil. Interestingly, when the surfactant-rich phase was separated from the foam with stabilized with C_{10}-EO_4 (tetraethylene glycol mono-n-decyl ether), the aqueous solution with a diluted concentration of surfactant formed a stable foam 4 ˚C above the cloud point of the surfactant (20 ˚C).[149]

The temperatures at which the C/W foam could not be observed as a function of the nonionic surfactant structure are presented in Table 3.1. This temperature is no more than 4 ˚C above the cloud point for all the surfactants except DOG-EO_{12}. Observations of the C/W foams formed with 2EH-PO_5-EO_9 showed rapid stability changes when the temperature approached the cloud point. The foam undergoes a transition from a highly stable non-coalescing foam to only slugs of the two phases with only 1-2 ˚C increase in temperature (~ 57 ˚C). The rapid stability transition of the foams near the cloud point endorses a destabilization mechanism from surfactant precipitation, for example the bridging mechanism.

3.3.2 Foam Stability

Table 3.2 presents the interfacial properties of several surfactants at the C-W interface including the interfacial tension (γ) and surface pressure (π) at 0.01% w/w surfactant (in the aqueous phase), the area per molecule at the interface (A_m), and the efficiency (pC20) at 2000 psia and 24 ˚C as previously reported.[146] The pC20 is much

Table 3.2: Surfactant properties at the C-W interface and stability of highly sheared (Q_{total} of 12-15 ml/min) foams over 120 s (sand pack of 14.7 cm long, 0.76 cm inner diameter tube with 10 μm pores). The conditions are 2000 psia and 24 ˚C unless specified. The CMC of the surfactants as determined from surface tension at A-W interface are also included. The foams contain 90% v/v CO_2 and 1% v/v surfactant. γ_o for the C-W interface at 24 ˚C and 2000 psia is 27.7 mN/m. $^{\alpha}$ indicates t_f of 80 s. $^{\beta}$ indicates data from Chapter 2.

Surfactants	**CMC (% w/w)**	**HLB**	γ^{β} **0.01 % w/w (mN/m)**	π^{β} **0.01 % w/w (mN/m)**	A_m^{β} **(A^2/ molecule)**	**pC20$^{\beta}$ 24 ºC**	**pC20$^{\beta}$ 40 ºC**	**pC20$^{\beta}$ 60 ºC**	D_{sm} **At t_o (μm)**	D_{avg} **At t_o (μm)**	***dv/dt*** **t_f = 120 s (μm^3/s)**
2EH-PO_5-EO_9	0.28	13.6	7.5	20.2	219	3.9	4.2	4.5	-	-	-
2EH-PO_5-EO_{15}	0.28	15.6	5.6	22.1	233	4.3	5.2	5.2	1.3	1.0	140
1Hex-PO_5-EO_{15}	1.47	16.5	8.5	19.2	339	3.5	4.4	5.5	5.3	1.2	130
DOG-EO_{12}	0.015	13.9	4.1	23.6	-	5.1	5.7	-	1.3	1.0	50
LA-EO_{12}	0.21	15.2	7.9	19.8	-	< 3.8	-	-	7.3	2.1	> 530
2EH-$EO_{11.8}$	0.99	16.2	12.8	14.9	-	-	-	-	2.4	1.2	375$^{\alpha}$
2EH-PO_5-EO_{11}	0.42	14.4	7.6	20.1	-	< 4.0	-	-	3.4	1.0	101

larger for the DOG-EO_{12} compared to the other surfactants. Foams consisting of 90% v/v CO_2 and 1% v/v surfactant (in the water) at 24 ˚C and 2000 psia formed with high shear (Q_{total} of 12-15 ml/min) through 10 μm pores were studied for coalescence stability. The high shear reduced foam polydispersity relative to the coarser sand pack and lower flow rates in the studies of Table 3.1. The growth rates of these foams (defined as the change in volume, v, of large bubbles, $D_{bubble} > 0.4$ μm, over time is denoted dv/dt) over 120 s are presented in Table 3.2 along with initial D_{sm} and D_{avg} values. Figure 3.3 presents dv/dt for these surfactants. The dv/dt for 2EH-$EO_{11.8}$ is measured for the first 85 s as few foam bubbles smaller than 0.4 μm in diameter persisted beyond this time. Although the π of LA-EO_{12} is about the same as for 2EH-PO_5-EO_{11} and 1Hex-PO_5-EO_{15}, it has the highest dv/dt of all the surfactants. For LA-EO_{12} the bubble size increases before the foam even reaches the microscope cell. The dv/dt for LA-EO_{12} is estimated assuming no large bubbles exist at the sand pack exit and that growth to the initial microscopy photo occurs during the 23 s residence time of flow from the exit of the sand pack to the microscope cell. Figure 3.4 presents the evolution of D_{sm} and U_{poly} over time for the foams stabilized with 1% v/v DOG-EO_{12}, 2EH-$EO_{11.8}$, and 2EH-PO_5-EO_{11}. Figure 3.5 presents D_{sm}^3 versus time for 2EH-PO_5-EO_9 foams of 0.1-1% v/v surfactant at 24 and 55 ˚C. At 0.1% v/v 2EH-PO_5-EO_9 at 24 ˚C and 0.2% v/v 2EH-PO_5-EO_9 at 55 ˚C no foam was formed, slugs of the phases were observed. The foam with 0.2% at 24 ˚C had larger bubbles and a higher polydispersity relative to the foams with higher concentrations. Micrographs of the DOG-EO_{12} stabilized foam (Figures 3.3-3.4) are presented in Figure 3.6 over time. The foams in Figure 3.7 stabilized with 2EH-$EO_{11.8}$ show more rapid growth over the 91 s after reaching the microscope. The foam stabilized with LA-EO_{12} is presented in Figure 3.8 when it initially reached the microscope (although 23 s passed from formation).

Table 3.3 compares the CO_2 distribution coefficients (% w/w surfactant in the

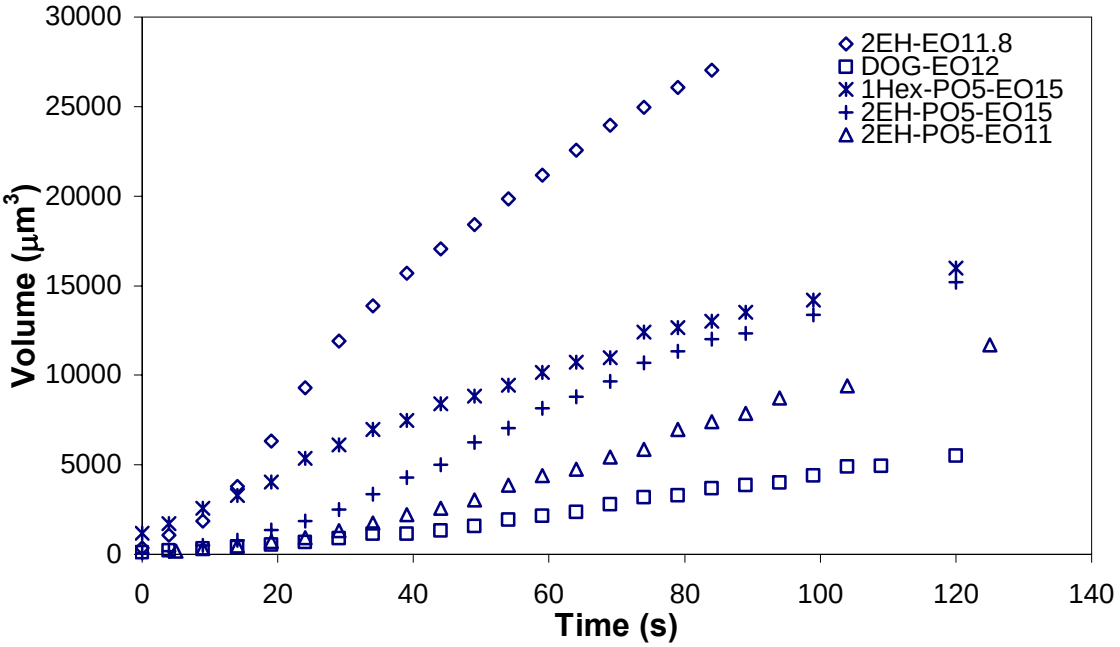

Figure 3.3: Changes in volume over short times of highly sheared foams stabilized by 2EH-$EO_{11.8}$, DOG-EO_{12}, 2EH-PO_5-EO_{11}, 2EH-PO_5-EO_{15}, and 1Hex-PO_5-EO_{15} with 1% v/v surfactant and 90% v/v CO_2 at 24 ˚C and 2000 psia. Slopes (*dv/dt*) are listed in Table 3.2.

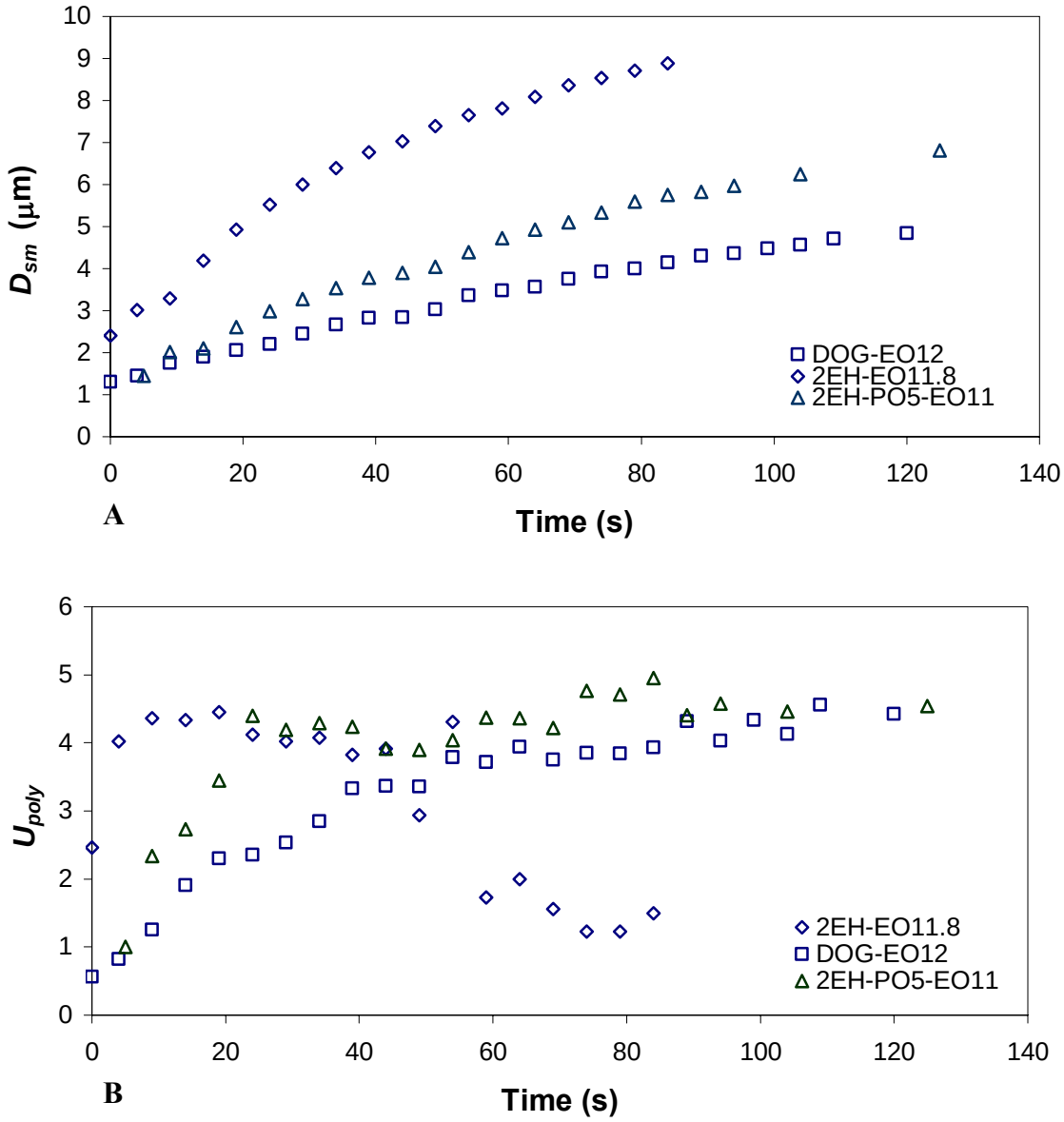

Figure 3.4: Changes in D_{sm} (plot A) and U_{poly} (plot B) over short times of highly sheared foams stabilized by 2EH-$EO_{11.8}$, DOG-EO_{12}, and 2EH-PO_5-EO_{11} with 1% v/v surfactant and 90% v/v CO_2 at 24 ˚C and 2000 psia.

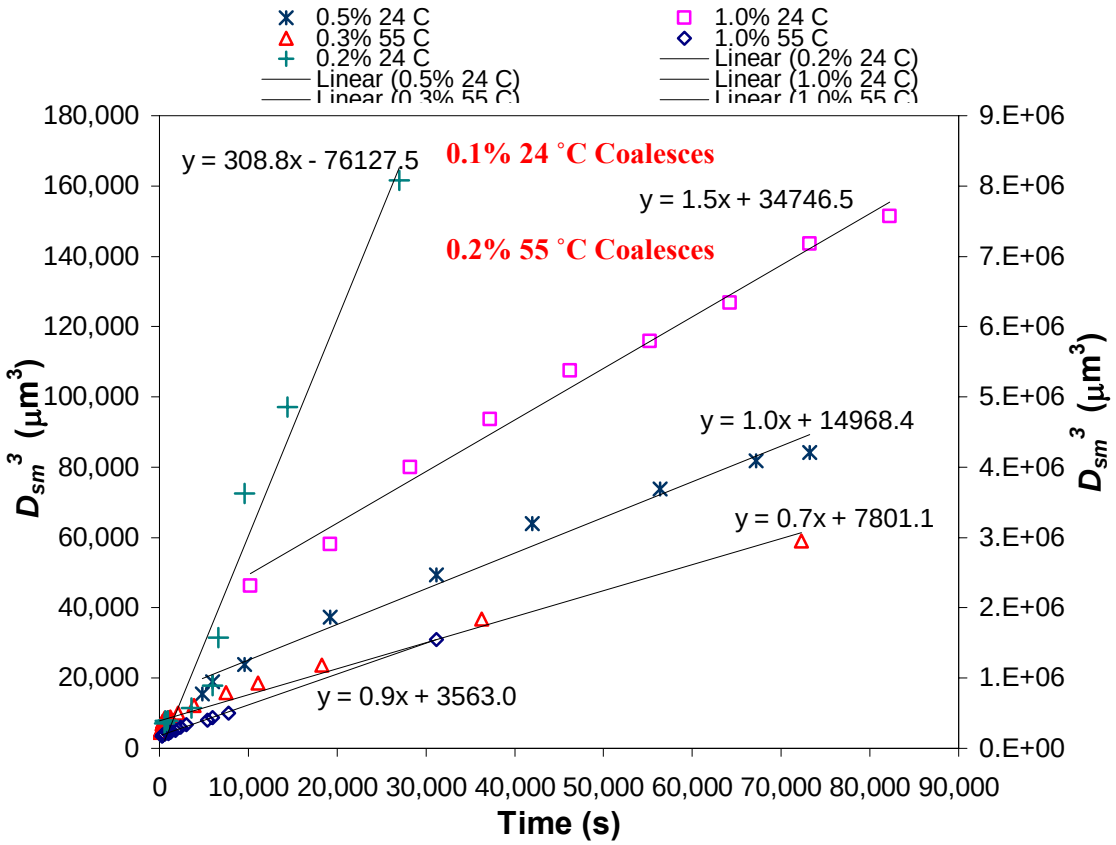

Figure 3.5: D_{sm}^3 as a function of time for various concentrations (% v/v) of 2EH-PO_5-EO_9 at 24 and 55 ˚C with 90% v/v CO_2 at 2000 psia where the linear slopes are Ω_3. 0.2% v/v at 24 ˚C uses right axis. All other conditions use left axis. 0.3% v/v at 55 ˚C is with brine.

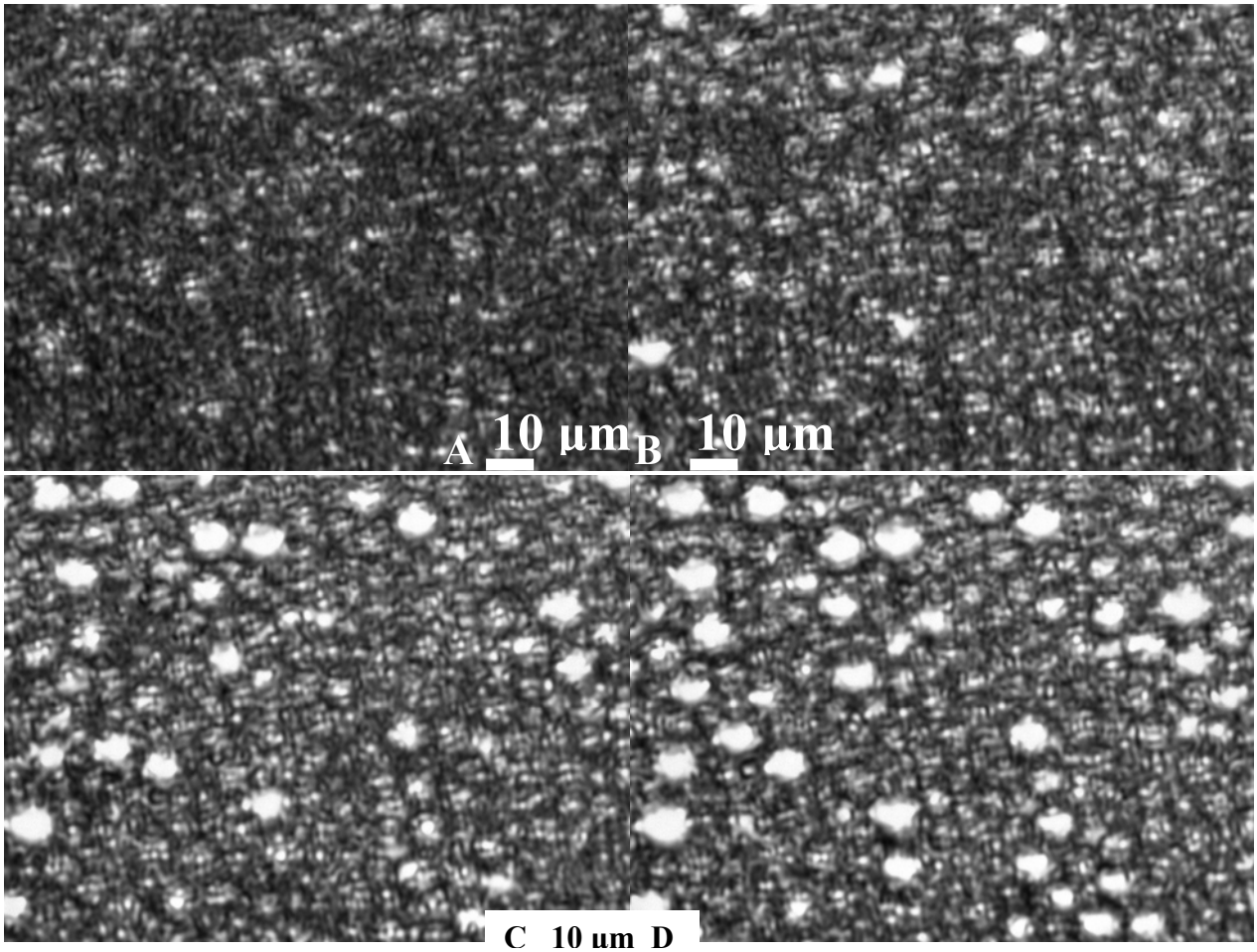

Figure 3.6: Micrographs of a 90% v/v CO_2 foam stabilized with 1% v/v DOG-EO_{12} highly sheared in a 10 µm pore sand pack at 24 ˚C and 2000 psia as a function of time, where A. is at 0 s, B. is at 30 s, C. is at 80 s, and D. is at 120 s. Scale bars are located in the micrographs.

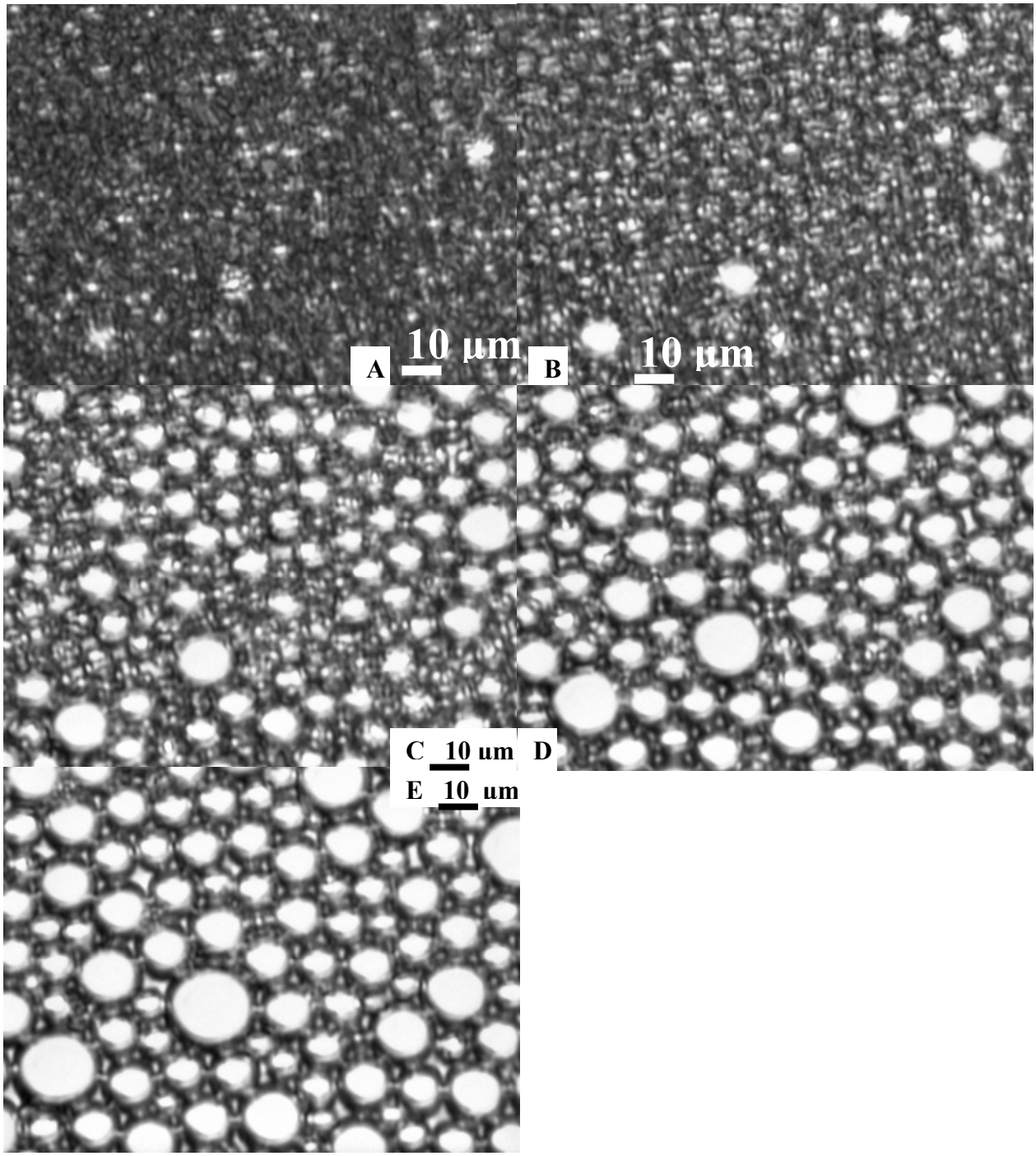

Figure 3.7: Micrographs of a 90% v/v CO_2 foam stabilized with 1% v/v 2EH-$EO_{11.8}$ highly sheared in a 10 µm pore sand pack at 24 ˚C and 2000 psia as a function of time, where A. is at 0 s, B. is at 10 s, C. is at 30 s, D. is at 60 s, and E. is at 91 s. Scale bars are located in the micrographs.

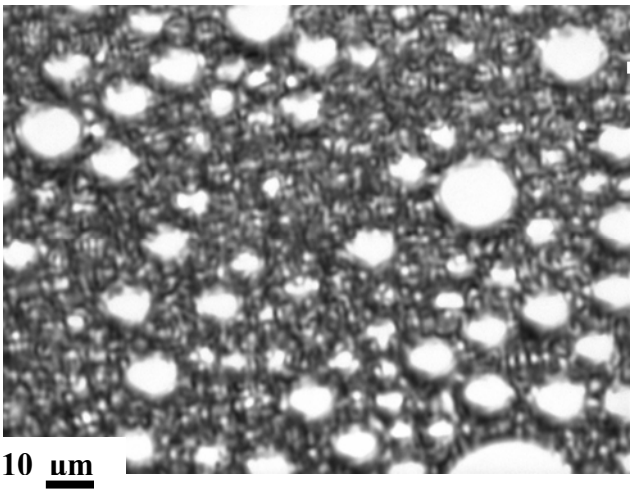

Figure 3.8: Micrograph of a 90% v/v CO_2 foam stabilized with 1% v/v LA-EO_{12} highly sheared in a 10 µm pore sand pack at 24 ˚C and 2000 psia at 0 s in the microscope (23 s after formation). Scale bar is located in the micrograph.

Table 3.3: The CO_2 distribution coefficient between the aqueous and CO_2-rich phases (% w/w based on total surfactant weight) for 2EH-PO_5-EO_9 and 2EH-PO_5-EO_{15} with changes in temperature at 2000 psia. Foam stabilities in terms of experimental Ω_3 values and U_{poly} changes are also included with the initial and final times, t_o and t_f. Foams include 1% v/v surfactant and 90% v/v CO_2 at 2000 psia. The foams were formed at the same conditions as in Table 3.4.

	T (°C)	**CO_2 Distribution Coefficient (% w/w)**	**Ω_3 dD_{sm}^3/dt ($\mu m^3/s$)**	**t_f (hr)**	**U_{poly}**	
					At t_o	**At t_f**
2EH-PO_5-EO_9 Cloud Point 61 ˚C	24	72%	1.6	23	2.7	0.3
	40	30%	-	-	-	-
	55	-	2.5	2.4	1.1	0.6
	60	10%	-	-	-	-
	75	8%	-	-	-	-
2EH-PO_5-EO_{15} Cloud Point 88 ˚C	24	58%	2.7	8	1	0.4
	40	11%	3.1	27	2.4	2.1
	60	8%	-	-	-	-
	70	3%	9.9	1	11	0.7

CO_2 phase as a fraction of the total surfactant weight in the water-CO_2 system) of 2EH-PO_5-EO_9[107] and 2EH-PO_5-EO_{15} at 2000 psia and 24-75 ˚C. The initial D_{sm} of the bulk foams (originally in Table 3.1) are also given. The measured Ω_3 (defined as the change in D_{sm}^3 with time, dD_{sm}^3/dt) for foams with 90% v/v CO_2, 1% v/v surfactant in the aqueous phase, formed with the 10 μm pore sand pack were studied through t_f (final time). The associated U_{poly} at initial time, t_o, and at t_f are also given. According to Bancroft's rule[150] W/C emulsions should be formed due to the high CO_2 distribution coefficients for 2EH-PO_5-EO_9 and 2EH-PO_5-EO_{15} at 24 ˚C.[67,70] The 2EH-PO_5-EO_9 and 2EH-PO_5-EO_{15} foams were not observed to coalesce in the microscope at any conditions below the cloud point temperature for the conditions in Table 3.3.

Table 3.4 presents a summary of the stability in terms of Ω_3 for 2EH-PO_5-EO_9, 2EH-PO_5-EO_{15}, and DOG-EO_{12} at 2000 psia under a variety of surfactant concentrations, foam qualities, salinities, and U_{poly} where the foams are stable to coalescence unless otherwise indicated. The behavior shown in Figures 3.9-3.11 is also included in Table 3.4. Figure 3.9 presents D_{sm}^3 as a function of time for two foams of varying U_{poly} (1.9 and 2.8, respectively) stabilized with 1% v/v 2EH-PO_5-EO_9 and a quality of 90%, at 24 ˚C and 2000 psia. Figures 3.10 and 3.11 present the changes in D_{sm}, U_{poly}, and D_{sm}^3 as a function of time for over 60 hrs for foams stabilized with 0.3% v/v 2EH-PO_5-EO_9 (in brine) and 0.3% v/v DOG-EO_{12}, respectively. Lamella rupture was not observed over the entire time of study for bubbles greater than 0.3 μm in diameter and visible by microscopy. Figure 3.12 presents the micrographs of the 0.3% v/v DOG-EO_{12} foam over time.

The nonionic surfactants of this investigation have a higher salinity tolerance than ionic surfactants, where salt screens the electrostatic repulsion between films. Moderate

Table 3.4: Experimental Ω_3 and U_{poly} values at various conditions for 2EH-PO_5-EO_9, 2EH-PO_5-EO_{15}, and DOG-EO_{12} at 2000 psia. 0.5% w/w $CaCl_2$ and 0.1% $MgCl_2$ are present unless no salt is added.

Surfactants	***c*** **(% v/v)**	**T (˚C)**	**CO_2 (% v/v)**	**Salt (% w/w)**	**Ω_3 dD_{sm}^3/dt ($\mu m^3/s$)**	***t_f*** **(hr)**	***U_{poly}***	
							At t_o	**At t_f**
2EH-PO_5-EO_9	0.1	24	90	0	unstable	-	-	-
	0.2	24	90	0	309	7.5	16.0	4.0
	0.5	24	90	0	2.2	2.7	4.5	0.5
	1	24	90	0	1.6	22.8	2.7	0.3
	1	24	90	0	0.06	48.3	0.6	2.8
	1	24	94	0	49	600 s	1.1	1.1
	0.2	55	90	0	unstable	-	-	-
	0.3	55	90	0	1.3	1	4.6	1.0
	0.3	55	90	2	0.46	60.5	2.0	0.5
	0.5	55	90	0	0.9	8.7	4.8	0.9
	1	55	90	0	10.5	8.8	7.9	2.4
	1	55	92.4	0	2.5	26	0.8	0.6
	1	55	92.4	2	7.9	1.8	24.5	2.1
2EH-PO_5-EO_{15}	1	24	90	0	2.7	8	1	0.4
	1	24	90	0	4.3	0.5	3.2	1.5
	1	24	90	2	2.9	21.8	2	0.6
	1	24	90	5	2.6	19.5	4.2	0.4
	1	40	90	0	3.1	27	2.4	2.1
	1	70	90	0	9.9	1	2.2	0.4
	1	70	90	2	92	1.8	11.2	0.7
DOG-EO_{12}	0.3	24	90	0	5.8	61.5	6	4.4
	0.2	50	90	0	1.4	6.8	4.8	1
	0.3	55	90	0	2.3	20	7.2	1.1

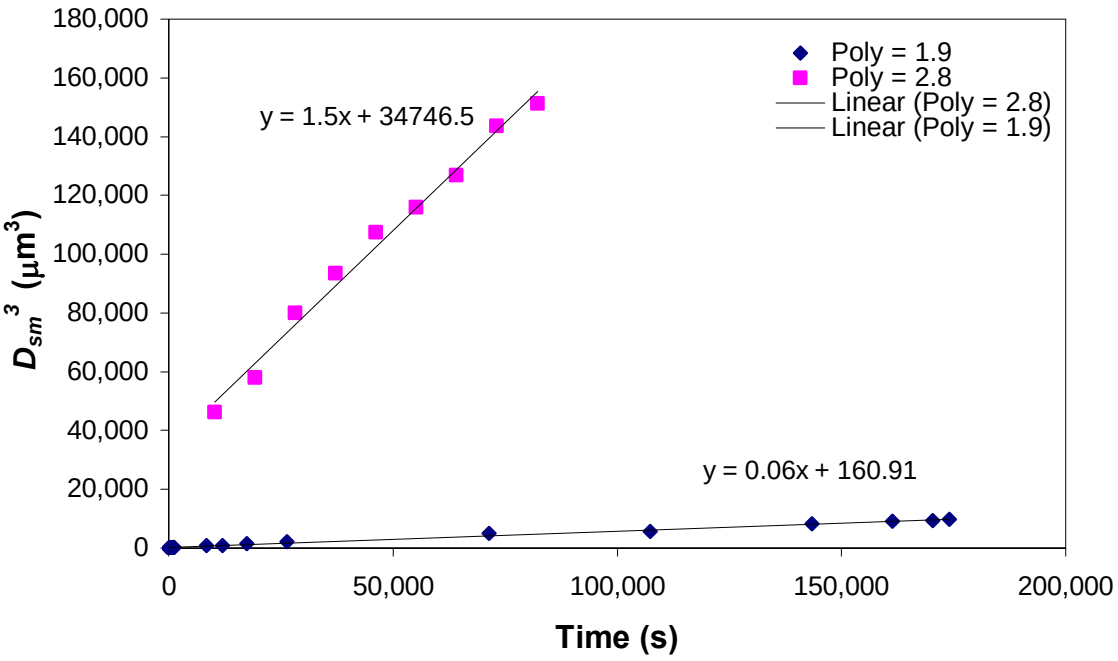

Figure 3.9: Change in D_{sm}^3 with time for 1% v/v 2EH-PO_5-EO_9 (in the aqueous phase) with 90% v/v CO_2 at 24 ˚C and 2000 psia at U_{poly} values of 1.9 and 2.8 where Ω_3 values are from the slopes (0.06 and 1.5 µm^3/s, respectively).

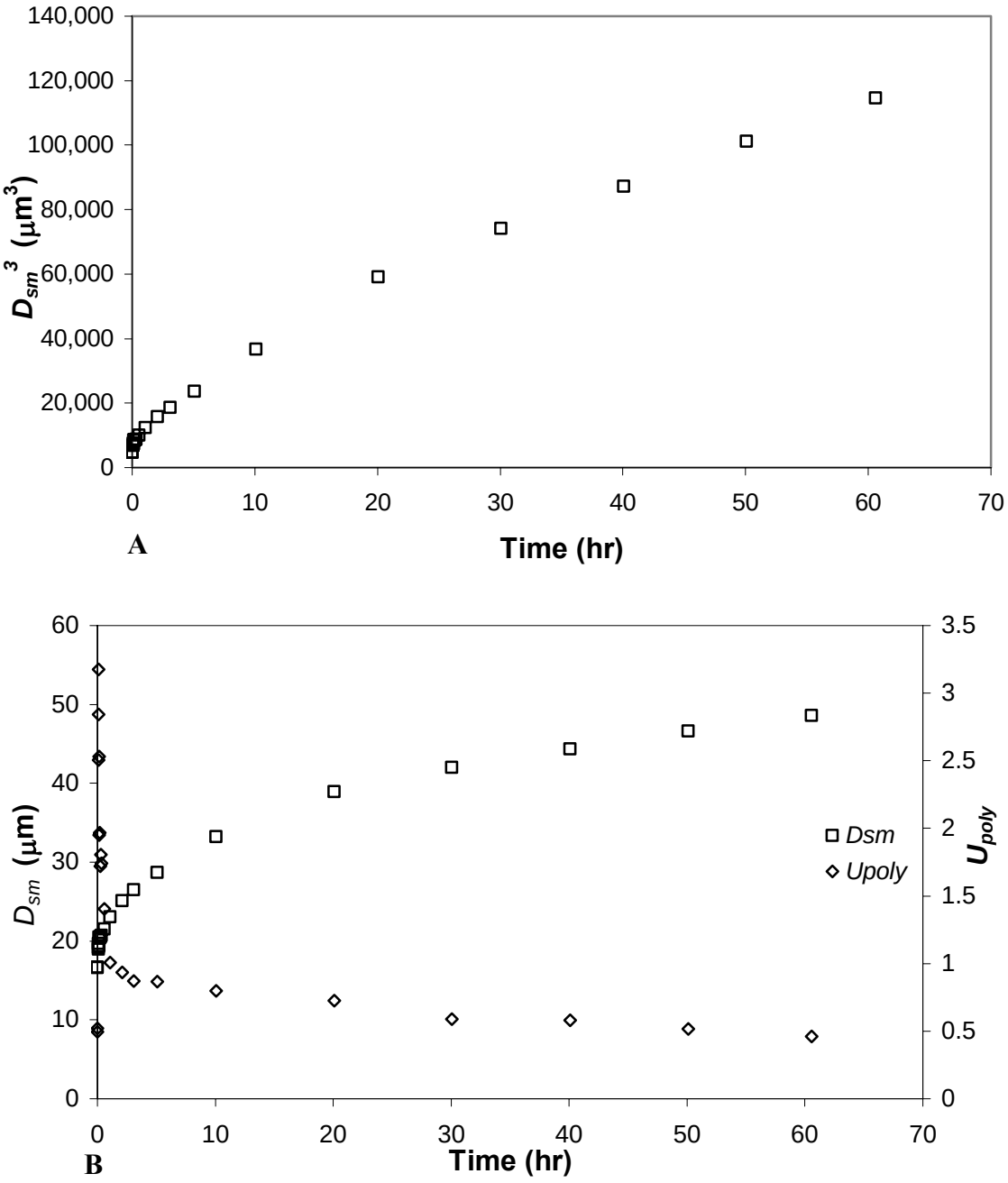

Figure 3.10: Change in D_{sm}^3 (plot A), D_{sm} (plot B left axis), and U_{poly} (plot B right axis) with time for a foam stabilized by 0.3% v/v 2EH-PO_5-EO_9 with brine at 55 ˚C and 2000 psia over 60.5 hrs.

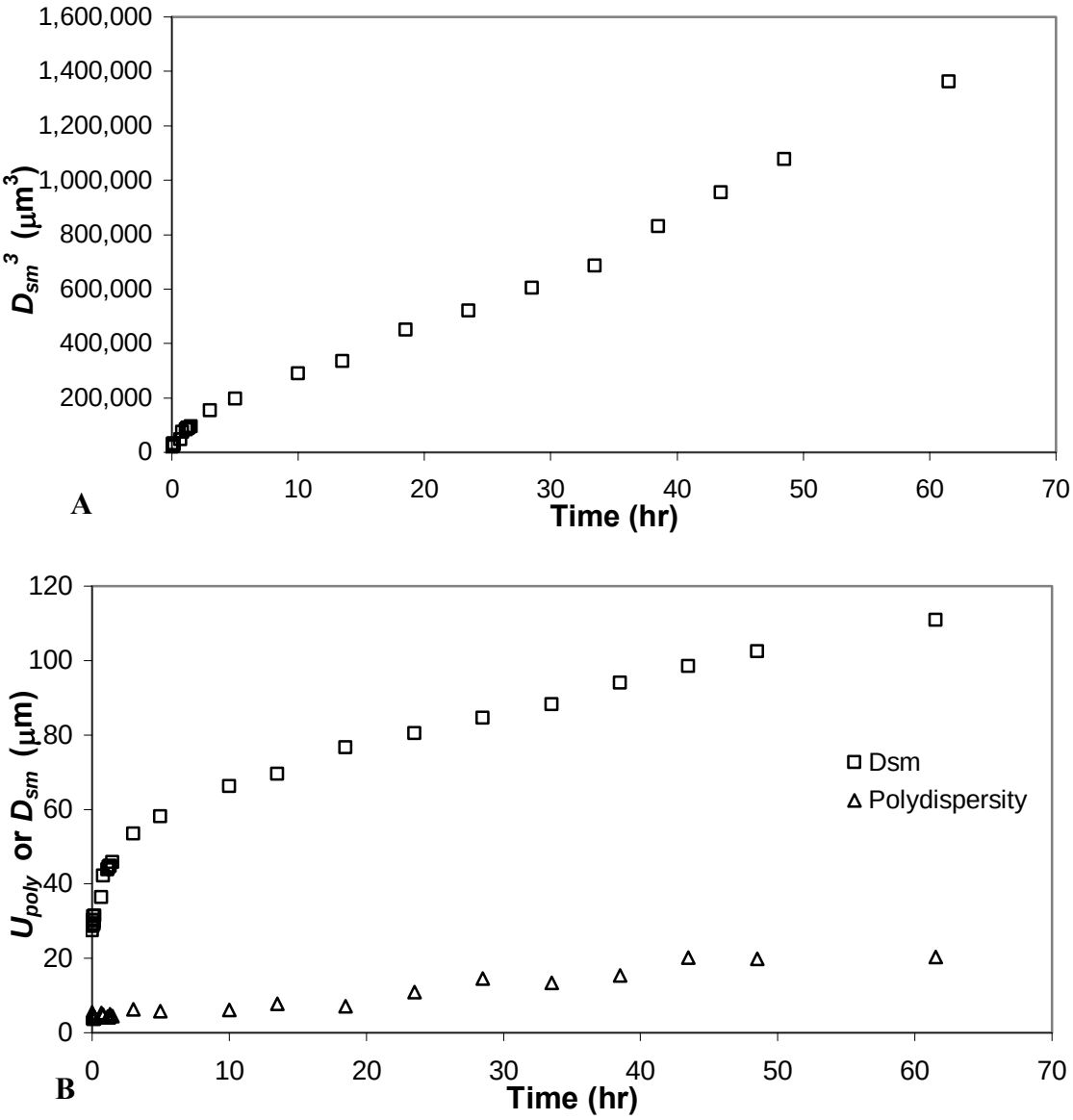

Figure 3.11: Change in D_{sm}^3 (plot A), D_{sm} (plot B), and U_{poly} (plot B) with time for a 0.3% v/v DOG-EO_{12} foam at 24 ˚C and 2000 psia over 61.5 hrs.

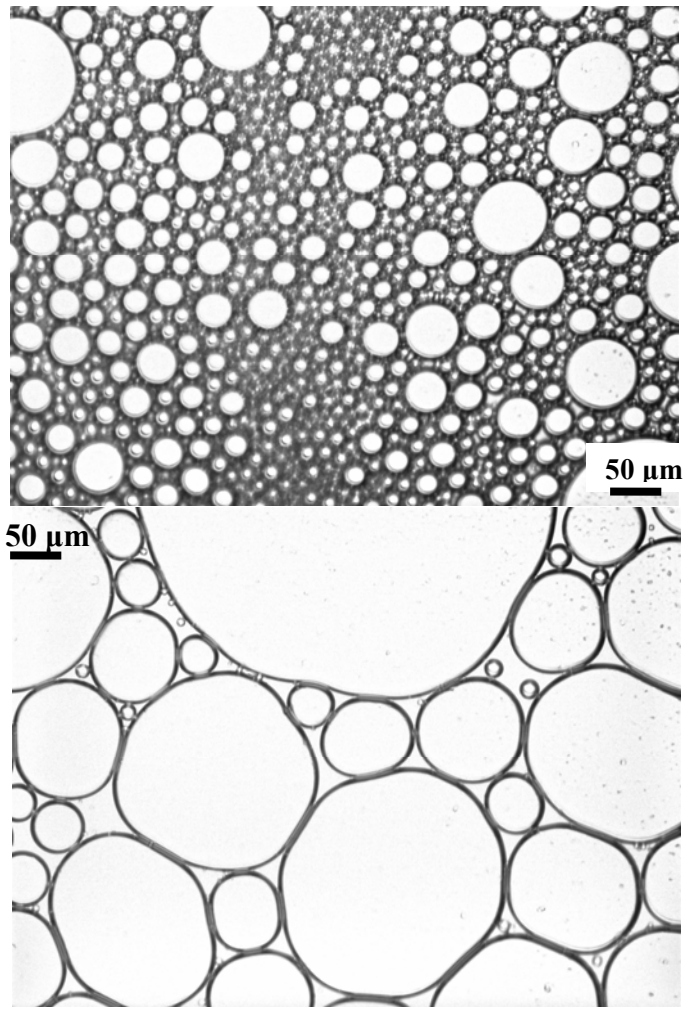

Figure 3.12: Micrographs of a C/W foam stabilized with 0.3% v/v DOG-EO_{12} at 24 ˚C and 2000 psia at 0 (top) and 59 hr (bottom) after reaching the microscope.

levels of salt and divalent ions are often present in reservoirs of interest in CO_2 sequestration and EOR. From Table 3.4 the 0.3% v/v 2EH-PO_5-EO_9 foam showed insignificant changes in Ω_3 at 55 ˚C with the addition of 2% NaCl, 1% $CaCl_2$, and 0.5% $MgCl_2$ w/w (Table 3.4). Also, the addition of 2-5% NaCl, 1% $CaCl_2$, and 0.5% $MgCl_2$ did not affect Ω_3 values of 2.6-2.9 for 1% v/v 2EH-PO_5-EO_{15} at 24 ˚C and 2000 psia (Table 3.4). A drop in the stability of the foam lamella due to salt is only observable at temperatures near the depressed (by salt) cloud point, indicating the foams will exhibit tolerance to salt at the appropriate temperatures in reservoir applications.

3.4 DISCUSSION

3.4.1 Surface Pressure and Disjoining Pressure

The weak van der Waals forces of CO_2, characterized by a low polarizability per unit volume, and low dielectric constant (ε = 1.0-1.6) often lead to poor solvation of linear surfactant hydrocarbon tails.[38] Thus, when the stability of the foam depends on the solvation of the tails by CO_2 in the thin films of the continuous phase, surfactant tail structure is crucial. However for the C/W foams, where the surfactant head groups are solvated by water in the foam lamella and stabilize the film, the solvation of surfactant tails is less important.

The adsorption of surfactant at the interface and reduction in γ must be sufficient to provide stable C/W foams.[80] The surface pressure ($\pi = \gamma_o - \gamma$) is strongly influenced by the degree of surfactant adsorption as described by the surface equation of state (SEOS).

For a nonionic surfactant the SEOS may be expressed as a "hard-disk" reference term (HD) for the head group and a perturbation term [105]

$$\pi = \pi_{HD} + (\pi_o + \pi_{el}) \quad [4]$$

where π_o is the solvent-tail interaction term, and π_{el} describes electrostatic interactions on the aqueous side of the interface. According to Flory-Krigbaum theory[106]

$$\pi_o = \frac{\alpha_a kT(1-2\chi)v_t^2}{2v_o m^{1/2}\alpha l}\frac{1}{A_m{}^2} \quad [5]$$

$$\chi = v_o(\delta_o - \delta_t)^2 / kT \quad [6]$$

where $\alpha_a = \pi^{1/2}/6$, v_o is the molar volume of the solvent (CO_2 for C/W foam), v_t is the volume of the tail, m is the degree of polymerization, l is the length of a tail segment, χ is the Flory interaction parameter, k is the Boltzmann constant, T is temperature, and $\alpha = 1$. The solubility parameters for the solvent and surfactant tail are δ_o and δ_t, respectively. If $\chi = ½$, then $\pi_o = 0$. In cases where CO_2 is an effective solvent for the tails, $\chi < ½$, and attractive forces favor interpenetration (mixing) of solvent and surfactant tails resulting in an increase A_m for a given π_o. Likewise, π_o increases for a given A_m. However, relative to oils, the weaker solvation of surfactant tails by CO_2, as a result of its low cohesive energy density, leads to larger χ values.[87]

Table 3.5 presents a summary of the differences between the properties of a C/W foams versus A/W and O/W foams or emulsions.[146] The lower γ_o at the C-W relative to both the A-W and O-W interfaces (Table 3.5) reduces Γ leading to larger A_m. At the A-W interface, high Γ and strong tail-tail interactions, such as those between linear surfactants, produce high pC20 values. At the C-W interface, where A_m is large, branched and double tails help separate the two phases to increase π and pC20, for example in the case of DOG-EO_{12} (Table 3.2).[146]

Table 3.5: Comparison between the properties of C/W foams and both A/W and O/W systems for branched hydrocarbon-PO-EO surfactants. ω indicates data from Chapter 2.

	C/W vs. A/W	**C/W vs. O/W**
γ_o	Lower	Lower
Tail Solvation	Higher	Lower
Hamaker Constant	Higher	Higher
π	Lower	Lower
$\Gamma = 1/A_m$	Lower	Lower
pC20	Similar $^{\omega}$	Similar
P_c	Lower	Similar
Drop Size	Smaller	Similar
Drainage:		
Capillary Suction	Lower	Lower
Gravity	Lower	Higher (certain ρs)
Marangoni Resistance to Flow	Lower	Lower
Monolayer Bending	N/A	Harder
Wave Formation ("Dimples") in Film	Lower	Similar

The adsorption of surfactant at the interface influences the disjoining pressure, Π_d, between two CO_2 droplets. The repulsive forces (electrostatic, steric, and structural)[151,141] must counteract the van der Waals attraction between the two film surfaces

$$\Pi_d = -\frac{A_H}{6\pi h_f^{\,3}} + 64\times10^3 c_{el} N_A kT \tanh^2\left(\frac{e\psi_o}{4kT}\right)\exp\left(-\kappa h_f\right) \qquad [7]$$

where h_f is the thin film thickness, A_H is the Hamaker constant, c_{el} is the molar concentration of electrolyte, ψ_o is the surface potential of a drop, N_A is Avogadro's number, and κ is the inverse Debye length.[152,153] For aqueous lamella, the EO groups of the surfactant head provide "hard wall" steric repulsion, although the range of this repulsion is short relative to the expected film thickness.[151] As h_f decreases, Π_d increases with increased electrostatic repulsion, until a maximum is reached at a critical film thickness (h_{crit}). If h_f decreases further, the van der Waals attraction between the drops can overcome the electrostatic repulsion, and only if the steric repulsion is large (with high surfactant adsorption) can the film survive as a Newton Black film.[80] For CO_2 bubbles[154] at 24 ˚C and 2000 psia the A_H value as determined according to Dhanuka[80] is about 0.04 eV, compared to the 0.003 eV for decane droplets (Table 3.5).[155,156] For nonionic surfactants, the electrostatic repulsion can result from hydroxide ions that naturally adsorb at the A-W and O-W interfaces.[157,158] The C-W interface can also be charged: zeta potentials have been measured for water droplets with nonionic surfactants.[159] The low pH of the C-W system (a value of about 3) will cause significant differences in ion adsorption relative to that at the O-W interface that will require future study.[80]

The disjoining pressure must oppose the Laplace pressure (capillary pressure, P_c) of the foam bubbles. Rapid spinodal decomposition of the films occurs when the Laplace pressure, $2\gamma/R$, exceeds the maximum of the disjoining pressure.[65-68] For C/W foams, the

lower γ will reduce the Laplace pressure relative to Π_d and enhance the stability of the foam relative to A/W and O/W systems for a given drop size. Thus smaller bubbles, in the range of 1-10 μm in Tables 3.3 and 3.4, will remain more stable than in the case of A/W foams, where bubbles are typically 0.1 to 10 mm in size with the lower γ. Aronson et al. found that higher disjoining pressures lead to stronger foams in porous media with larger flow resistance.[160]

3.4.2 Thin Film Drainage and Marangoni Stabilization

Metastable foams are destabilized by drainage of the lamella caused by two effects, gravity and capillary suction into the plateau borders. The much higher density of CO_2 relative to air reduces drainage due to gravity, (Table 3.5 and Supplementary Information). Figure 3.13 presents a schematic of the lamella between two CO_2 bubbles and the plateau borders with a radius of curvature R_{curv}.[161] For symmetrical cylindrical film geometry (Figure 3.13), the difference in pressure between the film and plateau border creates a drainage velocity. Reynolds described a similar drainage velocity for the flow of liquid from between two approaching solid plates

$$V_{RE} = - dh_f/dt = (h_f^3/3\eta_c R_{film}^2)\Delta P_{film} \quad [8]$$

where η_C is the viscosity of the continuous liquid phase, R_{film} is the film radius, and $\Delta P_{film} = 2(P_c - \Pi_d(h))$.[69,145] For a given h_f, the lower γ of the C/W foams produces a smaller P_c and ΔP_{film}, therefore the film drainage V_{RE}, relative to both A/W and some O/W systems (e.g. branched C_n-PO_x-EO_y surfactants) as summarized in Table 3.5. The slower drainage has the potential to enhance the stability of the films against various destabilization mechanisms described below.

Marangoni stabilization (resistance to film drainage) increases with gradients in γ as described by the dilational modulus

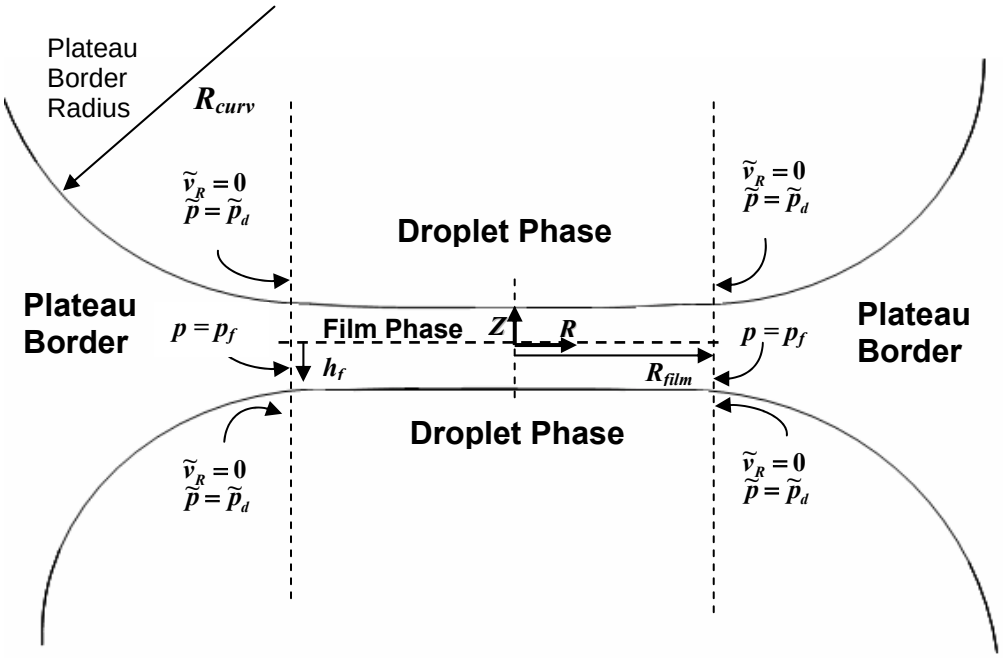

Figure 3.13: Drawing depicting the symmetric lamellar geometry for thin film drainage between two identical fluid droplets with the hydrodynamic boundary conditions.

$$\varepsilon = E_{Gibbs}/2 = d\gamma/d\ln A \qquad [9]$$

where A is the interfacial area of the disturbance.[162] The viscoelastic shear and dilational properties of the interface influence this flow.[163] For insoluble monolayers or cases where surfactant diffusion and adsorption are slow (frequency $\rightarrow \infty$)[69] ε becomes the limiting surface elasticity, $\varepsilon_o = d\gamma/d \ln \Gamma$. ε has been found to be nearly equivalent to ε_o for values of π up to approximately 16 mN/m for $C_{12}E_6$.[162] Here ε (and ε_o) increase with π in a relatively linear fashion. Thus, branched surfactants with higher values of π (greater than about 20 mN/m in Table 3.2) and hence ε_o are more likely to stabilize thin water films in CO_2 as observed.

For Langmuir adsorption,

$$\varepsilon_o = RT \cdot \Gamma_\infty c/c_{0.5} \qquad [10]$$

where Γ_∞ is the saturated adsorption, R is the gas constant, c is the surfactant concentration, and $c_{0.5}$ is the half saturation value.[162] Thus, an increase in Γ_∞, or a decrease in $c_{0.5}/c$, raise ε_o.[145] A steep Langmuir adsorption isotherm (small $c_{0.5}/c$) corresponds to a rapid increase in π or large pC20. Larger pC20 observed with branching favor an increase in ε_o, consistent with the observed enhancement in foam stability for these surfactants (Table 3.2).

As π increases beyond ~16 mN/m, diffusion of surfactant to the interface has been observed to cause ε to decrease with c and π, despite an increase in ε_o.[162] For the C/W foams where the surfactant partitions into CO_2, the diffusion may be expected to influence ε at a lower c than in the case of A/W foams. However, an increase in π and pC20 at a given bulk surfactant concentration with branching may still be expected to have a beneficial effect on ε.

If the time scale for surfactant diffusion and adsorption is shorter than the hydrodynamic time scale that creates the γ gradients, then the stability of the foam is not

improved significantly by the Marangoni effect.[164] This scenario arises when the surfactant is highly soluble in the dispersed phase, as the diffusion length to the lamellae is small. Ivanov et al. estimated an increase in the rate of film thinning by 10-100x when the surfactant is soluble in the dispersed phase relative to when it soluble in the continuous phase.[69] In addition, Varadaraj et al. demonstrated that branching of the ethoxylate surfactant tail increased the rate of surface tension reduction due to fast surfactant diffusion (measured by dynamic interfacial tension); consequently, A/W foam stability was low as surface tension gradients disappeared rapidly.[165] Therefore, emulsions and foams with high drainage rates require sufficiently slow diffusion and adsorption of surfactant at the interface in order for Marangoni flow to oppose the drainage. The slower drainage of the C/W foams makes Marangoni stabilization less important than for A/W or some O/W foams or emulsions (Table 3.5). Therefore, the stabilities of the C/W foams in Table 3.3 were high even when the surfactant favored the CO_2 phase, and Bancroft's rule was no longer obeyed.

3.4.3 Spatial and Surfactant Density Fluctuations Forming Holes

Spatial fluctuations (interfacial waves or "dimples") and surfactant density fluctuations, which are coupled, can lead to spinodal decomposition when the Laplace pressure becomes large relative to or exceeds the disjoining pressure.[66] These waves can also lead to asymmetric lamella drainage and film rupture.[144] The Gibbs free energy barrier for a spatial fluctuation depends upon γ, the elastic and shear dilational moduli, as well as the amplitude and wavelength of the wave. An increase in the elastic and shear dilational moduli dampens surface fluctuations and raises film stability. The smaller film sizes for C/W foam relative to A/W foam reduce the disturbance wavelength and thereby raise the barrier against fluctuations.[66,166] In contrast, the lower γ for the C/W foam

lowers the barrier. For a fluctuation in surfactant concentration, the probability of exposing a bare surface of size a is proportional to $\exp(-\varepsilon_o a/kT)$.[66] Thus, an increase in ε_o and ε produced by an increase in π with branching (equation 10) will dampen both spatial and surfactant density fluctuations, and thus improve foam stability as observed.[144,145] In addition, the lower interfacial tension gradients for the C-W systems will reduce the growth of the fluctuations.[144]

The phase behavior and curvature of a surfactant monolayer, and thus the resulting emulsion, can be manipulated by varying a formulation variable, such as the hydrophilic-lipophilic balance (HLB) of the surfactant, salinity, and temperature.[94,95] An analogous hydrophilic-CO_2-philic balance (HCB) has been defined and characterized for high pressure C-W systems.[42,96]

$$1/HCB = \frac{A_{TC} - A_{TT} - A_{CC}}{A_{HW} - A_{HH} - A_{WW}} \qquad [11]$$

where A_{ij} is the interaction energy for the various interactions between CO_2 (C), the surfactant tail (T), water (W) and the surfactant head (H). For a CO_2-philic surfactant, where 1/HCB > 1, the surfactant partitions more towards the CO_2 phase and bends about water, forming a W/C emulsion, as shown in Figure 3.14.[94,97] When 1/HCB < 1, the surfactant prefers the aqueous phase and the interface is concave with respect to CO_2, resulting in a C/W emulsion.[3,80,98] The CO_2 density, which may be tuned with pressure and temperature, has a profound effect on the emulsion phase behavior and the curvature of the surfactant monolayer as shown in Figure 3.14.

For O-W systems and some CO_2 systems, the emulsion undergoes a phase inversion at the balanced state when HLB or HCB = 1, where the surfactant exhibits an equal affinity for both phases[99] and the interfacial tension (γ) is a minimum (Figure 3.14).[37,82,100-102] The CO_2 distribution coefficients of 2EH-PO_5-EO_9 and 2EH-PO_5-EO_{15}

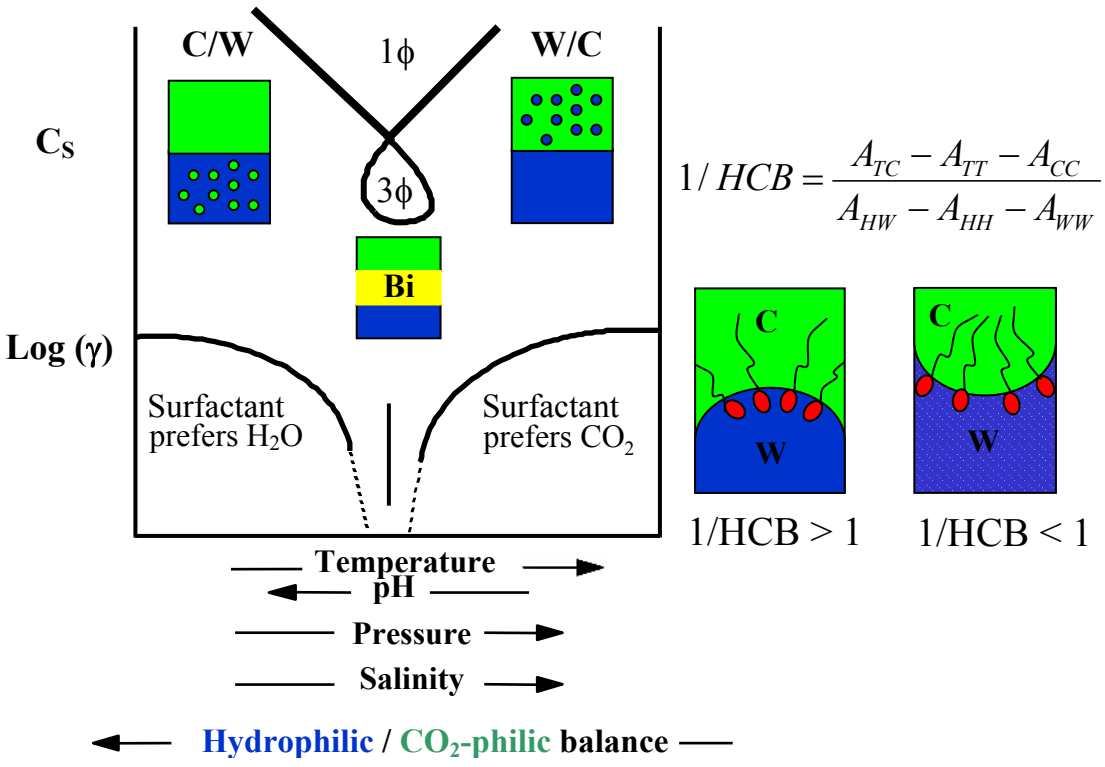

Figure 3.14: Schematic representation of the effect of formulation variables and HCB (hydrophilic-CO_2-philic balance) on the phase behavior and interfacial tension of a ternary water-CO_2-nonionic surfactant system.

(Table 3.3) show these surfactants are highly soluble in the dispersed CO_2 phase and the surfactant balance favors CO_2 (Figure 3.14). The EO head groups are moderately soluble in CO_2.[46] Even though these surfactants favored the CO_2 phase, C/W foams were formed and were stable against coalescence for over 60 h (Tables 3.3 and 3.4), in violation of Bancroft's rule. Da Rocha et al. has also reported the formation of C/W emulsions with CO_2-philic surfactants.[148] It was argued that viscous stresses through water were sufficient to shear CO_2 to form bubbles, whereas stresses through CO_2 were too weak to form water droplets.

Coalescence of foam bubbles can occur through a mechanism of hole formation and loss of the lamella. Holes of various radius, r_h, appear and disappear in the thin liquid films due to thermal fluctuations that produce spatial and surfactant density fluctuations.[67,70,167] If the hole radius is $\geq r_h^*$ (the critical radius), the hole will grow and the foam film will rupture to produce coalescence. The activation energy for formation of a hole (W_h) includes the energy penalty for creation of interfacial area and the high interfacial curvature at the edge of the hole (Figure 3.15). The Boltzmann probability of hole formation is $\exp(-W_h/kT)$.[67,70] Babak et al. added variable film thickness (h_f) to previous hole formation theories with the result

$$W^* \cong \frac{h_f^2 \gamma_h^2}{\gamma_p} \qquad [12]$$

where γ_p is the interfacial tension of the planar interface and γ_h is the interfacial tension of a curved border of the hole.[67] The stability of C/W foams is enhanced by the low ΔP_{film} and thus slow drainage of the lamella that inhibits the decrease in h_f according to equation 8.

To examine curvature effects, consider a surfactant that favors water over CO_2. In this case for C/W/C films (Figure 3.15a), there is a large penalty for bending the

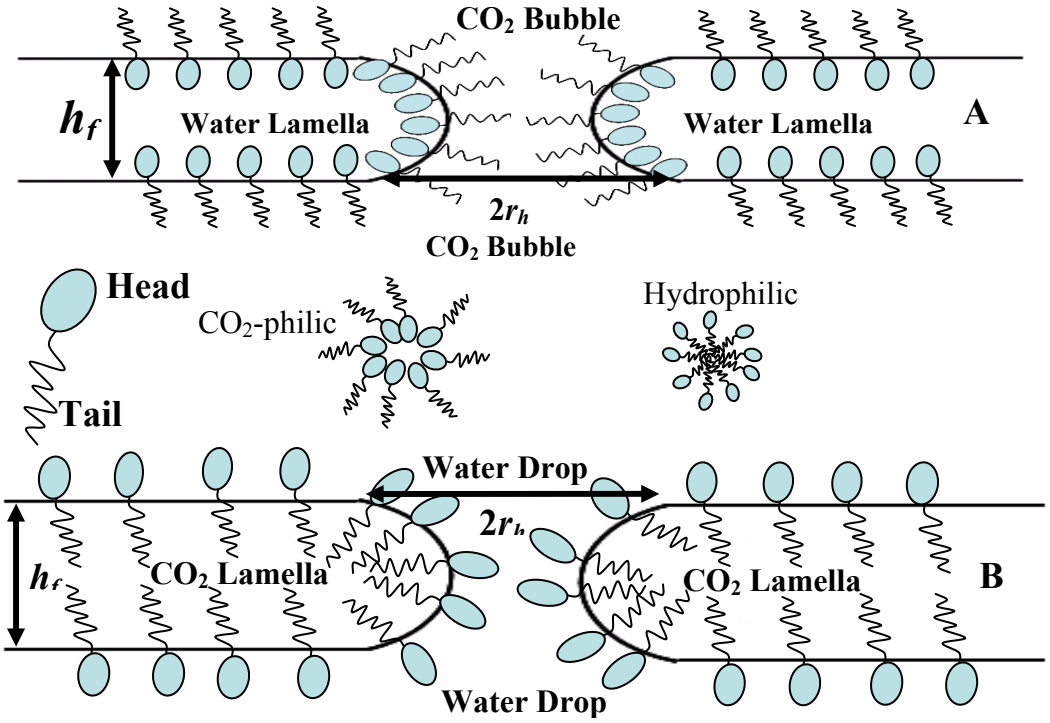

Figure 3.15: The formation of a hole in a water lamella (A, for a C/W foam) and a CO_2 lamella (B, W/C foam). The spontaneous monolayer curvature is also shown to compare the with the interfacial bending at the hole interface.

surfactant about water to open a CO_2 hole. The penalty is much smaller to open up a water hole for a W/C/W film (Figure 3.15b). Thus a C/W foam would be favored in accordance with Bancroft's rule as shown by the HCB schematic in Figure 3.14.

At the balanced state where γ is ultra-low (<< 0.1 mN/m), O-W emulsions are often highly unstable. Here the small energy to form a hole in the film (equation 12) often leads to rapid coalescence. In the case of C/W emulsions, the energy to form a hole will be much greater given the much larger γ at the balanced point.[37] Therefore, our emulsions were observed to remain stable even when the surfactant moved through the balanced point with a variation in temperature and pressure (Table 3.3). Babak et al. cites an interfacial tension of 0.1-1 mN/m as optimal for stability of 1-10 μm droplets for O-W systems, which is just below the range of the values for our C/W foams.[67]

The simple theory in equation 12 does not explain the violation of Bancroft's rule, whereby C/W foams are stable for highly CO_2-philic surfactants. These surfactants prefer to bend about water lamellae as shown in Figure 3.15a, based on relatively favorable CO_2- tail interactions, resulting in a relatively low W^*. Here hole formation would be probable in contrast with the stable foams. As shown in Figure 3.15a, the surfactant tails from the two curved interfaces are in close proximity when a hole is formed in the water lamella. For CO_2, the typical solvation of hydrocarbon tails is not sufficiently strong to prevent flocculation of water drops in W/C microemulsions and miniemulsions,[33,36,127,148] as explained more fully in Appendix B. Flocculation of the tails may act to close the hole and prevent coalescence, an important effect not included in equation 12. This flocculation is much weaker for O/W emulsions where tail solvation is stronger (Table 3.5) and the holes can form more readily and cause coalescence, consistent with the unstable emulsions for the 2EH-PO_5-EO_n surfactants. Bending of A/W films to open

water channels in water lamellae is also difficult due to the dense packing of the surfactant at the interface (Table 3.5).

The short time stability of C/W foams with small bubbles is characterized in terms of the growth rates (*dv/dt*). DOG-EO_{12} has the highest π in Table 3.2 and correspondingly the highest stability (lowest *dv/dt* value) (Table 3.2 and Figures 3.3 and 3.4). The higher π, which is favored by the double tail, lowers the Laplace pressure resulting in slower drainage. In addition, a higher π will produce a larger ε and ε_o against fluctuations that produce spinodal decomposition and hole formation. It will also enhance stability against drainage (Marangoni stabilization).

The *dv/dt* values of 2EH-PO_5-EO_{11}, 2EH-PO_5-EO_{15}, and 1Hex-PO_5-EO_{15} (with lower π) are slightly higher than that of DOG-$EO_{12;}$ however, the small bubbles persist for over 10-30 min. For 2EH-$EO_{11.8}$ with the lowest π value, *dv/dt* is 3x greater than that of 2EH-PO_5-EO_{11}. The small tail of 2EH-$EO_{11.8}$ does not balance the large head of the molecule (indicated by the HLB of 16.1) leading to lower adsorption at the C-W interface.[146] As a result of the lower π, a higher Laplace pressure and lower Π_d, plus a lower ε, ε_o, and γ gradients each contribute to a higher coalescence rate (Figure 3.3 slope).

The stability for LA-EO_{12} relative to the more efficient surfactants was lower than expected from the π values alone. The π can be used as a guide for surfactant adsorption, which influences the Laplace pressure, ε, and the steric and electrostatic repulsive interactions of Π_d; however, additional effects are present. The linear tail of the surfactant is not solvated by CO_2 as well as bulkier tails.[79] The linear tails block less area of the interface than the EO head groups, thus the number of EO units and resulting change in HLB are important. The C_{12-14}-EO_7 surfactant with a linear tail does not form a foam at 1% v/v surfactant and 24 ˚C, (Table 3.1), while the similar methylated C_{8-14}-$PO_{2.5}$-EO_7 stabilizes a foam with only 0.5% v/v surfactant (both surfactants have HLB values of

12.1). However, when a larger number of EO units are included in the surfactant head, a larger area is occupied at the liquid-liquid interface (given the modest CO_2-philicity of EO groups) and lamella can be stabilized with these higher HLB surfactants. 1% v/v C_{12}-EO_{12} with an HLB of nearly 16 forms a stable non-coalescing C/W foam (bubble size ranging from 1-30 μm) with a 90% quality at 24 ˚C and 2000 psia using sand pack with 50 μm pores at a total foam flow rate of 6 ml/min.

In most cases foam stability decreased markedly at temperatures no more than 4 ˚C above the cloud point in water, as the surfactant precipitated. Only DOG-EO_{12} supports a foam up to about 14 ˚C above the cloud point (46 ˚C in Table 3.1). The large size of the DOG-EO_{12} tail at the C-W interface (due to the dual tail chains that can independently spread at the interface) is more likely to keep the surfactant solvated at the interface as the solubility in water decreases.[146] The polydispersity in the number of EO groups can also decrease the temperature sensitivity.[168] Eventually, as the temperature is raised beyond 60 ˚C even the surfactants with the higher EO number precipitate from the water and the foams become unstable.

Foam and emulsion stability decreased with a reduction in surfactant concentration as was shown in Figure 3.5 and Table 3.4. A decrease in c raises ΔP_{film} and lowers Π_d (equation 7), π, and thus ε. These factors increase drainage rates, hole formation, and spinodal decomposition, each of which reduces foam stability. The effect of surfactant diffusion is also lowered, thus ε approaches ε_o at a lower c value. This loss of stability is demonstrated for 0.1% v/v 2EH-PO_5-EO_9 C/W foam at 24 ˚C (Figure 3.5) where slugs of the phases are observed. An increase to 0.2% v/v 2EH-PO_5-EO_9 increases the stability of the foam lamellae, although small bubbles are still relatively unstable. For higher c, much greater stability is present (as seen for 0.5-1% v/v surfactant in Figure 3.5). When the interfacial concentration of the surfactant is reduced due to surfactant

precipitation at the approach to the cloud point (at 55 ˚C and 2000 psia), the 0.2% v/v 2EH-PO_5-EO_9 foam becomes unstable again with only slugs of the CO_2 and aqueous phases produced. However, coalescence is mitigated with a slight increase in *c* to 0.3% v/v or higher, even in the presence of salt, which depresses the cloud point temperature to about 55 ˚C (Figure 3.5).

3.4.4 Ostwald Ripening and Long Term Stability

Foam ageing also occurs via Ostwald ripening as a function of the polydispersity in bubble size. Ostwald ripening is described by Lifshitz and Slyozov,[169] as updated by Wagner[170] (LSW) for dilute emulsions. The LSW theory assumes that the diffusion is from a curved bubble to a flat interface such that

$$\Omega_3 = \frac{dD_{sm}^3}{dt} = \frac{64\gamma D_{diff} S V_m}{9RT} F \qquad [13]$$

where D_{diff} is the molecular diffusion coefficient, S is the bulk solubility, and V_m is the molar volume of the dispersed phase (CO_2).[171] A correction factor, F, is included to increase the ripening rate for small diffusion lengths and non-dilute conditions.[171] For a quality of 90%, F is 25.[172]

For a given polydispersity, Ω_3 did not vary significantly among the various systems as the relevant properties in equation 13 were similar, with the exception of modest variations in γ. As expected, variation of the foam polydispersity leads to large changes in measured Ω_3 for 2EH-PO_5-EO_9 (Figure 3.9 and Table 3.4). The slopes (Ω_3) vary nearly 100x due to the polydispersity differences between the foams under otherwise similar conditions. Over long times (> 60 hours) coalescence was not observed visually for the C/W foams; however, Ostwald ripening was present (Figures 3.10 and 3.11). The polydispersity of the foams decreases over time as the small bubbles disappear which

then acts to decrease Ω_3 over ensuing time periods. For example, the Ω_3 decreases from 7.5 to 0.5 for 0.3% v/v 2EH-PO_5-EO_9 foam (Figure 3.5) as the polydispersity drops from 3.2 to 0.5 over 60.6 hours. Here, the Ostwald ripening becomes very slow.

Although Ostwald ripening reduces the polydispersity of the foam, coalescence increases the polydispersity (Figure 3.4, Table 3.2). The high *dv/dt* for the poor surfactant (low π) 2EH-$EO_{11.8}$ leads to rapid increase in D_{sm} and U_{poly} (Figure 3.4) as larger bubbles are formed during coalescence. Thus the driving force for Ostwald ripening increases as well. In Figure 3.4, U_{poly} increases for 2EH-$EO_{11.8}$ rapidly for the first 10 s, and then declines from about 50 s as the Ostwald ripening rate increases. On the other hand, the U_{poly} of the DOG-EO_{12} and 2EH-PO_5-EO_{11} do not experience large drops in U_{poly} from Ostwald ripening in this time frame. Here the initial coalescence occurs more slowly resulting in a lower driving force for Ostwald ripening. At lower concentrations, for example 0.2% v/v 2EH-PO_5-EO_9 (Figure 3.5), where some coalescence creates large bubbles and accordingly a higher U_{poly} (4x greater than foams with higher concentrations), a higher Ω_3 (300 $\mu m^3/s$) also results relative to the higher concentrations (Ω_3 values near 1 $\mu m^3/s$). Changes to the foam conditions in terms of temperature and salinity do not vary Ω_3 significantly for a given polydispersity, as a result of small changes in the relevant properties in equation 13.

3.5 CONCLUSIONS

Investigation of stabilities and morphologies of C/W foams formed with nonionic hydrocarbon surfactants by *in-situ* optical microscopy and viscosity measurements, combined with recent measurements of interfacial properties,[146] provides novel insight

into foam stability mechanisms. Both coalescence and Ostwald ripening were identified and characterized via microscopy over time frames from seconds to days. At the C-W interface where a low γ_o creates a low driving force for adsorption, A_m and thus the contact between phases is greater, relative to the A-W and O-W interfaces. Therefore, reducing contact between the phases by the molecular design of the surfactant is more important at the C-W versus the A-W and O-W interfaces.

Branching of the surfactant tail reduces contact of the CO_2 and water phase relative to a linear tail. Thus, at low hydrophilic-lipophilic balance (HLB) values (less than about 14) linear tails are poor foam stabilizers. At a constant HLB of 12.1, the linear $C_{12\text{-}14}$-EO_7 did not form a foam at 1% v/v surfactant (Table 3.1), while the similar methylated $C_{8\text{-}14}$-$PO_{2.5}$-EO_7 stabilized a foam at only 0.5%. However, if the number of EO units in the head is increased (which also raises the HLB) the surfactant occupies a larger area at the liquid-liquid interface and lamella can be stabilized, such as for C_{12}-EO_{11} with an HLB of nearly 16.

In addition, a reduction in contact between phases with branching of the tails or inclusion of PO units, which raises π and similarly the surfactant efficiency (pC20),[146] was found to be beneficial for the production of stable foams. Because of the low γ of the C/W foams, micron sized bubbles were formed relative to mm-sized bubbles for A/W foams. For surfactants with PO, tail branching, or double-chain tails, for example, 1% v/v DOG-EO_{12}, 2EH-PO_5-EO_9, or 2EH-PO_5-EO_{15}, coalescence of the C/W foam bubbles was rare once the diameters were greater then about 0.5 μm over 60 hours. At similar conditions, A/W foams began coalescing immediately and decane/water emulsions could not even be formed. The greater stability of the C/W foams to coalescence compared with the A/W foams may be attributed to the smaller γ and P_c, lower drainage rates, smaller

film size and a sufficient π and thus dilational modulus to hinder spatial and surface density fluctuations that lead to coalescence.

Branched surfactant structures with HLB values ranging from 8.8-16.5 were used to stabilize C/W foam. Unexpectedly, on the basis of Bancroft's rule, C/W foams were stable even when the surfactant preferred the CO_2 phase. We attribute the violation of Bancroft's rule to three effects. Firstly, the viscous stresses through water are sufficient to shear CO_2 to form bubbles, whereas stresses through CO_2 are too weak to form water droplets. However, this is not the case for an oil-water system such as decane-water where water can be sheared into droplets thus inverting the emulsion, which is the case when 2EH-PO_5-EO_9 and 2EH-PO_5-EO_{15} were studied with 90% v/v decane and water although γ values were similar to the CO_2-water experiments.

The second effect is the low drainage rate for C/W foams, from the low γ and thus P_c, which makes Marangoni stabilization of less consequence. Marangoni stabilization can be important for A/W systems as well as some O/W systems (when higher drainage rates and high γ values are present).

The last effect is the formation of lamella holes. On the approach to the balanced state, hole formation in the water lamellae followed by coalescence becomes prevalent for O/W emulsions as γ becomes << 1 mN/m.[70] In CO_2, this hole formation is less favored given larger γ values on the order of 1 mN/m. The CO_2 holes in the water lamellae can close as a consequence of strong tail flocculation. This flocculation is typically not present for oils that solvate tails more strongly and can result in reduced stability of the oil/water emulsions compared with C/W foams (as seen with the decane-water systems).

A variety of nonionic surfactant structures were investigated at the C-W interface in terms of C/W foam stability. Stabilization of C/W foams can be accomplished with

low molecular weight surfactants where the tail is branched or includes PO groups to increase the area occupied by the tail at the C-W interface. When the structure of the surfactant tail is linear, a larger number of EO units (greater than about 12) can also lead to stable C/W foams due to the larger size of the surfactant head at the interface. Furthermore, double-tail surfactants, where the two alkyl chains can independently spread at the interface occupying the largest interfacial area and leading to the largest measured π values, also produce the most stable C/W foam with small submicron bubbles. Interestingly, the surfactants may be highly soluble in the dispersed CO_2 phase, consequently a low HCB (or HLB) does not result in low stability of the C/W foam as discussed above. The high solubility of PO and branching in CO_2, combined with the moderate solubility of EO by CO_2 can lead to a high solubility of certain surfactant structures in CO_2 (such as 2-EH-PO_5-EO_n surfactants). Thus, a large number of nonionic surfactant structures have been used to form stable C/W foams.

For EOR where the foams will be in the ground for weeks to months, the long time stability against coalescence of the C/W foams measured for several days is an important advance. Furthermore, the ability to selectively form stable C/W emulsions when oil is absent, and unstable C/W emulsions when oil is present is highly beneficial, to provide low CO_2 mobilities in oil depleted zones, and high mobilities in oil-rich zones. Finally, CO_2 soluble surfactants with distribution coefficients that favor CO_2 can be injected with CO_2 to lower well-bore pressures and minimize surfactant loses to water in the reservoir.

Chapter 4: Rheology and Viscosity of Carbon Dioxide-in-Water Foams with Nonionic Hydrocarbon Surfactants

The mobility of carbon dioxide (CO_2) is shown to be reduced substantially through the formation of highly viscous CO_2-in-water (C/W) foams with novel nonionic hydrocarbon surfactants. The pressure drop across a 762 μm inner diameter capillary tube was determined to characterize the apparent viscosity of the bulk foams at high pressures (> 1000 psia). In addition, *in-situ* optical microscopy of the foam texture (bubble size) reveals cell diameters ranging from sub-micron to hundreds of microns. The CO_2 foams contained at least 74% v/v CO_2 to form lamellae between the dispersed CO_2 drops. The number of lamella mainly determines the viscosity of the foam due to the shear stress of the lamellar liquid inhibiting the flow. Thus, foam bubble or cell sizes as determined by the generation conditions and stabilization of the lamella by the surfactant are of primary importance. Viscosities greater than 200 cP were achieved relative to pure CO_2 viscosities ranging from 0.04 to 0.1 cP. The relationship between shear rate and shear stress is described by either Newtonian or Power-law behavior or a combination of the two. The viscosity measurements are rapid and can be used as a screening technique to test various surfactant structures.

4.1 INTRODUCTION

Enhanced oil recovery by carbon dioxide flooding is of great interest to remove the estimated 40-60% of oil remaining in the reservoir after primary and secondary recoveries. Carbon dioxide (CO_2) is an environmentally benign, non-toxic, non-flammable, and recyclable solvent that in many cases is inexpensively available near oil reservoirs. CO_2 enhanced oil recovery (EOR) is often limited when the gas contacts and sweeps only a small portion of the oil in the reservoir, due to the low viscosity of the injected CO_2 (0.01-0.09 cP).[59] Concentrated CO_2-in-water (C/W) emulsions (foams) can decrease the mobility of CO_2 by 100 to 1000 fold and improve the sweep efficiency markedly.[56,173-175] However, the understanding of high-pressure CO_2 foam rheology has been limited by the difficulty in visualization and other characterization of the foam in the pores of rock cores.[58,63,64,176]

Rossen et al. have reviewed foams for use in EOR, including CO_2 foams.[59] The systematic evaluation of numerous surfactant structures on CO_2 foam properties would be very time consuming in traditional core-flood experiments, where a single flood may require up to 24 hours or more. A rapid technique for determining the preference of the surfactant for the water phase versus the CO_2 phase, the foam texture, and the foam apparent viscosity would facilitate surfactant-screening studies for choosing surfactant structures for the time consuming core floods.

The structure of CO_2 foams, also known as high internal phase emulsions, where the internal phase volume fraction is greater than 74%, have been studied previously in visual cells. Da Rocha et al.[98] explored nonionic block copolymers as stabilizers for C/W emulsions with up to 70% v/v CO_2 and demonstrated stability against coalescence and flocculation for greater than 48 hours. Dhanuka et al.[80] studied the hydrocarbon surfactant

commercially known as Tergitol TMN 6 by Dow (90% poly (ethylene glycol) 2,6,8-trimethyl-4-nonyl ether and 10% water w/w) as a stabilizer for 50-90% v/v CO_2 foams with cell sizes of less than 10 μm and stabilities in excess of 24 hours for a 90% v/v CO_2 foam.

In order to be able to measure a large increase in viscosity upon formation of a CO_2 foam, the foams must have sufficient stability through the viscometer. The instabilities of CO_2 foams over time due to coalescence and Ostwald ripening were recently investigated for several nonionic hydrocarbon surfactant structures (in Chapter 3). A slower growth rate of foam bubbles has been linked to a high interfacial activity via surface pressure measurements for C/W foams. Coalescence was avoided for most surfactant structures under a variety of conditions when the bubble size was 0.5 μm or larger. Foam stability for weeks to months would be desirable in certain cases in EOR.

Reidenbach et al. studied the rheology of nitrogen and CO_2 foams under laminar and turbulent flow and developed corresponding models where substituting CO_2 for nitrogen gave similar laminar rheology.[177] The quality, continuous phase, and texture of the foam was used to describe the laminar flow as a Herschel Bulkley yield-psuedoplastic type relationship. Hutchins et al. has also developed a foam rheometer (a circulating-foam loop) to evaluate foam formulations at the temperature, pressure, pH, and shear rates of use for foam fracturing.[178] The foams are investigated via rheology measurements over time, foam persistence (stability) data, and bubble size distributions, where CO_2 foam viscosities were measured ranging from less than 10 cP to over 200 cP depending on the conditions. However, most of these foams used a gelling agent or clay stabilizer in the aqueous phase in addition to a surfactant, and thus the effect of the surfactant structure alone on the rheology of the foam was not fully investigated. Phillips et al. also used a high- temperature, high-pressure pipe viscometer to measure the properties of CO_2

foams in which higher concentrations of surfactant and gelling agent were required to stabilize CO_2 foams as compared with nitrogen foams.[84] In addition, the rheology of the nitrogen foams could not be used to describe the same system with CO_2 as the dispersed phase. Although, the surfactants used to stabilize the foams were not revealed.

Smith et al. investigated the viscosities of CO_2 foams (with water and brine) stabilized by either a nonionic, cationic, or anionic surfactant at flow rates of 0.001-0.01 ml/s using a capillary viscometer without a gelling agent, however foam bubble sizes were not measured.[179] Viscosities ranging from 0.4-500 cP were measured and a power-law dependence was found for the shear-thinning foams. An increase in the foam quality (to 90-95% CO_2) or surfactant concentration (from 5% by weight in the water) led to exponentially higher foam viscosities, although a maximum in the foam viscosity was found as the salinity of the system was increased from 0-8% by weight in the water phase.

The primary objective of this work is to investigate novel nonionic hydrocarbon surfactants for C/W foams to raise the viscosity and decrease the mobility of the CO_2. The viscosity of these foams is determined from the pressure drop across a 762 μm inner diameter capillary tube and foam texture (bubble size) measurements are made by *in-situ* optical microscopy. The CO_2 foams are stabilized with various surfactant structures with at least 74% v/v CO_2 to form lamellae between the dispersed CO_2 drops. The surfactants must stabilize these thin foam lamellae, especially for small bubbles with high Laplace pressures, to produce viscous foams. The foam quality (volume fraction CO_2) and velocity are varied, as well as formulation variables including temperature, salinity, and CO_2 density (ρ). Viscosities of greater than 200 cP and bubble diameters of less than 1 μm were achieved relative to pure CO_2 viscosities ranging from 0.04 to 0.1 cP. The relationship between shear rate and shear stress is described by Newtonian and Power-

law behavior. In addition, complimentary experiments are presented to describe the effect of the hydrocarbon surfactant structure on the cloud point temperature.

4.2 EXPERIMENTAL METHODS

4.2.1 Materials

Sodium chloride (GR crystals) from EM Science was used as received. Decane (certified n-decane), magnesium chloride (hexahydrate, enzyme grade), and calcium chloride (certified ACS dihydrate) were used as received from Fisher Scientific. Deionized (DI) water from a Nanopure II (Barnstead, Dubuque, IA) with an average conductance of 16 ohms was used throughout. Brine solutions were made consisting of 2-10% NaCl, 0.5% $CaCl_2$, and 0.1% $MgCl_2$ by weight (w/w) in DI H_2O. Surfactants listed in Table 4.1 and depicted in Figure 4.1 (where PO stand for a propylene oxide unit, and EO stands for an ethylene oxide unit) were from Dow Chemical and were used as received. Instrument-grade carbon dioxide (> 99.99% pure, Praxair Distribution Inc.) was used. Measurements by volume are represented by v/v.

4.2.2 Cloud Point Measurements

The cloud point temperature of the surfactant in the aqueous phase was measured with a surfactant concentration of 1% v/v. The aqueous phase consisted of either pure DI water or a brine solution (2% NaCl, 0.5% $CaCl_2$, and 0.1% $MgCl_2$ w/w in water). The surfactant solutions were heated slowly from 24 to 80 ˚C and the temperature at which

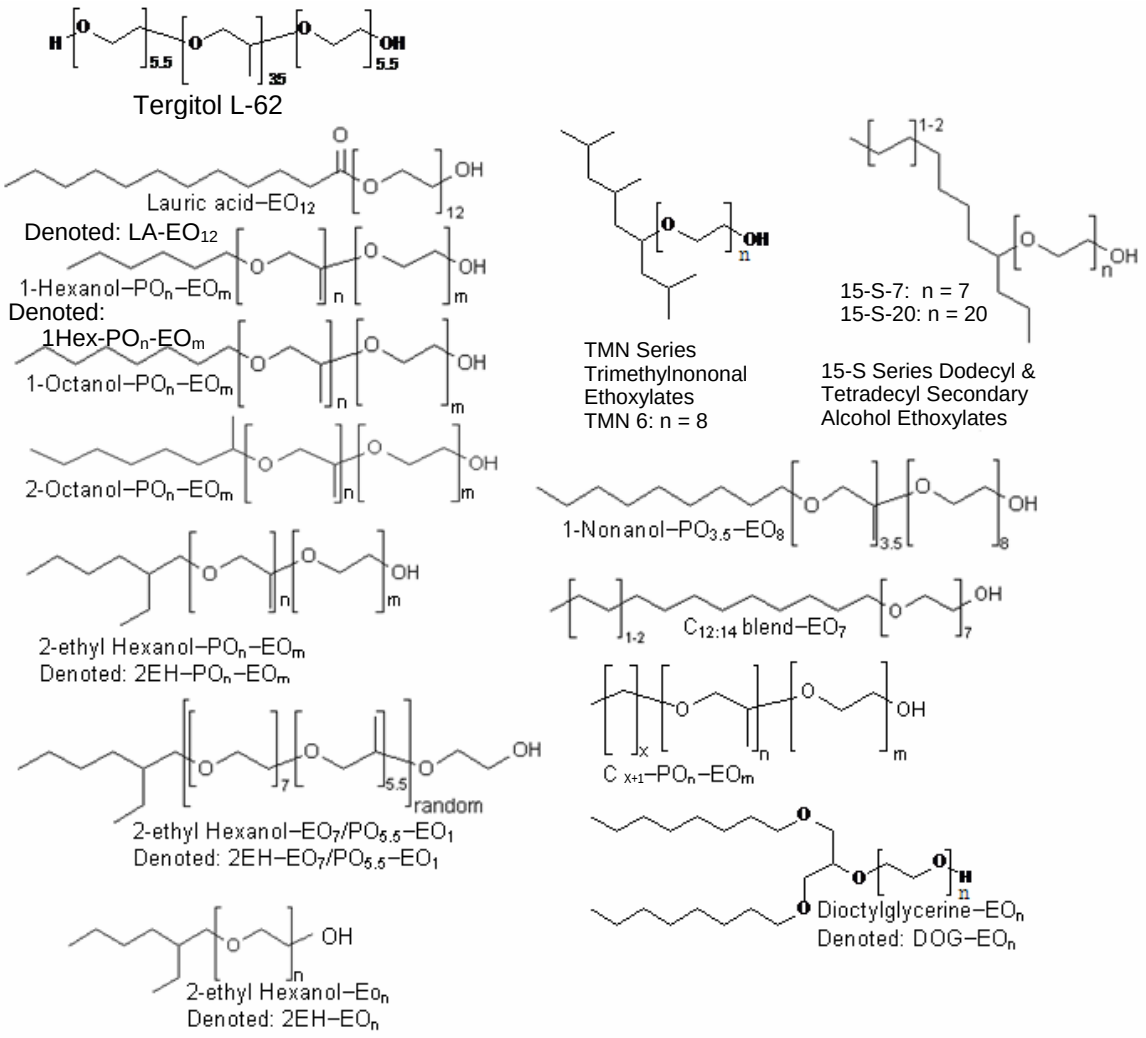

Figure 4.1: Schematics and naming scheme of surfactants.

Table 4.1: Surfactant properties, bulk foam apparent viscosities, and initial D_{sm} are listed (at Q_{total} of 6 ml/min, 2000 psia, 90% v/v CO_2, and 1% v/v surfactant where the coarse sand pack with 50 μm pores was used). $^{\delta}$ indicates 87% v/v CO_2, $^{\varepsilon}$ indicates 88% v/v CO_2, $^{\Psi}$ indicates Q_{total} of 4 ml/min, ^{a} indicates 0.5% v/v surfactant, $^{\beta}$ indicates 1% v/v TMN 6, and $^{\Theta}$ indicates No foam with 1% v/v TMN 6 24 ˚C.

Surfactant	Cloud Point (ºC)		HLB	Foam (with Water) at Q_{total} of 6 ml/min							
				24 ˚C		40 ˚C		60 ˚C		70 ˚C	
	Water	Brine		η_{foam} (cP)	D_{sm} (μm)	η_{foam} (cP)	D_{sm} (μm)	η_{foam} (cP)	D_{sm} (μm)	η_{foam} (cP)	D_{sm} (μm)
L62	(32)	27	8.8	130$^{\Psi}$	33	No foam		No foam			
TMN 6 (5 %)$^{\Theta}$	(36)$^{\beta}$	31$^{\beta}$	12.9	74	18	18$^{\varepsilon}$	27	No foam			
15-S-7	(37)	32	12.5	45	51	17	46	No foam			
15-S-20	(>100)		16.5	141	21	94	26	53	34	51	19
Lutensol XP70	58		-	16	90	17	42	7	Slugs	-	
$C_{8\text{-}14}$-$PO_{2.5}$-EO_7 ^{a}	60		12.1	38	65	22	50	No foam			
TM NP-9	(54)		(12.9)	140	20	40	18	No foam			
LA-EO_{12}	56		15.2	14	61	-		No foam			
1Hex-PO_5-EO_9	49		14.6	31	106	73	55	No foam			
1Hex-PO_5-EO_{11}	64		15.4	49	66	94	29	35	46	No foam	
1Hex-PO_5-EO_{13}	78		16	36	63	90	24	49	35	No foam	
1Hex-PO_5-EO_{15}	> 80		16.5	46	80	87	25	55	37	59	52
1-Octanol-$PO_{4.5}$-EO_8	58		13.4	35	57	No foam		-			
1-Octanol-$PO_{4.5}$-EO_{12}	59		14.9	9	41	No foam		-			
1-Nonanol-$PO_{3.5}$-EO_8	58		13.2	110	43	76	42	No foam			
C_{13}-$PO_{1.5}$-EO_6	34		10.8	31	52	-		No foam			
C_{11}-PO_2-EO_7	50	42	12.2	79	53	61	46	No foam			
$C_{12\text{-}14}$-EO_7	52		12.1	No foam		-		-			
C_9-PO_4-EO_8	56		13	156	34	99	18	No foam			
2-Octanol-PO_9-EO_9	45	36	12.4	140	47	86	40	No foam			
2EH-PO_2-EO_4	< 24		11.2	10	63	No foam		No foam			
2EH-PO_3-EO_3	< 24		9.7	No foam		-		-			
2EH-PO_5-EO_8	54	40	13.2	88	39	41	50	No foam			
2EH-PO_9-EO_9	40	34	12.4	145	27	78	47	No foam			
2EH-PO_{12}-EO_{11}	39	32	12.3	135	20	55	47	No foam			
2EH-PO_5-EO_9	60	54	13.6	125	27	101	28	26	61	No foam	
2EH-PO_5-EO_{11}	71		14.4	190	13	96	46	50	40	No foam	
2EH-PO_5-EO_{13}	> 80		15.1	137	14	100	18	49	41	No foam	
2EH-PO_5-EO_{15}	> 80		15.6	153	22	140	26	57	35	53	38
2EH-EO_5	< 24		12.8	19	26	2$^{\delta}$	48	No foam			
2EH-$EO_{11.8}$	> 80		16.2	60	39	49	28	43	25	40	35
DOG-EO_{12}	46	38	13.9	116	30	74	48	24	-	No foam	

each solution turned hazy was recorded and repeated with a maximum error of approximately ± 1 ˚C. The cloud point temperature of commercially available surfactants was given as reported by the manufacturer (see Table 4.1).

4.2.3 Bulk Foam Apparent Viscosity Measurements

The apparatus for the measurement of foam viscosity has been previously described in Chapter 3. Briefly, an Isco syringe pump (model 260D) with a series D pump controller and a LDC/Milton Roy consta Metric III metering pump were used to inject the CO_2 and aqueous surfactant solution (respectively) simultaneously into the system at set flow rates. The mixture of CO_2 and surfactant solution entered a sand pack with hydrophilic pores for foam generation (10.2 cm long, 0.386 cm inner diameter tubing packed with pre-washed 20-40 Mesh sand held in place by wire screens affixed to tubing ends) at total volumetric flow rates of 1.5 to 9 ml/min. The sand pack for the TMN 6 experiments used packed cotton at the tubing ends instead of the wire screens. In later experiments, a differential pressure meter was used to measure the pressure drop across the sand pack using a differential pressure transducer with 100 psia diaphragm (Validyne model CD23).

The foam generated in the sand pack flowed through a capillary (0.0762 cm inner diameter, 195 cm long). The differential pressure (ΔP) across the capillary was measured by either a high-range or low-range differential pressure transducer (Validyne model CD23). The high ranged pressure meter contained either a 100 or 250 psia diaphragm, while the low ranged pressure meter contained either a 20 or 50 psia diaphragm, as larger ΔP ranges were found necessary after some experiments. An average ΔP value was obtained by averaging the values recorded over at least 2 minutes, when the foam is

flowing at approximately steady state, with ΔP varying less than about 15% of the mean value.

Finally the foam flowed through the heated (40 ˚C or higher with a water bath) back-pressure regulator (BPR) (Swagelok model SS-4R3A adjustable relief valve with either a R3A-E spring for 2250-3000 psia back pressure setting or a R3A-F spring for 3000-4000 psia) where CO_2 expanded to atmospheric conditions and the surfactant solution was captured for disposal.

4.2.4 Microscopy Measurements

The *in-situ* characterization of bubble sizes of the C/W foam was measured by diverting foam flow after the sand pack or capillary to a high-pressure microscopy cell[137] with two six-port injection valves (Valco Instruments, model C6W) and then back to the flow cycle. One valve determined the sampling point for the foam and the other controlled flow through the microscopy cell. The microscopy cell was mounted on a microscope (Nikon Eclipse ME600). The sapphire windows (Swiss Jewel Company, W6.36, 0.635 cm diameter and 0.229 cm thickness) were separated with foil spacers creating a path length of approximately 25 μm.[80] Microscopy images were captured when flow through this cell was stopped via a Photometrics CoolSNAP CF CCD camera connected to a computer. Foam was flowed through the microscopy cell for several cell volumes prior to image recording to ensure foam photographed did not age significantly.

The images were analyzed with ImageJ software by setting the scale (microscopy standards were used), adjusting the threshold value of the image, and using the measure particles function. In most cases, the bubble areas with a circularity of 0.60 or greater were obtained, and thus converted to effective spherical radii. Size distribution parameters and average radii were then calculated. The minimum bubble size that could

be measured had a diameter of 0.4 μm at 50x magnification, 0.88 μm at 20x magnification, and 1.8 at 10x magnification; bubbles smaller than these values could not be detected with the microscope and were excluded. Average bubble sizes were obtained by generally analyzing 6-9 microscope images at each condition, which corresponds to at least several 100 bubbles and up to 10,000 bubbles. In Appendix C, typical micrographs of foam are presented.

4.3 THEORY

As foams are a dispersion of two phases, the rheological behavior is more complex than that of either of the phases. The foams often exhibit elastic behavior due to the compressibility of the dispersed phase and reversible deformation of the foam structure.[68] The interconnected properties of the continuous phase also influence the rheological properties of the foam, especially when the viscosity of the internal phase is low (as it is for typical air-water foams and C/W foams).[180] Thus, a yield stress is commonly found for foams due to the elastic nature of this interconnected network of fluid films.[181]

The structure of the continuous phase also determines the apparent viscosity of the bulk foam (η_{foam}). The foam viscosity is highly dependent on the quality and bubble sizes, which directly determine the number of lamellae in the foam. The shear stresses are concentrated at the lamellae and the thin liquid film that forms on the capillary wall. A diagram magnifying the foam near the capillary wall is presented in Figure 4.2. With the assumption of the no-slip boundary condition, the shear stresses in the liquid phase are translated through the thin film and the lamellae near the capillary wall. Therefore, the

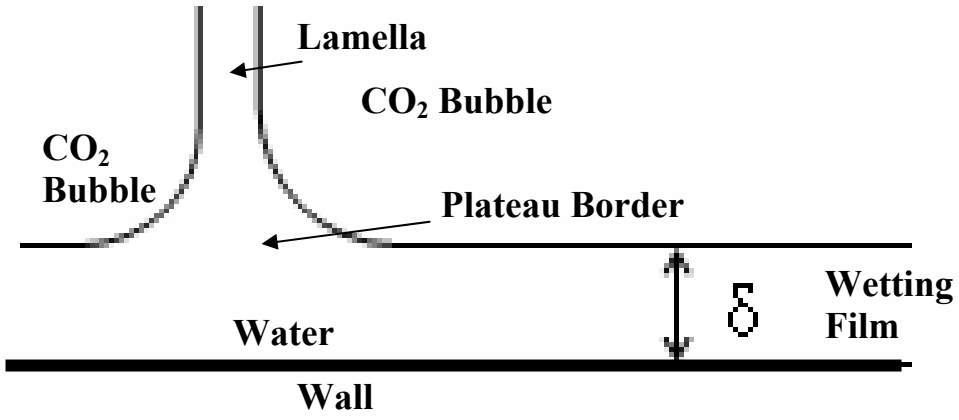

Figure 4.2: Diagram of the magnified view of the thin liquid wetting film and foam lamella at the capillary tube wall.

continuous liquid phase is responsible for the majority of the resistance to flow and consequently the high viscosity of the foam. The number of lamellae, the interfacial tension, continuous phase viscosity, and quality are the main factors that determine the foam viscosity.

A proposed equation for the viscosity of a concentrated emulsion (η_{HIPE}) in 3D derived from a 2D geometry-based model by Princen et al.[182] is

$$\eta_{HIPE} = \frac{\tau_o}{\dot{\gamma}} + C(\phi)\eta_c\left(\frac{\gamma}{\eta_c R_{sm}\dot{\gamma}}\right)^{1/3} \quad [1]$$

where $\dot{\gamma}$ is the shear rate, R_{sm} is the Sauter mean radius of the internal phase, γ is the interfacial tension, τ_o is the yield stress, η_c is the viscosity of the continuous phase, and $C(\varphi)$ is a numerical factor. Although this equation has been used to describe modulus and yield stress data, viscosity data can be fitted only by changing the exponent to of the last term to ½ from $^1/_3$ and using τ_o and C as fitting parameters.[180,182]

The apparent viscosities of the bulk foams (η_{foam}) investigated here are calculated from the known $\dot{\gamma}$ and measured pressure difference (ΔP) across the capillary with a length (L) of 195 cm. The shear stress (τ) and $\dot{\gamma}$ are calculated from $\Delta PR/2L$ and the velocity gradient (U/R), respectively. An additional geometric scaling term, λ, is used to calculate the apparent foam viscosity

$$\eta_{foam} = \frac{\tau}{\dot{\gamma}} = \frac{\left(\frac{\Delta P \cdot R}{L}\right)}{\left(\frac{U}{R}\right)}\lambda = \frac{\lambda R^2 \Delta P}{LU} \quad [2]$$

where R is the capillary tube radius, λ = 0.5 which also absorbs the factor of 2 in the denominator of τ. The average velocity, U, is determined from the total volumetric flow rate of the foam (Q_{foam}, the sum of the flow rates for the two phases) divided by the cross sectional area of the capillary tube. Unlike Newtonian fluids, plug flow generally occurs away from the wall in foams. The velocity profile of a foam and a Newtonian fluid in a

capillary tube are depicted in Figure 4.3. The addition of a geometric scaling term, λ, takes into account the fact that τ mainly occurs only in the regions near the capillary wall, not throughout the entire radius of the capillary. The scaling factor was set to an arbitrary value of 0.5. Although topological transitions can occur in foams, where foam cells change position and effectively hop to the next metastable disordered state,[181,183] plug flow was observed for all the C/W foams investigated here.

The Sauter mean diameter of a given foam, D_{sm}, and the polydispersity U_{poly} are calculated as follows

$$D_{sm} = \frac{\sum_i D_i^3}{\sum_i D_i^2} \quad [3]$$

$$U_{poly} = \frac{1}{D_{med}} \frac{\sum_i D_i^3 \left| D_{med} - D_i \right|}{\sum_i D_i^3} \quad [4]$$

where D_i is the diameter of a foam bubble and D_{med} is the median bubble diameter of the foam. Number average diameters, D_{avg}, can also be calculated from the D_i values.

4.4 RESULTS AND DISCUSSION

Table 4.1 presents the measured cloud point temperatures for the surfactants in water and brine (2% NaCl, 0.5% $CaCl_2$, and 0.1% $MgCl_2$ w/w in water) at 1% v/v surfactant in the aqueous phase. The hydrophilic-lipophilic balance (HLB) of the surfactants is also listed as calculated from the group contribution method of Guo et al.[147] The HLB of the commercial surfactants as reported by the manufacturer are presented in parenthesizes. The η_{foam} as measured by the ΔP (equation 2) are also listed in the table

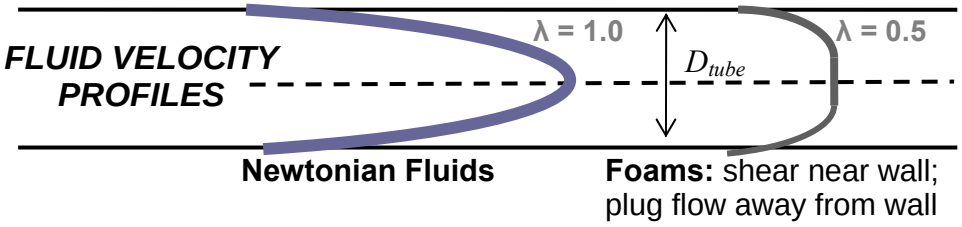

Figure 4.3: The velocity profiles for a Newtonian fluid (left) and a foam (right) under going plug-type flow in the cross-section of a capillary tube.

along with the initial D_{sm} (equation 3) of the foam at 24-70 ˚C and 2000 psia with a quality of 90% v/v CO_2 and 1% v/v surfactant in the aqueous phase unless otherwise noted. A Q_{foam} of 6 ml/min was used with the coarse sand pack of 50 μm as the foam generator. A listing of "no foam" indicates that slugs of the CO_2 and aqueous surfactant solution were observed.

Table 4.2 presents the η_{foam} and D_{sm} for C/W foams with water and brine (composed of 2% NaCl, 0.5% $CaCl_2$, and 0.1% $MgCl_2$ w/w in water) with 1% v/v 2EH-PO_5-EO_9 and 1% v/v DOG-EO_{12} in the aqueous phase at 24, 40, and 60 ˚C. The η_{foam} are measured at a Q_{foam} of 6 ml/min using the coarse 50 μm sand pack as the foam generator with qualities as listed.

4.4.1 Effect of Shear Rate

Shear rate ($\dot{\gamma}$) versus shear stress (τ) plots (calculated from U/R and $\Delta P R/2L$, respectively), known as flow curves, were generated for the bulk foams; typical examples are presented in Figures 4.4-4.7. Additional plots are presented in the Appendix C, in addition to a table of all the η_{foam} and D_{sm} measured for the surfactants investigated.

For a Newtonian fluid, the ratio of τ to $\dot{\gamma}$ gives a constant value equal to the viscosity (η). A C/W foam that fits the Newtonian model is presented in Figure 4.4a for a 5% v/v TMN 6 foam with 80% v/v CO_2 at 24 ˚C and 2300 psia at $\dot{\gamma}$ from 140-870 s^{-1}. Figure 4.4b gives the corresponding change in η_{foam} with $\dot{\gamma}$. The flow curve for the Newtonian fluid is a straight line with a slope equal to η_{foam} that goes through the origin if no yield stress occurs. This is not the case for most foams as a yield stress is often found.[184] In the case of TMN 6 in Figure 4.4, the Newtonian behavior is not expected to occur for all shear rates and thus the slope does not intersect the origin. At low shear rates the elasticity of the foam structure and yield stress are expected to make the foam non-

Table 4.2: The effect of brine (2% NaCl, 0.5% $CaCl_2$, 0.1% $MgCl_2$ w/w in water) on the apparent bulk viscosity and D_{sm} of C/W foams.

Surfactant	Cloud Point (˚C)	24 ˚C 90% v/v CO_2		40 ˚C 92% v/v CO_2		60 ˚C 95% v/v CO_2	
		η_{foam} (cP)	D_{sm} (µm)	η_{foam} (cP)	D_{sm} (µm)	η_{foam} (cP)	D_{sm} (µm)
DOG-EO_{12} (with water)	46	116	30	19	48	No Foam	
DOG-EO_{12} (with brine)	38	116	32	No Foam		No Foam	
2EH-PO_5-EO_9 (with water)	60	125	27	151	16	90	34
2EH-PO_5-EO_9 (with brine)	54	112	30	149	25	15	57

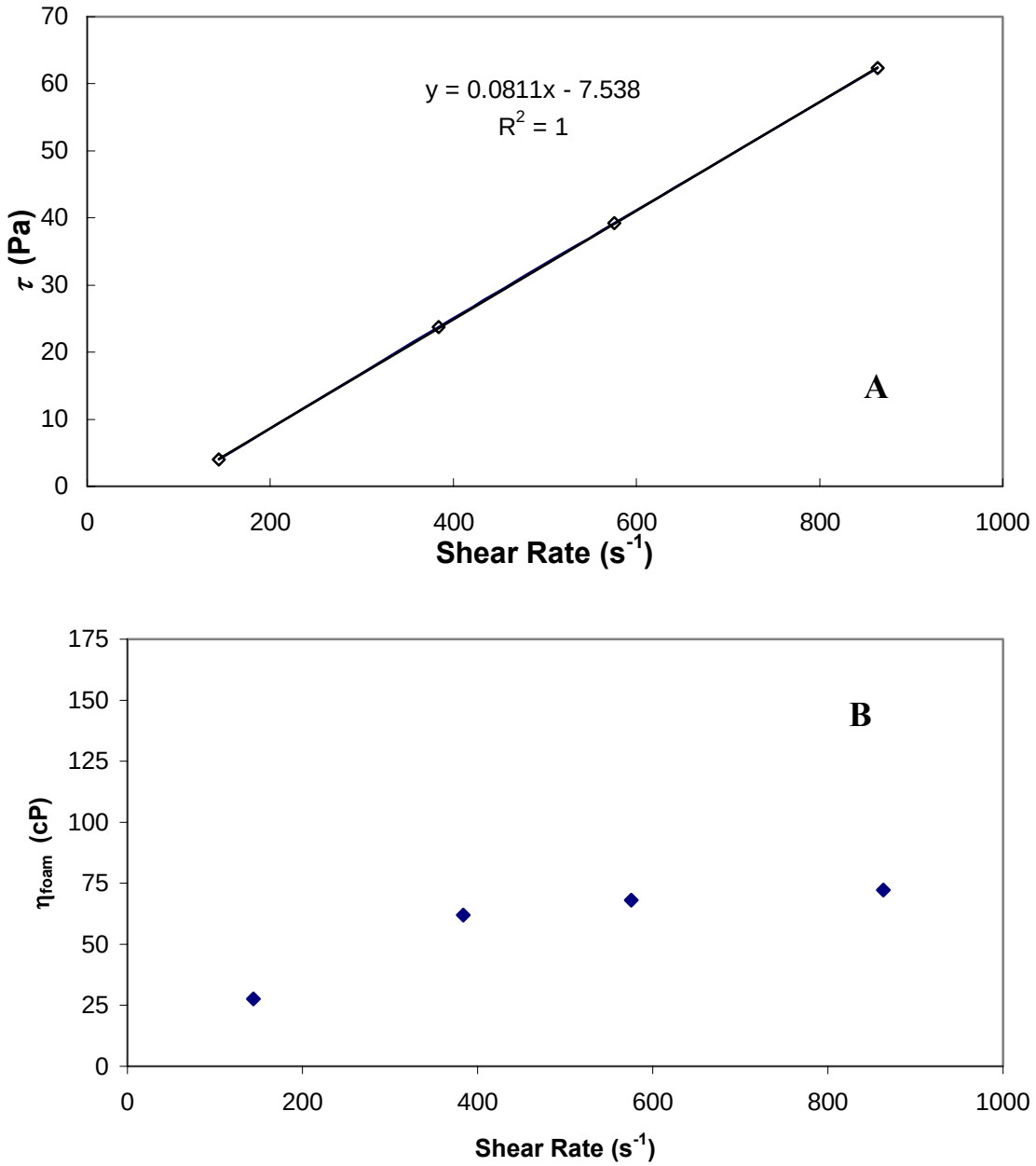

Figure 4.4: Newtonian flow curve (plot A) and η_{foam} as a function of shear rate (plot B) for a C/W foam with 5% v/v TMN 6 and 80% v/v CO_2 at 2300 psia and 24 ˚C.

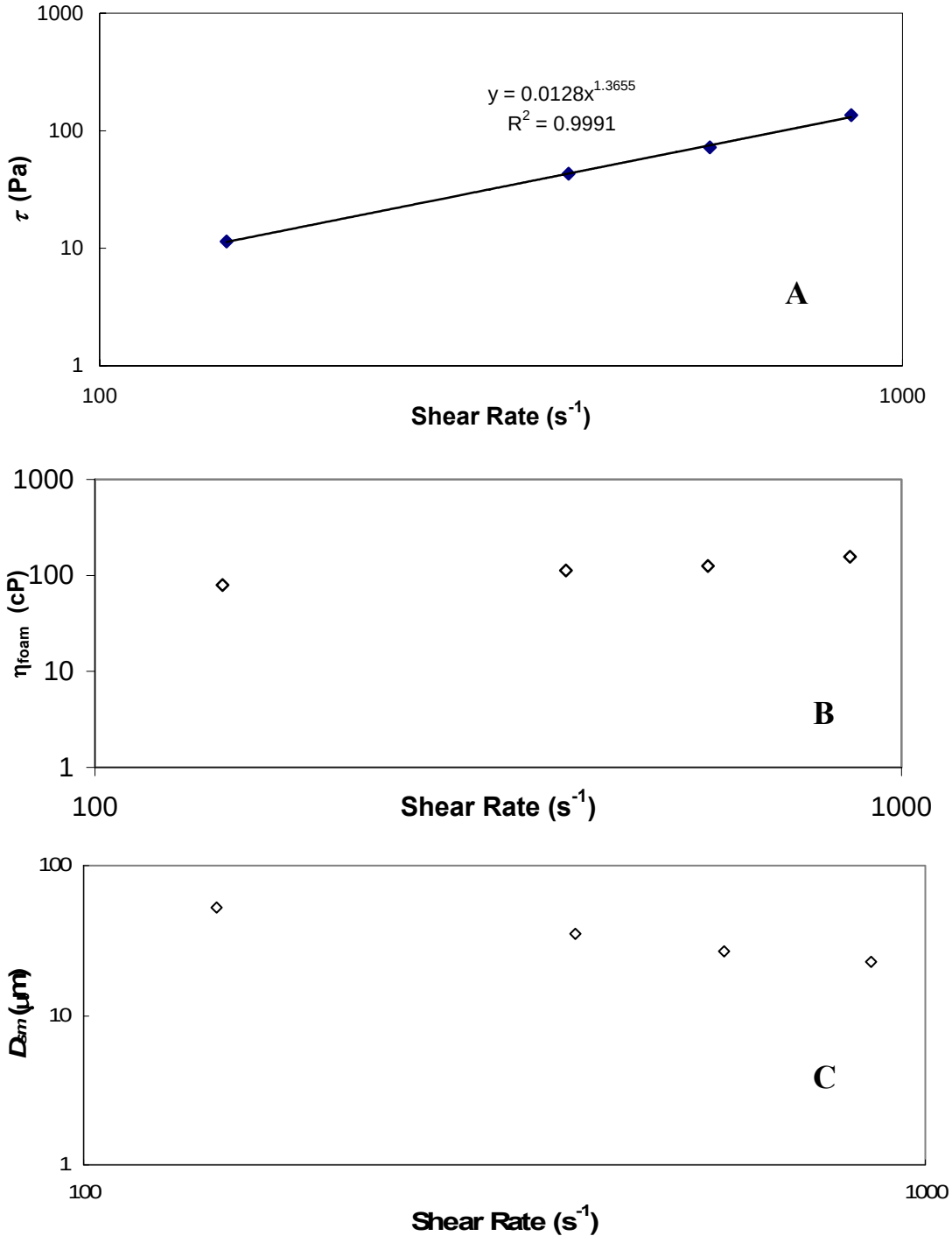

Figure 4.5: τ, η_{foam}, and D_{sm} as a function of shear rate for the C/W foam stabilized with 1% v/v 2EH-PO_5-EO_9 and 90% v/v CO_2 at 24 ˚C and 2000 psia (plot A, B, and C, respectively).

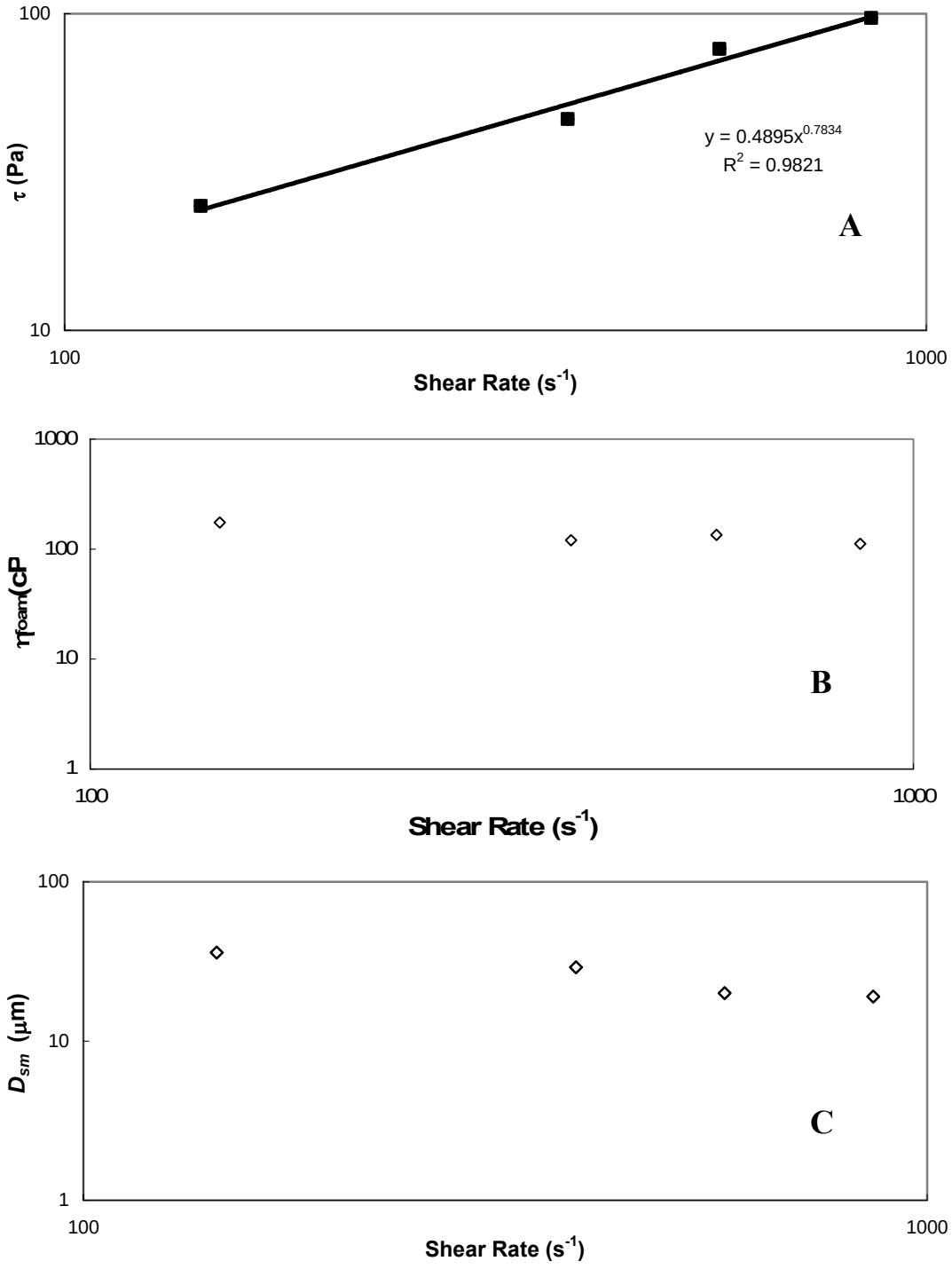

Figure 4.6: τ (plot A), η_{foam} (plot B), and D_{sm} (plot C) as a function of shear rate for the C/W foam stabilized with 1% v/v 2EH-PO_{12}-EO_{11} with 90% v/v CO_2 at 24 ºC and 2000 psia.

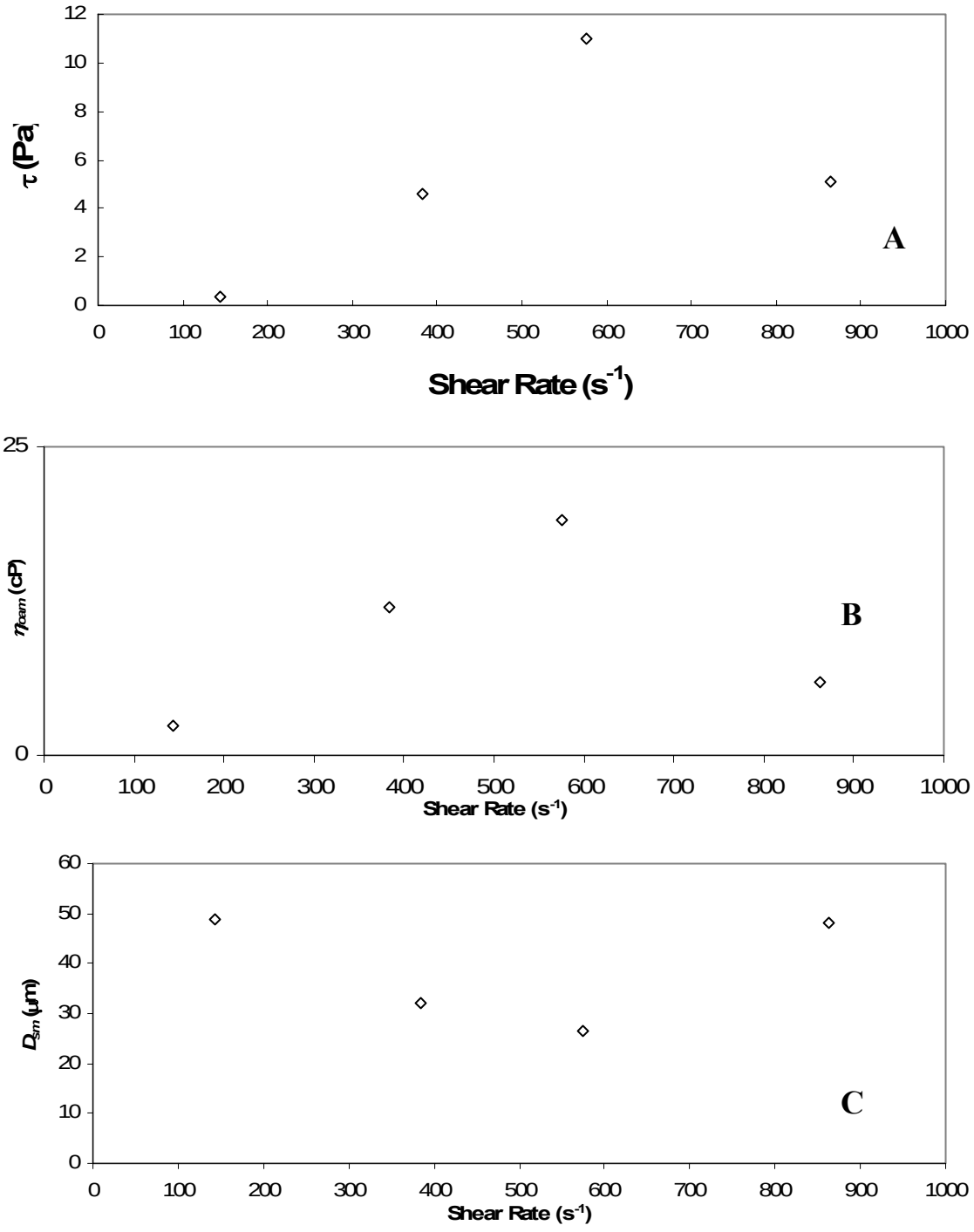

Figure 4.7: The shear stress (plot A), η_{foam} (plot B), and D_{sm} (plot C) as a function of shear rate for the C/W foam stabilized with 1% v/v 2EH-EO_5 and 90% v/v CO_2 at 24 ˚C and 2000 psia.

Newtonian. Different regimes of τ response to a given $\dot{\gamma}$ have been recorded for foams previously.[181]

Another behavior commonly encountered with foam rheology is that of the power-law model. The power-law fluid model is

$$\tau = k\dot{\gamma}^n \qquad [6]$$

where n and k are the two parameters of the model found from experimentally fitting the data. The flow curve of a power law fluid is linear if $\dot{\gamma}$ and τ are plotted on a log scale as seen in Figures 4.5-4.6. The power law model is generally used to represent the behavior of polymer solutions and melts[185] and has been used with a yield stress term in some cases to describe foams.[181] For example, Hutchins et al. found that shear rate changes near 100 s^{-1} produced power-law type relationships for C/W foams with additives.[178] Figures 4.5 and 4.6 show a power-law relationship between $\dot{\gamma}$ and τ for $\dot{\gamma}$ values in the range 140-870 s^{-1}. Figure 4.5 presents plots of τ, η_{foam}, and D_{sm} as a function of $\dot{\gamma}$ (respectively) for a C/W foam stabilized with 1% v/v 2EH-PO_5-EO_9 in the aqueous phase at 24 ˚C and 2000 psia for a quality of 90% v/v CO_2. Figure 4.6 displays the change of τ, η_{foam}, and D_{sm} with $\dot{\gamma}$ (respectively) for a foam stabilized with 1% v/v 2EH-PO_{12}-EO_{11} in the aqueous phase for 90% v/v CO_2 at 24 ˚C and 2000 psia.

For many power law fluids, at very low shear rates the materials can become Newtonian as n tends to approach 1.[185] When a foam has a combination of Newtonian and power-law properties for the $\dot{\gamma}$ of interest, a polynomial fit of $\dot{\gamma}$ as a function of τ results (as presented in the Appendix C). When $n < 1$, the power-law fluid is shear-thinning which indicates that the viscosity decreases with increasing $\dot{\gamma}$ as shown in Figure 4.6 for 2EH-PO_{12}-EO_{11}. When $n > 1$, the fluid is shear-thickening with η_{foam} rising on increasing $\dot{\gamma}$ (Figure 4.5). However, the shear-thickening or shear-thinning behavior of the foam does not depend on the $\dot{\gamma}$-τ relationship.

Due to the specifics of the viscosity equipment, as Q_{foam} and $\dot{\gamma}$ are increased, the flow rate through the foam generator (the sand pack) is also increased, thus changes in bubble size result. The changes in foam texture, as described by D_{sm}, need to be investigated in terms of the changes in η_{foam}. Figure 4.5 gives τ, η_{foam}, and D_{sm} as a function of $\dot{\gamma}$ for a shear-thickening foam stabilized by 2EH-PO_5-EO_9 where D_{sm} decreases (indicating smaller cell sizes) with an increase in Q_{foam} (and $\dot{\gamma}$). As the bubble size is decreased, more bubbles are formed for a given volume of CO_2 and consequently there are more lamellae at the capillary wall. The resulting higher shear stress increases η_{foam} (Figure 4.5b). Smaller bubble sizes and a more narrow size distribution have previously been found with higher rates of shear for nitrogen foams when the concentration of surfactant is sufficient to stabilize the newly formed interface.[186] Thus, shear-thickening behavior occurs as long as the surfactant can stabilize the smaller bubbles formed with an increase in $\dot{\gamma}$.[59]

If the bubble size remains fairly constant with increasing velocity of a foam or HIPE, shear-thinning behavior has been measured.[59,174,175] Shear-thinning behavior is seen in Figure 4.6, where a change in $\dot{\gamma}$ from 144 to 384 s^{-1} decreases D_{sm} slightly from 35 to 30 μm; however, η_{foam} decreases from 170 to 120 cP with the change. An increase in $\dot{\gamma}$ from 384 to 576 s^{-1}, D_{sm} decreases from 30 to 20 μm and produces a slight increase in η_{foam} from 120 to 135 cP as observed for the shear-thickening foams. For the last increase in $\dot{\gamma}$ to 863 s^{-1}, the D_{sm} remains constant and η_{foam} drops again to 110 cP. The shear-thinning behavior at constant cell size is attributed to instability in the disordered foam structure corresponding to rearrangement of the foam cells.[187] If the number of lamellae does not increase to cancel out this effect by smaller bubble sizes, η_{foam} decreases.

Another cause of shear-thinning behavior is due to poor stabilization of the foam cells by the surfactant. If the foam lamellae are not adequately stabilized by the surfactant, as $\dot{\gamma}$ is increased coalescence occurs, raising D_{sm} and correspondingly decreasing η_{foam} as seen in Figure 4.7 at the highest $\dot{\gamma}$. η_{foam} and D_{sm} as a function of $\dot{\gamma}$ are shown in Figure 4.7 for a C/W foam stabilized with 1% v/v 2EH-EO_5 at 24 ˚C and 2000 psia with 90% v/v CO_2. Bubbles of all sizes are observed to coalesce in foams stabilized with 2EH-EO_5 at all conditions due to the small size of both the head and tail of the surfactant, demonstrating the instability of the foam (which is unusual for the surfactants listed in Table 4.1). There is also a sharp drop in the shear stress response of the foam at the highest $\dot{\gamma}$ as the coalescence disrupts the foam structure (Figure 4.7a).

The combined effects of changing bubble sizes and foam structure can produce complex rheological behavior of foams with changes in $\dot{\gamma}$, making the measurement of bubble sizes important for understand foam rheology. Interestingly, Harris used a recirculating pipeline viscometer to measure changes in foam texture versus foam viscosity and found that the quality and the continuous phase properties primarily determined the viscosity of the foam, whereas the effect of the texture was smaller for bubbles with an volume mean bubble diameter of 700-1100 μm.[186] In our case, for a given quality and the same continuous liquid phase (water and surfactant), the much smaller bubble sizes become important for determining the foam viscosity.

4.4.2 Effect of Temperature and CO_2 Density

η_{foam} drops dramatically as the temperature approaches the cloud point of the surfactant, until finally no foam can be formed due to a dramatic drop in the lamella stability. Consequently, the maximum temperature where a foam can be generated depends strongly on the cloud point of the aqueous solution (Table 4.1). Furthermore, the

presence of salts typically makes the surfactants less soluble and depresses the cloud point as seen in Table 4.1. Bonfillon-Colin and Langevin attribute the rupture of foam films at the cloud point to bridging of the foam films by droplets of the surfactant-rich phase.[149]

As the temperature is increased for η_{foam} measurements, the pressure was kept constant, resulting in a decrease in the density of CO_2 (ρ) and a reduced solvation of surfactant tails. For example, the η_{foam} of 2EH-PO_5-EO_{15} drops from 140 to 57 cP as the temperature is increased from 40 to 60 ˚C at a constant pressure of 2000 psia, as ρ drops from 0.76 to 0.55 g/ml. A drop in the interfacial activity of the surfactant is expected, leading to a greater Laplace pressure of the bubbles and reduced lamella stability (Chapter 2 and 3). Foam generation can also be affected by the change in temperature and ρ via changes in γ[188] as well as the reduced viscosity of the CO_2 phase (0.9 to 0.4 at 24 and 60 ˚C, respectively, at 2000 psia) to increase the bubble size and drop η_{foam}.

4.4.3 Effect of Quality

The quality of a foam is an important variable for altering η_{foam}.[186] As the quality is increased from 74% v/v η_{foam} increases as well, due to the increased number of bubbles and lamellae in the foam from the additional volume of dispersed phase.[64,179,189-191] As the quality is continually increased, a maximum η_{foam} is reached at qualities near approximately 90-99%, followed by a drop in η_{foam}. Foams with very high qualities have little aqueous solution, thus the liquid lamellae are thinner resulting in bubble coalescence (Chapter 3). η_{foam} decreases as the lamella stability is reduced due to a drop in the number of lamellae. The effect of foam quality on η_{foam} is shown in Figure 4.8 at a Q_{foam} of 4 ml/min with 0.5%v/v DOG-EO_{12} at 24 ˚C and 2200 psia. A maximum in η_{foam} is visible at a quality of 91% and the foam lamella stability drops when the quality is increased

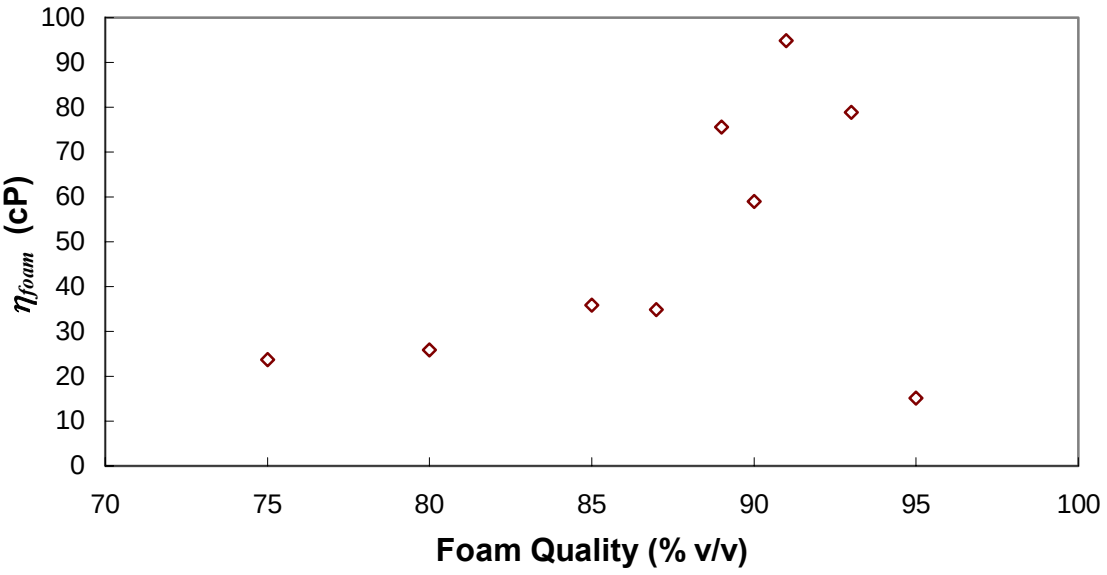

Figure 4.8: The η_{foam} of C/W foam stabilized with 0.5% v/v DOG-EO_{12} at Q_{foam} of 4 ml/min, 24 ˚C, and 2200 psia as a function of the foam quality (% v/v CO_2).

further. Additional quality plots are accessible in the Appendix C. The ability to vary η_{foam} via quality changes allows for some control of the foam in EOR uses, as the gas injection strategy can be altered to either increase or decrease η_{foam}. Friedmann et al. found that higher quality foams (90%) propagated better than wet foams (40%) in porous media,[192] thus it is anticipated that qualities producing the greatest η_{foam} may work best for EOR.

4.4.4 Effect of Salinity

The addition of salt (2% NaCl, 0.5% $CaCl_2$, 0.1% $MgCl_2$ w/w in water) to a surfactant solution at ambient pressure decreases the cloud point temperature (Table 4.1). The lower cloud point of the brine solutions decreases the maximum temperature where the foam can be formed for all surfactants tested. However, at lower temperatures well below the cloud point, the tolerance of the nonionic surfactants for the salt and divalent ions is high and the change in the rheology of the foams is small.

The cloud points of 2EH-PO_5-EO_9 in water and brine are 60 and 54 ˚C, respectively, showing that the salt drops the cloud point about 6 ˚C. At 24 and 40 ˚C the apparent viscosities of the foams with water and brine are within experimental error (Table 4.2), however there is a large change in η_{foam} at 60 ˚C due to the drop in the cloud point when salt is present. The increase in bubble size for the foam with salt at 60 ˚C, indicates a decrease in lamella stability, which is expected from the salt depressed cloud point. This same change in η_{foam} near the cloud point is visible in Table 4.2 for the DOG-EO_{12} foams with water and brine at 40 ˚C, where the cloud point is reduced from 42 to 38 ˚C. No foam is formed for the system with brine, however a foam with an apparent viscosity of 20 cP is formed for the system with water. Thus, the change in the foam rheology with salt is primarily due to the depressed cloud point temperature and no

significant change in the foams is visible when the temperature is well below this point. This indicates excellent salt tolerance for the nonionic surfactant as compared with ionic surfactants.

4.4.5 Scaling Plot for Apparent Foam Viscosity

Figure 4.9 presents a scaling analysis proposed by Otsubo and Prud'homme[191] for concentrated oil-in-water emulsions and used by Herzhaft et al.[193] for aqueous foams, respectively. The scaling analysis is used to understand the effect of γ, bubble (or droplet) size, and $\dot{\gamma}$ on the ratio η_{foam}/η_c for a series of emulsions or foams of a given quality, where η_{foam} and η_c are the apparent viscosity of the foam and the continuous phase, respectively. Otsubo and Prud'homme found that the curves of several concentrated oil-in-water emulsions with a given quality could be reduced to a near-universal curve on this scaling plot.[191] The plot of $D_{sm}\eta_{foam}/\gamma\eta_c$ versus $\eta_c\dot{\gamma}$ is shown in Figure 4.9 for foams with a CO_2 quality of 90% and 1% v/v surfactant in the water phase, where η_c is assumed to be 1 cP and γ was either measured or assumed to be 3 mN/m. The data from several surfactant structures show in general a negative slope, especially at the higher $\dot{\gamma}$. This negative slope indicates that an increase in $\dot{\gamma}$ results in either a decrease in D_{sm} or η_{foam}, assuming η_c and γ are constant. Therefore, the scaling plot correctly predicts a shear-thinning foam for constant D_{sm}. The scaling plot (Figure 4.9) also indicates that an increase in η_{foam} is correlated with a decrease in bubble size as expected. Other correlations can also be seen from Figure 4.9, where a decrease in γ should bring about an increase in $D_{sm}\eta_{foam}$, although our γ values were often too close to substantiate the correlation. In addition, increasing η_c, possibly by adding polymers or gelling agents, should naturally produce foams that are more viscous due to changes in the lamellae liquid phase. These relationships have been shown for other dispersed systems from

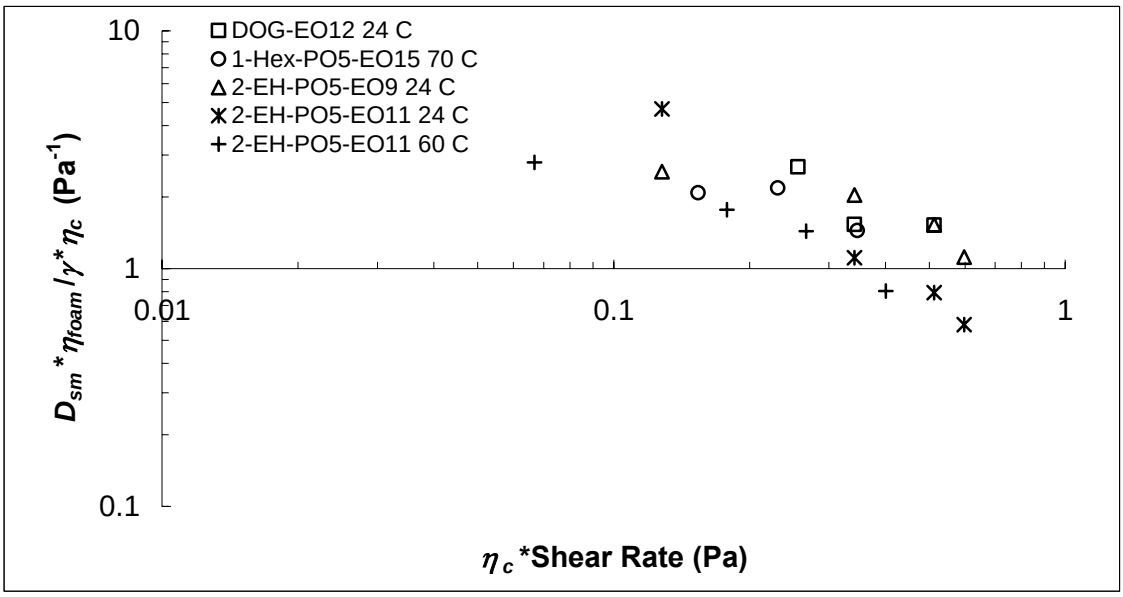

Figure 4.9: Scaling analysis for foams with a CO_2 quality of 90% v/v at 24-70 °C at approximately 2200 psia with 1% v/v surfactant in the water phase.

concentrated oil-in-water emulsions[191] to aqueous foams,[193] although the high-pressure C/W foam data are slightly more scattered in the curve (due to additional error in the high-pressure measurements). The similarity of the rheology for emulsions and foams indicates that the greater η_{foam} is due to the structure of the foam and the continuous phase lamellae.

4.5 CONCLUSIONS

The formation of highly viscous C/W foams with novel nonionic hydrocarbon surfactants have been used to reduce the mobility of CO_2. The η_{foam} of these foams have been characterized through measurements of the pressure drop over a capillary tube (762 μm inner diameter). η_{foam} values of greater than 200 cP (Table 4.1) have been recorded, which is over 1000 times greater than the viscosity of pure CO_2 (0.04-0.1 cP). In addition, *in-situ* optical microscopy has been used to measure the foam texture (bubble sizes) which bubble diameters ranged from less than 1 μm to several hundred microns. In addition, the effect of temperature, quality, and salinity on η_{foam} was investigated. A scaling analysis was used to describe the effect of bubble size, continuous phase viscosity, shear rate, and interfacial tension on η_{foam} for a foam with a given quality.

The flow curves (shear stress versus shear rate plots) of the C/W foams were analyzed and both Newtonian and power-law relationships were found. The changes in the foam velocity and correspondingly $\dot{\gamma}$ can cause substantial changes in bubble size and η_{foam} through changes in the number of foam lamellae. Increasing the foam velocity through the sand pack (foam generator) in many cases caused the formation of smaller bubbles, resulting in shear-thickening behavior. In a limiting case, where the increase in

foam velocity had little effect on the bubble size, the behavior was shear-thinning, as has been shown for aqueous foams and concentrated emulsions.[59,174,175] Shear-thinning behavior is also seen when the foam lamellae are unstable. As $\dot{\gamma}$ increases, greater shear stresses lead to coalescence of the lamellae and thus a drop in η_{foam} from the reduction of the number of lamellae.

The cloud point of the surfactant also affects the number of stable lamellae of the foam and the associated η_{foam}. When the surfactant precipitates from the aqueous phase, the lamella stability is reduced, thereby defining the maximum temperature where a stable foam can be formed. Depression of the cloud point by increasing the salinity reduces η_{foam} near this temperature (Table 4.2). However, salinity of the aqueous phase does not significantly affect η_{foam} at temperatures well below the cloud point, indicating excellent salt tolerance of the nonionic surfactants. The loss of lamella stability is also responsible for drop in η_{foam} at high foam qualities. The maximum η_{foam} occurred near 91% v/v CO_2 for DOG-EO_{12}. The variation of η_{foam} with foam quality is useful for both increasing and decreasing η_{foam}, which could be beneficial for EOR.

The rapid measurement of high-pressure C/W foam viscosities is a useful tool in screening surfactant structures as well as understanding foam rheology. A range of foam conditions (shear rates, temperatures, salinity, or pressures) is tested in a single day using this foam equipment. The viscosity and texture results can also be used to rank surfactant structures under identical conditions. In addition, these results can be used for the selection of surfactant structures for further study, such as time consuming core flood experiments for EOR purposes.

Chapter 5: Solid Particles as Alternative Emulsion Stabilizers: Water-in-Carbon dioxide Emulsions Stabilized Solely with Hydrophobic Silica Particles

W/C emulsions were stabilized using hydrophobic silica particles adsorbed at the interface, resulting in average droplet diameters as low as 7.5 μm. A porous cross-linked shell was formed about a hydrophilic (colloidal and fumed) silica core with a trifunctional silylating agent, (heptadecafluoro-1,1,2,2-tetrahydrodecyl)triethyoxy silane, to render the particles CO_2-philic. The stability of emulsions comprising equal weights of CO_2 and water was assessed with visual observations of settling fronts and the degree of emulsion coalescence, and the average drop size was measured by optical microscopy. The effect of CO_2 density on both emulsion stability and droplet size was determined quantitatively. The major destabilizing mechanism of the emulsions was settling, whereas Ostwald ripening and coalescence were not visible at any density, even over 7 days. Flocculation of the settling droplets did not occur, although gelation of the emulsions through particle interactions resulted after longer periods of time. CO_2-philic particles offer a new route to highly stable W/C emulsions, with particle energies of attachment on the order of 10^6 kT, even at CO_2 densities as low as 0.78 g/ml. At these low densities, surfactants rarely stabilize emulsions as the result of poor surfactant tail solvation.

5.1 INTRODUCTION

Carbon dioxide (CO_2) is the second most abundant solvent on earth after water. CO_2 offers benefits over traditional organic solvents in that it is essentially nontoxic, nonflammable, and relatively inexpensive. Because CO_2 does not have a permanent dipole and has weak van der Waals forces, as characterized by a low polarizability per unit volume, it is often a poor solvent. However, emulsions of CO_2 and water can expand the utility of CO_2. CO_2 and water can form micelles,[44,194-197] microemulsions,[26,31,42,48 ,198-200] miniemulsions,[33,36,99] macroemulsions,[2,34,35,45,77,201,202] and concentrated emulsions[80,148] stabilized by surfactant molecules. The tunable solvent strength of expanded liquid and supercritical CO_2 allows for control of colloidal interactions. Stable CO_2 and water emulsions can be useful for applications such as nanoparticle synthesis[9,22,203] and deposition,[204,205] enzymatic catalysis,[206,207] dry cleaning,[24] photoresist drying,[19] and cleaning of low dielectric insulators in semiconductor manufacturing.[20,208]

Surfactant tails are often poorly solvated by CO_2 leading to poor stability of CO_2 and water emulsions. Tail solvation is improved with low molecular weight surfactants,[39] or "stubby" hydrocarbon surfactants with little tail overlap[34,40-42] and a low free volume at the CO_2-water interface.[41,43] For polymeric stabilizers where solvation is weaker, it is usually necessary to choose monomers with low cohesive energy densities, for example siloxanes, trisiloxanes, fluoroalkanes, fluoroethers, and fluoroacrylates.[2,33,34,44-48]

Recently, Dhanuka et al.[80] formed a concentrated CO_2-in-water emulsion with a highly branched nonionic hydrocarbon surfactant (Tergitol TMN-6) that had cell sizes smaller than 10 μm and a stability of over 24 h. In addition, TMN-6 has been used to facilitate electrostatic stabilization of W/C emulsions with 5% w/w (by weight) water by

preventing ion pairing despite the ultralow dielectric constant of CO_2 of 1.5.[159] Furthermore, micron-sized TiO_2 particles were also dispersed in liquid and supercritical CO_2 via electrostatic stabilization.[209]

Water-in-CO_2 (W/C) emulsions are more difficult to stabilize than CO_2-in-water (C/W) emulsions because of thermodynamic and transport limitations for CO_2, particularly when it is the continuous phase. At low densities, surfactant tails are often poorly solvated and collapse, resulting in attractive interdroplet tail interactions, flocculation, and coalescence. Settling rates of water drops are unusually large in W/C emulsions due to the low viscosity of CO_2 (0.06 - 0.1 cP) and the large density difference between water and CO_2.

Solid particles can act as emulsifying agents without the use of surfactants.[210] Colloidal particles adsorb at the liquid-liquid interface[211] and create a rigid protective barrier around each dispersed drop. The particles stabilize emulsions by inhibiting coalescence of approaching emulsion drops.[212] The stabilization of colloidal particles depends on particle size, shape, concentration, wettability, and particle-particle interactions at the liquid-liquid interface.[213]

Surfactant-free C/W emulsions stabilized by solid silica particles with 50% w/w CO_2 were reported by Dickson et al.[214] Silica particles of varying hydrophilicity were used to stabilize water drops approximately 20 μm in diameter at CO_2 densities as low as 0.739 g/ml. Emulsion stability was found to increase with a slight decrease in particle hydrophilicity (76% compared with 100% SiOH), an increase in the shear rate, and an increase in particle concentration. In addition, the use of particles as emulsifiers removed the severe challenge of tail solvation by the CO_2-phase, even at low CO_2 densities.

CO_2 and water Pickering emulsions (solid-stabilized emulsions) may be utilized in ocean and geologic sequestration of CO_2,[215,216] coal beneficiation, and binary solvent

extraction.[217] C/W emulsions with CO_2 globule diameters ranging from 100-300 μm were formed using hydrophilic particles including beach sand, flyash, shale, and a magnesium silicate rock.[217] In addition, W/C emulsions composed of globules of unknown size were stabilized with Teflon, carbon black, and pulverized coal.[217] The ability to tune the density of the CO_2 phase via pressure changes is one aspect that makes CO_2 and other supercritical fluids unique. The effect of these changes in CO_2 density have not been examined with respect to stability and droplet size for W/C emulsions stabilized with solid particles.

A wide variety of types of solid particles may be dispersed in water to stabilize C/W emulsions.[214-217] However, it is challenging to design CO_2 dispersible particles for W/C emulsions. Dispersion of micron-sized inorganic particles, such as silica, in CO_2 is difficult as the weak van der Waals forces of CO_2 lead to strong Hamaker attraction between the particles, which must be overcome with polymeric steric stabilizers.[14,218,219] Recently, hydrophobic core-shell silica particles were dispersed in CO_2 at pressures as low as the vapor pressure.[218,219] Both fumed[219] and colloidal silica[218] particles were coated with a fluorinated cross-linked shell to weaken the Hamaker interactions between particles. A high-pressure homogenizer was required to disperse the fumed silica aggregates.[219] However, the colloidal silica based core-shell particles dispersed to form reversible aggregates with diameters of a few hundred nm with only a stir-bar. In addition, decreasing the density of CO_2 increased the interparticle interactions, as demonstrated by a decrease in the negative second viral coefficents.[218] This approach bypassed the limitation of uncross-linked polymeric stabilizer that collapse at low densities.

The objectives of this study are to stabilize W/C emulsions (with average droplets smaller than 100 μm) using hydrophobic silica particles comprising equal weights of

water and CO_2 and to quantitatively determine the effect of CO_2 density on emulsion stability and droplet size. The droplet diameter and stability of W/C emulsions has not been reported for solid-stabilized emulsions. The use of CO_2-philic particles as emulsifiers removes the limitation of poor surfactant tail solvation by CO_2, offering the possibility of highly stable emulsions even at lower CO_2 densities. Cross-linked porous fluorosilica shells were added to hydrophilic fumed silica and electrostatically stabilized silica nanoparticles, which were dispersible in CO_2. W/C emulsions, with nearly equal masses of CO_2 and water, were formed by shear of the CO_2-water-particle mixture through a fine orifice with a pressure drop of approximately 3.4 MPa in a high-pressure homogenizer. Emulsion stability was assessed with visual observations of settling fronts and the degree of emulsion coalescence, and the average drop size was measured by optical microscopy. The emulsion properties are discussed in terms of the droplet size, particle wettability, and energies of attachment for the various silica particles at the water-CO_2 interface. Differences between surfactant-stabilized and solid-stabilized emulsions are discussed with respect to emulsion destabilization mechanisms.

5.2 EXPERIMENTAL METHODS

5.2.1 Materials

Aerosil 300 fumed silica with a surface area of 300 m²/ g and an average particle diameter reported as 7 nm was obtained from Degussa. Upon addition to water, the hydrophilic silica particles were easily dispersible. Ludox TM-50 and Ludox SM-30 colloidal silica was obtained from Grace Davison. The as-received silica particles were

electrostatically stabilized in water at a pH of 9. From dynamic light scattering, the average size based on intensity of the as-received TM-50 silica particles was 24 nm and the SM-30 was 14 nm.

The silylating agent (heptadecafluoro-1, 1, 2, 2-tetrahydrodecyl) triethoxy silane was purchased from Gelest and used as received. Ethanol, acetic acid, and 1, 1, 2-trichlorotrifluoroethane (Freon -112) were purchased from AAPER, Fisher Scientific, and Aldrich, respectively, and used as received. Water was deionized (Nanopure II) and research grade carbon dioxide (Matheson) was passed through an oxygen trap before introduction to the system.

5.2.2 Silane Grafting

Hydrophilic silica particles were modified by silylation with (heptadecafluoro-1, 1, 2, 2-tetrahydrodecyl) triethoxy silane in an aqueous alcohol.[218] The procedure for the dry fumed silica particles[219] differs slightly from that for the aqueous dispersion of Ludox TM-50 and SM-30 particles,[218] which have both been reported previously. For the fumed silica, the silane:silica (wt:wt) ratios investigated include 1:1, 1.3:1, 1.5:1, and 1.7:1. The results presented here are mainly focused on the 1.7:1 silane:silica ratio by weight. A mass of 250 mg of the fumed silica power was added to the silanol solution with stirring and the mixture was sonicated for at least 30 minutes to form the cross-linked shell over the particles. The solvent was removed from the particles by evaporation, which is known to cause aggregation of the particles. For the 1.7:1 particles (named Fumed-1.7), the mass of hydrophobic dried particles was approximately 250 mg. The particles were re-dispersed in 15-20 ml of Freon 112 to facilitate the subsequent dispersion of the particles in CO_2.[218] The size distributions of the silylated particles in Freon 112 were measured with dynamic light scattering (DLS) using a BI-ZetaPlus from Brookhaven Instruments

Corporation, with a 90° scattering angle. The reproducibility was within 10% of the average size. The mean particle size after silylation for the fumed-1.7 was measured as 870 nm with a size distribution ranging from 640-1085 nm. An aggregated state of the core-shell particles is expected due to initial aggregation of the fumed silica particles, the evaporation processes, and the high degree of interparticle attractions in Freon 112 (and CO_2) due to the relatively low ratio of the shell to silica.[219]

A schematic illustrating the cross-linked polymer shell surrounding the Ludox silica core is shown in Figure 5.1. For the Ludox TM-50 and SM-30 colloidal silica, the silane-coupling agent was added in one rapid injection with stirring. The amount of the silylating agent added was varied to achieve the desired silane:silica (wt:wt) ratio. For the Ludox SM-30 silane:silica (wt:wt) ratios investigated include 2.5:1, 4.5:1, and 6:1. The silane:silica (wt:wt) ratios investigated with the Ludox TM-50 silica particles include 1.5:1 (the main focus of this work and known as TM50-1.5), 2.5:1, and 4.5:1. The solvent was removed from the particles by evaporation which is known to cause aggregation of the core-shell particles, thus disrupting the ideal core-shell structure depicted in Figure 5.1.[218] The particles were re-dispersed in 15-20 ml of Freon 112 to facilitate the subsequent dispersion of the particles in CO_2.[218] The size distributions of the silylated particles in Freon were measured with dynamic light scattering (DLS) using a BI-ZetaPlus from Brookhaven Instruments Corporation, with a 90° scattering angle. The mean particle size of the TM50-1.5 particles was 270 nm with a size distribution ranging from 120-460 nm.

5.2.3 Emulsion Formation

A Branson Sonifier (VWR Scientific, model 250) equipped with a micro-tip was used to enhance dispersion of the particles in Freon-112 for approximately 5 minutes.

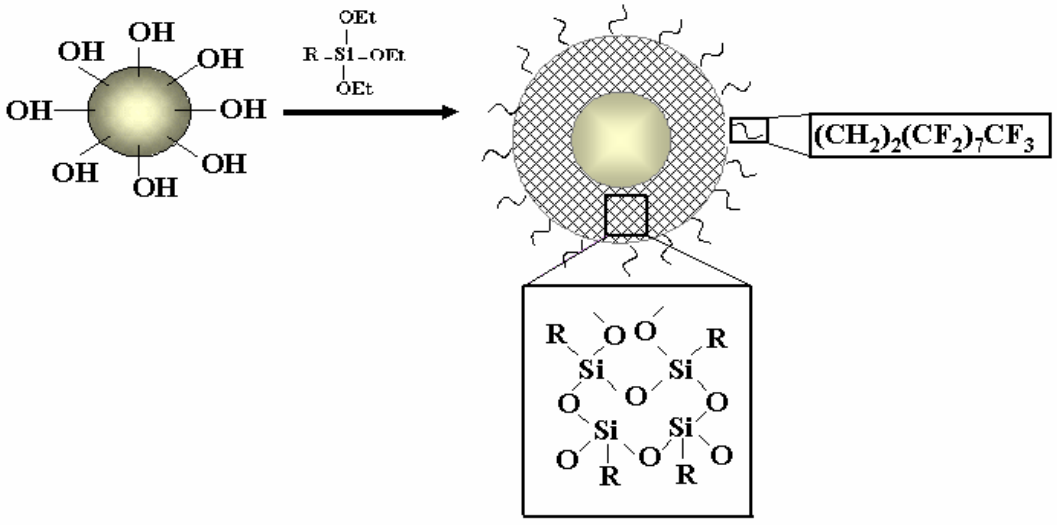

Figure 5.1: Silylation of silica particles to create core-shell hydrophobic particles. The R group of the silane is $(CH_2)_2(CF_2)_7CF_3$.

The sonified particle dispersion was then transferred to the front portion of a high-pressure variable-volume view cell and allowed to fully dry, leaving a layer of particles visible on the bottom of the cell. Next, a specific volume of deionized water and a magnetic stir-bar (Fisher Scientific) were added to the front of the variable-volume view cell. Finally, a known mass of carbon dioxide was added to the cell at a constant density using a computer-controlled high-pressure syringe pump (Isco, model 260 D). The Fumed-1.7 system includes 0.9% particles, 49.7% CO_2, and 49.4% w/w water. The TM50-1.5 system initially had 2.4% particles, 49.6% CO_2, and 48% w/w water. Additional CO_2 was injected to the TM50-1.5 system resulting in 2.1% particles, 55.7% CO_2, and 42.2% w/w water.

The backpressure on the cell was maintained utilizing the Isco syringe pump with CO_2 as the pressurizing fluid. The pressure of the cell was detected to ± 35 kPa with a Sensotec pressure transducer and the emulsions were formed at room temperature, 24 ˚C. Once the desired pressure was achieved, the contents of the cell were sheared though an orifice with a high-pressure homogenizing pump (Avestin, model C-5). The cell contents were sheared with a 3.4 MPa pressure drop across the fully open homogenizing valve, while the cell contents were mixed with the magnetic stir-bar. In general, unless otherwise noted, the mixture was sheared for 15 minutes at each condition prior to stability measurements or optical microscopy.

5.2.4 Emulsion Stability Assessment

To assess stability of the emulsions to sedimentation, the time was recorded for a clear excess top phase to form at a specific vertical cell height after stirring and shearing were stopped. The criterion for the Fumed-1.7 stabilized emulsions was a height of 1.8 mm from the top of the cell, equal to approximately 10% of the cell diameter. The

settling front reached a final height near 10-15% of the cell diameter within a few hours and then remained stable for greater than 24 hours at all conditions studied for the Fumed-1.7 silica. The Ludox TM50 silica stabilized emulsions settled more slowly and reached a final height of less than 10% of the cell diameter, thus the settling height was defined as only 1 mm. In addition, CO_2 was added to dilute the emulsions (resulting in 2.1% particles, 55.7% CO_2, and 42.2% w/w water) and thus created a final settling front that was visible for measurement.

5.2.5 Optical Microscopy

The water droplet sizes for emulsions under varying conditions were measured via *in situ* optical microscopy. The emulsions were recirculated with the high-pressure homogenizing pump (Avestin, model C-5) through a high-pressure microscopy cell (Figure 5.2), which was mounted on a microscope (Nikon Eclipse ME600). Specially designed steel spacers (path length of 229 μm) were used to separate the optical cell windows. A two-way valve before and after the microscopy cell were used to stop the flow in the high-pressure microscopy cell, as shown schematically in Figure 5.2. Freeze-frame droplet images were taken with a Photometrics CoolSNAP cf CCD camera that was connected to a computer. The system was allowed to recirculate (shear) for at least 15 min before the pump was turned off, the optical cell was isolated, and the measurements were performed. The microscopy images were analyzed with ImageJ software by setting the scale (via microscopy standards) and measuring the diameter of droplets.

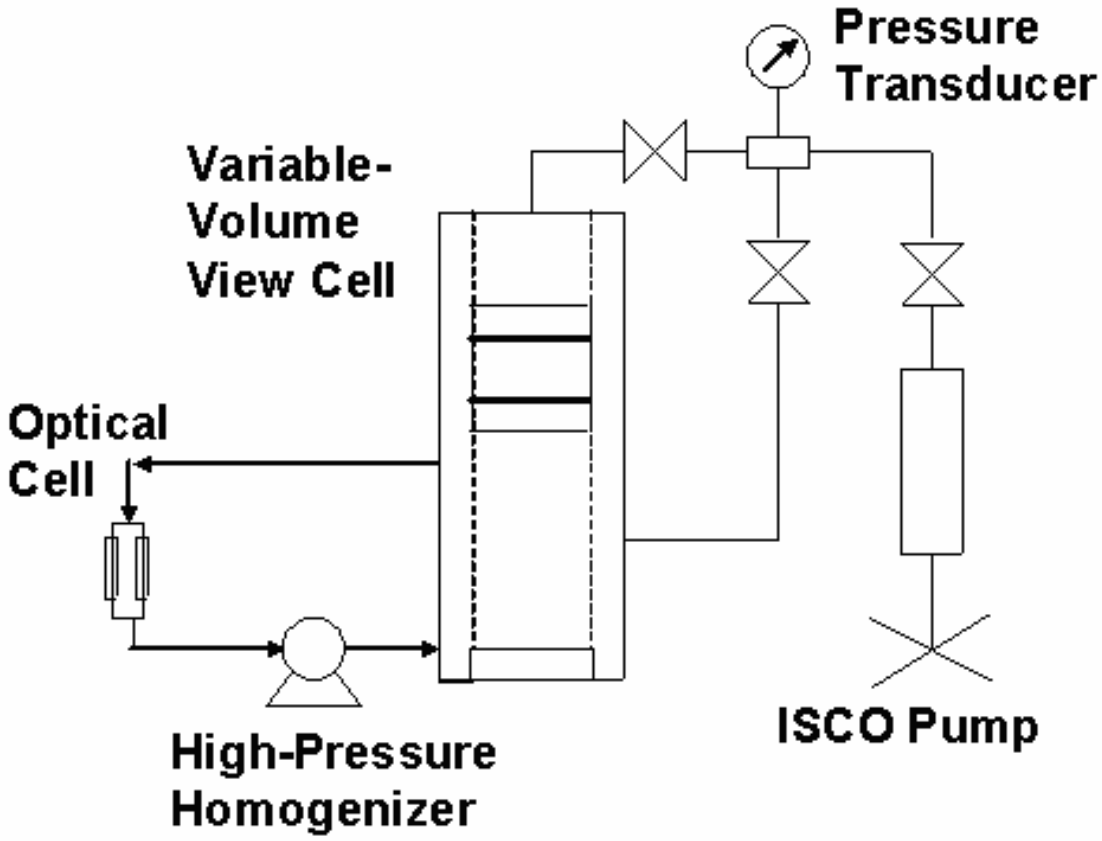

Figure 5.2: Variable-volume view cell and high-pressure equipment used to create and investigate W/C emulsions.

5.3 RESULTS

W/C emulsions were observed for the three different silica systems (fumed silica, Ludox TM-50, and Ludox SM-30) with the various silane:silica (wt:wt) systems previously mentioned that vary from 1:1 to 6:1. For all the particle-stabilized systems, after the particle-water-CO_2 system was pressurized to 13.8 MPa and stirred gently, the water phase remained clear and the CO_2 phase became hazy, indicating particles partitioned to the CO_2 phase and not water, which is consistent with the hydrophobic surfaces. Additional particles remained on the walls of the view cell or at the planar CO_2-water interface. For all the systems, shearing the cell contents for as little as 3 minutes formed uniform milky-white emulsions that occupied over 50% of the cell volume. After shear was stopped, the emulsions settled to the bottom of the view cell and stayed pure white, thus indicating sedimentation of water droplets and a water-in-CO_2 (W/C) emulsion. The volume of the settled emulsions was dependent on the amount of CO_2 in the cell, which was 50-70% w/w CO_2. The systems with 70% w/w CO_2 formed emulsions that occupied approximately 50% of the cell volume. As the mass of H_2O was increased, the volume of the settled emulsion increased (discussed below). No excess water was visible in any of the W/C emulsion systems.

Specifically, for the Fumed-1.7 and TM50-1.5 particle systems, shearing of the cell contents for longer times, approximately 5-15 minutes, was sufficient to emulsify the excess CO_2 and the subsequent W/C emulsions filled the entire cell volume. Figure 5.3 presents a digital photo of the W/C emulsion formed by 0.9% w/w of the Fumed-1.7 particles with 49.7% CO_2 and 49.4% w/w water. Water droplets in all of the W/C emulsions were too small to be visible except by microscopy. Only small clear water

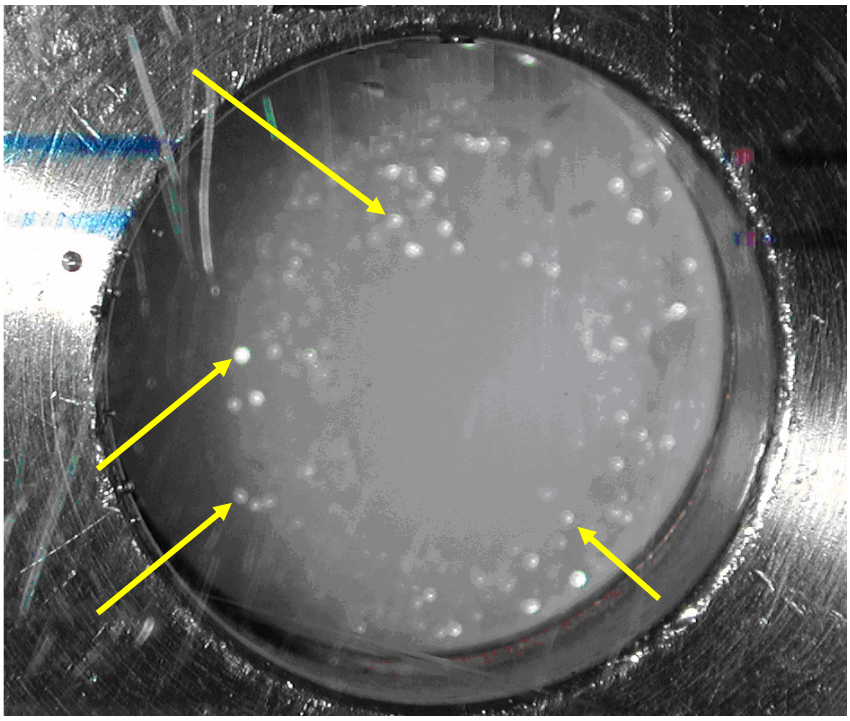

Figure 5.3: Digital photograph of W/C emulsion stabilized with 0.9% Fumed-1.7 particles with 49.4% water and 49.7% w/w CO_2 at 34,500 kPa and 24 ºC immediately after shearing was stopped. Water drops on cell window indicated by arrows. The diameter of the hole in the stainless steel cell front cap is 1.75 cm.

drops attracted to the hydrophilic sapphire windows of the variable-volume cell were visible as reflective specks on the window and can be seen in Figure 5.3 (with the aid of arrows). These water droplets could not be removed by scraping the stir-bar across the sapphire window surface, and the volume of the droplets was estimated to be a negligible fraction of the total water of the system.

The time for the 0.9% w/w Fumed-1.7 particle-stabilized emulsion to settle 1.8 mm as a function of CO_2 density is presented in Figure 5.4. The time increases from 1 to 15 min as the CO_2 density is increased (Table 5.1). Figure 5.5 presents digital photographs of the settled W/C emulsion at CO_2 densities of 0.87 and 0.99 g/ml immediately after shearing was stopped and at specified times thereafter. After the W/C emulsions settled a small amount (Figure 5.5 b and d), there was no change in the position of the setting front or the emulsion appearance for several hours. In most cases, the emulsions were stable overnight with no change in appearance. The stability of the W/C emulsions to coalescence is exemplified by the fact that no change in appearance or volume fraction occurred at 19 MPa for 7 days without stirring, beyond the minor amount of initial settling. After the 7 days, the emulsion became too viscous to stir or recirculate with the high-pressure homogenizer indicating some type of gelation.

W/C emulsions stabilized by TM50-1.5 particles were also stable against coalescence. At a CO_2 density of 0.82 g/ml, the emulsion was left over 17 hours and no coalescence was visible (no bottom water phase was present). The time measured for the TM50-1.5 Pickering emulsion (comprised of 2.1% TM50-1.5, 55.7% CO_2, and 42.2% w/w water) to settle 1.0 mm as a function of CO_2 density is presented in Figure 5.6. The settling time for the TM50-1.5 W/C emulsion also increases from 1.4 to 270 minutes as the density of CO_2 is increased (Table 5.1).

Table 5.1: Properties of W/C emulsions stabilized by TM50-1.5 and Fumed-1.7 particles as a function of CO_2 density. *To make the settling front visible, CO_2 was added to the system resulting in 2.1% TM50-1.5 particles, 55.7% CO_2, and 42.2% w/w water.

		2.4% TM50-1.5 Particles, 49.6% CO_2, 48% w/w water				0.9% Fumed-1.7 Particles, 49.7% CO_2, 49.4% w/w water			
Pressure	**Density**	**Avg Drop Diameter**	**Stand Dev of D**	**Settling Time* 1 mm**	**Stoke's Calc of Drop Diameter***	**Avg Drop Diameter**	**Stand Dev of D**	**Settling Time 1.8 mm**	**Stoke's Calc of Drop Diameter**
kPa	**g/ml**	**μm**	**μm**	**min**	**μm**	**μm**	**μm**	**min**	**μm**
7,600	0.778	7.6	2.4	1.4	11.8				
9,700	0.821	7.5	2	5.5	7.5				
11,400	0.845							1	
13,800	0.872	7.5	1.8	9.9	7.6	73	61.9	2	33.4
17,200	0.901					39	9.2	4	29.3
17,900	0.906	7.6	1.8	14.5	8.1				
21,700	0.930					37	16.2	6	31.2
24,800	0.947	6.9	2.4	60.4	5.9				
27,200	0.959					28	11.3		
34,500	0.989	6.9	1.8	270	6.8	23	10.3	15	57.9

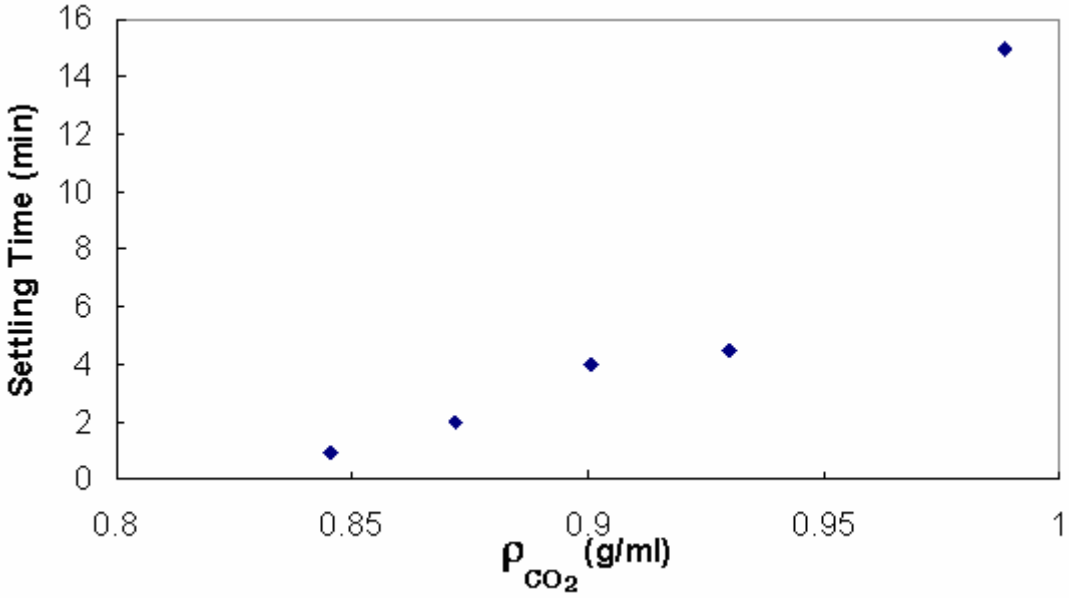

Figure 5.4: Time for W/C emulsion to settle 1.8 mm. Emulsion stabilized by 0.9% Fumed-1.7 particles with 49.4% water and 49.7% w/w CO_2 at 24 ºC.

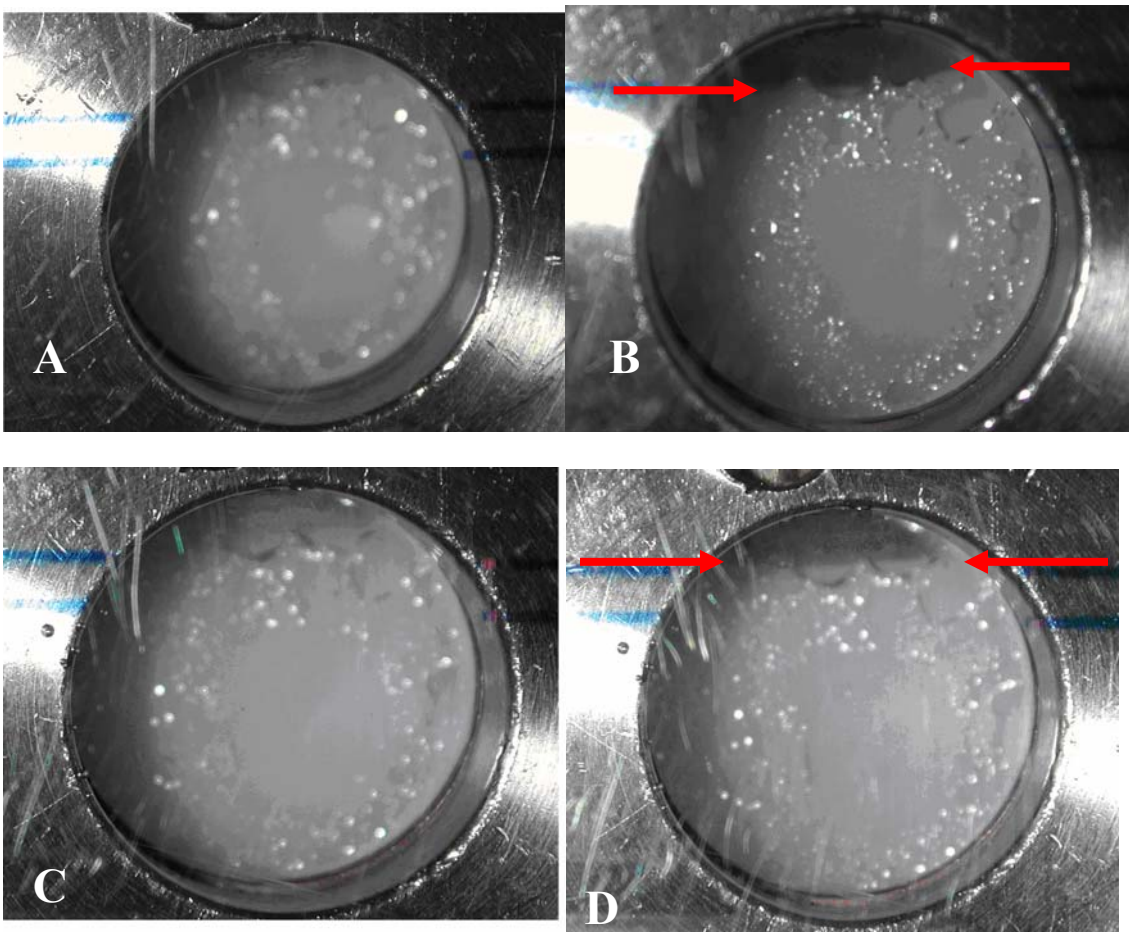

Figure 5.5: Digital photographs of W/C emulsions stabilized with 0.9% Fumed-1.7 particles with 49.4% water and 49.7% w/w CO_2 at 13,800 kPa (0.87 g/ml) and 24 ºC immediately after shearing was stopped (A) and 2 minutes later (B). Emulsion at 34,500 kPa (0.99 g/ml) and 24 ºC immediately after shearing was stopped (C) and 15 minutes later (D). Settling front indicated by arrows in B and D. The diameter of the hole in the stainless steel cell front cap is 1.75 cm.

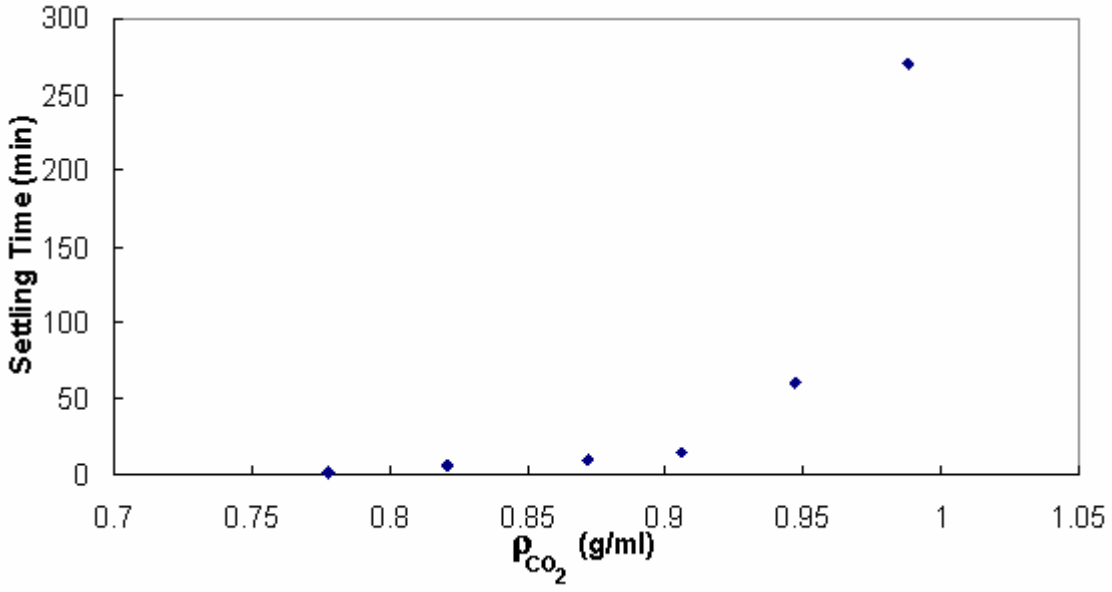

Figure 5.6: Time for W/C emulsion stabilized with 2.1% TM50-1.5 particles, 55.7% CO_2, and 42.2% w/w water to settle 1 mm in cell at 24 °C as a function of CO_2 density.

The average droplet diameter as a function of CO_2 density was investigated for both the Fumed-1.7 and TM50-1.5 particle systems. Micrographs of the W/C emulsion stabilized with the Fumed-1.7 particles (0.9% w/w) are presented in Figure 5.7, and the average droplet diameters from the micrographs are presented in Figure 5.8. The average droplet diameter decreases from 73.3 to 22.7 μm as the CO_2 density increases from 0.87 to 0.99 g/ml, respectively. The standard deviation of the average droplet diameters (D_{avg}) also decreases with the increase in CO_2 density (Table 5.1). Alternatively, micrographs for the TM50-1.5 particle emulsions are presented in Figure 5.9 (2.4% TM50-1.5, 49.6% CO_2, and 48% w/w water). The average droplet diameter was constant at 7.2 ± 0.3 μm over a CO_2 density range of 0.99 to 0.77 g/ml. The standard deviation of the average droplet diameter was also constant at 2.1 ± 0.3 μm.

5.4 DISCUSSION

For surfactant-stabilized emulsions with CO_2 and water, the hydrophilic-CO_2-philic balance (HCB analogous to the hydrophilic-lipophilic balance, HLB, for oil-water systems) governs the preference for a water-in-CO_2 (W/C) versus CO_2-in-water (C/W) emulsion.[45] The HCB can be altered by changes in the surfactant head and tail groups.[34,35] The morphology and stability of the emulsions are also affected by changes in formulation variables (such as temperature, pressure, and salinity) which influence the surfactant partitioning. Surfactants often partition strongly to the water phase (with a high HCB) as a result of the poor solvent strength of CO_2 for the tails. Relatively few low HCB CO_2-philic surfactants have been designed to partition into a CO_2 continuous phase to form W/C emulsions.[35,42]

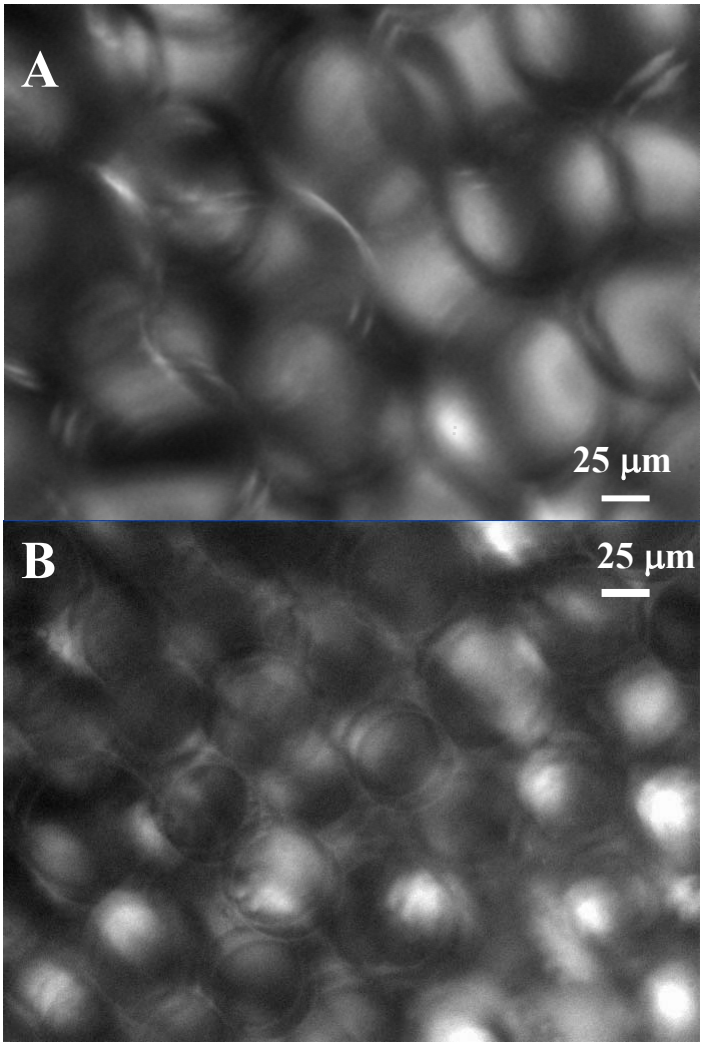

Figure 5.7: Micrographs of W/C emulsion stabilized with 0.9% wt. Fumed-1.7 particles and 49.4% wt. water and 49.7% wt. CO_2 at (A) 17,200 kPa (0.90 g/ml) and (B) 34,500 kPa (0.99 g/ml), and 24 °C.

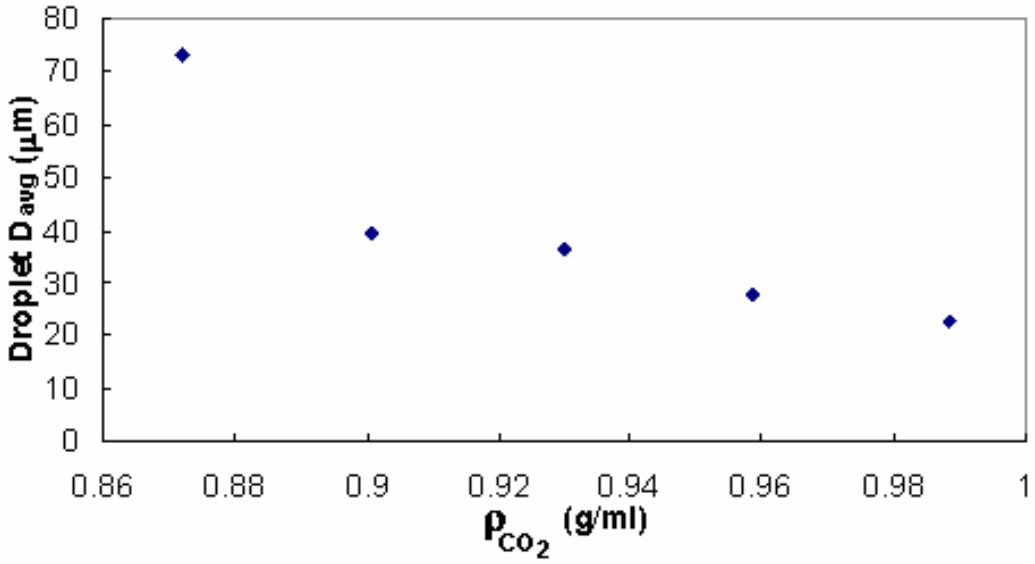

Figure 5.8: Average droplet diameter of W/C emulsion stabilized by 0.9% Fumed-1.7 particles, 49.4% water, and 49.7% w/w CO_2 as a function of CO_2 density.

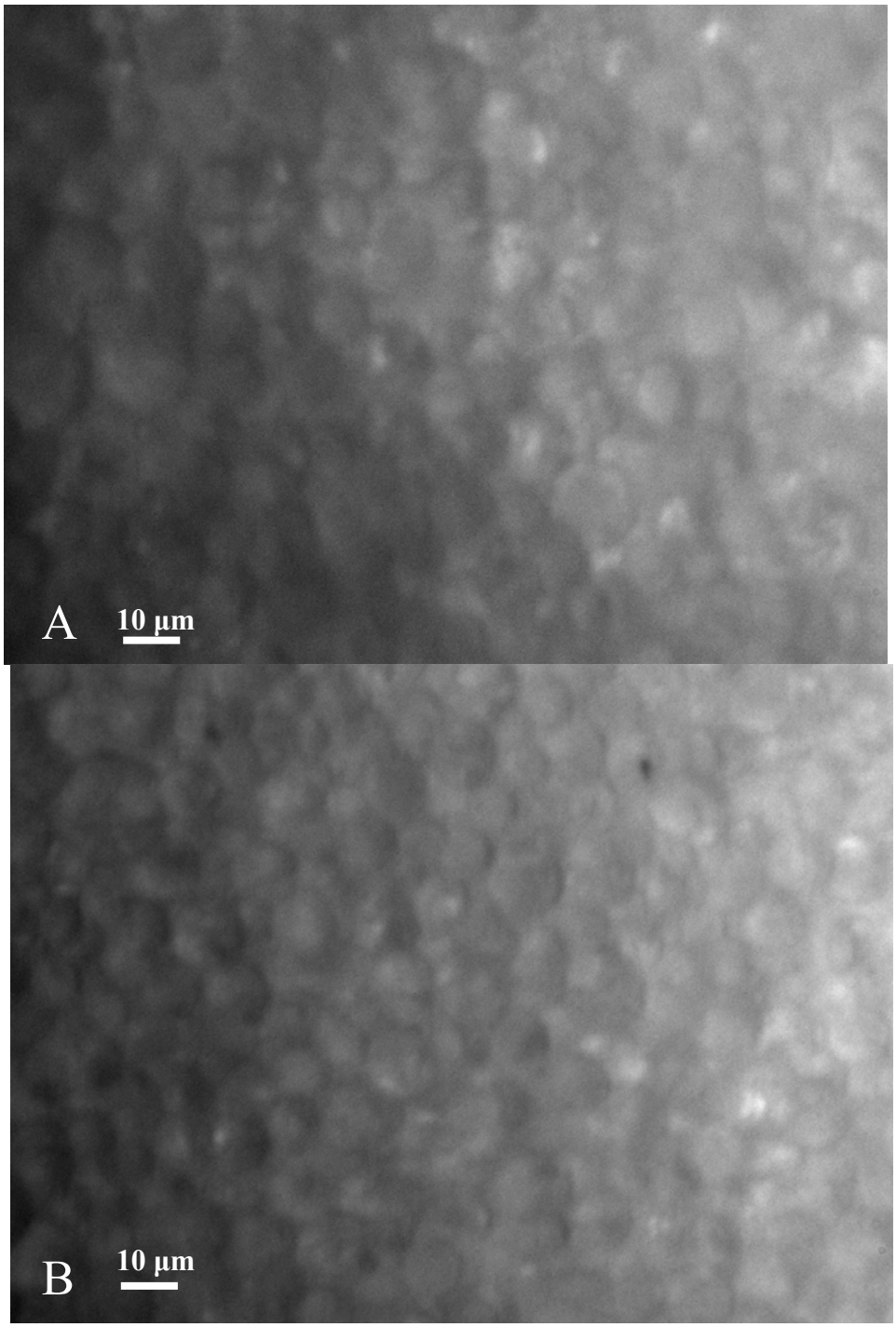

Figure 5.9: Micrographs of W/C emulsion stabilized with 2.4% TM50-1.5 particles, 49.6% CO_2, and 48% w/w water, at (A) 7,600 kPa, 24 °C and (B) 34,500 kPa, 24 °C.

When colloidal particles are used as the emulsifying agents, the contact angle of the particle with the liquid-liquid interface governs emulsion stability and curvature. If the contact angle of a spherical particle at the CO_2-water interface measured through the aqueous phase is less than 90°, the particles are hydrophilic, as shown in Figure 5.10. Hydrophilic particles, such as silica, are wetted more by the water phase leading to a C/W emulsion, in which the interface bends around CO_2.[214] Conversely, if the particle contact angle is more than 90°, the particles are hydrophobic and oriented towards the CO_2 phase, with the expectation of a W/C emulsion (Figure 5.10), as demonstrated in this study. Changes in the contact angle of a solid particle at the CO_2-water interface can be accomplished via adjustments in the surface chemistry of particles. Such a change may be more easily performed than alteration of surfactant architecture to modify the HCB, given that HCB values of surfactants are often high, particularly for those with ionic head groups. The contact angle of a solid particle at the CO_2-water interface has not been reported and is beyond the scope of this work, as it would require specialized high-pressure equipment and *in-situ* optical techniques.

Alternatively, Dickson et al.[220] have measured the contact angle of a water drop on planar hydrophobic glass slides in the presence of CO_2 at various densities. The contact angles measured for the 12 and 37% SiOH slides were approximately 160 and 100º, respectively in liquid CO_2. The contact angles were higher for the glass-water-CO_2 system than the glass-water-air systems indicating the surfaces became less hydrophilic, as a result of physisorption of CO_2 on the SiOH moieties.

Previously, C/W emulsions were stabilized by hydrophilic silica with silanol contents of 76 and 100%.[214] The hydrophobic silica particles used in the current study disperse in CO_2 and do not disperse in water. The preference for CO_2 and the stabilization of W/C emulsions suggest a contact angle of $\leq$ 90º as described by Figure 5.10. Recently,

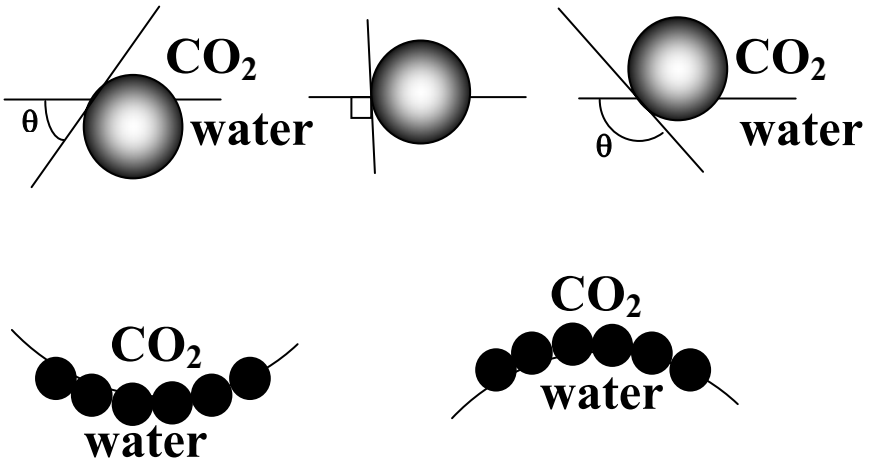

Figure 5.10: Changes in the contact angle of a spherical particle at the CO_2-water interface and the corresponding curvature of the interface.

it was shown that O/W emulsions could be inverted to W/O morphologies for silica-stabilized emulsions. The silica particles had a contact angle of approximately 90º and adjustments in pH were enough to change the wettability of the particles.[221] The tuning of the CO_2-philicity and hydrophilicity of solid particles via surface chemistry offers a means to control of the emulsion curvature.

Relative to surfactant stabilizers, particles often adsorb more strongly at the CO_2-water interface. Surfactant molecules are mobile, whereby adsorption and desorption occur continuously at the interface.[222] The energy of attachment, E, of a hydrophobic solid particle of radius R adsorbed at the CO_2-water interface is

$$E = \pi R^2 \gamma_{cw} \left(1 \pm \cos\theta\right)^2 \qquad [1]$$

where γ_{cw} is the CO_2-water interfacial tension and θ is the contact angle of the particle at the interface measured through the water phase. The sign in front of cos θ in equation 1 becomes negative if the particle is hydrophilic ($\theta < 90°$) and positive if the particle is hydrophobic ($\theta > 90°$).[223] Thus, E is the energy to remove the particle into the water phase for $\theta < 90°$ or to remove the particle into the CO_2 phase for $\theta > 90°$. γ_{cw} is equal to approximately 20 mN/m, a value less than half that of a typical n-alkane-water system (~50 mN/m), reducing the driving force for the particle to adsorb at the interface. The Fumed-1.7 and TM50-1.5 hydrophobic silica particles are both dispersible only in the CO_2 phase and thus it can be concluded that the particle contact angles are 90º or greater. For the TM50-1.5 and Fumed-1.7 silica particles, with average diameters of 270 nm and 870 nm, respectively, E/kT values are enormous on the order of 10^6 kT over a significant range in θ about the maximum, $\theta = 90°$, as shown in Figure 5.11. Once the particles are adsorbed at the CO_2-water interface, it will be difficult to dislodge them.

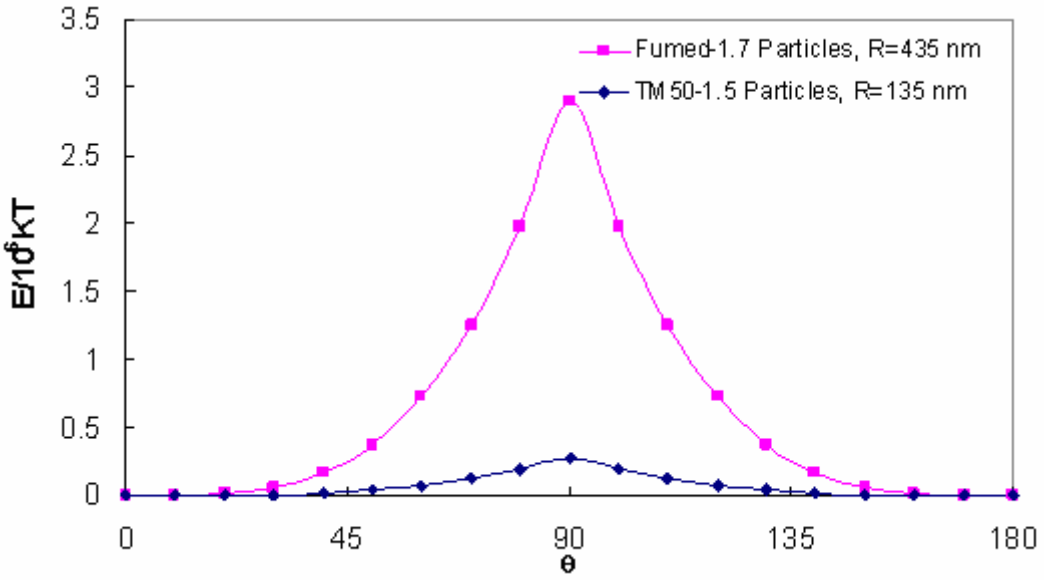

Figure 5.11: Energy of attachment (E) of a spherical Fumed-1.7 or TM50-1.5 particle at the CO_2-water interface as a function of the contact angle (θ).

Assuming all of the particles adsorb at the CO_2-water interface at θ = 90°, a maximum surface coverage of 42% is estimated for the TM50-1.5 particles. This calculation is based on a mean particle diameter of 270 nm and mean droplet diameter of 7.5 μm, at all densities. The surface coverage for the Fumed-1.7 particles varies from 50 to 16% as the density is raised from 0.87 to 0.99 g/ml and the droplet size decreases. Here the mean particle diameter was 870 nm and mean droplet diameters were 73 and 23 μm, respectively. The density of the hydrophobic particles was calculated as the volume-averaged density utilizing 1.4 and 2.2 g/ml as the densities for the silane and silica, respectively. The area occupied by the particles at the C-W interface was based on a circular cross-section with a diameter equal to the mean particle diameter. Previously, Midmore et al. calculated a minimum coverage of 29% necessary to achieve stabilization against coalescence of oil/water emulsions using silica spheres with a diameter of 12 nm.[224] In addition, Tarimala et al. showed a 3D fluorescent image of a stationary poly(dimethysiloxane)-in-water emulsion droplet stabilized by polystyrene particles treated with sulfate.[225] The polystyrene particles covered 46% of the droplet surface leaving particle-free domains on the surface. Therefore, the surface coverage estimated for the TM50-1.5 and Fumed-1.7 particles appears to be reasonable.

The destabilization mechanisms of emulsions include settling/creaming, flocculation, coalescence, and Ostwald ripening. The settling velocity of the dispersed droplets in a non-flocculated, dilute emulsion can be determined using Stoke's law:

$$u_s = \frac{2r^2 \Delta\rho g}{9\mu_c} \qquad [2]$$

where r is the droplet radius, $\Delta\rho$ is the density difference between the continuous and dispersed phases, and μ_c is the viscosity of the continuous phase. Settling is a major

problem for W/C emulsions due to the density difference between the water droplets and the CO_2-continuous phase, as well as the low CO_2 viscosity. The presence of the droplets in a non-dilute emulsion will reduce the sedimentation velocity as follows 17:

$$u = u_s(1-\Phi)^{6.55} \quad [3]$$

where Φ is the dispersed phase volume fraction. To assess the effect of CO_2 density on emulsion stability, these settling equations can be used to calculate average droplet radii, as shown in Table 5.1. The measured average droplet diameters from microscopy are within a factor of 1.6 of the calculated values (Table 5.1) for both the Fumed-1.7 and the TM50-1.5 stabilized drops. Figure 5.12 presents the settling time measured visually and calculated via equations 2 and 3 for the Fumed-1.7 and TM50-1.5 emulsions as a function of $\Delta\rho$. The values are in good agreement in nearly all cases, except at the smallest $\Delta\rho$ where the slow movement of the settling front increases the error of the measurement. The larger sizes calculated from the sedimentation velocity equations may reflect polydispersity in the droplet sizes and possibly small amounts of droplet aggregation. Additionally, the effect of the weight of the adsorbed particles on the water drops is neglected. The effect of dispersed particles will affect the viscosity of the continuous CO_2 phase by 10% or less. Sedimentation appeared to be the major destabilization mechanism of the W/C emulsions.

Flocculation of droplets occurs when electrostatic or steric repulsive forces cannot overcome the attractive van der Waals forces between water drops. Recently, electrostatic stabilization has been used to stabilize micron sized water drops in CO_2.[40,159] The counterions were stabilized by reverse micelles of a highly branched, nonionic hydrocarbon surfactant (octa(ethylene glycol)-2,6,8-trimethyl-4-nonyl ether). In addition,

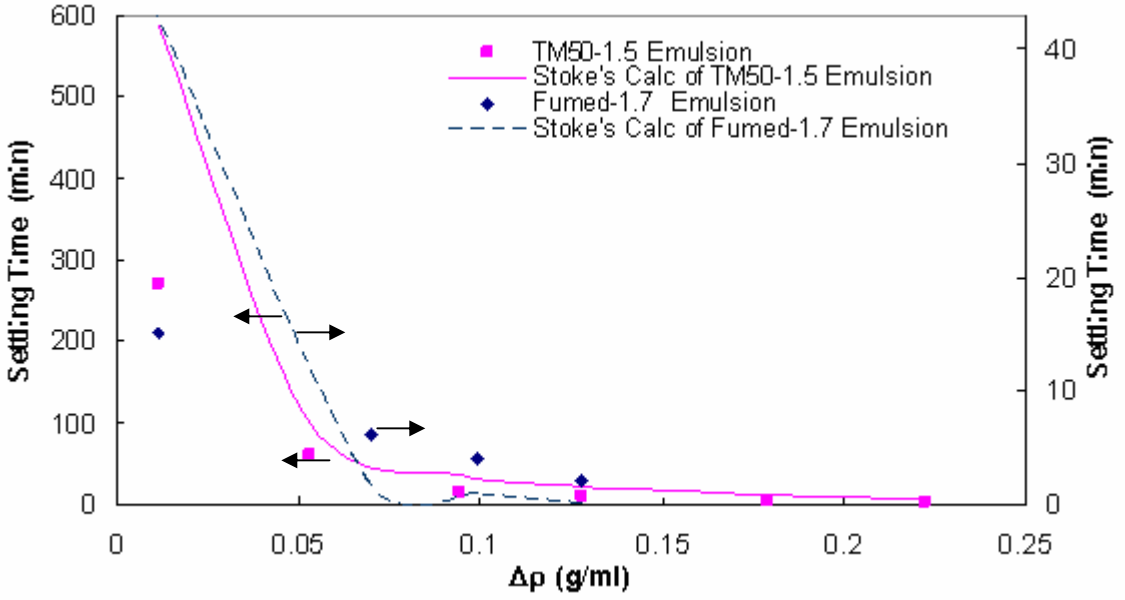

Figure 5.12: Settling time versus the density difference ($\Delta\rho$) of CO_2 and water for the Fumed-1.7 (right axis) and TM50-1.5 emulsions (left axis) (conditions as in Table 5.1). Arrows indicate y-axis for data points or calculated lines.

micron-sized TiO_2 particles were dispersed and stabilized electrostatically in CO_2 with a low-molecular weight cationic perfluoropolyether trimethylammonium acetate surfactant to prevent ion pairing on the surface of the particles.[209]

More commonly, steric stabilization via surfactant adsorption is used to prevent flocculation in CO_2, as the ultra low dielectric constant (1.5) makes it challenging to prevent ion pairing. Flocculation of water droplets is a common problem for surfactant-stabilized W/C emulsions[33,34] as a consequence of poor solvation of the surfactant tail groups by CO_2, especially at lower densities. Below the critical flocculation density (CFD), surfactant tails collapse and interdroplet tail-tail interactions become attractive for the poorly solvated tails.

The stabilization of emulsions with particles in CO_2 circumvents the problem of poor solvation of surfactant tails. The silica particle can be thought of as a highly "stubby" surfactant tail that blocks more of the water-CO_2 interface than traditional narrower surfactant tails.[41,43] In addition, these particles overlap much less than long narrow surfactant tails upon the approach of two drops. Thus, the particles increase the separation distance between two approaching water droplet cores. Further, the driving force for flocculation and ensuing coalescence is reduced as the interdroplet attractive forces are decreased. The W/C emulsions formed with TM50-1.5 hydrophobic silica (2.1% TM50-1.5 particles, 55.7% CO_2, and 42.2% w/w water) are extremely stable at CO_2 densities as low as 0.78 g/ml, near the vapor pressure density of CO_2 at 24 °C. Initially during settling, significant flocculation, even at a CO_2 density of 0.78 g/ml, is avoided for the W/C Pickering emulsions as shown by the Stoke's equation calculations in Table 5.1.

Coalescence of the Pickering W/C emulsions, visible in the form of a separated water phase at the bottom of the cell, was not observed at any of the conditions

investigated over many hours or even days. In contrast, coalescence of water drops has been observed for surfactant stabilized W/C emulsions within 3-4 hours at 15 MPa and 45 ºC for a W/C emulsion stabilized by 1% w/w PDMS-*b*-PAA (10K-1.5K) with 50% w/w CO_2.[45] Further, dilute W/C emulsions (1% w/w water) stabilized by 1% w/w $((CH_3)_3SiO)_2Si(CH_3)(CH_2)_3EO_7OH$ coalesced after only 7 minutes.[34] The stability of the Pickering emulsions to coalescence is favored by the rigid barrier formed by the particles that coat each water drop and the high energy of attachment of the particles at the interface, even though surface coverage by the particles is calculated as 50% or less.

The stability of the rigid particle barriers against Ostwald ripening is unknown. For the TM50-1.5 system, the droplet diameters had a low degree of polydispersity (standard deviations of only 2 μm) indicating a low driving force for Ostwald ripening. The Fumed-1.7 system has a larger degree of polydispersity, especially at lower CO_2 densities, with a maximum standard deviation of 62 μm at 0.87 g/ml. However, Ostwald ripening was not observed to produce any visual changes even over 7 days (not shown).

An additional factor that aids stability of the Pickering emulsions is flocculation of the particles at the CO_2-water interface. Binks et al.[226] have found that maximum flocculation of particles at the oil-water interface increases the stability of O/W emulsions as the nanoparticles become more closely packed. In the case of W/C emulsions, the low Hamaker constant for CO_2 will produce strong attractive van der Waals interactions on the CO_2 side of the particles. The unusually low Hamaker constant for CO_2 increases the attractive force between two silica spheres by a factor of 10 over that in ethanol, 0.123 eV (at 6.9 MPa and 23 °C) and 0.01 eV, respectively.[218] This attraction will favor more closely packed particles creating a more densely packed particle barrier around the water drops, which will enhance stabilization against coalescence. Dickson et al.[218] measured the size of silica particles dispersed in CO_2 with dynamic light scattering. The silica

particles were silylated with the same reagent used here in a ratio of 3.1:1 silane to silica by weight. The DLS results showed that the thin fluorinated shell formed by the silane did not completely screen the Hamaker attractions of the core silica particles, even at high CO_2 densities. Flocculation of the dispersed particles increased as the density of CO_2 was decreased.[218]

The Fumed-1.7 and TM50-1.5 particles have nearly half the silane content of the particles in Dickson's work,[218] and therefore interparticle attraction would be expected to be even greater in this case. The flocculation of the Fumed-1.7 and TM50-1.5 particles at the W-C interface will increase as the density and thus the Hamaker constant of CO_2 is decreased. The similar droplet sizes for the TM50-1.5 emulsion at varying CO_2 densities may be due to the strong interparticle interactions of the adsorbed particles and the resulting rigid interface. The high stability of the TM50-1.5 and the Fumed-1.7 systems to coalescence support the concept of a relatively impenetrable barrier of particles at the CO_2-water interface.

In addition, contact angle measurements have shown that physisorbed CO_2 will cap silanol groups on solid substrates resulting in a decrease of the hydrophilicity of the substrate.[220] FTIR measurements have also shown physisorption of CO_2 with silanol groups on the surface of silica particles.[227] The physisorbed CO_2 can extract water from the surface of the silica particles. Capping of the silanol groups on the TM50-1.5 and Fumed-1.7 silica particles will decrease the surface charge of the particles, thus favoring flocculation of the particles at the CO_2-water interface and enhancing emulsion stability. Previously, Binks et al.[228] showed that stability of O/W emulsions containing hydrophilic silica could be changed by varying particle wettability and surface charge. A decrease in the surface charge of particles decreased the repulsion between particles at the interface and the resulting tighter packing enhanced the stability of the emulsion. Increasing the

wettability of the hydrophilic particles by the oil phase caused higher levels of particle adsorption at the interface and again caused an increase in stability.

Flocculation of the droplets coated by silica particles appeared to result in gelation of the W/C emulsion, as was observed previously for W/C emulsions stabilized by polydimethylsiloxane-based block copolymer ionomers.[45] The formation of a gel would explain why the W/C emulsions filled a large volume of the cell after settling when only 37-50% of the cell volume was water. The attractive interparticle interactions in the gel prevented the water drops from settling to a close-packed structure. In addition, gelation would explain why the Fumed-1.7 emulsion could no longer be sheared with the homogenizer or stirred with the stir-bar after 7 days. The formation of a gel due to flocculation of the particle stabilized water droplets would greatly increase the viscosity of the CO_2 continuous emulsion, a concept of great interest in enhanced oil recovery using CO_2. Particle-stabilized oil and water emulsions have been utilized for oil recovery with gas (such as CO_2) injected to adjust the viscosity of the emulsion,[229,230] thus with the right particles, CO_2 Pickering emulsions could be utilized.

The average droplet diameter for the TM50-1.5 particle-stabilized emulsions was only 7.5 μm, while it was 23-73 μm for the Fumed-1.7 particles. The Fumed-1.7 particles have a mean diameter of 870 nm, larger than that of the 270 nm TM50-1.5 particles (measured in Freon 112). Binks et al. observed an increase in the average droplet diameter in heptane-in-water emulsions with 2 $x10^{-4}$ M DTAB (n-dodecyltrimethyl-ammonium bromide) as the diameter of the silica particle stabilizers was increased from 5.5 to 34 nm.[228] The higher number of particles for a smaller diameter, at a constant weight fraction of particles, stabilizes a larger interfacial area and thus smaller water droplets can result. In addition, the weight fraction of TM50-1.5 particles was 2.4% w/w compared to 0.9% w/w for the Fumed-1.7 particles.

The Fumed-1.7 particle system underwent a decrease in the size of the emulsion drops with increasing CO_2 density. The deformation of drops is determined by the ratio of external stress to the Laplace pressure as described by the Weber number (*We*) and is given by

$$We = \frac{G\eta_c R}{\gamma} \qquad [4]$$

where η_c is the shear viscosity of the continuous phase (CO_2), G is the shear rate (du/dz), R is the droplet radius, and γ is the interfacial tension.[231] This decrease in droplet size could be due to the increase in the viscosity of the continuous CO_2 phase as the density is increased, and thus the greater shear transmitted during rupture to form droplets. Also, more effective dispersion of the silica particles with a higher CO_2 density would facilitate contact between the particles and the water droplets.[218] The larger 870 nm Fumed-1.7 silica particles, relative to the 270 nm TM50-1.5 particles, would require larger CO_2 densities to facilitate particle dispersion. Therefore, it is reasonable to observe a stronger density effect on droplet size for the larger particles. The C/W emulsions stabilized with hydrophilic silica reported by Dickson et al.[214] did not show a change in droplet size with CO_2 density. The solvent properties of water are not affected significantly by pressure, thus dispersion of the silica particles was not increased. In addition, the change in the solvation properties of the dispersed CO_2 phase had little influence on the shear transmitted through the continuous phase.

5.5 CONCLUSIONS

Surfactant-free W/C emulsions, with water droplets smaller than 10 μm, were formed utilizing hydrophobic silica as the emulsifying agent. The droplets occupied approximately 90% of the volume of the vessel and were stable against coalescence even at densities down to 0.78 g/ml at 24 ˚C, despite the unusually low viscosity of CO_2, 0.068 cP. The initial settling rates of the emulsion water droplets were predicted with Stoke's law, indicating minimal initial flocculation even at densities as low as 0.78 g/ml. In addition, coalescence was not visible at any of the conditions investigated, even after 7 days at a density of 0.91 g/ml. The strong adsorption of particles to the water-CO_2 interface, indicated by an energy above 10^6 kT, resulted in rigid barriers surrounding each water drop creating highly stable emulsions. This study^o complements a previous study of particle stabilized C/W emulsions,[214] demonstrating that the emulsion curvature may be inverted by changing the degree of hydrophilicity/CO_2-philicity of the particles. In this case the porous shells on the silica particles, and the fluorine atoms within the shells, increased the dispersibility of the particles in CO_2,[218] and consequently, the CO_2-philicity.

The formation of stable W/C emulsions using solid particles overcomes significant limitations encountered in surfactant-stabilized emulsions. The weak solvent strength of CO_2, especially at the lower densities, rarely provides sufficient solvation of surfactant tails to counterbalance the head group solvation by water. As a result, the hydrophilic-CO_2-philic balance (HCB) of most surfactants is sufficiently high that the preferred curvature is a C/W emulsion.[80] Furthermore, the interdroplet tail-tail attractive interactions and limited surfactant adsorption lead to flocculation and coalescence of the dispersed phase. All of these limitations may be overcome with "stubby" particle

stabilizers. They adsorb strongly at the interface to block droplet growth and coalescence. Furthermore, the smaller degree of overlap of particles on approaching droplets leads to less attractive interactions. The ability to form W/C emulsions with particle stabilizers, even at low densities, may be expected to aid the development of a variety of applications of carbon dioxide based emulsions in green chemistry including separations, environmental science for waste minimization and treatment, reaction engineering, polymer chemistry, and materials science.

Appendices

APPENDIX A

Additional tables present interfacial properties measured at the C-W interface for several nonionic hydrocarbon surfactants under various conditions of temperature and pressure. The interfacial tension (γ) is measured using the captured bubble technique described in Chapter 2. The calculations to determine the efficiency (pC20), critical micelle concentration (CMC), surface pressure (π) and area per surfactant molecule (A_m) were performed according to the equations and procedures in Chapter 2.

Table A1: Interfacial tension and surface pressure measurements for several surfactants at the C-W interface at 24-60 ˚C and 2000 psia. The efficiencies (pC20 values) are also included, as well as the CMC of the surfactants at the A-W interface and the interfacial tension of the surfactant free C-W interface (γ_o).

Surfactants at 24 °C and 2000 psia γ_o **= 27.7 mN/m**	**CMC A-W (wt%)**	γ **0.01% w/w (mN/m)**	γ **0.1% w/w (mN/m)**	γ **1% w/w (mN/m)**	π **0.01% w/w (mN/m)**	π **0.1% w/w (mN/m)**	π **1% w/w (mN/m)**	**pC20**
2EH-PO_5-EO_9	0.275	7.5	3.2	2.1	20.2	24.5	25.6	3.9
2EH-PO_5-EO_{15}	0.284	5.6	2.8	1.8	22.1	24.9	25.9	4.3
1Hex-PO_5-EO_{15}	X	8.5	6.3	2.4	19.2	21.4	25.3	3.5
DOG-EO_{12}	0.015	4.1	2.6	X	23.6	25.1	X	5.1
Surfactants at 40 °C and 2000 psia γ_o **= 29.0 mN/m**	**CMC A-W (wt%)**	γ **0.01% w/w (mN/m)**	γ **0.1% w/w (mN/m)**	γ **1% w/w (mN/m)**	π **0.01% w/w (mN/m)**	π **0.1% w/w (mN/m)**	π **1% w/w (mN/m)**	**pC20**
2EH-PO_5-EO_9	X	7.3	3.4	X	21.7	25.6	X	4.2
2EH-PO_5-EO_{15}	X	4.8	2.9	2.4	24.2	26.1	26.6	5.2
1Hex-PO_5-EO_{15}	X	9.4	4.4	2.3	19.6	24.6	26.7	4.4
DOG-EO_{12}	X	3.5	3.2*	X	25.5	25.8	X	5.7
Surfactants at 60 °C and 2000 psia γ_o **= 31.0 mN/m**	**CMC A-W (wt%)**	γ **0.01% w/w (mN/m)**	γ **0.1% w/w (mN/m)**	γ **1% w/w (mN/m)**	π **0.01% w/w (mN/m)**	π **0.1% w/w (mN/m)**	π **1% w/w (mN/m)**	**pC20**
2EH-PO_5-EO_9	X	8.5	3.6	X	22.5	27.4	X	4.5
2EH-PO_5-EO_{15}	X	4.9	3.6	3.3	26.1	27.4	27.7	5.2
1Hex-PO_5-EO_{15}	X	7.5	3.1	3.1	23.5	27.9	27.9	5.5

Table A2: Interfacial properties (CMC, pC20, and A_m) for several surfactants at the C-W interface as a function of temperature and pressure (density of CO_2).

	T (°C)	P (psi)	Density (g/ml)	C-W CMC (M)	C-W CMC (wt%)	pC20	A_m (A^2/molecule)
2EH-PO_5-EO_9	24	1000	0.755	0.0031-0.0049	0.21-0.34	4.0	250
	24	2000	0.872	0.018-0.0019	0.13	3.9	220
	24	2500	0.900	0.0013-0.0014	0.09-0.1	3.9	215
	24	4000	0.960	0.0011-0.0012	0.07-0.08	3.5	200
	40	2000	0.760	x	x	4.2	x
	40	2500	0.811	x	x	4.3	x
	40	4000	0.897	x	x	3.9	x
2EH-PO_5-EO_{15}	24	1000	0.755	x	x	4.4	230
	24	2000	0.872	x	x	4.3	240
	24	2500	0.900	x	x	4.2	275
	24	4000	0.960	x	x	4.4	340
	40	1850	0.739	0.00047-0.00064	0.048-0.067	5.2	240
	40	2000	0.760	0.00026-0.0006	0.027-0.062	5.2	220
	40	4000	0.897	x	x	5.3	285
	60	2000	0.552	0.00012-0.00014	0.012-0.014	5.2	180
	60	3050	0.739	0.00039-0.00076	0.040-0.079	5.5	245
	60	4000	0.811	0.00042-0.0007	0.044-0.073	5.5	270
	70	2000	0.446	0.00013-0.00004	0.013-0.0044	5.2	130
	70	3650	0.739	0.00012-0.00014	0.012-0.014	5.0	155
1Hex-PO_5-EO_{15}	24	1000	0.755	x	x	3.5	265
	24	2000	0.872	x	x	3.5	340
	24	4000	0.960	x	x	3.2	345
	40	1850	0.739	x	x	4.2	190
	40	2000	0.760	x	x	4.4	195
	40	4000	0.897	x	x	3.8	220
	60	2000	0.552	0.00066	0.068	5.5	200
	60	3050	0.739	0.0011	0.11	4.6	220
	60	4000	0.811	0.0014-0.0016	0.14-0.16	4.7	250
	70	2000	0.446	0.00056	0.058	5.0	200
	70	3650	0.739	0.00048-0.00056	0.050-0.058	4.5	195
DOG-EO_{12}	24	1000	0.755	x	x	5.2	x
	24	1500	0.831	x	x	5.2	x
	24	2000	0.872	x	x	5.1	x
	24	4000	0.960	x	x	5.8	x
	40	2000	0.760	x	x	5.7	x
	40	2150	0.778	x	x	5.6	x
	40	2500	0.811	x	x	5.6	x
	40	4000	0.897	x	x	5.4	x

APPENDIX B

The equations to calculate pore sizes in sand packs and to determine shear rates in porous media are presented in a discussion of foam generation. The stability of foams is also discussed in terms of coalescence and Ostwald ripening. The drainage of foam lamella, Marangoni forces, and flocculation of surfactant tails are discussed in more detail than in Chapter 3. Experimental and theoretical Ostwald ripening rates are also presented. Additional micrographs are presented of C/W foams as a function of time (Figures B1-B3). Figure B1 presents the micrographs of a C/W foam with 90% v/v CO_2 stabilized with 1% v/v 2EH-PO_5-EO_9 at 24 ˚C and 2000 psia as a function of time. Figure B2 presents the effect of time on a C/W foam with 90% v/v CO_2 stabilized with 1% v/v 2EH-PO_5-EO_9 at 55 ˚C and 2000 psia with brine (2% w/w NaCl, 0.5% w/w $CaCl_2$, and 0.1% w/w $MgCl_2$). Micrograph of an unstable C/W foam with 90% v/v CO_2 stabilized with 1% v/v 1-Octanol-$PO_{4.5}$-EO_{12} at 24 ˚C and 2000 psia is presented in Figure B3 which shows the coalescence of bubbles over a 2 sec time interval. Circles connected by arrows show specific examples of bubble coalescence between the frames.

B.1 Foam Generation

The foam generation in the sand pack is important as it gives the initial bubble size distribution, which then influences the stability behavior. The Blake-Kozeny equation is used to estimate the permeability, k, of the sand pack

$$k = \left(\frac{D_{sand}^2}{150} \right) \frac{\phi^3}{(1-\phi^2)} \qquad [B1]$$

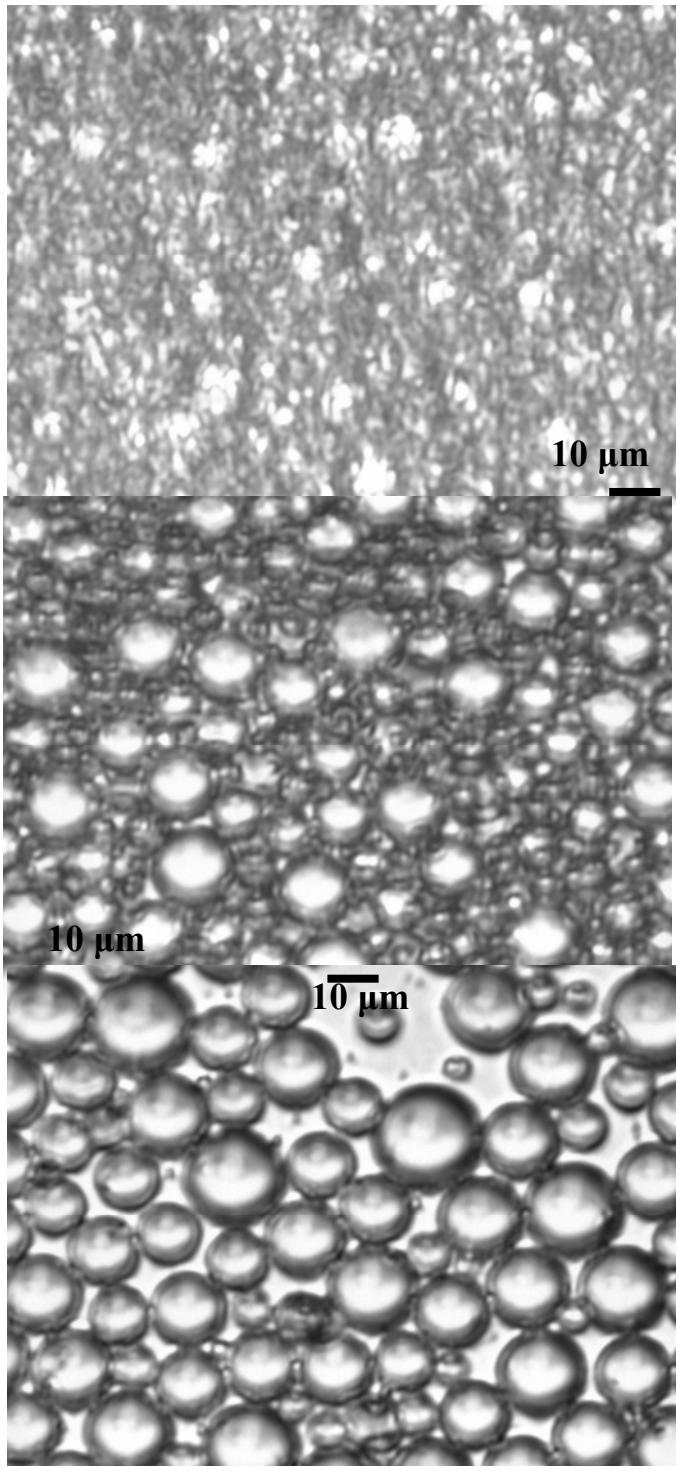

Figure B1: Micrographs of a C/W foam with 90% v/v CO_2 stabilized with 1% v/v 2EH-PO_5-EO_9 at 24 ˚C and 2000 psia as a function of time. Top image is at 0 min, middle image is at 20 min, and bottom image is at 110 min.

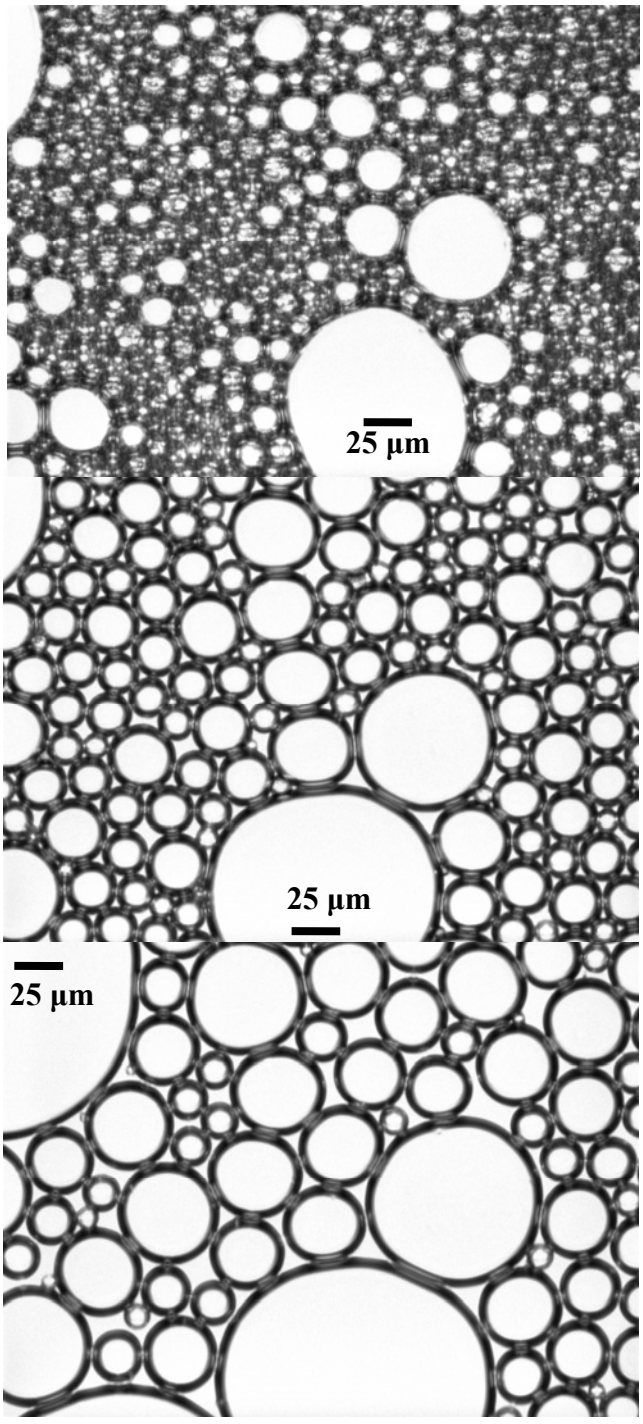

Figure B2: Micrographs of a C/W foam with 90% v/v CO_2 stabilized with 1% v/v 2EH-PO_5-EO_9 at 55 ˚C and 2000 psia with brine (2% w/w NaCl, 0.5% w/w $CaCl_2$, and 0.1% w/w $MgCl_2$) as a function of time. The top image is at 0 min, the middle image is at 20 min, and the bottom image is at 110 min. Scale bars are included.

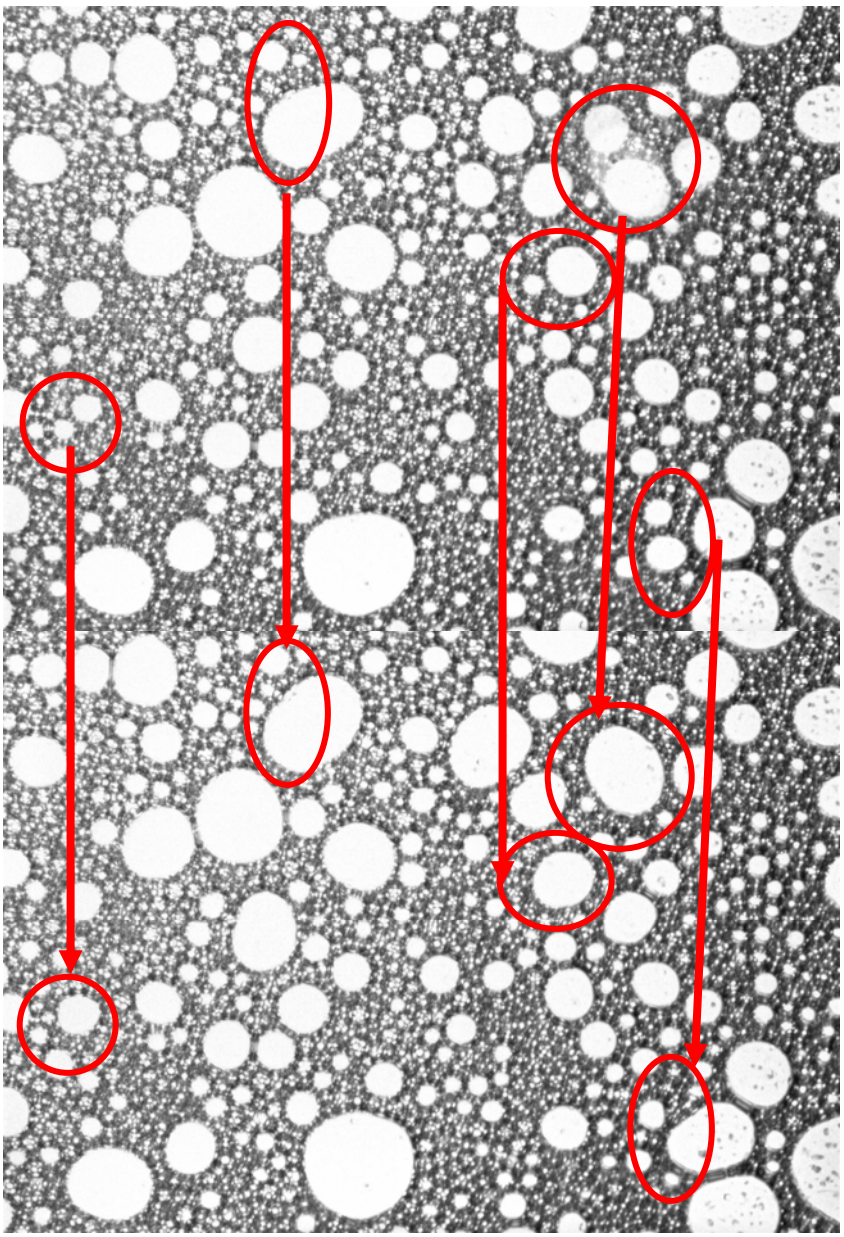

Figure B3: Micrograph of a C/W foam with 90% v/v CO_2 stabilized with 1% v/v 1-Octanol-$PO_{4.5}$-EO_{12} at 24 ˚C and 2000 psia showing the coalescence of bubbles over a 2 sec time interval. Circles connected by arrows show bubble coalescence between frames.

where D_{sand} is the effective spherical diameter of a sand particle and φ is the porosity.[232] The porosity of the sand pack is determined by the type of packing of the sand grains. The sand can pack loosely in a cubic type packing order for which case

$$\boldsymbol{D_{sand} = \frac{d_{pore}}{\sqrt{2}-1} = 2.41 d_{pore}} \quad \text{[B2]}$$

where d_{pore} is the spherical diameter of the pore between the sand and φ has a value of 0.476. The sand can pack tightly in a hexagonal close packed order where the following equation can be used with φ value of 0.260.

$$\boldsymbol{D_{sand} = 6.46 d_{pore}} \quad \text{[B3]}$$

To account for the non-spherical shape of sand, the d_{pore} value calculated from either equation B2 or B3 has been halved due to the extra packing of the random shapes.

The initial sand pack used as a foam generator was 10.2 cm long with a 3.8 mm inner diameter and was filled with large non-spherical sand particles that were 420-840 μm in diameter. For tight packing for a hexagonal close geometry, k of 37.7-151 darcies (μm^2) is calculated and the φ value of 0.26 is used. The d_{pore} estimated for this sand pack is 33-65 μm due to the large size of the sand, and it is denoted the 50 μm pore sand pack. For the sand pack which was 12.1 cm long with an inner diameter of 7.6 mm filled with 125 μm non-spherical sand, the hexagonal close packing geometry gives a k of 3.3 darcy and a φ value of 0.26. The d_{pore} of this system is about 10 μm, which is a similar average pore size as typical Texas cream carbonate core samples from the Wasan reservoir (about 20 μm); however the k of the core sample is only about 1-3 milidarcies. The large impenetrable portions of the carbonate pore decrease k relative to the sand pack.

Foam generated at low shear rates in porous media is expected to create bubbles that are no smaller than the pores.[59] Normally, bubble formation is attributed to lamella divison, snap-off, and leave behind mechanisms that take place at the size of the pores. However, both the 10 μm and 50 μm pore sand packs form bubble sizes smaller than 1

μm. Estimates of the pore body and throat diameters of the sand packs can be accomplished by following the method of Rossen[233] for either a meeting of 8 pore throats or a meeting of 4 pore throats

$$\begin{aligned} l_{8,pore} &\approx 1.73 R_{sand}, \\ \frac{r_{8,Body}}{l_{8,pore}} &\approx 0.24, \\ \frac{r_{8,throat}}{l_{8,pore}} &\approx 0.086 \end{aligned} \qquad \text{[B4]}$$

$$\begin{aligned} l_{4,pore} &\approx R_{sand}, \\ \frac{r_{4,Body}}{l_{4,pore}} &\approx 0.23, \\ \frac{r_{4,throat}}{l_{4,pore}} &\approx 0.155 \end{aligned} \qquad \text{[B5]}$$

where $l_{i,pore}$ is the pore length, $r_{i,Body}$ is the radius of the pore body, $r_{i,Throat}$ is the radius of the pore throat, R_{sand} is the radius of spherical sand in the pack, and i is number of pore throats meeting (either 4 or 8). For non-spherical sand, $l_{i,pore}$, $r_{i,Body}$, and $r_{i,Throat}$ are halved. Thus for the 10 μm pore sand pack, the $l_{i,pore}$, $r_{i,Body}$, and $r_{i,Throat}$ are 31-54, 7.2-13, and 4.6-4.8 μm, respectively. For the 50 μm pore sand pack using a R_{sand} value of 210 μm, the values are 105-182, 24-44, and 15.6-16.3 μm, respectively. The resulting foam bubble sizes can reach values smaller than even the estimated pore throats, indicating the large shear forces may be present in the sand packs to generate the small bubbles.

To form a bubble, the shear stress must be greater than the Laplace pressure of the bubble. For a bubble with a diameter of 1 μm, assuming a γ of 3 mN/m, the shear stress must exceed 12,000 Pa. The lower γ of the C-W interface relative to the air-water or oil-water interfaces leads to the formation of smaller bubbles with a given shear stress. The magnitude of the shear rate for a non-Newtonian fluid in permeable media flow is estimated using

$$\dot{\gamma}_{eq} = \frac{4Q}{A_{cs}\sqrt{8k\phi}} \qquad \text{[B6]}$$

where Q is the total flowrate, A_{cs} is the cross-sectional area, k is the permeability, and φ is the porosity. Currently, a relationship between the shear rate and shear stress in porous media is lacking, thus the shear rates cannot be used to effectively determine whether the shear stress has been overcome. For the 50 μm pore sand pack, at 6 ml/min the shear rate is 3962 s^{-1} with k of 37.7 μm^2 and φ of 0.26. The 10 μm pore sand pack at 6 ml/min with k of 3.3 μm^2 and φ of 0.26 has a shear rate of 3300 s^{-1}. At 1.5 ml/min the shear rate for the 10 μm pore sand pack is only 840 s^{-1} although typical bubble sizes are smaller than those produced with the 50 μm pore sand pack at 6 ml/min. However, the residence time of the foam in the 50 μm pore sand pack is only 8.6 sec at 6 ml/min, and at 1.5 ml/min for the 10 μm pore sand pack it is 163 sec. The longer time through the sand pack, smaller pores size, and increased number of pores in the 10 μm pore sand pack reduce the cell sizes of the resulting foam.

B.2 Drainage of Thin Films

For symmetrical film geometry (Figure B4) that is assumed cylindrical the quasistatic Stokes equations can be assumed for both the droplet phase[142] and the thin film phase to describe the drainage of the liquid in the thin film. For a thin film of thickness h_f, if $R_{film} << h_f$, then the lubrication approximation is used for the film phase[142] in the R direction

$$\frac{\partial p}{\partial R} = \mu \frac{\partial^2 v_R}{\partial z^2} \qquad [B7]$$

where p is pressure in the film, μ is the viscosity of the film liquid, and v_R is the velocity of the lamellar fluid in the R direction. The difference in pressure between the film and plateau border creates the flow of film liquid which varies in the z direction due to shear

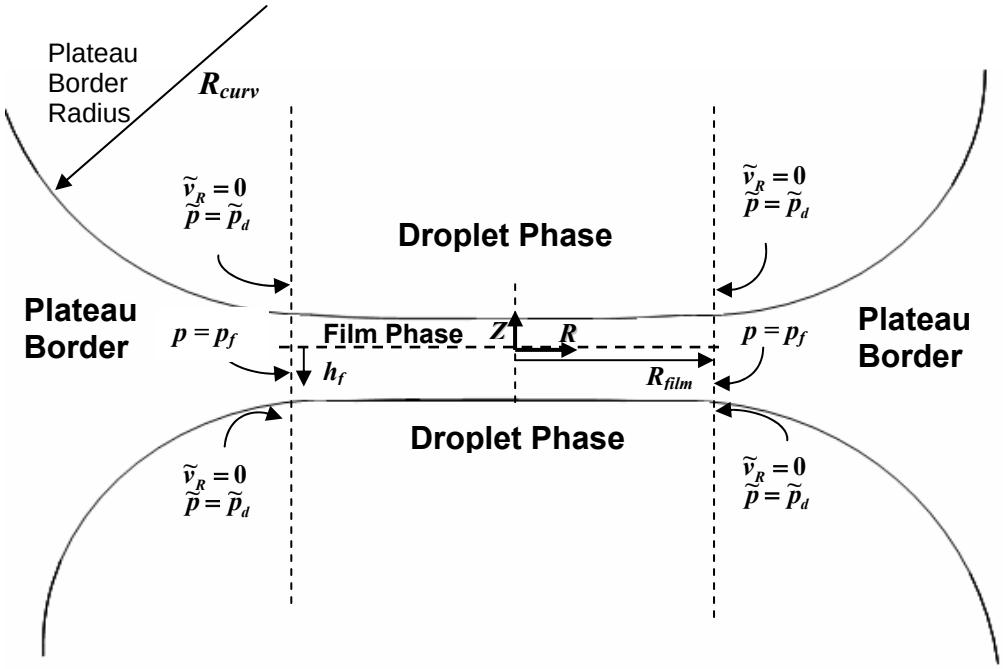

Figure B4: Drawing depicting the symmetric lamellar geometry for thin film drainage between two identical fluid droplets with the hydrodynamic boundary conditions.

effects from the interfaces. The ultra low γ of the C/W foams lead to a lower pressure difference between the film and plateau border relative to both A/W and O/W systems. Accordingly, a lower v_R is expected for C/W foams increasing the time to reduce h_f resulting in slower film drainage times and increased stability. Thus, the C/W foams have slower drainage times than A/W and O/W systems enhancing the stability of the films.

Bhakta et al. found the drainage velocity of liquid through the network of plateau borders (v_{pb}) for a 3D standing foam (assuming identical pentagonal dodecahedral foam cells and no change in the thin films) is

$$v_{pb} = \frac{c_v \alpha_{pb}}{20\sqrt{3}\mu}\left[\Delta\rho g + \gamma \frac{\partial}{\partial z}\left(\frac{1}{R_{curv}}\right)\right] \qquad \text{[B8]}$$

where c_v is the velocity coefficient (1 for high surfactant concentrations), α_{pb} is the cross-sectional area of the plateau border ($0.161 R_{curv}^2$), μ is the viscosity of the continuous phase, $\Delta\rho$ is the density difference between the continuous and dispersed phases, and g is the gravitational acceleration.[143] The first term in the brackets includes the gravitational driving force, while the second term in the brackets is the gradient of capillary suction of the plateau border, where the effect of γ is clearly seen.

B.3 Marangoni Forces

The drainage of fluid in the thin foam films creates Marangoni forces due the tangential stress of the interface. The tangential stress condition of the film-drop interface ($z = h_f$) is

$$\mu \frac{\partial v_R}{\partial z} - \tilde{\mu} \frac{\partial \tilde{v}_R}{\partial z} = (\kappa^s + \mu^s)\nabla_R\left(\frac{\partial v_s}{\partial R}\right) - \frac{E_{Gibbs}}{\rho_{1o}^s}\frac{\partial \rho_1^s}{\partial R} \qquad \text{[B9]}$$

when the interfacial tension gradient (last term on the right side) can be approximated due to a small departure from the surface compositional equilibrium.[142] κ^s is the interfacial

dilational viscosity, μ^s is the interfacial shear viscosity, $\rho^s{}_{1o}$ is the surface-excess surfactant species mass density at equilibrium, $\rho^s{}_1$ is the surface-excess surfactant species mass density, E_{Gibbs} is the Gibbs elasticity, and ∇_i is the gradient operator for the i axis. The tangential stress condition shows how the liquid flow in the film and droplet phases affects the interface by moving surfactant molecules from their equilibrium position and creating interfacial tension gradients. As interfacial tension gradients form, Marangoni flow of the liquid occurs toward the direction of high γ. The Marangoni flow opposes lamella drainage thus increasing the drainage time, h_f, and the stability of the foam.

B.4 Flocculation of W/C Emulsions

The lower adsorption of nonionic hydrocarbon surfactants (large A_m values) is due to the higher cohesive energy density of these surfactants than fluorinated surfactants and thereby lower tail solvation by CO_2. Da Rocha et al. found that the formation of W/C emulsions with nonionic surfactants were difficult and that when formed, flocculation to some degree usually occured.[148] Even with the fluorinated nonionic polymer PFOMA-EO a critical flocculation density of 0.86-0.90 g/ml (depending on system conditions) has been measured for W/C miniemulsions drops, such that below this density tail-tail interactions between the surfactant make the water droplets flocculate and settle.[33,127] Further more Lee et al. found that interdroplet interactions were greater for a W/C microemulsion than a W/O microemulsion stabilized with a fluorinated surfactant (perfluoropolyether based surfactant) due to poorer tail solvation by CO_2. SANS (small angle neutron scattering) was used to measure these interactions which were found to increase with droplet volume fraction.[234]

B.5 Theoretical and Experimental Ostwald Ripening Rates

Ostwald ripening is described by Lifshitz and Slyozov,[169] as updated by Wagner[170] (LSW) for dilute emulsions. The LSW theory assumes that the diffusion is from a curved bubble to a flat interface such that

$$\Omega_3 = \frac{dD_{sm}^3}{dt} = \frac{64\gamma D_{diff} S V_m}{9RT} F \qquad [B10]$$

where D_{diff} is the molecular diffusion coefficient, S is the bulk solubility, and V_m is the molar volume of the dispersed phase (CO_2).[171] A correction factor, F, is included to increase the ripening rate for small diffusion lengths and non-dilute conditions.[171] For a quality of 90%, F is 25.[172]

The experimental measured and theoretically calculated Ω_3 (equation B10) are provided in Table B.1 for 2EH-PO_5-EO_9, 2EH-PO_5-EO_{15}, and DOG-EO_{12} at 2000 psia under a variety of surfactant concentrations, foam qualities, salinities, and U_{poly}. The γ used in the calculation of the theoretical Ω_3 are also listed with the bold numbers being actual measured values and italic numbers as estimates. The Ω_3 values are many times orders of magnitude different form the measured Ω_3. The changes predicted by the theory also do not correlate with those measured, for example increasing the quality is expected to increase Ω_3 by about a factor of 2 when the measured Ω_3 increased by about 25. The changes in the foam lamella thickness vary the Ω_3 to a much greater degree than the corrected LSW theory. Other changes in Ω_3 are masked by the huge effect of the polydispersity of the foam. Another theoretical model that includes the full distribution of bubble sizes and small diffusion lengths is necessary to adequately estimate Ostwald ripening rates for foams, especially as the foam quality increases towards that of a dry foam.[235]

Table B1: Experimental and theoretical Ostwald ripening rates (Ω_3) (experimentally defined as the change in D_{sm}^3 over time, $d(D_{sm}^3)/dt$) are listed with the time studied (t_f), and the U_{poly} initially (at t_o) and at t_f. The γ in bold are measured values and other γ are estimated from measured values. When salt (in % w/w NaCl) is added to the aqueous phase, 0.5% w/w $CaCl_2$ and 0.1% w/w $MgCl_2$ are also added to the water. The concentration of surfactant in the water (c in % v/v), temperature (T), and quality (% v/v CO_2) of the foam are specified.

Surfactants	***c*** **(%)**	**T (°C)**	**CO_2 (%)**	**Salt (%)**	**γ (mN/m)**	**Ω_3 $d(D_{sm}^3)/dt$ ($\mu m^3/s$)**	***t_f***	***U_{poly}***		**Theory Ω_3 ($\mu m^3/s$)**
								At t_o	**At t_f**	
2EH-PO_5-EO_9	0.1	24	90	0	**3.2**	unstable	-	-	-	13.4
	0.2	24	90	0	**3**	309	7.5 hr	16.0	4.0	12.6
	0.5	24	90	0	**2.7**	2.2	2.7 hr	4.5	0.5	11.3
	1	24	90	0	**2.1**	1.6	22.8 hr	2.7	0.3	8.8
	1	24	90	0	**2.1**	0.06	48.3 hr	0.6	2.8	8.8
	1	24	94	0	**2.1**	49	600 s	1.1	1.1	15.7
	0.2	55	90	0	**5.7**	unstable	-	-	-	64.0
	0.3	55	90	0	**4.6**	1.3	1hr	4.6	1.0	51.7
	0.3	55	90	2	4.6	0.46	60.5 hr	2.0	0.5	51.7
	0.5	55	90	0	**3.8**	0.9	8.7 hr	4.8	0.9	42.7
	1	55	90	0	3.8	10.5	8.8 hr	7.9	2.4	42.7
	1	55	92.4	0	3.8	2.5	26 hr	0.8	0.6	63.6
	1	55	92.4	2	3.8	7.9	1.8 hr	24.5	2.1	63.6
2EH-PO_5-EO_{15}	1	24	90	0	**1.8**	2.7	8 hr	1	0.4	7.5
	1	24	90	0	**1.8**	4.3	30 min	3.2	1.5	7.5
	1	24	90	2	1.8	2.9	21.8 hr	2	0.6	7.5
	1	24	90	5	1.8	2.6	19.5 hr	4.2	0.4	7.5
	1	40	90	0	**2.4**	3.1	27 hr	2.4	2.1	7.9
	1	70	90	0	**3.9**	9.9	1 hr	2.2	0.4	97.4
	1	70	90	2	3.9	92	110 min	11.2	0.7	97.4
DOG-EO_{12}	0.3	24	90	0	3.2	5.8	61.5 hr	6	4.4	10.9
	0.2	50	90	0	2.6	1.4	6.8 hr	4.8	1	37.2
	0.3	55	90	0	2.6	2.3	20 hr	7.2	1.1	43.8

APPENDIX C

Additional flow curves, shear stress (τ) versus shear rate ($\dot{\gamma}$) plots are presented for several high-pressure C/W foams to supplement the foams discussed in Chapter 3. A Newtonian model is used to describe the flow curve of a 1% v/v DOG-EO_{12} foam in Figure C1. Power-law behavior is shown in Figures C2-C4. Figure C5 presents a foam with a combination of Newtonian and Power-law behavior that results in a polynomial fit. Additional plots showing the change in the apparent bulk foam viscosity (η_{foam}) and bubble size (Sauter mean diameter, D_{sm}, or number average diameter, D_{avg}) with shear rate (or foam velocity) are also presented to show other C/W foams that are both shear-thickening (Figures C2 and C3 with $n > 1$) and shear-thinning (Figure C4 with $n < 1$). Figure C6 presents the effect of quality on C/W foam stabilized with 5% v/v TMN 6 at two foam flow rates. At qualities greater than 95% v/v CO_2 the foams were unstable and η_{foam} could not be measured. A master table of all the foams investigated (Table C1) is also presented.

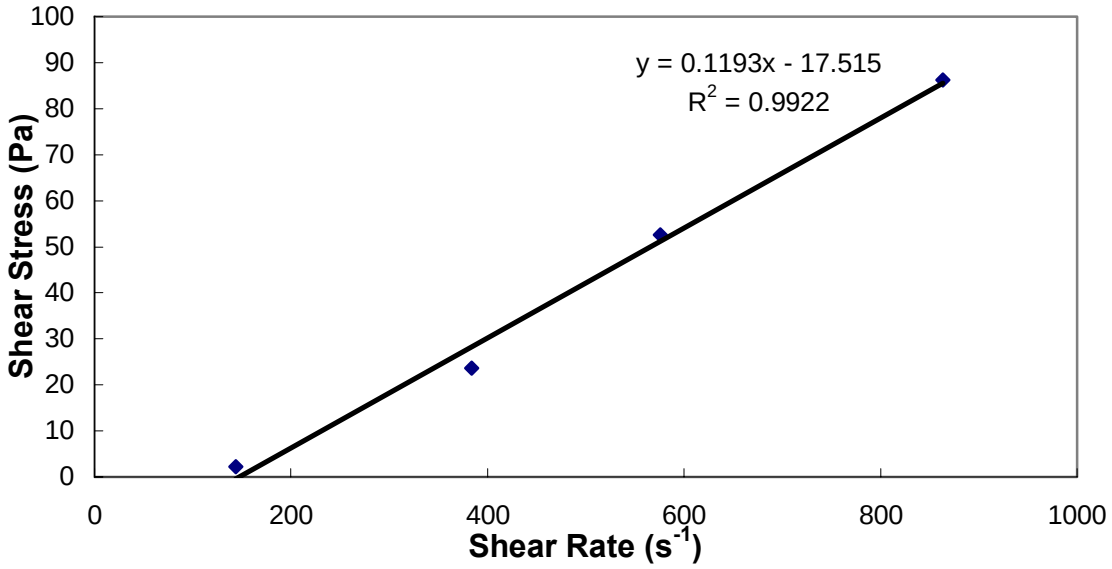

Figure C1: Flow curve for C/W foam stabilized with 1% v/v DOG-EO_{12} and 90% v/v CO_2 at 24 ˚C and 2000 psia showing Newtonian behavior.

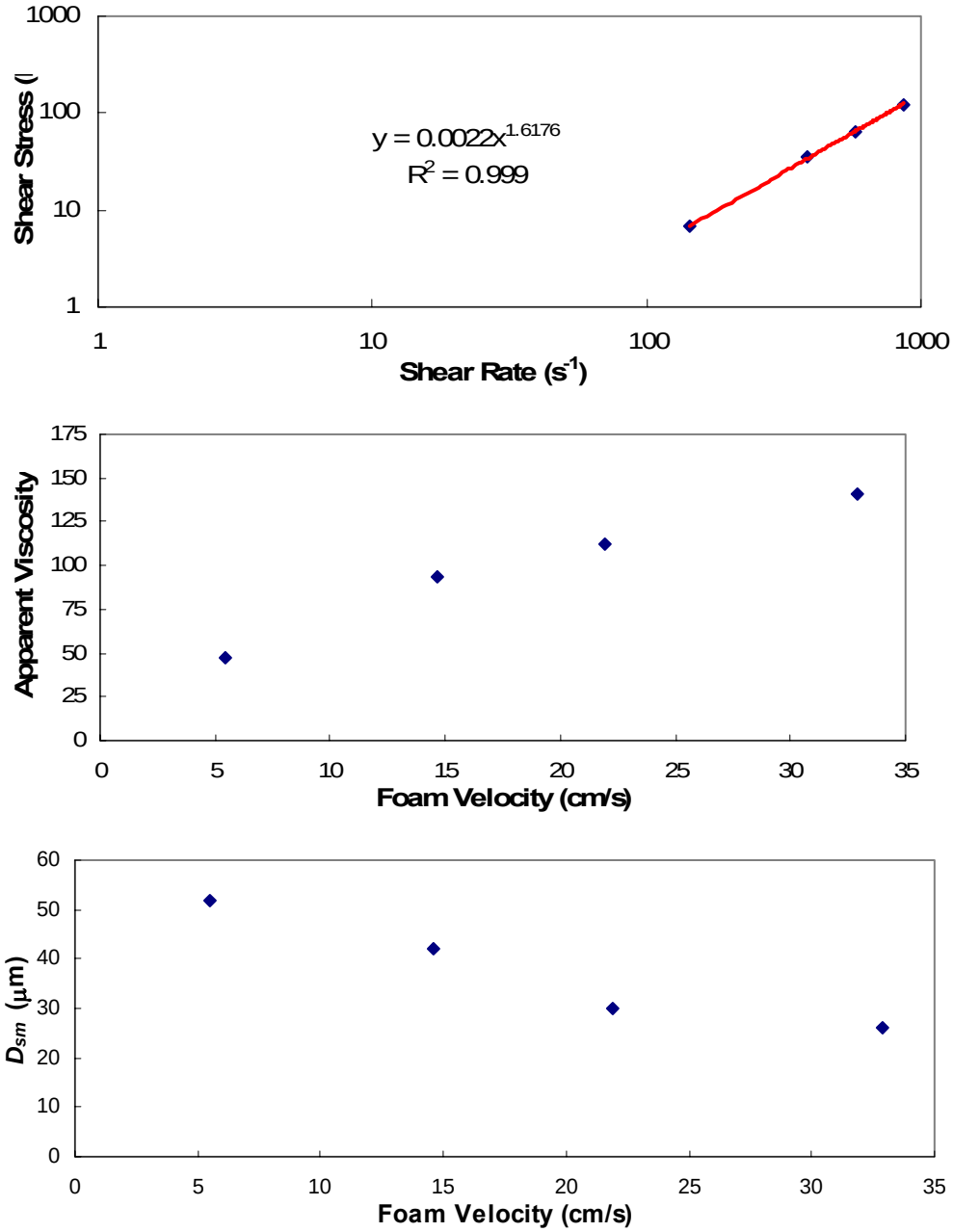

Figure C2: Shear stress versus shear rate (top plot), η_{foam} as a function of foam velocity (middle plot), and D_{sm} as a function of foam velocity (bottom plot) for C/W foam stabilized with 1% v/v 2EH-PO_5-EO_9 and 90% v/v CO_2 with brine (2% NaCl, 0.5% $CaCl_2$, 0.1% $MgCl_2$ w/w in water) at 24 ˚C and 2000 psia. A power-law relationship is shown in the top plot with $n > 1$. Shear-thickening behavior is presented in the middle plot with a drop in D_{sm} with increasing foam velocity (bottom plot).

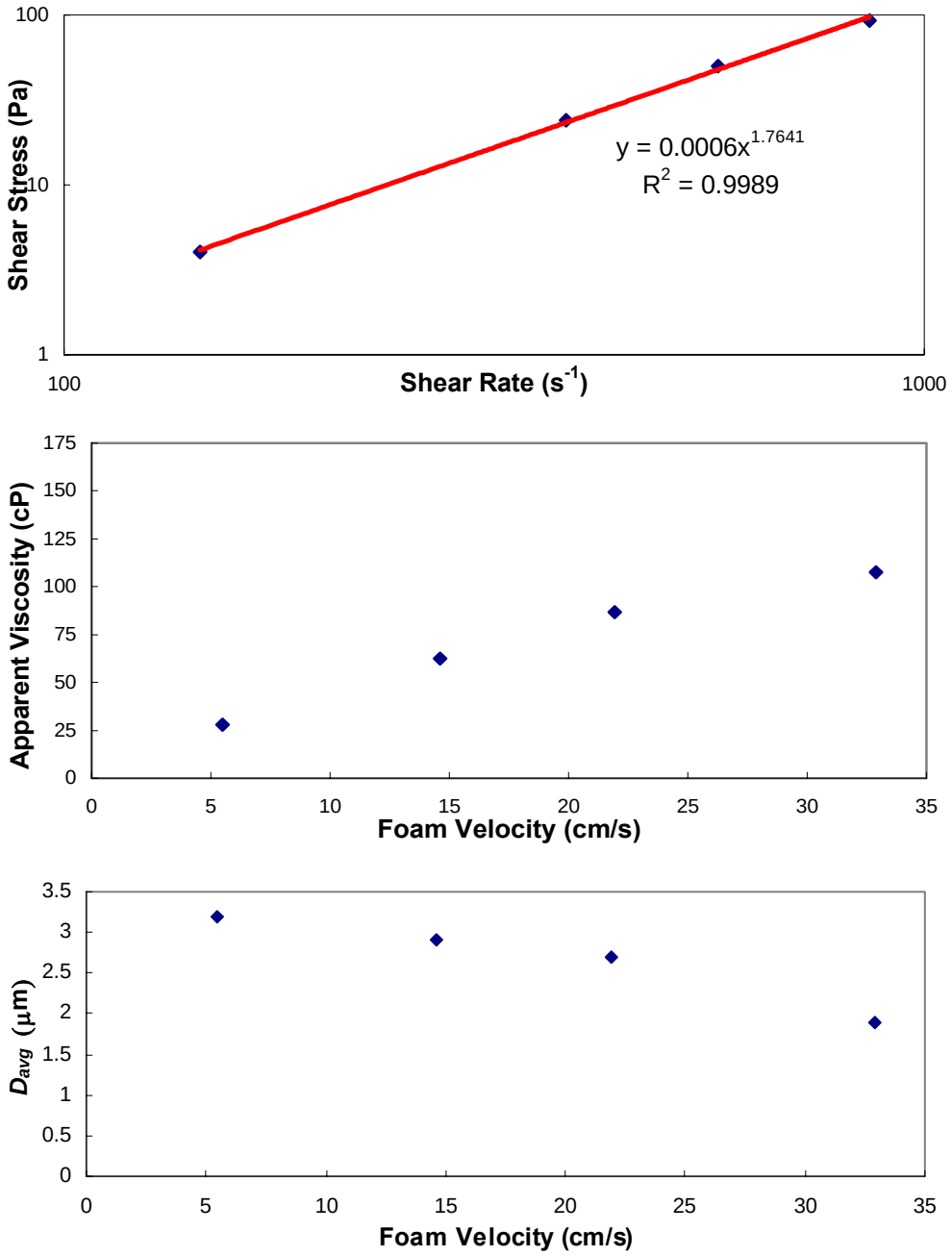

Figure C3: Shear stress versus shear rate (top plot), η_{foam} as a function of foam velocity (middle plot), and D_{avg} (number average diameter) as a function of foam velocity (bottom plot) for C/W foam stabilized with 5% v/v TMN 6 and 90% v/v CO_2 at 24 ˚C and 1700 psia. A power-law relationship is shown in the top plot with $n > 1$. Shear-thickening behavior is presented in the middle plot with a drop in D_{avg} with increasing foam velocity (bottom plot).

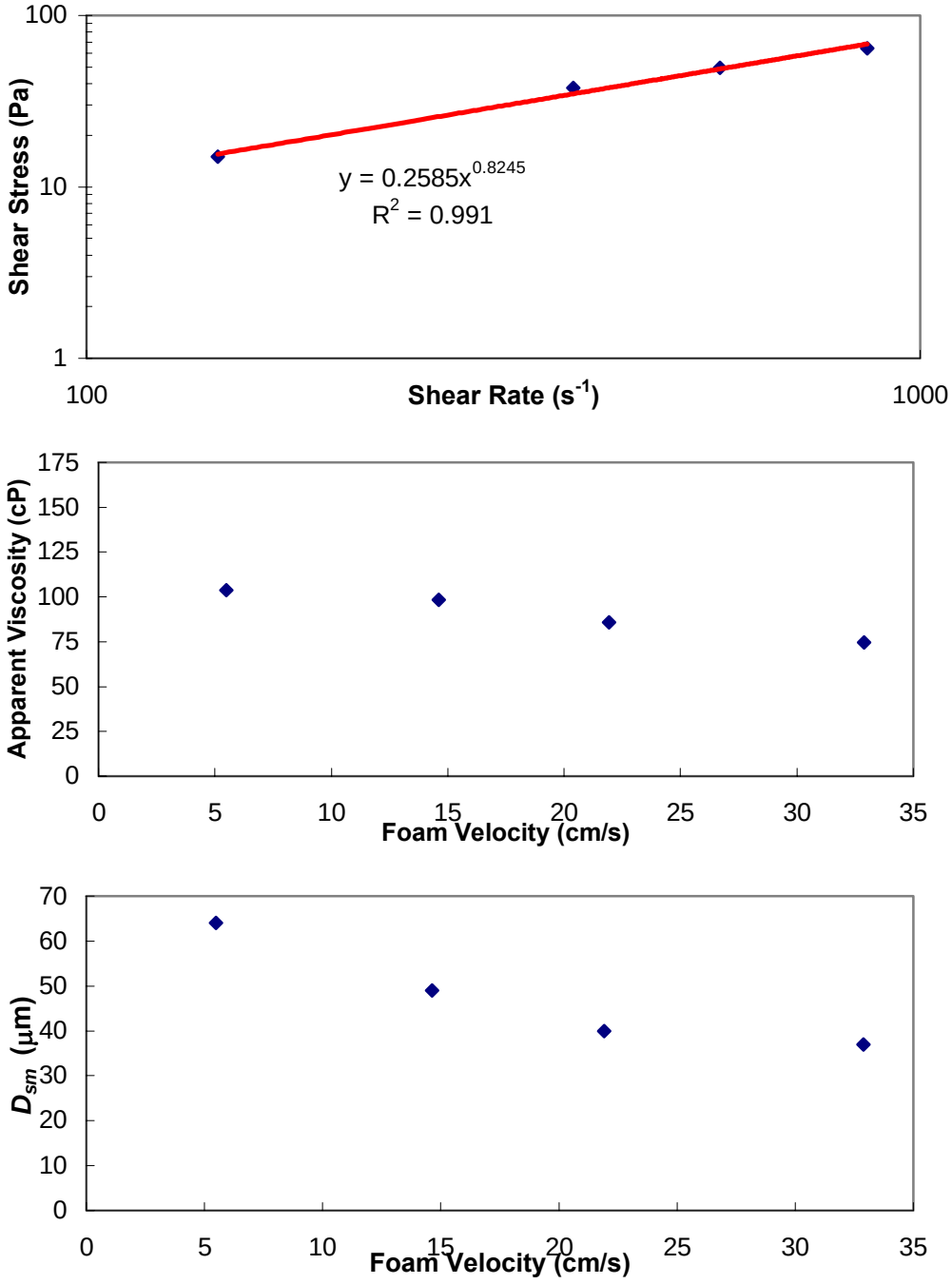

Figure C4: Shear stress versus shear rate (top plot), η_{foam} as a function of foam velocity (middle plot), and D_{sm} as a function of foam velocity (bottom plot) for C/W foam stabilized with 1% v/v 2-Octanol-PO_9-EO_9 and 90% v/v CO_2 at 40 ˚C and 2000 psia. A power-law relationship is shown in the top plot with $n < 1$. Shear-thinning behavior is presented in the middle plot.

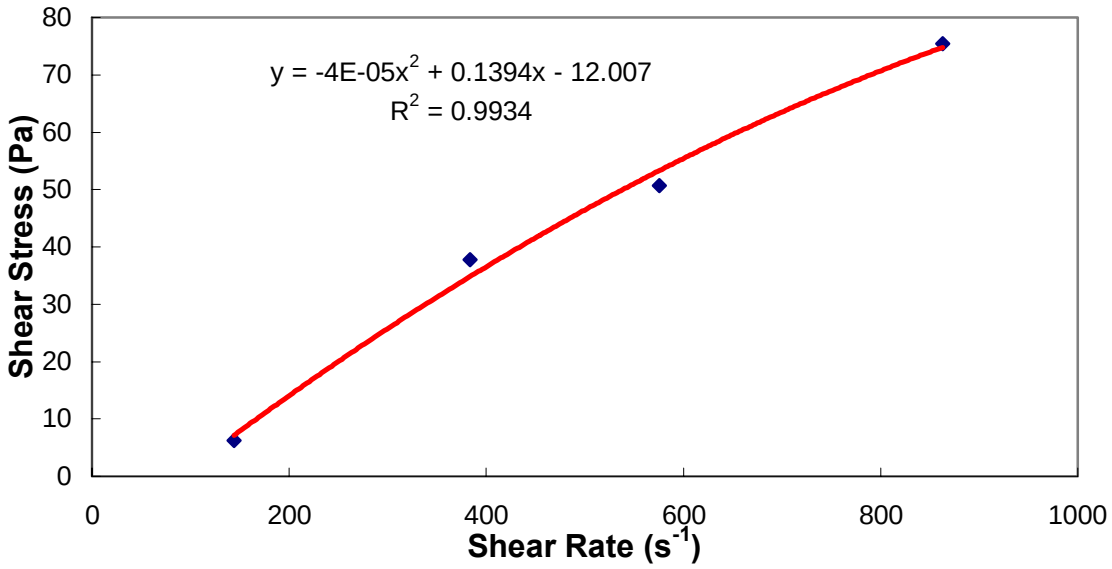

Figure C5: Shear stress versus shear rate plot showing polynomial relationship (combination of Newtonian and Power-law models) for a C/W foam stabilized with 1% v/v 2EH-PO_5-EO_8 and with 90% v/v CO_2 at 24 ºC and 2000 psia.

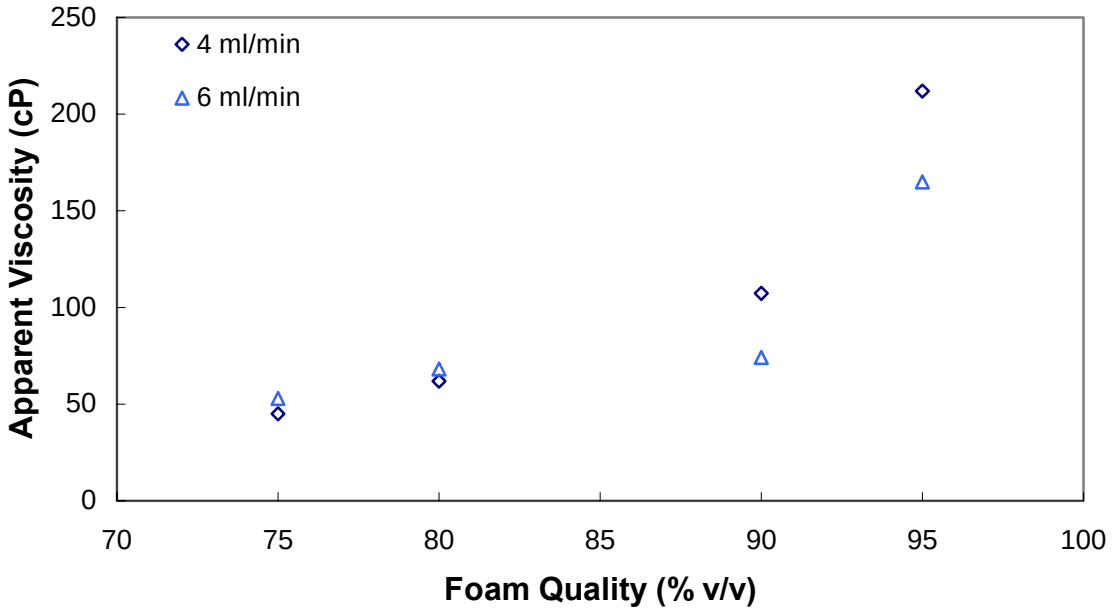

Figure C6: The effect of varying the foam quality on the η_{foam} is presented for a 5% v/v TMN 6 foam at 24 ºC and 2300 psia for Q_{foam} of 4 and 6 ml/min.

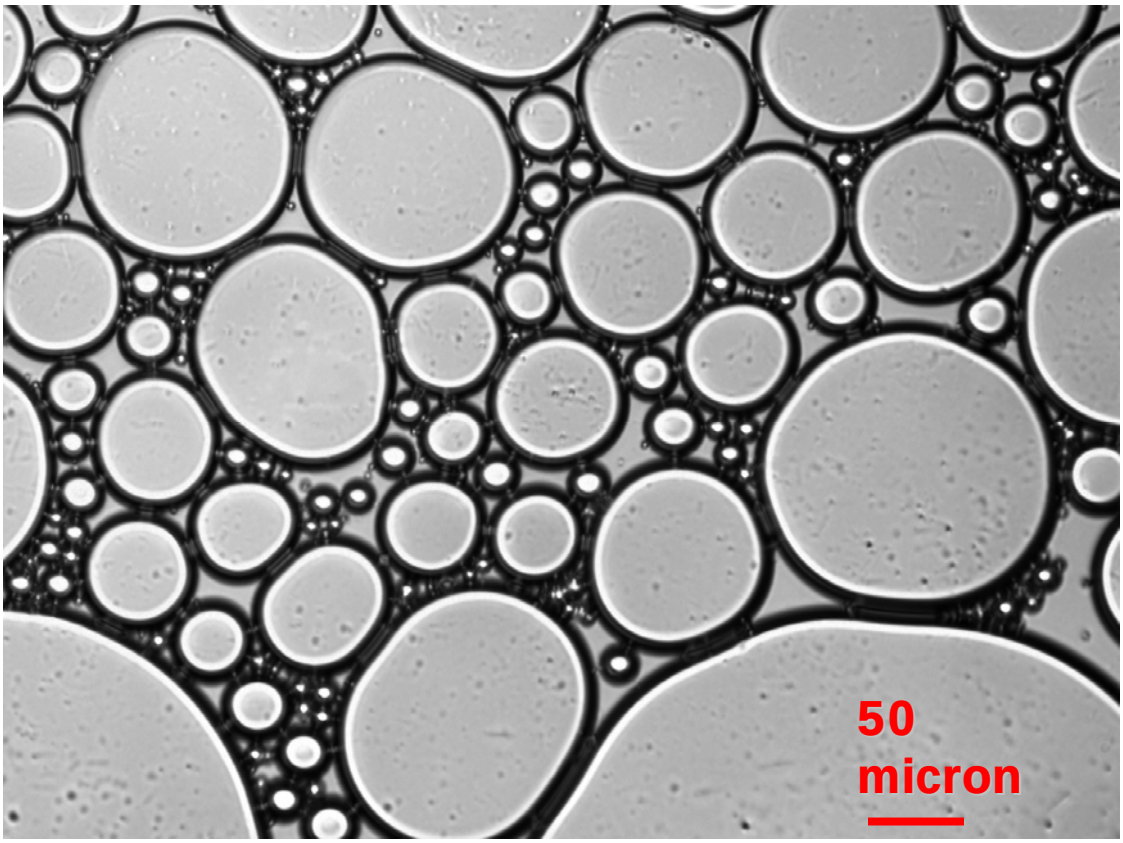

Figure C7: Micrograph of the C/W foam stabilized by 1% v/v 2EH-PO_2-EO_4 in water with a CO_2 quality of 90% v/v at 24 °C, 2100 psi, and a total foam flow rate of 9 ml/min. This is a typical picture of foam with large bubbles that are slightly deformed and corresponds to a relatively low apparent viscosity of the foam (20 cP) compared with the results of other surfactant structures. Scale bar as indicated in photo.

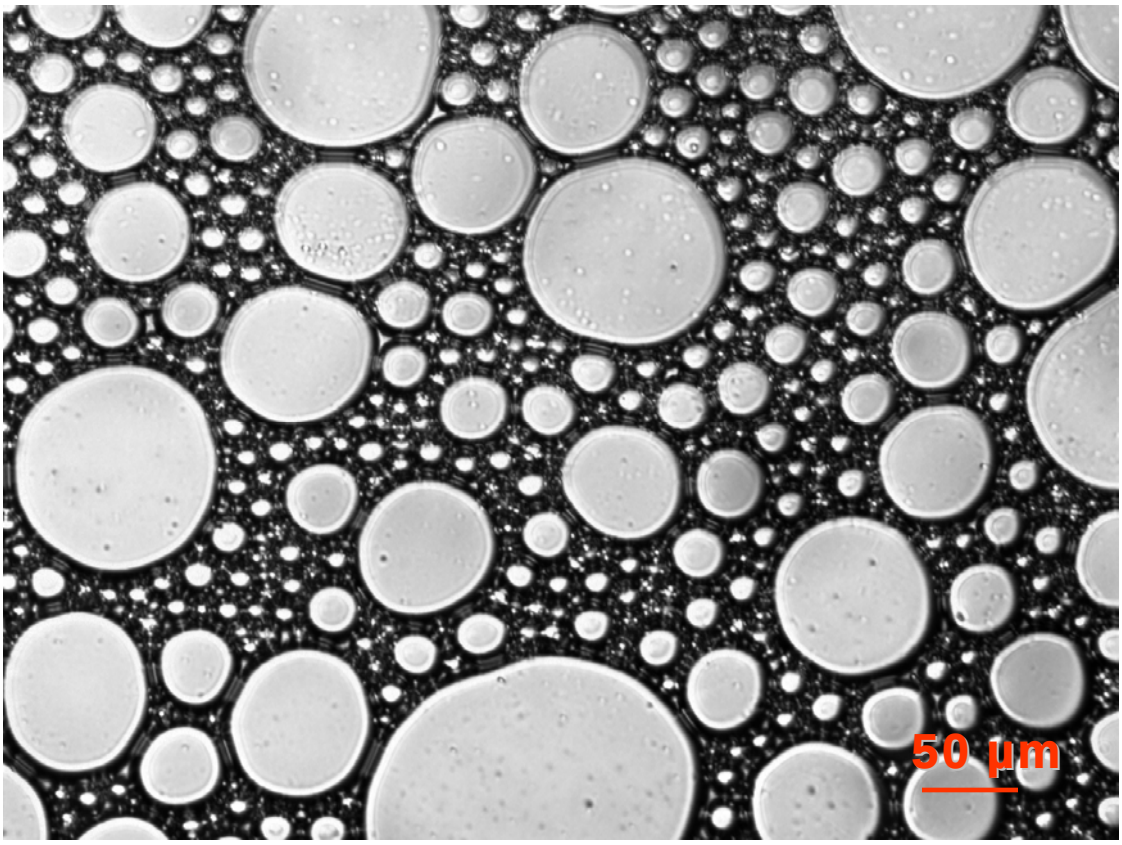

Figure C8: Micrograph of the C/W foam stabilized by 1% v/v DOG-EO_{12} in the aqueous phase with a CO_2 quality of 89% v/v at 40 °C, 3300 psi, and a total foam flow rate of 6 ml/min. This is a typical picture of a foam with a relatively moderate-to-high apparent viscosity (74 cP in this case) and a number average bubble radius of 5.1 µm. Scale bar indicated in photo.

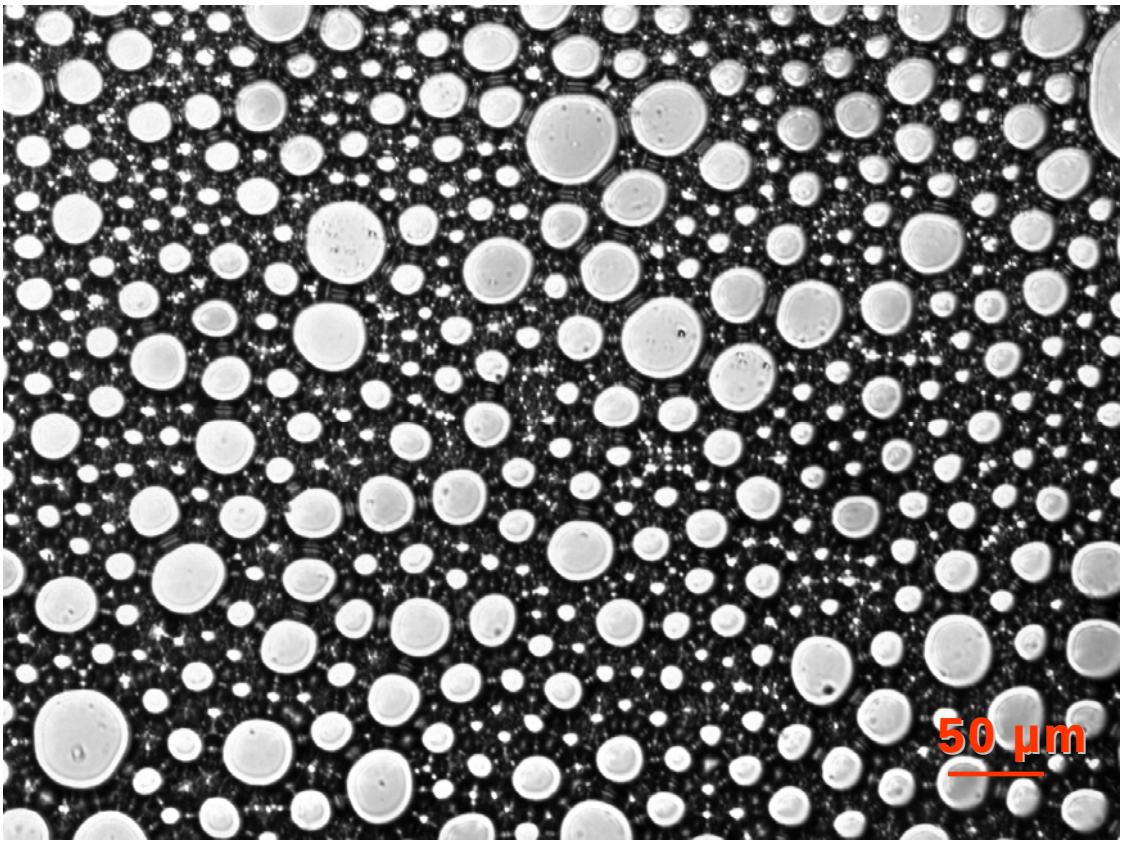

Figure C9: Micrograph of the C/W foam stabilized by 1% v/v DOG-EO_{12} in water with a CO_2 quality of 89% v/v at 40 °C, 3300 psi, and a total flow rate of 9 ml/min at a low magnification (10x, scale bar indicated in photo). This is a typical picture of a foam with a high apparent viscosity (115 cP in this case) and a number average bubble radius of 3.7 µm.

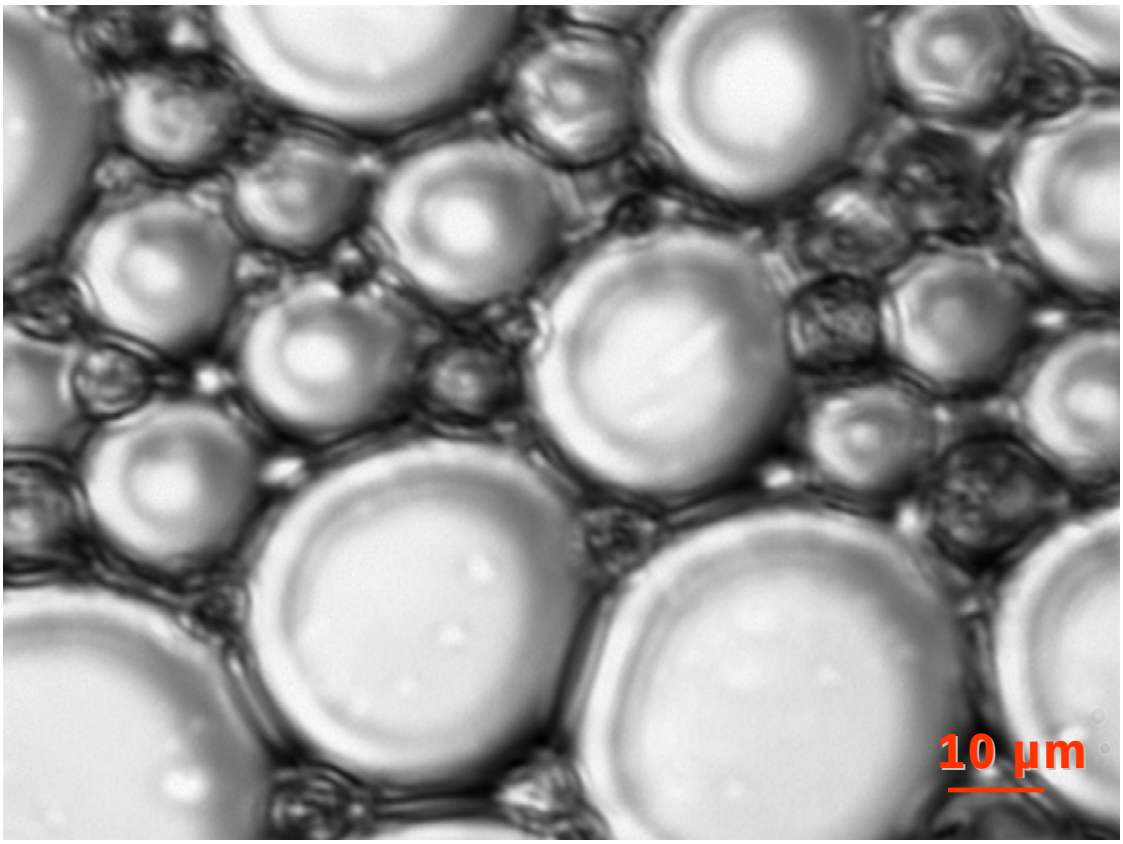

Figure C10: Micrograph of the C/W foam stabilized by 1% v/v DOG-EO_{12} in water with a CO_2 quality of 89% v/v at 40 °C, 3300 psi, and a total flow rate of 9 ml/min at a high magnification (50x, scale bar indicated in photo). The higher magnification (compared to the same foam in Figure C9) allows smaller bubbles to be seen tightly packed between the larger bubbles.

Table C1: Overview table of the bulk C/W foam apparent viscosity measurements and cell sizes. The concentration of surfactant (C_{surf}), foam quality (% v/v CO_2), flow rate (Q_{foam}), pressure (P), density (ρ_{CO2}), temperature (T) are specified with the measured pressure drop over the capillary ($\Delta P_{capillary}$) and the sand pack ($\Delta P_{sandpack}$) when measured are listed. The viscosity (η_{foam}, calculated from equation 2 in Chapter 3), the number average bubble radius (R_{avg}), Sauter mean diameter of the bubbles (D_{sm}, calculated from equation 3 in Chapter 3), and the standard deviation of the bubble radii (σ) are also listed in the table.

Surfactant	C_{surf} % v/v	CO_2 % v/v	Q_{foam} ml/min	P psia	ρ_{CO2} g/ml	T °C	$\Delta P_{capillary}$ psia	η_{foam} cP	$\Delta P_{sandpack}$ psia	R_{avg} µm	D_{sm} µm	σ
TMN 6	5	90	1.5	2300	0.89	24	11	52		3.5	44	5.5
	5	90	4	2300	0.89	24	61	107		4.9	59	5.5
	5	90	6	2300	0.89	24	64	74		3.1	18	2.9
	5	90	9	2400	0.90	24	133	104		2.3	9	1.4
	5	88	1.5	2800	0.83	40	2	6		2.3	76	4.4
	5	88	4	2800	0.83	40	5	9		3.6	50	6.1
	5	88	6	2800	0.83	40	15	18		6	27	4.7
	5	88	9	2800	0.83	40	18	14		2.7	9	3.2
	5	88	1.5	2800	0.71	60	no foam	x		x	x	x
	5	88	4	2800	0.71	60	no foam	x		x	x	x
	5	88	6	2800	0.71	60	no foam	x		x	x	x
	5	88	9	2800	0.71	60	no foam	x		x	x	x
	1	90	9	2000	0.87	24	no foam	x		x	x	x
	0.5	90	9	2000	0.87	24	no foam	x		x	x	x
Tergitol L-62	1	90	1.5	2000	0.87	24	no foam	x		x	x	x
	1	90	4	2100	0.88	24	74	130		5.6	33	5.4
	1	90	6	2200	0.88	24	>100	x		3.8	57	3.3
	1	90	9	2200	0.88	24	>100	x		3.6	19	3.2
	1	90	1.5	2100	0.77	40	no foam	x		x	x	x
	1	90	4	2100	0.77	40	no foam	x		x	x	x
	1	90	6	2100	0.77	40	no foam	x		x	x	x
	1	90	9	2100	0.77	40	no foam	x		x	x	x
	1	90	9	2100	0.61	60	no foam	x		x	x	x
$EO_{30\%}$-$BO_{70\%}$ MW 3500	1	90	1.5	2000	0.87	24	no foam	x		x	x	x
	1	90	4	2000	0.87	24	no foam	x		x	x	x
	1	90	9	2200	0.88	24	no foam	x		x	x	x

Table C2: Continuation of Table C1.

Surfactant	C_{surf} % v/v	CO_2 % v/v	Q_{foam} ml/min	P psia	ρ_{CO2} g/ml	T °C	$\Delta P_{capillary}$ psia	η_{foam} cP	$\Delta P_{sandpack}$ psia	R_{avg} µm	D_{sm} µm	σ
TM 15-S-7	1	90	1.5	2800	0.92	24	2	6		2.1*	51	3.6
	1	90	4	2800	0.92	24	20	34		4.3	59	7.3
	1	90	6	2800	0.92	24	38	45		6.6	51	8.3
	1	90	9	2800	0.92	24	65	51		5.7	46	6.7
	1	90	1.5	2800	0.83	40	2	7		4.7	58	8.1
	1	90	4	2800	0.83	40	12	21		4.7	52	7.3
	1	90	6	2800	0.83	40	15	17		4.9	46	7.1
	1	90	9	2800	0.83	40	40	31		6.2	44	7.7
	1	90	1.5	2800	0.71	60	no foam	x		x	x	x
	1	90	4	2800	0.71	60	no foam	x		x	x	x
	1	90	6	2800	0.71	60	no foam	x		x	x	x
	1	90	9	2800	0.71	60	18	14		8.8	52	9.3
TM 15-S-20	1	90	1.5	1900	0.87	24	13	60	5	6.5	29	4.7
	1	90	4	2000	0.87	24	50	87	8	2	35	2.4
	1	90	6	2000	0.87	24	121	141	10	1.8	21	2.2
	1	90	7	2100	0.89	24	166	130	11	1.9	37	3.4
	1	90	1.5	1900	0.75	40	5	25	5	2.8	25	3
	1	90	4	2000	0.76	40	45	78	7	1.9	24	2.2
	1	90	6	2000	0.76	40	81	94	8	2.2	26	2.8
	1	90	9	2100	0.77	40	128	100	9	small	x	x
	1	90	1.5	1900	0.51	60	7	32	5	6.4	41	6.9
	1	90	4	2000	0.55	60	25	43	6	3.5	27	3.9
	1	90	6	2000	0.55	60	46	53	6.5	2.7	34	3.7
	1	90	9	2100	0.58	60	81	63	8	2.2	16	2
	1	90	1.5	1900	0.41	70	no foam	x	1	x	x	x
	1	90	4	2000	0.45	70	14	25	6	5	20	2.9
	1	90	6	2000	0.45	70	43	51	7	1.9	19	2.1
	1	90	9	2100	0.48	70	49	38	7	1.6	30	1.9
TM 15-S-20 with Brine	1	90	1.5	2000	0.76	40	no foam	x	3	x	x	x
	1	90	4	2000	0.76	40	44	77	8	3.8	42	10.9
	1	90	6	2000	0.76	40	61	72	9	2.3	37	24.5
	1	90	9	2000	0.76	40	93	73	8	1.5	23	18.5

Table C3: Continuation of Table C1.

Surfactant	C_{surf} % v/v	CO_2 % v/v	Q_{foam} ml/min	P psia	ρ_{CO2} g/ml	T °C	$\Delta P_{capillary}$ psia	η_{foam} cP	$\Delta P_{sandpack}$ psia	R_{avg} µm	D_{sm} µm	σ
TM NP 9	1	90	1.5	2000	0.87	24	22	102	4	2	19	2.3
	1	90	4	2000	0.87	24	61	107	7	1.5	15	1.5
	1	90	6	2000	0.87	24	119	140	8	1.3	20	1.7
	1	90	9	2000	0.87	24	60	47	12	1.2	18	1.4
	1	90	1.5	2000	0.76	40	3	13	5	4.2	29	4.8
	1	90	4	2000	0.76	40	13	23	6	3.5	26	3.5
	1	90	6	2000	0.76	40	34	40	6.5	1.9	18	2
	1	90	9	2000	0.76	40	102	80	8	2.1	26	2.9
	1	90	1.5	2000	0.76	40	2.5	11	3	5.6	41	5.7
TM NP 9 with Brine	1	90	4	2000	0.76	40	15	26	4	3.3	31	3.4
	1	90	6	2000	0.76	40	26	30	4.5	1.4	23	1.7
	1	90	9	2000	0.76	40	42	33	4	1.6	22	1.9
Lutensol XP-70	1	90	1.5	2000	0.87	24	no foam	x		x	x	x
	1	90	4	2000	0.87	24	no foam	x		x	x	x
	1	90	6	2100	0.88	24	14	16		6.9	90	10.2
	1	90	9	2300	0.89	24	115	90		6.3	41	7.2
	1	90	1.5	2000	0.76	40	no foam	x		x	x	x
	1	90	4	2100	0.77	40	3	5		26.5	115	23.7
	1	90	6	2200	0.78	40	15	17		6.9	42	7.5
	1	90	9	2300	0.79	40	90	70		varied	x	x
	1	90	1.5	2000	0.55	60	no foam	x		x	x	x
	1	90	4	2000	0.55	60	no foam	x		x	x	x
	1	90	6	2000	0.55	60	6	7		slugs	x	x
	1	90	9	2100	0.61	60	34	26		5	34	5.3
LA-EO_{12}	1	90	1.5	2000	0.87	24	no foam	x		x	x	x
	1	90	4	2000	0.87	24	no foam	x		x	x	x
	1	90	6	2100	0.88	24	12	14		4	61	7
	1	90	9	2100	0.88	24	29	23		2.6	49	4.6
	1	90	9	2100	0.58	60	no foam	x		x	x	x

Table C4: Continuation of Table C1.

Surfactant	C_{surf} % v/v	CO_2 % v/v	Q_{foam} ml/min	P psia	ρ_{CO2} g/ml	T °C	$\Delta P_{capillary}$ psia	η_{foam} cP	$\Delta P_{sandpack}$ psia	R_{avg} µm	D_{sm} µm	σ
C8:C14 Blend-$PO_{2.5}$-EO_7	0.5	90	1.5	2000	0.87	24	no foam	x	2	x	x	x
	0.5	90	4	2000	0.87	24	12	22	4	slugs	x	x
	0.5	90	4.5	2000	0.87	24	23	36	4	8.5	97	11.5
	0.5	90	6	1900	0.87	24	32	38	5	6.1	65	7.4
	0.5	90	7	2100	0.88	24	54	55	6	6	75	8.7
	0.5	90	9	2200	0.88	24	49	38	8	6.3	79	8.6
	0.5	90	1.5	1900	0.75	40	no foam	x	2	x	x	x
	0.5	90	4	1900	0.75	40	5	8	3	slugs	x	x
	0.5	90	6	2000	0.76	40	19	22	4	8.8	50	9.3
	0.5	90	9	2000	0.76	40	36	28	6	5.4	47	6.7
	0.5	90	9	2000	0.55	60	no foam	x	2	x	x	x
C12:C14 Blend-EO_7	1	90	1.5	2100	0.88	24	no foam	x		x	x	x
	1	90	9	2300	0.89	24	no foam	x		x	x	x
	1	90	9	2300	0.79	40	no foam	x		x	x	x
C_9-PO_4-EO_8	1	90	1.5	2000	0.87	24	4	16	4	3.6	28	4.4
	1	90	4	2000	0.87	24	67	117	7	1.7	24	2.3
	1	90	6	2000	0.87	24	134	156	9	1.7	34	2.8
	1	90	7	2000	0.87	24	189	147	11	2.4	33	3.3
	1	90	1.5	2000	0.76	40	22	103	5	2	30	2.9
	1	90	4	2000	0.76	40	57	100	6.5	1.6	22	2.1
	1	90	6	2000	0.76	40	84	99	7	1.3	18	1.7
	1	90	9	2000	0.76	40	143	112	9	1.4	54	2.9
C_9-$PO_{3.5}$-EO_8	1	90	1.5	2100	0.87	24	no foam	x		x	x	x
	1	90	4	2200	0.87	24	59	103		6	52	7.5
	1	90	6	2100	0.87	24	94	110		5.3	43	6.5
	1	90	9	2200	0.87	24	136	106		5.4	34	5.8
	1	90	1.5	2200	0.78	40	3	11		slugs	x	x
	1	90	4	2100	0.77	40	35	61		8.3	52	8.5
	1	90	6	2200	0.78	40	65	76		8.5	42	7.1
	1	90	9	2200	0.78	40	97	76		7.8	34	5.8
	1	90	4	2100	0.61	60	no foam	x		x	x	x
	1	90	6	2100	0.61	60	no foam	x		x	x	x
	1	90	9	2100	0.61	60	no foam	x		x	x	x

Table C5: Continuation of Table C1.

Surfactant	C_{surf} % v/v	CO_2 % v/v	Q_{foam} ml/min	P psia	ρ_{CO2} g/ml	T °C	$\Delta P_{capillary}$ psia	η_{foam} cP	$\Delta P_{sandpack}$ psia	R_{avg} µm	D_{sm} µm	σ
C_{11}-PO_2-EO_7	1	90	1.5	2000	0.87	24	no foam	x		x	x	x
	1	90	4	2000	0.87	24	38	66		8.1	68	11.5
	1	90	6	2000	0.87	24	67	79		7.9	53	9.6
	1	90	9	2000	0.87	24	118	92		5.5	39	6.4
	1	90	1.5	2200	0.78	40	no foam	x		x	x	x
	1	90	4	2100	0.77	40	32	57		9.5	62	11.6
	1	90	6	2200	0.78	40	52	61		7.2	46	8.3
	1	90	9	2200	0.78	40	70	54		4.9	32	5.6
	1	90	9	2100	0.61	60	no foam	x		x	x	x
C_{13}-$PO_{1.5}$-EO_6	1	90	1.5	2000	0.87	24	yes	x		x	x	x
	1	90	4	2000	0.87	24	11	19		3.1	69	6
	1	90	6	2100	0.88	24	26	31		4.4	52	6
	1	90	9	2100	0.88	24	47	37		5.3	37	5.5
	1	90	9	2000	0.55	60	no foam	x		x	x	x
1-Octanol-$PO_{4.5}$-EO_8	1	90	1.5	2000	0.87	24	no foam	x		x	x	x
	1	90	4	2300	0.89	24	5	8		slugs	x	x
	1	90	6	2100	0.88	24	30	35		8.6	57	9
	1	90	9	2200	0.88	24	73	57		5.9	39	5.8
	1	90	9	2300	0.79	40	50	38		slugs	x	x
	1	90	6	2300	0.79	40	no foam	x		x	x	x
1-Octanol-$PO_{4.5}$-EO_{12}	1	90	1.5	2000	0.87	24	no foam	x	2	x	x	x
	1	90	4	2000	0.87	24	3		6	slugs	x	x
	1	90	6	2000	0.87	24	2.2		7	slugs	x	x
	1	90	9	2000	0.87	24	2		9	slugs	x	x
	1	90	9	2000	0.76	40	no foam	x		x	x	x

Table C6: Continuation of Table C1.

Surfactant	C_{surf} % v/v	CO_2 % v/v	Q_{foam} ml/min	P psia	ρ_{CO2} g/ml	T °C	$\Delta P_{capillary}$ psia	η_{foam} cP	$\Delta P_{sandpack}$ psia	R_{avg} µm	D_{sm} µm	σ
1-Hexanol-Octene Oxide-EO_{12}	1	90	1.5	2000	0.87	24	3	12	4	4.2	17	1.9
	1	90	4	2000	0.87	24	50	88	9	2.1	26	2.3
	1	90	6	2000	0.87	24	33	39	11	1.6	23	1.8
	1	90	9	2000	0.87	24	18	14	14	1.3	29	1.7
	1	90	1.5	2000	0.76	40	11	52	6	4.2	32	8
	1	90	4	2000	0.76	40	57	101	8	2.4	19	8.7
	1	90	6	2000	0.76	40	61	71	9	1.8	23	5.8
	1	90	9	2000	0.76	40	23	18	15	1.7	19	2
	1	90	1.5	2000	0.55	60	no foam	x	4	x	x	x
	1	90	4	2000	0.55	60	no foam	x	4	x	x	x
	1	90	9	2000	0.55	60	no foam	x	4	x	x	x
	1	90	9	2000	0.45	70	no foam	x		x	x	x
1-Hex-PO_5-EO_9	1	90	1.5	1900	0.87	24	no foam	x	2	x	x	x
	1	90	4	1900	0.87	24	2	3	3	slugs	x	x
	1	90	6	2000	0.87	24	26	31	5	9.6	106	15.1
	1	90	9	2100	0.88	24	78	61	7	7	55	8.8
	1	90	1.5	1900	0.75	40	no foam	x	2	x	x	x
	1	90	4	1900	0.75	40	32	57	3	6.2	51	8.2
	1	90	6	2000	0.76	40	63	73	3	6.2	55	8.6
	1	90	9	2100	0.77	40	165	128	3	5.2	49	7
	1	90	9	2000	0.55	60	no foam	x	1	x	x	x
1-Hex-PO_5-EO_{11}	1	90	1.5	1900	0.87	24	no foam	x	2	x	x	x
	1	90	4	1900	0.87	24	7	12	3	19.3	79	14.2
	1	90	6	2000	0.87	24	41	49	4	13.6	66	12.3
	1	90	9	2100	0.88	24	140	109	7	7.7	56	8.9
	1	90	1.5	1900	0.75	40	10	47	1	8.1	52	9.3
	1	90	4	1900	0.75	40	41	71	2	7.9	36	6.7
	1	90	6	2000	0.76	40	80	94	3	6.5	29	5.2
	1	90	9	2200	0.78	40	123	96	5	6.1	27	4.8
	1	90	1.5	1900	0.51	60	no foam	x	1	x	x	x
	1	90	4	2000	0.55	60	23	41	2	12.7	59	11.4
	1	90	6	2000	0.55	60	30	35	2.5	10.5	46	9.1
	1	90	9	2000	0.55	60	72	56	3	6.7	35	6.3
	1	90	9	2000	0.45	70	no foam	x	1	x	x	x

Table C7: Continuation of Table C1.

Surfactant	C_{surf} % v/v	CO_2 % v/v	Q_{foam} ml/min	P psia	ρ_{CO2} g/ml	T °C	$\Delta P_{capillary}$ psia	η_{foam} cP	$\Delta P_{sandpack}$ psia	R_{avg} µm	D_{sm} µm	σ
1-Hex-PO_5-EO_{13}	1	90	1.5	1800	0.86	24	no foam	x	2	x	x	x
	1	90	4	1800	0.86	24	5	8	3	19.1	132	22.5
	1	90	6	1900	0.87	24	31	36	5	11.6	63	9.8
	1	90	9	2000	0.87	24	128	99	7	7.5	36	6.2
	1	90	1.5	1800	0.73	40	11	50	1	11	54	9.3
	1	90	4	1800	0.73	40	61	107	2	8.4	36	6.5
	1	90	6	2000	0.76	40	77	90	3	6.2	24	4
	1	90	9	2000	0.76	40	152	119	4.5	5.7	20	3.1
	1	90	1.5	1800	0.47	60	no foam	x	1	x	x	x
	1	90	4	1900	0.51	60	31	54	3	11.6	48	9
	1	90	6	1900	0.51	60	42	49	5	8	35	6.2
	1	90	9	2000	0.55	60	57	45	6	7.9	28	5.1
	1	90	9	1800	0.37	70	no foam	x	1	x	x	x
1-Hex-PO_5-EO_{15}	1	90	1.5	1800	0.86	24	no foam	6	2	x	x	x
	1	90	4	1800	0.86	24	6	10	3	12.2	134	32.2
	1	90	6	1900	0.87	24	39	46	5	6.6	80	22.4
	1	90	9	2000	0.87	24	133	74	7	5.1	72	11.8
	1	90	1.5	1800	0.73	40	no foam	26	1	x	x	x
	1	90	4	1800	0.73	40	56	97	2	4.7	32	7
	1	90	6	2000	0.76	40	74	87	3	5	25	4.1
	1	90	9	2000	0.76	40	162	126	6	3.1	20	4
	1	90	1.5	1800	0.47	60	no foam	49	1	x	x	x
	1	90	4	1900	0.51	60	33	57	2	9.4	63	18.4
	1	90	6	1900	0.51	60	47	55	2.5	5.3	37	9.3
	1	90	9	2000	0.55	60	100	78	3	4.2	22	5.1
	1	90	1.5	1800	0.37	70	no foam	22	4	x	x	x
	1	90	4	1900	0.41	70	28	48	4	12.7	61	19.1
	1	90	6	2000	0.45	70	50	59	5	8.7	52	13.2
	1	90	9	2000	0.45	70	66	52	5	4.9	39	8.4
2-Octanol-$PO_{5.5}$-EO_7	1	90	1.5	2400	0.90	24	14	64		3.7	46	4.4
	1	90	4	2400	0.90	24	64	113		4	40	4.6
	1	90	6	2500	0.90	24	110	129		3.3	47	5
	1	90	9	2600	0.69	60	no foam	x		x	x	x

Table C8: Continuation of Table C1.

Surfactant	C_{surf} % v/v	CO_2 % v/v	Q_{foam} ml/min	P psia	ρ_{CO2} g/ml	T °C	$\Delta P_{capillary}$ psia	η_{foam} cP	$\Delta P_{sandpack}$ psia	R_{avg} µm	D_{sm} µm	σ
2-Octanol-PO_9-EO_9	1	90	1.5	2000	0.87	24	34	161		3.7	46	4.4
	1	90	4	2000	0.87	24	71	125		3.9	40	4.6
	1	90	6	2000	0.87	24	119	140		3.5	47	5.1
	1	90	9	2000	0.87	24	>100	-		4.9	23	4.2
	1	90	1.5	2200	0.78	40	22	104		7.4	64	9.9
	1	90	4	2200	0.78	40	56	98		7.5	49	8.3
	1	90	6	2200	0.78	40	74	86		6.5	40	7.2
	1	90	9	2100	0.77	40	96	75		5.7	37	6.3
	1	90	9	2100	0.61	60	no foam	x		x	x	x
2EH-PO_2-EO_4	1	90	1.5	2100	0.88	24	no foam	x		x	x	x
	1	90	4	2100	0.88	24	no foam	x		x	x	x
	1	90	6	2100	0.88	24	8	10		5.8	63	8.5
	1	90	9	2100	0.88	24	28			5.6	74	9.2
	1	90	9	2100	0.77	40	7			7.5	84	7.1
	1	90	6	2100	0.77	40	no foam	x		x	x	x
	1	90	9	2100	0.58	60	no foam	x		x	x	x
2EH-PO_3-EO_3	1	90	1.5	1900	0.87	24	no foam	x		x	x	x
	1	90	4	1900	0.87	24	no foam	x		x	x	x
	1	90	6	1900	0.87	24	no foam	x		x	x	x
	1	90	9	2000	0.87	24	no foam	x		x	x	x
2EH-PO_5-EO_8	1	90	1.5	2000	0.87	24	9	44		3.4	51	4.8
	1	90	4	2100	0.88	24	56	98		3.7	52	5.9
	1	90	6	2100	0.88	24	75	88		4.8	39	5.6
	1	90	9	2100	0.88	24	112	87		4.8	38	6.1
	1	90	1.5	2000	0.76	40	5	21		3.2	26	3.5
	1	90	4	2100	0.77	40	39	69		4.1	50	5.8
	1	90	6	2100	0.77	40	35	41		4	50	5.7
	1	90	9	2100	0.77	40	59	46		4.4	34	5.1
	1	90	9	2100	0.58	60	no foam	x		x	x	x
2EH-EO_7-$PO_{5.5}$-EO	1	90	1.5	2100	0.88	24	no foam	x		x	x	x
	1	90	4	2100	0.88	24	no foam	x		x	x	x
	1	90	6	2300	0.89	24	81	95		-	x	x
	1	90	9	2300	0.89	24	136	106		-	x	x
	1	90	9	2200	0.61	60	no foam	x		x	x	x

Table C8: Continuation of Table C1.

Surfactant	C_{surf} % v/v	CO_2 % v/v	Q_{foam} ml/min	P psia	ρ_{CO2} g/ml	T °C	$\Delta P_{capillary}$ psia	η_{foam} cP	$\Delta P_{sandpack}$ psia	R_{avg} µm	D_{sm} µm	σ
2EH-PO_5-EO_9	1	90	1.5	1700	0.85	24	28	129	2	7.2	37	6.8
	1	90	4	1900	0.87	24	77	136	6	5	28	4.9
	1	90	6	2000	0.87	24	102	119	8	3.7	24	3.6
	1	90	7	2000	0.87	24	122	123	9	2.9	17	2.6
	1	90	9	1900	0.87	24	>200	>156	14	small	-	-
	1	90	1.5	1700	0.71	40	31	147	2.5	6.9	37	6.7
	1	90	4	1800	0.73	40	75	132	4	4.3	25	4.2
	1	90	6	1900	0.75	40	98	112	6.5	3.1	24	3.4
	1	90	9	2000	0.76	40	143	112	9	1.8	24	2.6
	1	90	9	1700	0.41	60	no foam	x	1	x	x	x
2EH-PO_5-EO_{11}	1	90	1.5	1700	0.85	24	26	120	2	slugs	x	x
	1	90	4	2000	0.87	24	104	182	3	3.2	19	3
	1	90	6	2200	0.87	24	163	190	4	1.7	13	1.7
	1	90	7	2400	0.90	24	173	174	5	1.8	10	1.5
	1	90	9	2400	0.90	24	>200	>156	6	-	-	-
	1	90	1.5	1800	0.73	40	30	141	2	6.9	45	7.9
	1	90	4	1900	0.75	40	42	72	2.5	3.8	27	3.7
	1	90	6	2000	0.76	40	82	96	3	3.4	46	4.3
	1	90	9	2300	0.79	40	192	149	5	1.2	6	0.8
	1	90	1.5	1700	0.41	60	6	26	2.5	slugs	x	x
	1	90	4	1800	0.47	60	34	60	4	8.3	41	8.1
	1	90	6	1800	0.47	60	43	50	6	7.6	40	7.8
	1	90	9	1800	0.47	60	51	40	7	4.7	28	4.9
	1	90	9	1700	0.33	70	no foam	x	1.5	x	x	x

Table C9: Continuation of Table C1.

Surfactant	C_{surf} % v/v	CO_2 % v/v	Q_{foam} ml/min	P psia	ρ_{CO2} g/ml	T °C	$\Delta P_{capillary}$ psia	η_{foam} cP	$\Delta P_{sandpack}$ psia	R_{avg} µm	D_{sm} µm	σ
2EH-PO_5-EO_{13}	1	90	1.5	1700	0.85	24	33	155	2	slugs	x	x
	1	90	4	1900	0.87	24	65	114	3	3.8	21	3.6
	1	90	6	2100	0.88	24	117	137	4	2.1	14	2.2
	1	90	7	2100	0.88	24	206	207	5	1.9	13	1.9
	1	90	9	2200	0.87	24	>240	>187	5	-	-	-
	1	90	1.5	1800	0.73	40	22	104	1	7.5	47	8.2
	1	90	4	1900	0.75	40	48	85	2	4.2	26	4.2
	1	90	6	2100	0.77	40	85	100	3	2.2	18	2.7
	1	90	9	2100	0.77	40	187	146	5	2.9	18	3.2
	1	90	1.5	1700	0.41	60	8	38	1	slugs	x	x
	1	90	4	1800	0.47	60	31	54	3	10.1	46	9.4
	1	90	6	1900	0.51	60	42	49	5	5.5	41	6.6
	1	90	9	1900	0.51	60	57	45	6	6.3	34	6.1
	1	90	1.5	1700	0.33	70	no foam	x	1	x	x	x
	1	90	4	1700	0.33	70	no foam	x	2	x	x	x
	1	90	6	1700	0.33	70	no foam	x	2	x	x	x
	1	90	9	1800	0.37	70	no foam	x	1	x	x	x
2EH-PO_5-EO_{15}	1	90	1.5	1700	0.85	24	24	111	2	6	32	5.7
	1	90	4	2000	0.87	24	77	135	4	4.7	26	4.3
	1	90	6	2100	0.88	24	131	153	5	3.7	22	3.7
	1	90	7	1900	0.88	24	145	146	6	2.1	15	2.3
	1	90	9	2100	0.87	24	>200	-	-	-	-	-
	1	90	1.5	1700	0.73	40	10	46	1.5	7.4	32	6
	1	90	4	1800	0.75	40	59	103	3	4.3	25	4.1
	1	90	6	2000	0.77	40	120	140	4	4.8	26	4.2
	1	90	9	2100	0.77	40	152	119	6	1.7	9	1.4
	1	90	1.5	1600	0.36	60	17	79	2.5	slugs	x	x
	1	90	4	1800	0.47	60	37	64	3	7	55	8.6
	1	90	6	1800	0.47	60	48	57	3.5	5.5	35	6.2
	1	90	9	2000	0.55	60	90	70	5	2.8	24	4.3
	1	90	1.5	1700	0.33	70	no foam	x	1	x	x	x
	1	90	4	1700	0.33	70	36	63	3	10.5	41	9.5
	1	90	6	1700	0.33	70	46	53	4.5	6.1	38	6.8
	1	90	9	1800	0.37	70	70	53	6	4.5	36	5.2

Table C10: Continuation of Table C1.

Surfactant	C_{surf} % v/v	CO_2 % v/v	Q_{foam} ml/min	P psia	ρ_{CO2} g/ml	T °C	$\Delta P_{capillary}$ psia	η_{foam} cP	$\Delta P_{sandpack}$ psia	R_{avg} µm	D_{sm} µm	σ
2EH-PO_9-EO_9	1	90	1.5	1900	0.88	24	21	99		5.5	46	7
	1	90	4	2300	0.89	24	68	119		4	40	4.6
	1	90	6	2400	0.90	24	124	145		5.9	27	5
	1	90	9	2300	0.91	24	>100	-		3.9	24	3.9
	1	90	1.5	2000	0.76	40	18	87		3.7	46	4.4
	1	90	4	2000	0.76	40	44	77		4	40	4.6
	1	90	6	2100	0.77	40	66	78		3.5	47	5.1
	1	90	9	2100	0.77	40	135	105		3.6	21	3.4
	1	90	9	2100	0.61	60	no foam	x		x	x	x
2EH-PO_{12}-EO_{11}	1	90	1.5	2100	0.87	24	37	172		5.9	36	6.2
	1	90	4	2000	0.87	24	69	121		5.9	29	5.1
	1	90	6	2100	0.87	24	115	135		4.5	20	3.3
	1	90	9	2200	0.87	24	144	112		4.2	20	3.4
	1	90	1.5	2200	0.78	40	no foam	x		x	x	x
	1	90	4	2100	0.77	40	35	62		4.4	71	7.9
	1	90	6	2200	0.78	40	47	55		4.4	47	7.1
	1	90	9	2200	0.78	40	80	62		4.6	35	5.5
	1	90	9	2100	0.61	60	no foam	x		x	x	x
2EH-EO_5 coalesces	1	90	1.5	2000	0.87	24	no foam	x	1.5	x	x	x
	1	90	4	2000	0.87	24	7	12	5	2.9	32	3.3
	1	90	6	2000	0.87	24	16	19	6	2.5	26	3.1
	1	90	9	2000	0.87	24	8	6	8	2.4	48	3.8
	1	90	1.5	2000	0.76	40	2	9	2	6.9	192	11.7
	1	90	4	2000	0.76	40	2	3	3	4	41	5.3
	1	87	4	2000	0.76	40	2	2	3	4.2	50	5.2
	1	87	6	2000	0.76	40	2	2	3	3.8	48	4.7
	1	87	9	2000	0.76	40	8	6	3.5	3.6	37	4.4
	1	90	9	2000	0.55	60	no foam	x		x	x	x

Table C11: Continuation of Table C1.

Surfactant	C_{surf} % v/v	CO_2 % v/v	Q_{foam} ml/min	P psia	ρ_{CO2} g/ml	T °C	$\Delta P_{capillary}$ psia	η_{foam} cP	$\Delta P_{sandpack}$ psia	R_{avg} µm	D_{sm} µm	σ
2EH-$EO_{11.8}$ coalesces	1	90	1.5	2000	0.87	24	1	2	2	5.5	66	8.5
	1	90	4	2000	0.87	24	19	34	4	4.6	66	7.9
	1	90	6	2000	0.87	24	51	60	6	2.0	39	4.6
	1	90	9	2000	0.87	24	30	23	8	2.3	48	4.7
	1	90	1.5	2000	0.76	40	1.5	7	2	4.7	25	4
	1	90	4	2000	0.76	40	24	41	4	2.0	27	3.9
	1	90	6	2000	0.76	40	42	49	5	1.8	28	2.8
	1	90	9	2000	0.76	40	55	43	6	1.6	21	2.3
	1	90	1.5	2000	0.55	60	no foam	x	1	x	x	x
	1	90	4	2000	0.55	60	5.5	10	2	3.0	19	2.7
	1	90	6	2000	0.55	60	37	43	2.5	1.9	25	2.8
	1	90	9	2000	0.55	60	67	52	3	1.7	27	2.7
	1	90	1.5	2000	0.45	70	no foam	x	1	x	x	x
	1	90	4	2000	0.45	70	12	21	2	4.5	37	5.1
	1	90	6	2000	0.45	70	35	40	2	3.1	35	4.4
	1	90	9	2000	0.45	70	12	10	2	2.3	27	3.5
2EH-$PO_{4.5}$-EO_8 with Brine	1	90	1.5	2200	0.88	24	10	47		6.8	52	8.6
	1	90	4	2100	0.88	24	53	93		6.6	42	7.3
	1	90	6	2200	0.88	24	96	112		5.9	30	5.5
	1	90	9	2400	0.90	24	181	141		4.3	26	4.5
	1	92	1.5	2200	0.78	40	12	55		7.5	46	8.6
	1	92	4	2200	0.78	40	64	112		5.3	32	5.7
	1	92	6	2300	0.79	40	127	149		3.9	25	4.2
	1	92	9	2400	0.80	40	213	166		4.1	25	4.4
	1	95.1	4	2200	0.61	60	no foam	x		x	x	x
	1	95.1	6	2200	0.61	60	13	15		7.5	57	8.7
	1	95.1	9	2200	0.61	60	33	25		3.6	153	9.2

Table C12: Continuation of Table C1.

Surfactant	C_{surf} % v/v	CO_2 % v/v	Q_{foam} ml/min	P psia	ρ_{CO2} g/ml	T °C	$\Delta P_{capillary}$ psia	η_{foam} cP	$\Delta P_{sandpack}$ psia	R_{avg} µm	D_{sm} µm	σ
2EH-$PO_{4.5}$-EO_8	1	90	1.5	2200	0.88	24	23	106		8.1*	53	8.1
	1	90	4	2300	0.89	24	80	140		4.1	34	4.8
	1	90	6	2500	0.90	24	>100	>117		5.2	31	4.7
	1	90	9	2700	0.91	24	>100	>78		4.1	20	3.3
	1	90	1.5	2300	0.79	40	14	64		6.1	37	6.4
	1	90	4	2300	0.79	40	62	108		6.5	41	7
	1	90	6	2300	0.79	40	87	101		5.3	28	4.9
	1	90	9	2400	0.80	40	>100	>78		6	28	4.9
	1	90	4	2400	0.65	60	no foam	x		x	x	x
	1	87.7	6	2400	0.65	60	22	26		7.7*	61	8.4
	1	91.8	9	2300	0.63	60	41	32		4.8	34	5.4
	1	90	1.5	2200	0.88	24	17	80		7.5	53	8.7
	1	90	4	2300	0.89	24	64	112		6.2	35	6.1
	1	90	6	2300	0.89	24	107	125		5.7	27	4.8
	1	90	9	2400	0.90	24	201	157		4.5	23	4
	1	92	1.5	2000	0.76	40	7	33		14.4	60	12.4
	1	92	4	2000	0.76	40	53	93		6.7	36	6.6
	1	92	6	2300	0.79	40	129	151		2.8	16	2.5
	1	92	9	2300	0.79	40	212	165		2.3	15	2.1
	1	95.1	6	2200	0.61	60	77	90		5.2	34	5.6
	1	95.1	9	2100	0.58	60	218	170		4.3	25	4.2
DOG-EO_{12} with Brine	1	90	1.5	2000	0.87	24	18	82		slugs	x	x
	1	90	4	2100	0.88	24	59	104		6.1	43	7.2
	1	90	6	2200	0.88	24	99	116		5.4	32	5.6
	1	90	9	2300	0.89	24	169	132		3.9	19	3.2
	1	92	1.5	2200	0.78	40	no foam	x		x	x	x
	1	92	4	2100	0.77	40	no foam	x		x	x	x
	1	92	6	2100	0.77	40	no foam	x		x	x	x
	1	92	9	2200	0.78	40	12			slugs	x	x
	1	95.4	9	2100	0.61	60	no foam	x		x	x	x

Table C13: Continuation of Table C1.

Surfactant	C_{surf} % v/v	CO_2 % v/v	Q_{foam} ml/min	P psia	ρ_{CO2} g/ml	T °C	$\Delta P_{capillary}$ psia	η_{foam} cP	$\Delta P_{sandpack}$ psia	R_{avg} µm	D_{sm} µm	σ
DOG-EO_{12}	1	90	1.5	2600	0.91	24	no foam	x		x	x	x
	1	90	3	2800	0.92	24	43	101		6.5	62	7.5
	1	90	4	2800	0.92	24	59	104		5	34	5.1
	1	90	6	2800	0.92	24	99	116		4.8	30	4.8
	1	90	1.5	2900	0.82	40	yes	-		x	x	x
	1	90	4	2900	0.82	40	yes	-		x	x	x
	1	88.8	6	3300	0.86	40	63	74		5.1	48	5.9
	1	88.8	9	3300	0.86	40	99	115		3.7	34	4.5
	1	90	6	3500	0.78	60	14			8.4		8.1
	1	87.4	6	3700	0.77	65	no foam	x		x	x	x
	1	87.4	9	3700	0.77	65	5			13.2		
	1	90	6	3500	0.70	75	no foam	x		x	x	x
	1	90	9	3500	0.70	75	no foam	x		x	x	x
	1	90	1.5	2000	0.87	24	3	15		8.4	53	10.1
	1	90	4	2100	0.88	24	35	61		5.7	41	6.9
	1	90	6	2200	0.88	24	78	91		4.5	32	5.1
	1	90	9	2300	0.89	24	128	100		3.1	18	2.8
	1	92	1.5	2000	0.76	40	no foam	x		x	x	x
	1	92	4	2100	0.77	40	10	18		6.8	49	8.1
	1	92	6	2000	0.76	40	16	19		5.1	37	5.6
	1	92	9	2000	0.76	40	26	20		4.1	27	4.1
	0.25	90	1.5	1900	0.87	24	no foam	x		x	x	x
	0.25	90	4	1900	0.87	24	no foam	x		x	x	x
	0.25	90	6	1950	0.87	24	37	43		slugs	x	x
	0.25	90	9	1950	0.87	24	43	33		slugs	x	x
	0.25	90	7	2100	0.87	24	40	40		slugs	x	x

Table C14: Continuation of Table C1.

Surfactant	C_{surf} % v/v	CO_2 % v/v	Q_{foam} ml/min	P psia	ρ_{CO2} g/ml	T °C	$\Delta P_{capillary}$ psia	η_{foam} cP	$\Delta P_{sandpack}$ psia	R_{avg} µm	D_{sm} µm	σ
DOG-EO_{12}	0.5	90	1.5	2200	0.88	24	4	20		slugs	x	x
	0.5	90	4	2100	0.87	24	34	59		7.1	93	12.3
	0.5	90	6	2100	0.87	24	34	39		4.8	78	8
	0.5	90	9	2200	0.88	24	34	27		3.7	79	6.7
	0.5	75	4	2200	0.88	24	14	24		21.9		19.7
	0.5	80	4	2200	0.88	24	15	26		22.4		20.2
	0.5	85	4	2200	0.88	24	20	36		11.1		15.5
	0.5	87	4	2200	0.88	24	20	35		6.7		10.3
	0.5	89	4	2200	0.88	24	43	76		4.8		8
	0.5	91	4	2200	0.88	24	54	95		4.1		5.7
	0.5	93	4	2200	0.88	24	45	79		4.4		8.5
	0.5	95	4	2200	0.88	24	9	15		12		18.4
	0.5	90	1.5	2200	0.78	40	no foam	x		x	x	x
	0.5	90	4	2200	0.78	40	14	25		Slugs	x	x
	0.5	90	6	2200	0.78	40	39	45		3.5	41	4.4
	0.5	90	9	2200	0.78	40	57	44		4.2	37	4.8
	0.5	90	1.5	3800	0.89	40	no foam	x		x	x	x
	0.5	90	4	3700	0.88	40	28	48		slugs	x	x
	0.5	90	6	3800	0.89	40	41	48		5.3	43	6.5
	0.5	90	9	3700	0.88	40	41	32		4.9	44	6.4

Appendix D: Stable Colloidal Dispersions of a Lipase-Perfluoropolyether Complex in Liquid and Supercritical Carbon Dioxide

The technique of hydrophobic ion pairing has been used to solubilize the lipase from Candida rugosa in a fluorinated solvent, perfluoromethylcyclohexane (PFMC), in complex with a perfluoropolyether (PFPE) surfactant, KDP 4606. The enzyme-surfactant complex was determined to have a hydrodynamic diameter of 6.5 nm at atmospheric pressure by dynamic light scattering indicating that a single lipase molecule is stabilized by surrounding surfactant molecules. The complex formed a highly stable colloidal dispersion in both liquid and supercritical carbon dioxide at high CO_2 densities (> 0.92 and 0.847 g/mL, respectively), with 4 % by volume PFMC as a co-solvent, yielding a fluid that was orange, optically translucent, and very nearly transparent. Dynamic light scattering demonstrated aggregation of the enzyme-surfactant complexes in CO_2 at 25 and 40 ºC and various pressures (2000 - 5000 psia) with hydrodynamic diameters ranging from 50 to 200 nm. The mechanism by which the enzyme-surfactant particles aggregate is shown to be via condensation due to very low polydispersities as characterized by the size distribution moments. Interparticle interactions were investigated with respect to density and temperature, and it was shown that on decreasing the CO_2 density, the particle size increases, and the stability against settling decreases. Particle size also decreases as the temperature is increased to 40 ºC, at constant CO_2 density. Nanoparticle aggregates of an enzyme-surfactant complex in CO_2, which are nearly optically transparent and stable to settling, are a promising new alternative to previous types of dispersions of proteins in CO_2 that either required water/CO_2 microemulsions or were composed of large particles unstable to settling.

D.1 INTRODUCTION

Since the first report in the field of biocatalysis by Randolph et al.,[236] over two decades ago, there have been many advances in the field of biocatalysis in supercritical fluids (SCFs) and these have been recently reviewed in detail.[237] Due to the relatively low activity of crude preparations of enzymes in SCFs, many attempts have been made to utilize a stabilized form of an enzyme for use in such solvents. Examples include the use of immobilized enzymes,[238,239] lipid-coated enzymes,[240] sol-gels,[241] cross-linked enzyme crystals (CLECs),[242] cross-linked enzyme aggregates (CLEAs),[243,244] the use of reverse micelles or microemulsions,[48,245] and the use of whole cells.[246] More recently, a new approach for the dispersion of enzymes in supercritical carbon dioxide ($scCO_2$) has been described.[247] The technique of hydrophobic ion pairing (HIP) has previously been used to solubilize proteins in organic solvents by ion pairing between an anionic surfactant such as Aerosol OT (AOT) or sodium dodecyl sulfate (SDS), with the cationic residues (Lysine, Arginine and Histidine) on the surface of the protein.[248-250] In the case of enzymes, enhanced catalytic activity has been demonstrated.[250-254]

Here, the HIP method is adapted by using a CO_2-soluble perfluoropolyether (PFPE) surfactant to modify the surface of the enzyme forming an enzyme-surfactant complex soluble in fluorinated solvents and dispersible in $scCO_2$.[247] Two biomolecules, cytochrome c (Cc) and α-chymotrypsin (CMT) were readily ion paired with the fluorinated surfactant KDP 4606 and were shown to form either solutions or dispersions in perfluoromethylcyclohexane (PFMC) and in $scCO_2$ which were optically clear to the naked eye, in all cases. Dynamic light scattering (DLS) measurements were performed on KDP and these complexes in PFMC to determine the aggregate size. The mode

diameter of Cc-KDP was revealed to be 21.2 nm (c.f. Cc hydrodynamic radius of 1.78 nm by NMR[255]) and the mode diameter for CMT-KDP is 11.7 nm (c.f. CMT diameter 3.4 nm by x-ray diffraction[256]). Hence, it was suggested that both complexes contain small aggregates of protein molecules surrounded by surfactant. To the best of our knowledge, this is one of only a few reports to determine the diameter of HIP complexes using DLS. Paradkar *et al.* determined the diameter of CMT-AOT HIP complexes in isooctane at 6.8 nm and suggest that this is consistent with a spherical complex of a CMT ion pairing with AOT molecules.[251] Also, more recently, Akbar *et al*.[257] reported a direct solubilization of enzyme aggregates in nonaqueous media. In particular, subtilisin Carlsberg extracted with AOT into isooctane was shown to have a diameter of 6.1 nm and, on average, there was one protein molecule within the complex. This is in contrast to the larger diameter of 26.1 nm for reverse micelles (average number of protein molecules not determined).[257] It is anticipated that the higher the number of enzyme molecules per complex, the lower the number of active sites that will be available for catalysis. The flux of substrate to and product away from individual active sites is also likely to be restricted inside the aggregates. Future studies will determine if there is any correlation between surfactant-enzyme aggregate size and catalytic turnover.

Due to the insolubility of crude enzymes and many stabilized forms of enzymes in CO_2, there has been no opportunity for studying the size and aggregation mechanisms of these molecules in this high-pressure solvent. However, recent advances using the HIP methodology to disperse biomolecules in CO_2 using a PFPE surfactant[247] present us with the challenge of investigating these parameters with respect to the dispersed biomolecules under high pressure CO_2. Small changes in the system temperature and/or pressure can significantly affect the interactions between the solvent molecules and the stabilizing

PFPE ligands, which in turn will affect the steric stabilization of colloids,[258] such as these enzyme-surfactant complexes, and can result in aggregation.

Aggregation of colloids in CO_2 has been studied in systems using the techniques of light scattering,[218] turbidimetry,[126,127,259] optical microscopy,[35,260] X-ray scattering,[195,261] and neutron scattering.[234] In particular, flocculation and attractive interactions have been observed in many types of PFPE-stabilized colloidal systems such as water-in-CO_2 (W/C) emulsions,[35] W/C microemulsions,[234] hydrophilic silica,[14] and gold nanocrystals.[261] For example, Lee *et al.* investigated a W/C microemulsion stabilized with a PFPE-based surfactant and reported that, even at high CO_2 densities, the interaction strength measured by SANS exceeded the known value for water-in-alkane microemulsions.[234] Indeed, when longer PFPE chains were used a stronger stabilization was observed yet the attractive interactions were not entirely overcome,[35] indicating the strength of the attractive droplet interactions in CO_2 even when stabilized by a PFPE surfactant. In addition, aggregation of PFPE-coated gold nanocrystals in supercritical CO_2 was also observed by Saunders *et al.* using SAXS.[261] Reversible aggregation of the gold nanocrystals, also known as clustering, was observed at all investigated CO_2 densities due to relatively strong interparticle interactions. The attractive interactions between gold clusters, as described by the structure factor S(q), became stronger as the density decreased. Recently, Dickson et. al.[218] measured the density dependence of interactions in CO_2 between core-shell particles with silica cores and a porous cross-linked fluoro-silica shell by DLS. The particles with diameters on the order of a few hundred nanometers could be dispersed at 25 ºC at the vapor pressure of liquid CO_2 and the aggregate size increased with a decrease in the density of CO_2.

Here, we demonstrate the extraction of lipase from *Candida rugosa* (CRL) into a fluorinated solvent, PFMC, by means of HIP with the anionic PFPE surfactant, KDP

4606. Dynamic light scattering (DLS) measurements of CRL-KDP dispersions in PFMC at atmospheric pressure were compared with those in high pressure CO_2, as a function of temperature and pressure, to illustrate marked differences in the sizes of aggregates. Aggregates of the CRL-KDP molecules were greater than 50 nm in size, even at the highest CO_2 densities, where the dispersion appeared nearly transparent to the naked eye. In addition, the stability of the aggregates, based on changes in diameter with time, and the reversibility of aggregation with changes in pressure are reported. The moments of the size distribution are analyzed to determine how much of the aggregation is caused by condensation of protein molecules relative to coagulation. Thus, the mechanism of aggregation of HIP enzyme-surfactant complexes in CO_2 is elucidated.

D.2 EXPERIMENTAL METHODS AND MATERIALS

D.2.1 Materials

Lipase from *Candida rugosa* (CRL, type VII, E.C. 3.1.1.3, 1,140 U/mg) was purchased from Sigma-Aldrich and the protein content was determined as 16 % w/w by the bicinchoninic acid assay.[255] The perfluoropolyether surfactant KDP 4606 (KDP, mw ~1400) was kindly donated by DuPont and perfluoromethylcyclohexane (PFMC) was purchased from Fluorochem. Research grade CO_2 (Matheson) was used in all experiments and was filtered through an oxygen trap prior to introduction to the system.

D.2.2 Determination of Critical Micelle Concentration of KDP 4606 in PFMC

The method used to determine the critical micelle concentration (cmc) of fluorinated surfactants using UV-visible spectroscopy has been described previously.[262] Solutions of KDP (5 - 70 mM) in PFMC (1 mL) were stirred with 10 mM sodium phosphate buffer (1 mL, pH 7.0) at 500 rpm for 10 min and then centrifuged at 8000 rpm for two min to allow phase separation to occur. The lower fluorous phase was collected and the concentration of surfactant was analyzed by measuring the absorbance at 240 nm at room temperature using an Agilent 8453 UV spectrophotometer. This measurement was repeated in triplicate. By plotting absorbance against concentration of KDP it was possible to determine the cmc of KDP in PFMC as 48.4 mM at room temperature, the maximum on the graph shown in Figure D1.

D.2.3 Preparation of CRL-KDP

The preparation of protein-surfactant complexes has previously been described.[247] CRL (an off-white colored powder) dissolved in 10 mM sodium phosphate buffer, pH 7.0 (0.14 mM, 10 mL) was stirred with KDP dissolved in PFMC (23 mM, 5 mL) at 100 rpm for 10 min. The ratio of protein to surfactant was 1:2 w/w and KDP concentration was kept below its cmc (49.2 mM). The two resulting phases were left to separate overnight. CRL-KDP in the lower fluorous phase was collected and CRL content analysed by measuring UV absorbance at 280 nm (CRL-KDP ε_{280} = 47,500 $M^{-1}cm^{-1}$).[243]

The water content of the CRL-KDP complex in PFMC was analyzed by the Karl Fischer coulometric method and was found to be below the detection level of instrument (< 1 ppm). The known water content of samples could be accurately determined indicating that neither the PFMC nor the CRL-KDP complex interfered with the measurement.

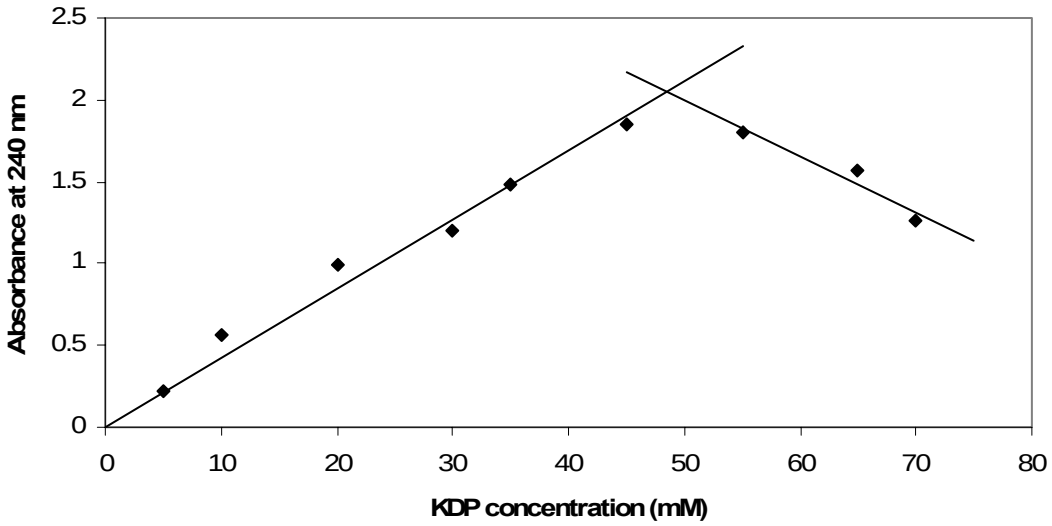

Figure D1: Determination of the cmc for KDP 4606 by UV/Vis absorption. Intersection of the two lines occurs at 48.4 mM, i.e. 48.4 mM is the cmc for KDP.

D.2.4 DLS at Atmospheric Pressure

DLS measurements at atmospheric pressure were carried out on a Zetasizer Nano S at Malvern Instruments. The instrument contains a 4 mW He-Ne laser operating at a wavelength of 633 nm. Each sample was filtered through a 0.2 μm filter (Whatton) prior to measurements, which were made at a detection angle of 173 ° (i.e. backscatter) and 20 °C. The particle size was taken as a mean value of three measurements. CRL (0.02 mM) dissolved in aqueous buffer, CRL-KDP (0.02 mM, protein concentration) and KDP (14 mM) dissolved in PFMC were measured. The data was analyzed using Auto:CONTIN[263] with the following fixed parameters: refractive index 1.333 (water), 1.277 (PFMC), 1.4 (surfactant) and 1.45 (protein) and viscosity (cP) 1.0019 (water) and 1.561 (PFMC).[264-266]

D.2.5 CRL-KDP Dispersion in CO_2

A protein dispersion was formed by adding CRL-KDP in PFMC (1.7 mM protein concentration, 0.95 mL) and CO_2 (~20 g) into a high pressure variable volume view cell (VVVC) described elsewhere.[267] The addition of the CRL-KDP sample to CO_2 as a dispersion in PFMC avoided drying, which is known to cause irreversible aggregation of colloids, as was also demonstrated in a recent study of colloidal interactions between silica particles in CO_2.[218] The amount of PFMC in the system was 4 % by volume and CRL-KDP was 0.42 % by weight of the total system. The contents of the high-pressure view cell were continuously mixed with a magnetic Teflon stir bar. The cell was heated to 25 °C and the pressure was increased to approximately 5000 psia by decreasing the volume of the cell using the hydraulic pump. The pressure was decreased slowly by

increasing the cell volume and visual observations were recorded. The procedure was repeated at 40 °C.

D.2.6 DLS in CO_2

A CRL-KDP dispersion in CO_2 was formed as described above, in a high-pressure VVVC suitable for carrying out DLS measurements as described elsewhere.[4,42] Briefly, a high-pressure VVVC was connected to a high pressure homogenizer (Avestin, model C-5), providing recirculation of the cell contents, which was connected to a scattering cell, which in turn was connected back to the VVVC. No filter was used within the system, as the aggregates tend to plug up filters. System temperature was controlled to ± 0.1 °C by immersing the view cell and homogenizer in water baths equipped with temperature controllers (Julabo, Inc). Recirculation lines were maintained at the desired temperature through the use of water-jackets; all other lines were insulated. The scattering cell was insulated with heating tape and temperature controlled to ± 0.1 °C by a digital controller (Micromega, model CN76000).

The protein dispersion was formed at 25 ºC and the system was pressurized to 5000 psia. The dispersion was re-circulated through the scattering cell for 3-5 minutes. The pressure drop across the homogenizing valve was 5000 psia. The scattering cell was isolated and equilibrated for ≥ 2 minutes to minimize convection currents. DLS scans were taken over 5-10 minutes and the measurements were conducted at least three times. The coherent light source was a 17 mW He-Ne laser at a wavelength of 632.8 nm, and the scattered light was collected by a collimator (NSG America, SELFOC microlens, 1.8 mm diameter, 0.25 pitch) coupled to an optical fiber (NSG America, single mode, specified wavelength of 630 nm), and detected by an avalanche photodiode (system designed by Brookhaven Instr.). A digital autocorrelator (Brookhaven Instruments

Corporation, model BI-9000AT) with 522 real time channels and non-negative least squares (NNLS) program were used to analyze the data and the measured detection angle was 15°. DLS measurements were repeated at various decreasing and increasing pressures. The temperature was increased to 40 ºC and the measurements were repeated in the same way. The measurements were also repeated at 25 ºC over 5 days. The polydispersity of each measurement was calculated (standard deviation as a percentage of CRL-KDP mean diameter).

D.2.7 Reversibility Study

CRL-KDP aggregation was examined for reversibility by subjecting the dispersion to large rapid changes in pressure. DLS measurements were conducted at 5000 psia and 25 °C, following ~3 minutes shearing by the homogenizer. The system was rapidly depressurized to 1000 psia. After 30 minutes at this pressure, the system was rapidly pressurized back to 5000 psia and sheared for 2 minutes before taking further DLS measurements.

D.2.8 Stability Study

CRL-KDP stability in CO_2 was investigated under the following conditions: 5000 psia/25 °C; 3350 psia/25 °C; 5000 psia/40 °C; and 3325 psia/40 °C. The dispersion was re-circulated for 5 minutes with the homogenizer, the scattering cell was then isolated and a series of 10-minute DLS scans were conducted over a 90-minute period, with no further re-circulation. Each time point was defined as the start of each scan (i.e. 0, 10, 20 etc. minutes). DLS intensity was normalized by dividing the intensity at each time point by the initial intensity for ease of comparison.

D.3 RESULTS

D.3.1 DLS at Atmospheric Pressure

DLS measurements for CRL in aqueous solution and KDP and CRL-KDP in PFMC were conducted on a Malvern Zetasizer Nano and are shown in Figure D2. CRL, a hydrophobic protein, is likely to aggregate and form large particles on dispersion in aqueous medium as shown by a mode diameter of 10.1 nm and high polydispersity. However, on solubilizing CRL in PFMC by means of ion pairing with the highly fluorinated surfactant KDP, the enzyme is stabilized as a single molecule surrounded by surfactant as seen by a mode diameter of 6.5 nm (c.f. literature maximum CRL diameter 5 nm).[268] The measurements were repeated using a BI-ZetaPlus DLS instrument (Brookhaven Instruments Corporation) and CRL-KDP was shown to be approximately 6.5 nm demonstrating excellent reproducibility of results. The CRL-KDP complex in PFMC was transparent and brown in color.

D.3.2 Dispersion Formation in CO_2

Figure D3 shows a series of photographs of the CRL-KDP dispersion in PFMC/CO_2 at 25 ºC in a custom made variable volume view cell (VVVC).[267] At higher pressures (> 3500 psia) the majority of the CRL-KDP complex was dispersed giving a characteristic orange translucent state (5050 psia, Figure D3). It is thought that the saturation point of the complex in this particular system was reached due to the observation of a few particles on the bottom of the cell that settled. Clearly, it was not

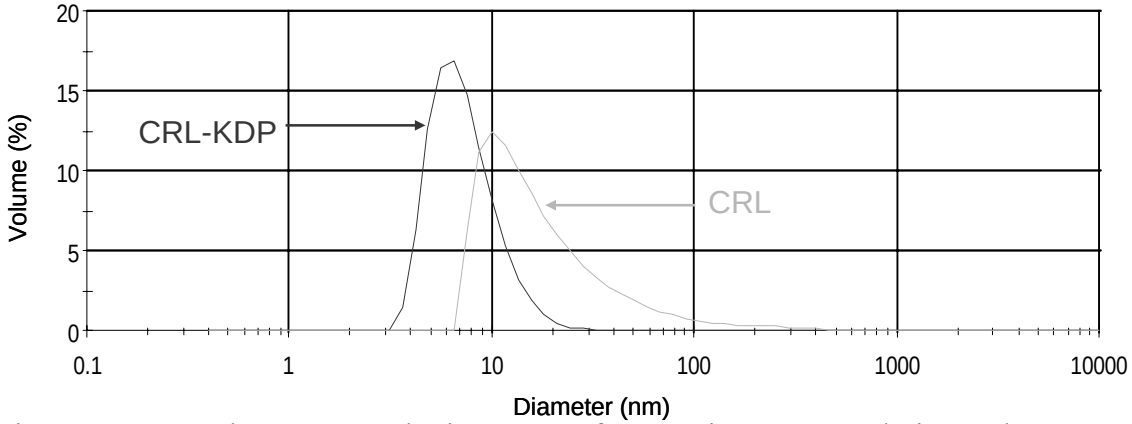

Figure D2: DLS data at atmospheric pressure for CRL in aqueous solution and CRL-KDP in PFMC.

possible to determine with the naked eye whether the individual protein chains were dissolved at the molecular level, as in the case of PFMC, or if the chains formed some type of dispersed aggregates that scattered light. It would be difficult to predict which of these possibilities is more likely from previous studies of related colloids in CO_2. Potential factors that disfavor dissolution of individual molecules are the relatively high molecular weight of the CRL-KDP complex and the unusually weak solvent strength of CO_2 for stabilizing attractive interactions between droplets in water/CO_2 microemulsions of similar size that are stabilized by PFPE surfactants.[234]

On decreasing the pressure below 3000 psia, aggregates were likely to be present as indicated by an orange hazy state. Further decrease in pressure resulted in significant particle growth yielding a highly turbid state below 2700 psia with particles depositing on the cell window at a much lower pressure (2150 psia, Figure D3). The aggregation process was demonstrated to be reversible, shown by an increase in dispersibility on increasing pressure and vice versa.

On increase of temperature to 40 ºC, i.e. supercritical conditions, similar observations were made. Complete dispersion of small aggregates (no settled particles observed) and an orange translucent state were obtained at higher pressures, suggesting that temperature as well as pressure plays an important role in the morphology of aggregates of CRL-KDP in CO_2. An orange hazy state was observed at 3300 psia and a highly turbid state at 3050 psia and below, slightly higher in pressure than that for the system at 25 ºC.

Following depressurization of the cell a small volume of PFMC (3.35 mL) was added to re-solubilize the remaining CRL-KDP complex. The CRL-KDP protein concentration was determined by UV/Vis spectroscopy as 16.5 mg/mL; hence, total mass recovered was 56 mg, 37 mg less than the starting mass. On dismantling the VVVC, an

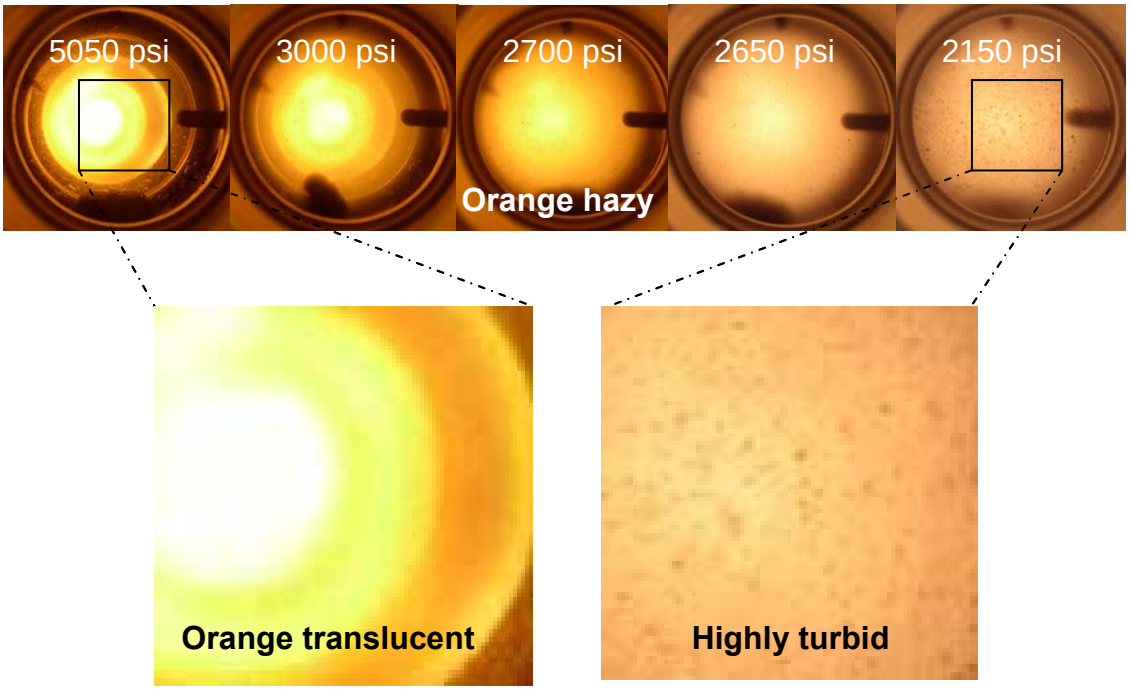

Figure D3: CRL-KDP states in the variable volume view cell (VVVC) at 25 °C at various pressures. At higher pressures CRL-KDP is almost fully soluble, the cell is observed to be orange translucent. Decreasing pressure results in a gradual decrease in CRL-KDP solubility indicated by cloudiness or orange hazy state at around 2700 psi. Below 2650 psi CRL-KDP particles start to precipitate and can be seen to deposit on the cell window yielding a highly turbid state.

off-white colored powder was observed on the back window of the cell. This was shown to be native CRL by its catalytic activity and excellent enantioselectivity for the esterification reaction of *rac*-1-phenylethanol with vinyl acetate. Both observations suggest that some of the CRL-KDP underwent a de-complexation process when under CO_2 pressure.

D.3.3 DLS in CO_2

CRL-KDP was dispersed in CO_2 in a high-pressure VVVC suitable for carrying out DLS measurements.[4,42] Similar observations were made at 25 and 40 ºC as described above and can be seen in Table D1 alongside the DLS data for each pressure and temperature. Changes in the CRL-KDP size distribution over a period of days at 25 °C were also investigated.

The autocorrelation function plot for four different CO_2 conditions is displayed in Figure D4. A single exponential decay was observed, and the NNLS fit to the autocorrelation function is displayed. Similar curves were observed at the other CO_2 conditions investigated (not shown). These results indicate relatively low polydispersity and the changes in the diffusion coefficient of the particles are observable with changes in solvent conditions.

The mean diameters of the CRL-KDP particles as a function of CO_2 density were determined from DLS measurements as shown in Figure D5. Interestingly, the mean diameter for CRL-KDP dispersed in CO_2 (Table D1 and Figure D5) is over 10 fold greater than that of CRL-KDP in PFMC (6.5 nm, Figure D2), indicating that the molecules form aggregates under these high-pressure conditions. At both temperatures, decreasing CO_2 density increases the mean diameter of CRL-KDP particles. As the solvation strength of CO_2 decreases, the interactions between particles led to growth of

Table D1: CRL-KDP dispersion sizes from DLS.

Press (psia) /Temp (º C)	Density (g/mL)	Appearance	Time (days)	Mean Diameter (nm)	Polydispersity [std dev/mean] (%)
5000/25	0.985	Orange Translucent	1 3 5	114 111 96	2 3 10
4000/25	0.956	Orange Translucent	1 3 5	120 121 112	1 2 1
3350/25	0.934	Orange Hazy	1 3 5	129 133 125	1 1 1
3000/25	0.920	Orange Hazy	1 3 5	153 155 159	1 1 1
2500/25	0.896	Highly Turbid	1	191	1
2000/25	0.866	Highly Turbid	1	N/A	N/A
5000/40	0.933	Orange Translucent	2	73	5
4600/40	0.920	Orange Translucent	2	108	4
3975/40	0.896	Orange Translucent	2	127	6
3325/40	0.865	Orange Hazy	2	161	2
3000/40	0.847	Orange Hazy	2	316	1
2500/40	0.812	Highly Turbid	2	N/A	N/A

Mean diameter and polydispersity (standard deviation as a percentage mean diameter) of CRL-KDP complex in CO_2 at various CO_2 densities. Appearance as described in Figure D2, time is number of days the protein was dispersed in CO_2 when measurement was taken. At lower densities count rate considerably increased, indicating multiple scattering and preventing accurate measurements to be taken (N/A).

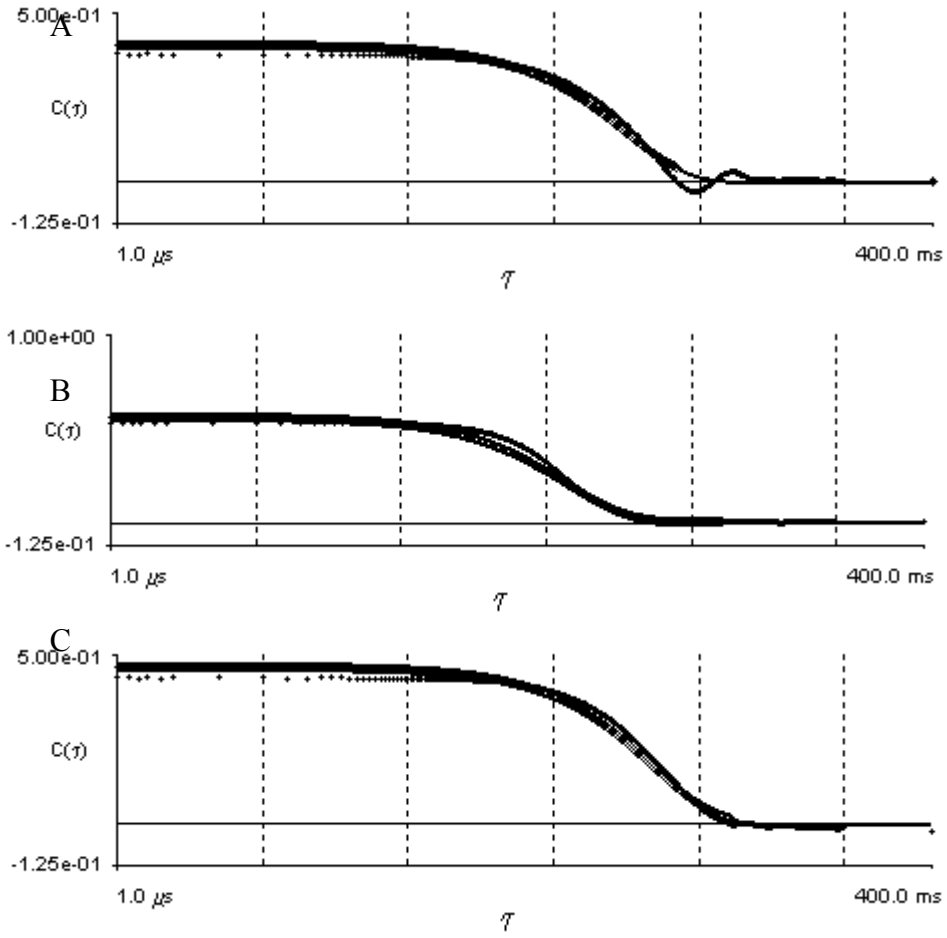

Figure D4: Autocorrelation function graphs of CRL-KDP in CO_2 (dotted) and NNLS fit (solid). A: 0.985 g/mL, 25 °C; B: 0.866 g/mL, 25 °C; C: 0.847 g/mL, 40 °C.

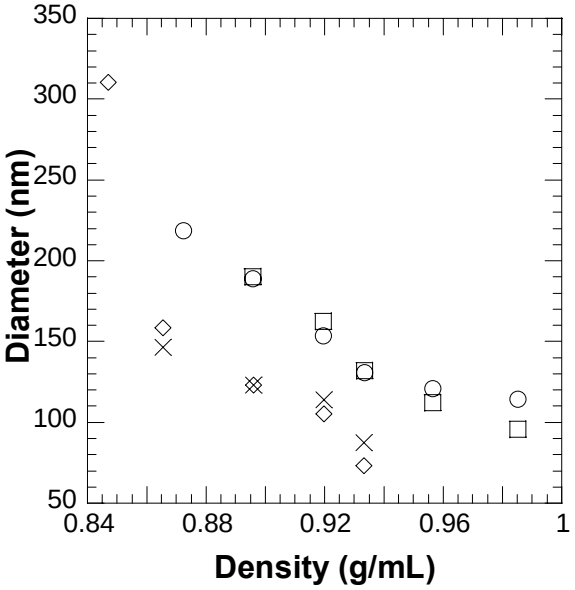

Figure D5: Protein diameter versus CO_2 density on decreasing and increasing pressure. ○ depressurizing at 25 ºC; □ pressurizing at 25 ºC; ◊ depressurizing at 40 °C; x pressurizing at 40 °C.

the aggregate size. Surprisingly, during depressurization and pressurization, little hysteresis was observed indicating that the density dependent aggregation was highly reversible. Given that these aggregates were shown to be nearly transparent and stable against settling, they may be termed soluble aggregates.

Figure D6 presents the size distributions for three CO_2 densities which are unimodal with narrow polydispersities ($\leq$ 2 %). These are remarkably low compared with polydispersities observed for several core-shell silica particle dispersions in CO_2 (10-15 %)[218] and for perfluorodecanethiol-stabilized silver nanocrystals synthesized in supercritical CO_2 (21-92 %).[269] One exception is at 0.985 g/mL (day 5, 25 ºC) where the polydispersity was shown to be slightly higher at 10 % (Table D1). This may be because at this density the solution was homogenized for only 2 minutes compared to the usual 3 or more minutes.

D.3.4 Reversibility Study

Following rapid depressurization from 5000 to 1000 psia, the system became opaque and then the protein particles were observed to settle out of solution, creating a viscous brown coating on the bottom of the cell, which prevented the stir bar from moving. After 30 minutes, the system was quickly pressurized back to 5000 psia and subjected to shearing for 2 minutes. The dispersion returned to the orange translucent state. The protein aggregate diameter returned to the original value before depressurization, indicating that aggregation was reversible as the CO_2 density was cycled. The size distribution showed a slight increase in the polydispersity (standard deviation as a percentage of mean diameter), probably due to the short shear time.

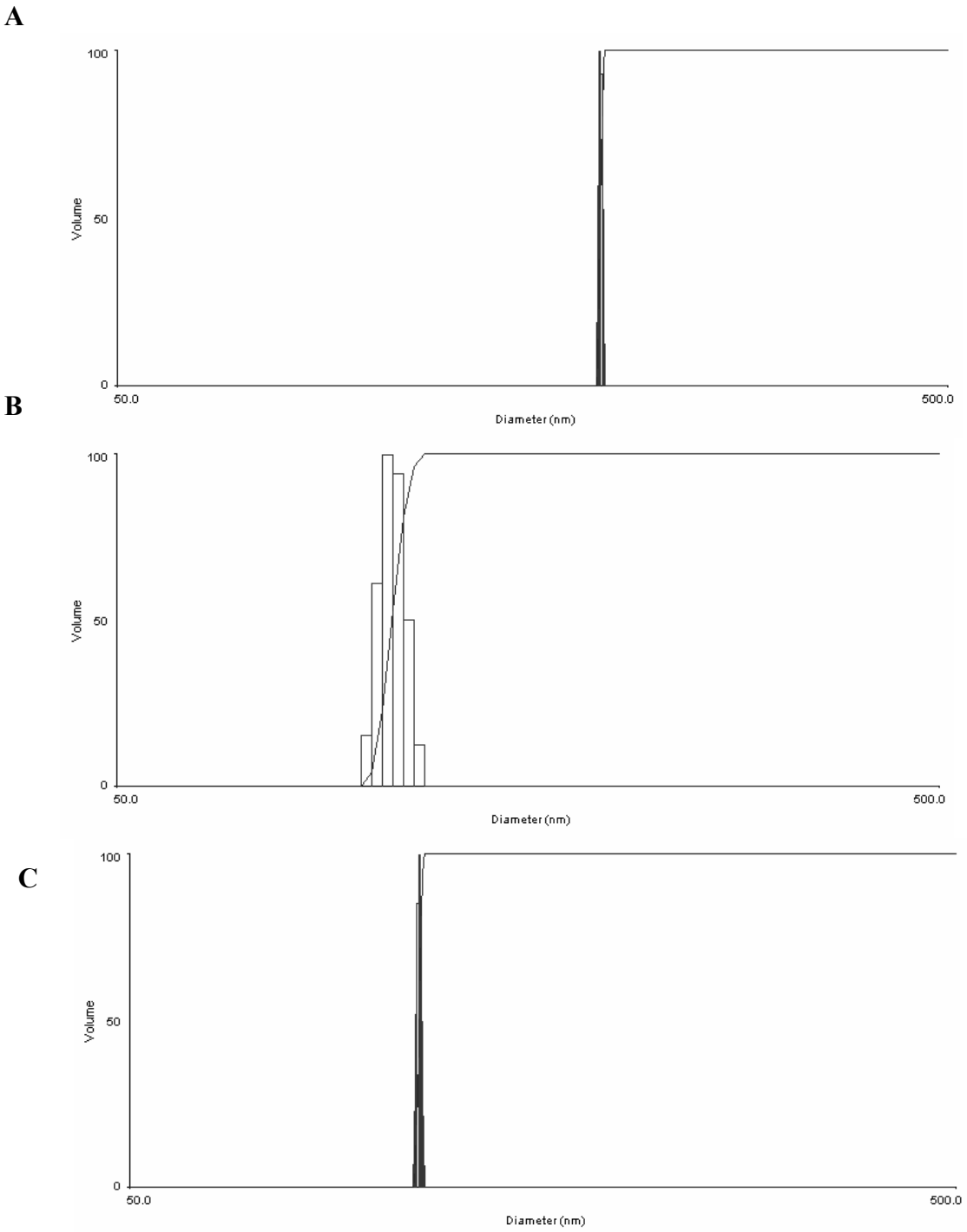

Figure D6: Size distributions of CRL-KDP at various CO_2 densities. A: 0.866 g/mL, 25 ºC; B: 0.920 g/mL, 40 ºC; C: 0.985 g/mL, 25 ºC.

D.3.5 Stability Study

Mean diameters of CRL-KDP at four different conditions and various time points are shown in Figure D7. Figure D8 shows the normalized intensity for CRL-KDP particles for the highest and lowest CO_2 densities studied. From this, it can be seen that intensity only changes ca. 20 % over the 90-minute duration at 0.985 g/mL. However, at 0.865 g/mL the particle diameter increased from 170 to 230 nm (a 75 % increase) followed by a sharp decrease to 115 nm. The behavior of CRL-KDP particles with respect to particle diameter over a period of 90 minutes suggests further aggregation of the proteins followed by settling of these larger aggregates out of solution at the lowest CO_2 density studied. The higher CO_2 densities did not show this pattern of aggregation and settling, and appeared more stable.

D.4 DISCUSSION

D.4.1 Comparison of Protein Dispersion in CO_2

The weight fraction of complexes in CO_2 was 1.25 %. The weight fraction of protein in CO_2, excluding the weight of PFPE, was 0.42 %. This level may be compared with 0.0057 % by weight for BSA in W/C microemulsions.[48] Relative to these microemulsions, the HIP strategy of the current paper leads to much higher concentrations of protein in CO_2. The ratio of weight of protein to the combined weight of protein and surfactant was 0.42:1.25 (about 1:3), much higher than the typically observed value of 1:10 to 1:1000 for proteins in reverse micelles in an organic solvent

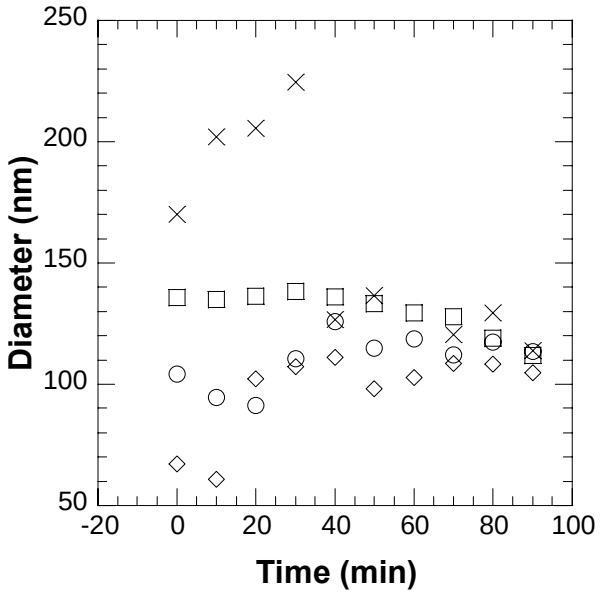

Figure D7: ○: 0.985 g/mL at 25 °C, □: 0.934 g/mL at 25 °C, ◊: 0.933 g/mL at 40 °C, x: 0.865 g/mL at 40 °C.

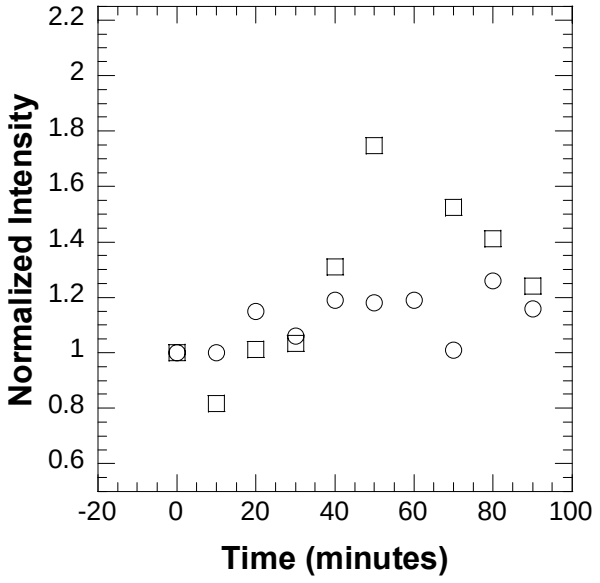

Figure D8: ○: 0.985 g/mL, 25 °C, and □: 0.856 g/mL, 40 °C.

[270-272] or the approximate 1:32 ratio of weight of protein to the combined weight of protein and surfactant for subtilisin and Krytox reverse micelles in liquid carbon dioxide reported by Ghenciu et al.[273] One of the reasons for the higher loadings in CO_2 is that this approach does not depend upon the self-assembly of water and surfactant to form thermodynamically stable microemulsions, with a small water core, and thus a limited payload to dissolve the protein. For reverse micelles or microemulsions, large amounts of surfactant are needed to drive the aggregation of the surfactant to form the micelles. For the complexes, only a small amount of surfactant is required to form an aggregate with weak enough interactions between the aggregates to form a kinetically stable dispersion.

D.4.2 Aggregation of Colloids in CO_2 and Analysis of Growth Mechanisms

Smaller CRL-KDP particles were measured in PFMC therefore it can be said that attraction between protein primary particles is generally much greater in CO_2, even at high densities. In CO_2 it is likely that the PFPE stabilizing ligands were unable to completely screen the Hamaker attraction between the CRL-KDP particles, hence aggregation occurred (Figure D5), as seen in other PFPE stabilized systems.[35,234,261]

Condensation and coagulation are the two primary growth mechanisms by which the aggregation of protein colloids may arise. Condensation occurs as individual protein primary particles add to the aggregate forming a relatively monodisperse size distribution. In contrast, coagulation of two small aggregates, composed of primary particles, to form a larger aggregate results in a broader size distribution.[274] Size distribution moments, μ_1 and μ_3, are used to determine whether aggregation is dominated by condensation or coagulation as shown by the following equations:

$$\mu_1 = \frac{r_3}{r_h} = \left(\frac{3}{\sqrt{\sum r_i^3 / N_\infty}} \right) \Bigg/ \left(\frac{N_\infty}{\sum \left(\frac{1}{r_i} \right)} \right) \qquad [1]$$

$$\mu_3 = \frac{r_1}{r_3} = \left(\frac{\sum r_i}{N_\infty} \right) \Bigg/ \left(\frac{3}{\sqrt{\sum r_i^3 / N_\infty}} \right) \qquad [2]$$

where r_1 is the arithmetic mean radius, r_3 is the cube mean radius, r_h is the harmonic mean radius, and N_∞ is the total number of particles. For aggregates formed by condensation, the size distribution moments reflect a monodisperse system, $\mu_1 = \mu_3 = 1$, whereas the size distribution moments for aggregation by coagulation are $\mu_1 > 1.25$ and $\mu_3 < 0.905$.[274]

Table D2 summarizes the calculated size distribution moments for the data presented in Table D1. It is clear that μ_1 and μ_3 approach 1 for all conditions listed and since the size distribution moments are a ratio of two radii (r_3 and either r_h or r_1) whose values differ by a maximum of 0.02 at 25 °C, it can be said that the calculated moments (μ_1 and μ_3) are very close to unity. This strongly suggests that the enzyme-surfactant complexes aggregate predominantly by a condensation mechanism. This result is also supported by the observation of the very narrow size distributions (see Figure D6).

One reason for the monodisperse distribution of protein aggregates in CO_2 could be a decrease in the kinetics of aggregation as the unimer is depleted. The rate of condensation due to Brownian motion is proportional to the number of aggregates and the number of primary particles present.[275] Therefore, as protein particle aggregates grow from 6.5 nm to 100 nm, the number of primary particles decreases, hence decreasing the rate of growth by condensation. The rate of condensation will also decrease as the

Table D2: Calculated size distribution moments at various conditions.

Pressure (psi)	Temperature (ºC)	Density (g/mL)	μ_1	μ_3
5000	25	0.985	1.000	1.000
4000	25	0.956	1.000	1.000
3350	25	0.934	1.000	1.000
3000	25	0.920	1.000	1.000
2500	25	0.866	1.000	1.000
5000	40	0.933	1.004	0.998
4600	40	0.920	1.003	0.999
3975	40	0.896	1.004	0.998
3325	40	0.865	1.001	1.000
3000	40	0.847	1.000	1.000

particles grow due to entropy loss of each individual primary particle as it joins an aggregate. If a balance occurs between this entropy loss and the attractive forces between the aggregates and primary particles, then the size distribution may be "kinetically trapped" in a metastable state[218] with a low degree of polydispersity.

Other investigations of the aggregation kinetics of colloids have used techniques such as DLS,[218,276,277] SLS,[278] and TEM.[279] Okuda *et al.* investigated the time-dependent complex formation of DNA by DLS.[276] They observed that as particle size increased with short to intermediate incubation time, polydispersity remained low, but with longer incubation times, this value increased. This was also reported by Ju *et al.* who studied the aggregation of colloidal silica particles by DLS.[277] In addition, polydispersities of 10-15 % were seen for a fluorinated core-shell silica dispersion in liquid CO_2.[218] Furthermore, aerosol studies have shown that a "self-preserving" condition can exist.[279-282] This occurs after a growth period and is evident by a consistent aggregate size and/or polydispersity over time.

Shah and colleagues investigated perfluorodecanethiol-stabilized silver nanocrystals synthesized in supercritical CO_2 with sizes of 20-40 Å depending the CO_2 density.[269] Calculation of μ_1 and μ_3 demonstrated that condensation dominated growth at high CO_2 densities with little coagulation. However, at low CO_2 densities (below 3950 psia and 80 ºC) the particles grew by coagulation, and this was due to insufficient solvation of the stabilizing ligands by CO_2. A similar mechanism may be expected to be operative for proteins stabilized by fluorinated surfactant in this study.

The lack of coagulation between protein aggregates may have been facilitated, in part, by void spaces filled with CO_2 between the individual primary particles within the aggregates. The composite Hamaker constant will be lower than that of the primary particles due to the presence of CO_2. Void spaces are not present in the primary particles,

thus condensation of a primary particle with an aggregate will be favored over the coagulation of two aggregates, and this is again reflected in low polydispersities (Figure D6).

D.4.3 Density-Dependent Interparticle Interactions

As the density of CO_2 decreases, the solvation of stabilizing surfactant tails decreases. Neutron scattering,[234] X-ray scattering,[261] light scattering,[259] lattice-fluid theory,[283,284] and Monte Carlo[285] simulation have all suggested the link between tail solvation, CO_2 density and the effect on colloid stability. The aggregation of CRL-KDP particles increases as the density of CO_2 is decreased. The CO_2 expands away from the PFPE tails to gain entropy[128] as the density is reduced. The tails become less extended into the CO_2 and attractive interparticle tail-tail interactions become stronger, favoring condensation at even lower densities, as shown in Table D1. In addition, the already low Hamaker constant for CO_2 decreases even further as density is reduced, increasing the difference of the Hamaker constants between CO_2 and PFPE. The result is an increase in the van der Waals force between the CRL-KDP particles. Thus, both a decrease in steric repulsion of the particles and an increase in attractive van der Waals interactions, increases the degree of particle aggregation as the density of CO_2 is reduced (Figure D5). The interparticle attractive interactions between the PFPE tails at low densities were reduced at high densities upon repeated cycling indicating reversibility.

The stability of the dispersed protein aggregates in CO_2 is enhanced by the void spaces between individual protein molecules, which are filled with CO_2. These void spaces weaken the Hamaker attraction between aggregates, as a result of the lower Hamaker constant of CO_2 relative to the protein. This phenomenon was reported by Dickson *et al.* in their DLS study of core-shell silica particles in liquid CO_2.[218] In

addition, the overall density of the aggregates is reduced with the inclusion of voids, which lowers the settling rate. Thus at high CO_2 densities, the mean aggregate diameter only changed from approximately 105 to 115 nm over 90 minutes at a density of 0.985 g/ml and 25 ºC (Figure D7).

The aggregation and settling of the protein dispersion at a lower CO_2 density (0.856 g/mL, Figure D7), indicates a decrease in colloid stability. The settling rate of a spherical particle, v_s, due to gravity can be calculated from Stoke's Law.[275]

$$v_s = \left[2R_s^2\left(\rho_s - \rho_f\right)g\right]/\left(9\eta_f\right) \qquad [3]$$

where R_s is the radius of the sphere, η_f is the viscosity of the fluid (CO_2), and ρ_s and ρ_f are the densities of the sphere and fluid, respectively. The radii were obtained from Table D2, the density and viscosity of CO_2 were known, and the density of the protein was estimated at 1.41 g/mL.[286] The resulting settling rates for the protein at CO_2 densities of 0.985 and 0.934 g/mL at 25 °C were calculated as 5.8 and 10.1 μm/min, respectively. At 40 °C, for CO_2 at 0.933 and 0.865 g/mL the settling rates were 3.3 and 22.0 μm/min, respectively. All of these rates are negligible compared with the 1.8 cm height of the scattering cell. Thus, observation of particles in the bottom of the cell indicated extensive aggregation to produce much larger particles than those shown in Figure D7 for 0.865 g/mL.

As the CO_2 density is lowered, the calculated settling rates of the aggregates increased due to the larger size of the aggregates (Figures D7 and D8). The enhanced interparticle interactions are caused by the lower Hamaker constant for CO_2 and the decreased solvation of the PFPE, leading to stronger interactions between PFPE ligands. The more rapid settling of the large aggregates, visible as particles settling on the bottom of the cell, is also influenced by the lower solvent viscosity, and increased solvent-solute density differences, as seen in equation (3).

D.4.4 Temperature-Dependent Interparticle Interactions

The effect of thermal energy on the solvation properties of CO_2 has been studied utilizing Monte Carlo simulations,[130] SANS,[128,129] turbidimetry,[18,126,127] and optical microscopy.[35] Sirard *et al.* showed that an increase in the temperature, at constant density, increased the extension of end-grafted PDMS polymer brushes in CO_2.[128] This was also seen in the simulation work of Luna Barcena and colleagues, where the mean square end-to-end distance of a Lennard-Jones (L-J) polymer chain increased monotonically as the temperature was raised, at constant density, in a L-J solvent.[130] Melnichenko and co-workers saw a linear increase in the radius of gyration of a polymer in CO_2 as the temperature was raised, at constant density, above the theta condition.[129] A reduction in flocculation, indicating better solvation with higher temperatures, has been observed with increasing temperatures for W/C miniemulsions stabilized with poly(1,1-dihydroperfluoroctyl methacrylate)-b-poly(ethylene oxide) surfactants[127] and silica with end-grafted poly(1H,1H-dihydrofluorooctyl methacrylate).[126]

The size of the protein aggregates was smaller at 40 °C relative to 25 °C, as expected due to the increased thermal energy, at constant CO_2 density (Figure D5). In addition, the CRL-KDP was dispersible at a lower minimum density at 40 °C than 24 °C, 0.83 g/mL and 0.89 g/mL, respectively. The thermodynamic driving force for condensation will be reduced by an increase in thermal energy relative to the long-ranged attractive Hamaker interactions between CRL-KDP particles, and the attractive interparticle tail-tail interactions between PFPE chains.[130] In addition, the stabilizing chains are likely to be more extended as temperature increases providing greater repulsion between particles. This effect leads to smaller particles, despite the faster diffusion and collision rates at higher temperatures.

D.4.5 Possible Role of Decomplexation of CRL-KDP in CO_2

It was shown that the CRL-KDP complexes are highly dispersed at CO_2 pressures >3000 psia and 25 or 40 ºC. On decreasing pressure, the aggregate size increased (Figure D5) and then decreased upon repressurization. Complete removal of the CO_2 solvent via depressurization could strip some of the PFPE molecules off the protein molecules hence leaving behind the native CRL powder that was found to be insoluble in PFMC. In addition, decomplexation of the complex may also have contributed to the changes in aggregate size with pressure. KDP is highly soluble in CO_2 in its own right, whereas native CRL is insoluble. On initial pressurization with CO_2 to intermediate pressures, some of the KDP may be stripped off the CRL, resulting in relatively large native CRL aggregates that are not highly dispersible in CO_2. On increasing pressure further it is possible that KDP could coat the CRL aggregates more effectively enabling them to be become smaller and more dispersible in CO_2. The decomplexation may contribute to the high particle diameters (> 100 nm) for this sample, in contrast to the smaller diameters (6.5 nm) measured at atmospheric pressure. The observation of native CRL in the cell following complete depressurization supports the concept of decomplexation; however, further investigation would be required to characterize the degree of complexation *in situ* as a function of pressure.

D.5 CONCLUSIONS

Lipase from *Candida rugosa* was modified by ion pairing with an anionic PFPE surfactant, KDP 4606. The concentration of KDP was kept below that of its critical micelle concentration to ensure that this method was distinguishable from a microemulsion method such as that reported by Panza, Russell and Beckman[287] whereby an enzyme was solubilized in a fluorous solvent by means of forming fluorinated reverse micelles. The enzyme-surfactant complex was 6.5 nm in diameter by dynamic light scattering at atmospheric pressure, which strongly suggests that one lipase molecule is surrounded by several surfactant molecules, rendering it soluble in perfluoromethylcyclohexane.

CRL-KDP is readily dispersed in liquid and supercritical CO_2 with gentle stirring using PFMC as a co-solvent at densities above 0.92 g/mL (25 ºC) and 0.847 g/mL (40 ºC) to from a nearly transparent orange dispersion. At these densities and above, particle sizes were measured by high-pressure dynamic light scattering and shown to be more than an order of magnitude greater than at atmospheric pressure in PFMC, ranging from 50 to 200 nm, indicating aggregates of the enzyme-surfactant complexes. The growth mechanism for this aggregation was shown to be via condensation as characterized by relatively monodisperse size distributions moments ($\mu_1 \approx \mu_3 \approx 1$). On decreasing the density, the enzyme-surfactant aggregate size increases, similar to the behavior for other colloids including water/CO_2 microemulsions and inorganic particles. [218,234] Upon decreasing density, an increase in attractive interactions between complexes is driven by a gain in the entropy of CO_2 molecules, as they expand away from the complexes and an increase in the difference in the Hamaker constants for CO_2 and the enzyme complex.

Aggregate size was lower at 40 ºC than at 25 ºC at comparable densities, as the thermal energy becomes stronger relative to the attractive interactions between complexes. Aggregation of CRL-KDP particles in CO_2 at 25 or 40 ºC was shown to be reversible with CO_2 pressure. The protein to total solids weight ratio was only 1:3, despite a relatively high solids weight fraction in CO2 of 1.25 %. These reversible and stable concentrated protein nano-aggregates are highly robust and versatile, offering a new route to protein uptake into CO_2 with relatively small surfactant concentrations.

References

(1) Shah, P. S.; Hanrath, T.; Johnston, K. P.; Korgel, B. A. Nanocrystal and Nanowire Dispersability in Supercritical Fluids. *Journal of Physical Chemistry B* **2004**, *108*, 9574-9587.

(2) Singley, E. J.; Liu, W.; Beckman, E. J. Phase Behavior and Emulsion Formation of Novel Fluoroether Amphiphiles in Carbon Dioxide. *Fluid Phase Equilibria* **1997**, *128*, 199-219.

(3) Lee, C. T.; Psathas, P. A.; Johnston, K. P.; deGrazia, J.; Randolph, T. W. Water-in-Carbon Dioxide Emulsions: Formation and Stability. *Langmuir* **1999**, *15*, 6781-6791.

(4) Psathas, P. A.; da Rocha, S. R. P.; Lee, C. T.; Johnston, K. P.; Lim, K. T.; Webber, S. E. Water-in-Carbon Dioxide Emulsions with PDMS based Block Copolymer Ionomers. *Industrial & Engineering Chemistry Research* **2000**, *39*, 2655-2664.

(5) da Rocha, S. R. P.; Dickson, J. L.; Cho, D.; Rossky, P. J.; Johnston, K. P. Stubby Surfactants for Stabilization of Water and CO2 Emulsions: Trisiolxanes. *Langmuir* **2003**, *19*, 3114-3120.

(6) Ji, M.; Chen, X.; Wai, C. M.; Fulton, J. L. Synthesizing and Dispersing Silver Nanoparticles in a Water-in-Supercritical Carbon Dioxide Microemulsion. *Journal of American Chemical Society* **1999**, *121*, 2631-2632.

(7) Holmes, J. D.; Bhargava, P. A.; Korgel, B. A.; Johnston, K. P. Synthesis of Cadmium Sulfide Q Particles in Water-in-Carrbon Dioxide Microemulsion. *Langmuir* **1999**, *15*, 6613-6615.

(8) Shah, P. S.; Holmes, J. D.; Doty, C.; Johnston, K. P.; Korgel, B. A. Steric Stabilization of Nanocrystals in Supercritical CO2 using Fluorinated Ligands. *Journal of the American Chemical Society* **2000**, *122*, 4245-4246.

(9) Wai, C. M.; Ohde, H. Synthesizing nanoparticles in supercritical carbon dioxide. *Journal of the Chinese Institute of Chemical Engineers* **2001**, *32*, 253-261.

(10) Shah, P. S.; Husain, S.; Johnston, K. P.; Korgel, B. A. Role of Steric Stabilization on the Arrested Growth of Silver Nanocrystals in Supercritical Carbon Dioxide. *Journal of Physical Chemistry B* **2002**, *106*, 12178-12185.

(11) Shah, P. S.; Novick, B. J.; Hwang, H. S.; Lim, K. T.; Carbonell, R. G.; Johnston, K. P.; Korgel, B. A. Kinetics of Nonequilibrium Nanocrystal Monolayer Formation: Deposition from Liquid Carbon Dioxide. *Nano Letters* **2003**, *3*, 1671-1675.

(12) McLeod, M. C.; McHenry, R. S.; Beckman, E. J.; Roberts, C. B. Synthesis and Stabilization of Silver Metallic Nanoparticles and Premetallic Intermediates in

Perfluoropolyether/CO2 Reverse Micelles. *Journal of Physical Chemistry B* **2003**, *107*, 2693-2700.

(13) DeSimone, J. M.; Maury, E. E.; Menceloglu, Y. Z.; McClain, J. B.; Romack, T. J.; Combes, J. R. Dispersion polymerizations in supercritical carbon dioxide. *Science* **1994**, *265*, 356-359.

(14) Calvo, L.; Holmes, J. D.; Yates, M. Z.; Johnston, K. P. Steric Stabilization of Inorganic Suspensions in Carbon Dioxide. *Journal of Supercritical Fluids* **2000**, *16*, 247-260.

(15) Yates, M. Z.; Shah, P. S.; Lim, K. T.; Johnston, K. P. Steric Stabilization of Colloids by Poly(dimethylsiloxane) in Carbon Dioxide: Effects of Cosolvents. *Journal of Colloid and Interface Science* **2000**, *227*, 176-184.

(16) Sirard, S. M.; Castellanos, H. J.; Hwang, H. S.; Lim, K. T.; Johnston, K. P. Steric Stabilization of Silica Colloids in Supercritical Carbon Dioxide. *Industrial and Engineering Chemistry Research* **2004**, *43*, 525-534.

(17) Dickson, J. L.; Shah, P. S.; Binks, B. P.; Johnston, K. P. Steric Stabilization of Nanoparticles in Liquid Carbon Dioxide at the Vapor Pressure. *Langmuir* **2004**, *20*, 9380-9387.

(18) Visintin, P. M.; Carbonell, R. G.; Schauer, C. K.; DeSimone, J. M. Chemical Functionalization of Silica and Alumina Particles for Dispersion in Carbon Dioxide. *Langmuir* **2005**, *21*, 4816-4823.

(19) Goldfarb, D. L.; Pablo, J. J. d.; Nealey, P. F.; Simons, J. P.; Moreau, W. M.; Angelopoulos, M. Aqueous-based photoresist drying using supercritical carbon dioxide to prevent pattern collapse. *J. Vac. Sci. Technol. B* **2000**, *18*, 3313-3317.

(20) Zhang, X.; Pham, J. Q.; Martinez, H. J.; Wolf, J.; Green, P. F.; Johnston, K. P. Water-in-Carbon Dioxide Microemulsions for Removing Postetch Residues from Patterned Porous Low-k Dielectrics. *Journal of Vacuum Science & Technology, B: Microelectronics and Nanometer Structures* **2003**, *21*, 2590-2598.

(21) Campbell, M. L.; Apodaca, D. L.; Yates, M. Z.; McCleskey, T. M.; Birnbaum, E. R. Metal Extraction from Heterogeneous Surfaces Using Carbon Dioxide Microemulsions. *Langmuir* **2001**, *17*, 5458-5463.

(22) Ohde, H.; Hunt, F.; Wai, C. M. Synthesis of silver and copper nanoparticles in a water-in-supercritical-carbon dioxide microemulsion. *Chemistry of Materials* **2001**, *13*, 4130-4135.

(23) Holmes, J. D.; Steytler, D. C.; Rees, G. D.; Robinson, B. H. Bioconversions in a Water-in-CO2 Microemulsion. *Langmuir* **1998**, *14*, 6371-6376.

(24) DeSimone, J. M. Practical Approaches to Green Solvents. *Science* **2002**, *297*, 799-803.

(25) Harrison, K. L.; Johnston, K. P.; Sanchez, I. C. Effect of Surfactants on the Interfacial Tension between Supercritical Carbon Dioxide and Polyethylene Glycol. *Langmuir* **1996**, *12*, 2637-2644.

(26) Harrison, K.; Goveas, J.; Johnston, K. P.; O'Rear, E. A. Water-in-Carbon Dioxide Microemulsions with a Fluorocarbon-Hydrocarbon Hybrid Surfactant. *Langmuir* **1994**, *10*, 3536.

(27) Eastoe, J.; Cazelles, M. H.; Steytler, D. C.; Holmes, J. D.; Pitt, A. R.; Wear, T. J.; Heenan, R. K. Water-in-CO2 Microemulsions Studied by Small-Angle Neutron Scattering. *Langmuir* **1997**, *13*, 6980-6984.

(28) Zielinski, R. G.; Kline, S. R.; Kaler, E. W.; Rosov, N. A Small Angle Neutron Scattering Study of Water in Carbon Dioxide Emulsions. *Langmuir* **1997**, *13*, 3934-3937.

(29) Lee, C. T., Jr.; Psathas, P. A.; Ziegler, K. J.; Johnston, K. P.; Dai, H. J.; Cochran, H. D.; Melnichenko, Y. B.; Wignall, G. D. Formation of Water-in-Carbon Dioxide Microemulsions with a Cationic Surfactant: A Small-Angle Neutron Scattering Study. *Journal of Physical Chemistry B* **2000**, *104*, 11094-11102.

(30) Liu, Z.; Erkey, C. Water in Carbon Dioxide Microemulsions with Fluorinated Analogues of AOT. *Langmuir* **2001**, *17*, 274-277.

(31) Keiper, J. S.; Simhan, R.; DeSimone, J. M. New Phosphate Fluorosurfactants for Carbon Dioxide. *Journal of the American Chemical Society* **2002**, *124*, 1834-1835.

(32) Psathas, P. A.; Janowiak, M.; Garcia-Rubio, L. H.; Johnston, K. P. Formation of Carbon Dioxide-in-Water Miniemulsions Using the Phase Inversion Temperature Method. *Langmuir* **2002**, *18*, 3039-3046.

(33) Dickson, J. L.; Psathas, P. A.; Salinas, B.; Ortiz-Estrada, C.; Luna-Barcenas, G.; Hwang, H. S.; Lim, K. T.; Johnston, K. P. Formation and Growth of Water-in-CO_2 Miniemulsions. *Langmuir* **2003**, *19*, 4895-4904.

(34) da Rocha, S. R. P.; Dickson, J. L.; Cho, D.; Rossky, P. J.; Johnston, K. P. Stubby Surfactants for the Stabilization of Water and CO2 Emulsions: Trisiloxanes. *Langmuir* **2003**, *19*, 3114-3120.

(35) Lee, C. T., Jr.; Psathas, P. A.; Johnston, K. P.; DeGrazia, J.; Randolph, T. W. Water-in-Carbon Dioxide Emulsions: Formation and Stability. *Langmuir* **1999**, *15*, 6781-6791.

(36) Johnston, K. P.; Cho, D.; da Rocha, S. R. P.; Psathas, P. A.; Ryoo, W.; Webber, S. E.; Eastoe, J.; Dupont, A.; Steytler, D. C. Water in Carbon Dioxide Macroemulsions and Miniemulsions with a Hydrocarbon Surfactant. *Langmuir* **2001**, *17*, 7191-7193.

(37) Psathas, P. A.; Sander, E. A.; Lee, M. Y.; Lim, K. T.; Johnston, K. P. Mapping the stability and curvature of emulsions of H2O and supercritical CO2 with

interfacial tension measurements. *Journal of Dispersion Science and Technology* **2002**, *23*, 65-80.

(38) Saito, S. Research activities on supercritical fluid science and technology in Japan - a review. *J. Supercrit. Fluids* **1995**, *8*, 177-204.

(39) Eastoe, J.; Gold, S.; Steytler, D. C. Surfactants for CO2. *Langmuir* **2006**, *22*, 9832-9842.

(40) Ryoo, W.; Webber, S. E.; Bonnecaze, R. T.; Johnston, K. P. Long-Ranged Electrostatic Repulsion and Crystallization of Emulsion Droplets in an Ultralow Dielectric Medium Supercritical Carbon Dioxide. *Langmuir* **2006**, *22*, 1006-1015.

(41) Stone, M. T.; Smith, P. G.; da Rocha, S. R. P.; Rossky, P. J.; Johnston, K. P. Low Interfacial Free Volume of Stubby Surfactants Stabilize Water-in-Carbon Dioxide Microemulsions. *Journal of Physical Chemistry B* **2004**, *108*, 1962-1966.

(42) Ryoo, W.; Webber, S. E.; Johnston, K. P. Water-in-Carbon Dioxide Microemulsions with Methylated Branched Hydrocarbon Surfactants. *Industrial & Engineering Chemistry Research* **2003**, *42*, 6348-6358.

(43) Stone, M. T. d. R., S. R. P.; Rossky, P. J.; Johnston, K. P. Molecular Differences between Hydrocarbon and Fluorocarbon Surfactants at the CO2/Water Interface. *J. Phys. Chem. B.* **2003**, *107*, 10185-10192.

(44) Hoefling, T. A.; Enick, R. M.; Beckman, E. J. Microemulsions in near-critical and supercritical carbon dioxide. *Journal of Physical Chemistry* **1991**, *95*, 7127-7129.

(45) Psathas, P. A.; Da Rocha, S. R. P.; Lee, C. T., Jr.; Johnston, K. P.; Lim, K. T.; Webber, S. Water-in-Carbon Dioxide Emulsions with Poly(dimethylsiloxane)-Based Block Copolymer Ionomers. *Industrial & Engineering Chemistry Research* **2000**, *39*, 2655-2664.

(46) O'Neill, M. L.; Cao, Q.; Fang, M.; Johnston, K. P.; Wilkinson, S. P.; Smith, C. D.; Kerschner, J. L.; Jureller, S. H. Solubility of Homopolymers and Copolymers in Carbon Dioxide. *Industrial Engineering and Chemistry Research* **1998**, *37*, 3067-3079.

(47) Lee, D.; Hutchinson, J. C.; DeSimone, J. M.; Murray, R. W. Diffusive Transport of Micelles and Monomeric Solutes in Supercritical CO2. *Journal of the American Chemical Society* **2001**, *123*, 8406-8407.

(48) Johnston, K. P.; Harrison, K. L.; Clarke, M. J.; Howdle, S. M.; Heitz, M. P.; Bright, F. V.; Carlier, C.; Randolph, T. W. Water-in-carbon dioxide microemulsions: an environment for hydrophiles including proteins. *Science* **1996**, *271*, 624-626.

(49) Sarbu, T.; Styranec, T.; Beckman, E. J. Non-fluorous polymers with very high solubility in supercritical CO2 down to low pressures. *Nature* **2000**, *405*, 165-168.

(50) Raveendran, P.; Wallen, S. L. Sugar Acetates as Novel, Renewable CO2-philes. *Journal of the American Chemical Society* **2002**, *124*, 7274-7275.

(51) Liu, J.; Han, B.; Li, G.; Zhang, X.; He, J.; Liu, Z. Investigation of Nonionic Surfactant Dynol-604 Based Reverse Microemulsions Formed in Supercritical Carbon Dioxide. *Langmuir* **2001**, *17*, 8040-8043.

(52) Ryoo, W.; Webber, S. E.; Johnston, K. P. Water-in-Carbon Dioxide Microemulsions with Methylated Branched Hydrocarbon Surfactants. *Industrial and Engineering Chemistry Research* **2003**, *42*, 6348-6358.

(53) Kuuskraa, V. A.; Koperna, G. J. "Evaluating the Potential for "Game Changer" Improvements in Oil Recovery Efficiency from CO2 Enhanced Oil Recovery," U.S. Department of Energy, Office of Fossil Energy, Office of Oil and Natural Gas, 2006.

(54) Yuan, H.; Johns, R. T.; Egwuenu, A. M.; Dindoruk, B. Improved MMP correlations for CO2 floods using analytical gasflooding theory. *SPE Reservoir Evaluation & Engineering* **2006**, *9*, 290.

(55) Yuan, H.; Johns, R. T.; Egwuenu, A. M.; Dindoruk, B. Improved MMP correlations for CO2 floods using analytical gasflooding theory. *SPE Reservoir Evaluation & Engineering* **2005**, *8*, 418-425.

(56) Heller, J. P. CO2 foams in enhanced oil recovery. *Advances in Chemistry Series* **1994**, *242(Foams: Fundamentals and Applications in the Petroleum Industry)*, 201-234.

(57) Jessen, K.; Kovescek, A. R.; Orr, F. M. Increasing CO_2 Storage in Oil Recovery. *Energy Conversion and Management* **2005**, *46*, 293-311.

(58) Zhu, T.; Ogbe, D. O.; Khataniar, S. Improving the Foam Performance for Mobility Control and Improved Sweep Efficiency in Gas Flooding. *Industrial & Engineering Chemistry Research* **2004**, *43*, 4413-4421.

(59) Rossen, W. R. In *Foams: Theory, Measurements, and Applications*; Prudhomme, R. K., Khan, S. A., Eds.; Marcel Dekker: New York, 1996.

(60) Gauglitz, P. A.; Friedmann, F.; Kam, S. I.; Rossen, W. R. Foam Generation in Porous Media. *Chemical Engineering Science* **2002**, *57*, 4037-4052.

(61) Kornev, K. G.; Neimark, A. V.; Rozhkov, A. N. Foam in porous media: thermodynamic and hydrodynamic peculiarities. *Advances in Colloid and Interface Science* **1999**, *82*, 127-187.

(62) Nguyen, Q. P.; Currie, P. K.; Zitha, P. L. J. Motion of foam films in diverging-converging channels. *Journal of Colloid and Interface Science* **2004**, *271*, 473-484.

(63) Kovscek, A. R.; Bertin, H. J. Foam Mobility in Heterogeneous Porous Media. *Transport in Porous Media* **2003**, *52*, 37-49.

(64) Asghari, K.; Khalil, F. Effect of Operation Parameters on CO2-Foam process. *Petroleum Science and Technology* **2005**, *23*, 189-198.

(65) Bibette, J. Stability of Thin films in Concentrated Emulsions. *Langmuir* **1992**, *8*, 3178-3182.

(66) Bergeron, V. Forces and Structure in Thin Liquid Soap Films. *J. Phys.: Condens. Matter* **1999**, *11*, R215-R238.

(67) Babak, V. G.; Stebe, M.-J. Highly concentrated emulsions: Physicochemical principles of formulation. *Journal of Dispersion Science and Technology* **2002**, *23*, 1-22.

(68) Exerowa, D.; Kruglyakov, P. M. *Foam and Foam Films: Theory, Experiment, Application*; Elsevier: Amsterdam, 1998; Vol. 5.

(69) Ivanov, I. B.; Kralchevsky, P. A. Stability of emulsions under equilibrium and dynamic conditions. *Colloids and Surfaces A: Physicochemical and Engineering Aspects* **1997**, *128*, 155-175.

(70) Kabalnov, A.; Wennerstrom, H. Macroemulsion Stability: The Oriented Wedge Theory Revisited. *Langmuir* **1996**, *12*, 276-292.

(71) Wasan, D. T.; Koczo, K.; Nikolov, A. D. Mechanisms of Aqueous Foam Stability and Antifoaming Action with and without Oil. *Advances in Chemistry Series 242* **1994**, 47.

(72) Schramm, L. L. Foam Sensitiviety to Crude Oil in Porous Media. *Advances in Chemistry Series 242* **1994**, 165.

(73) Kuhlman, M. L. Visualizing the Effectof Light Oil on CO2 Foams. *Journal of Petroleum Engineering* **1990**, 902-908.

(74) Yang, S. H.; Reed, R. L. Mobility Control Using CO2 Foams. *Society of Petroleum Engineers Meeting, San Antonio, TX, October 8-11, 1989* **1989**, 603-618.

(75) Johnston, K. P. *Journal of Supercritical Fluids* **(In press)**.

(76) Butler, R.; Davies, C. M.; Cooper, A. I. Emulsion templating using high internal phase supercritical fluid emulsions. *Advanced Materials (Weinheim, Germany)* **2001**, *13*, 1459-1463.

(77) Butler, R.; Hopkinson, I.; Cooper, A. I. Synthesis of Porous Emulsion-Templated Polymers Using High Internal Phase CO2-in-Water Emulsions. *Journal of the American Chemical Society* **2003**, *125*, 14473-14481.

(78) Sagisaka, M.; Ozaki, Y.; Yoda, S.; Takebayashi, Y.; Otake, K.; Kondo, Y.; Yoshino, N.; Sakai, H.; Abe, M. Phase behavior and interfacial properties of water-in-supercritical CO2 microemulsions formed with aid of fluorinated surfactants. *Material Technology (Tokyo, Japan)* **2003**, *21*, 36-42.

(79) Dickson, J. L.; Smith, P. G., Jr.; Dhanuka, V. V.; Srinivasan, V.; Stone, M. T.; Rossky, P. J.; Behles, J. A.; Keiper, J. S.; Xu, B.; Johnson, C.; DeSimone, J. M.; Johnston, K. P. Interfacial Properties of Fluorocarbon and Hydrocarbon Phosphate Surfactants at the Water-CO2 Interface. *Industrial & Engineering Chemistry Research* **2005**, *44*, 1370-1380.

(80) Dhanuka, V. V.; Dickson, J. L.; Ryoo, W.; Johnston, K. P. High internal phase CO2-in-water emulsions stabilized with a branched nonionic hydrocarbon surfactant. *Journal of Colloid and Interface Science* **2006**, *298*, 406-418.

(81) da Rocha, S. R. P.; Johnston, K. P.; Rossky, P. J. Surfactant-Modified CO2-Water Interface: A Molecular View. *Journal of Physical Chemistry B* **2002**, *106*, 13250-13261.

(82) da Rocha, S. R. P.; Harrison, K. L.; Johnston, K. P. Effect of Surfactants on the Interfacial Tension and Emulsion Formation Between Water and Carbon Dioxide. *Langmuir* **1999**, *15*, 419-428.

(83) Psathas, P. A.; Sander, E. A.; Ryoo, W.; Mitchell, D.; Lagow, R. J.; Lim, K. T.; Johnston, K. P. Interfacial studies of the formation of microemulsions of water in carbon dioxide with fluorinated surfactants. *Journal of Dispersion Science and Technology* **2002**, *23*, 81-92.

(84) Phillips, A. M.; Couchman, D. D. High temperature rheology of CO2 foam fracturing fluids. *Proceedings of the Annual Southwestern Petroleum Short Course* **1987**, *34th*, 102-106.

(85) Rosen, M. J. *Surfactants and Interfacial Phenomena*; 3 ed.; John Wiley & Sons, Inc.: New York, 2004.

(86) Harrison, K. L.; Da Rocha, S. R. P.; Yates, M. Z.; Johnston, K. P.; Canelas, D.; DeSimone, J. M. Interfacial Activity of Polymeric Surfactants at the Polystyrene-Carbon Dioxide Interface. *Langmuir* **1998**, *14*, 6855-6863.

(87) da Rocha, S. R. P.; Johnston, K. P. Interfacial Thermodynamics of Surfactants at the CO2-Water Interface. *Langmuir* **2000**, *16*, 3690-3695.

(88) Dupont, A.; Eastoe, J.; Martin, L.; Steytler David, C.; Heenan Richard, K.; Guittard, F.; Taffin de Givenchy, E. Hybrid fluorocarbon-hydrocarbon CO2-philic surfactants. 2. formation and properties of water-in-CO2 microemulsions. *Langmuir* **2004**, *20*, 9960-9967. .

(89) Sagisaka, M.; Fujii, T.; Ozaki, Y.; Yoda, S.; Takebayashi, Y.; Kondo, Y.; Yoshino, N.; Sakai, H.; Abe, M.; Otake, K. Interfacial Properties of Branch-Tailed Fluorinated Surfactants Yielding a Water/Supercritical CO2 Microemulsion. *Langmuir* **2004**, *20*, 2560-2566.

(90) Johnston, K. P.; Harrison, K. L.; Clarke, M. J.; Howdle, S. M.; Heitz, M. P.; Bright, F. V.; Carlier, C.; Randolph, T. W. Water-in-Carbon Dioxide Microemulsions: A New Environment for Hydrophiles Including Proteins. *Science* **1996**, *271*, 624.

(91) Nave, S.; Eastoe, J.; Penfold, J. What Is So Special about Aerosol-OT? 1. Aqueous Systems. *Langmuir* **2000**, *16*, 8733-8740.

(92) McClain, J. B.; Londono, D.; Combes, J. R.; Romack, T. J.; Canelas, D. A.; Betts, D. E.; Wignall, G. D.; Samulski, E. T.; DeSimone, J. M. Solution Properties of

a CO_2-Soluble Fluoropolymer via Small Angle Neutron Scattering. *Journal of the American Chemical Society* **1996**, *118*, 917-918.

(93) Lee, C. T.; Ryoo, W.; Smith, P. G.; Arellano, J.; Mitchell, D. R.; Lagow, R. J.; Webber, S. E.; Johnston, K. P. Carbon Dioxide-in-Water Microemulsions. *Journal of the American Chemical Society* **2003**, *125*, 3181-3189.

(94) Aveyard, R.; Binks, B. P.; Clark, S.; Fletcher, P. D. I. Effects of temperature on the partitioning and adsorption of dodecyl pentaethylene glycol ether in heptane-water mixtures. *Journal of the Chemical Society, Faraday Transactions* **1990**, *86*, 3111-3115.

(95) Binks, B. P. Relationship between microemulsion phase behavior and macroemulsion type in systems containing nonionic surfactant. *Langmuir* **1993**, *9*, 25-28.

(96) Harrison, K. L.; Johnston, K. P.; Sanchez, I. C. Effect of Surfactants on the Interfacial Tension between Supercritical Carbon Dioxide and Polyethylene Glycol. *Langmuir* **1996**, *12*, 2637-2644.

(97) Salager, J. L.; Quintero, L. R., Ennodio; Anderez, Jose M. Properties of surfactant/oil/water emulsified systems in the neighborhood of the three-phase transition. *Journal of Colloid and Interface Science* **1980**, *77*, 288-289.

(98) da Rocha, S. R. P.; Psathas, P. A.; Klein, E.; Johnston, K. P. Concentrated CO2-in-Water Emulsions with Nonionic Polymeric Surfactants. *Journal of Colloid and Interface Science* **2001**, *239*, 241-253.

(99) Psathas, P. A.; Janowiak, M. L.; Garcia-Rubio, L. H.; Johnston, K. P. Formation of Carbon Dioxide in Water Miniemulsions Using the Phase Inversion Temperature Method. *Langmuir* **2002**, *18*, 3039-3046.

(100) Aveyard, R.; Binks, B. P.; Clark, S.; Mead, J. Interfacial Tension Minima in Oil-Water-Surfactant Systems: Behavior of Alkane-Aqueous NaCl Systems containing Aerosol OT. *J. Chme. Soc. Faraday Trans. I* **1986**, *82*, 125-142.

(101) Bourrel, M.; Schechter, R. S. *Microemulsions and Related Systems: Formation, Solvency, and Physical Properties*; Marcel Dekker: New York, 1988; Vol. 30.

(102) Aveyard, R.; Binks, B. P.; Clark, S.; Fletcher, P. D. I. Cloud points, solubilization, and interfacial tensions in systems containing nonionic surfactants. *Journal of Chemical Technology and Biotechnology* **1990**, *48*, 161-171.

(103) Varadaraj, R.; Bock, J.; Valint, P., Jr.; Zushma, S.; Thomas, R. Fundamental interfacial properties of alkyl-branched sulfate and ethoxy sulfate surfactants derived from Guerbet alcohols. 1. Surface and instantaneous interfacial tensions. *Journal of Physical Chemistry* **1991**, *95*, 1671-1676.

(104) Varadaraj, R.; Bock, J.; Zushma, S.; Brons, N.; Colletti, T. Effect of Hydrocarbon Chain Branching on Interfacial Properties of Monodisperse Ethoxylated Alcohol Sufactants. *Journal of Colloid and Interface Science* **1991**, *147*, 387.

(105) Huh, C. Equilibrium of a microemulsion that coexists with oil or brine. Soc. Pet. *Eng. J* **1983**, *23*, 829-847.

(106) Flory, P. J.; Krigbaum, W. R. Statistical mechanics of dilute polymer solutions. II. *Journal of Chemical Physics* **1950**, *18*, 1086-1094.

(107) Chen, X.; Adkins, S. S.; Sanders, A.; Nguyen, Q. P.; Johnston, K. P. Interfacial Tension and the Behavior of Microemulsions and Macroemulsions of Water and Carbon Dioxide with a Branched Hydrocarbon Nonionic Surfactant. *In prep* **2008**.

(108) Prokop, R. M.; Jyoti, A.; Eslamian, M.; Garg, A.; Mihaila, M.; del Rio, O. I.; Susnar, S. S.; Policova, Z.; Neumann, A. W. A study of captive bubbles with axisymmetric drop shape analysis. *Colloids and Surfaces, A: Physicochemical and Engineering Aspects* **1998**, *131*, 231-247.

(109) Schick, M. J.; Editor *Surfactant Science Series, Vol. 23: Nonionic Surfactants: Physical Chemistry*, 1987.

(110) Zhang, Z.; Xu, G.; Wang, F.; Du, G. Aggregation behaviors and interfacial properties of oxyethylated nonionic surfactants. *Journal of Dispersion Science and Technology* **2005**, *26*, 297-302.

(111) Penfold, J.; Thomas, R. K. Solvent distribution in non-ionic surfactant monolayers. *Physical Chemistry Chemical Physics* **2002**, *4*, 2648-2652.

(112) Hebach, A.; Oberhof, A.; Dahmen, N.; Kogel, A.; Ederer, H.; Dinjus, E. Interfacial Tension at Elevated Pressures-Measurements and Correlations in the Water + Carbon Dioxide System. *Journal of Chemical and Engineering Data* **2002**, *47*, 1540-1546.

(113) Lucassen-Reynders, E. H. Adsorption at fluid interfaces. *Surfactant Science Series* **1981**, *11*, 1-54.

(114) Ghaicha, L.; Leblanc, R. M.; Chattopadhyay, A. K. Ellipsometric study of surfactants comprising linear and branched hydrocarbon chains at the air-water interface. *Journal of Physical Chemistry* **1992**, *96*, 10948-10953.

(115) Aveyard, R.; Carr, N.; Slezok, H. Monolayers of mono- and dioxyethylene dodecyl ethers at air-water and alkane-water interfaces. *Canadian Journal of Chemistry* **1985**, *63*, 2742-2746.

(116) Kuhn, H.; Rehage, H. Molecular orientation of monododecyl pentaethylene glycol at water/air and water/oil interfaces. A molecular dynamics computer simulation study. *Colloid and Polymer Science* **2000**, *278*, 114-118.

(117) Wormuth, K. R.; Zushma, S. Phase behavior of branched surfactants in oil and water. *Langmuir* **1991**, *7*, 2048-2053.

(118) McFann, G. J. *Formation and Phase Behavior of Reverse Micelles and Microemulsions in Supercritical Fluids: Ethane, Propane and Carbon Dioxide. Ph.D. Dissertation*; The University of Texas at Austin: Austin, TX, 1994.

(119) Shervani, Z.; Liu, J.; Ikushima, Y. Very high solubilities of hydrogenated n-alkyl CO2-philes in sc CO2 at moderately low temperature and pressures. *New. J. Chem.* **2004**, *28*, 666-668.

(120) Drohmann, C.; Beckman, E. J. Phase behavior of polymers containing ether groups in carbon dioxide. *J. Supercrit. Fluids* **2002**, *22*, 103-110.

(121) Takishima, S.; O'Neill, M. L.; Johnston, K. P. Solubility of Block Copolymer Surfactants in Compressed CO2 Using a Lattice Fluid Hydrogen Bonding Model. *Ind. Eng. Chem. Res.* **1997**, *36*, 2821-2833.

(122) Rekvig, L.; Kranenburg, M.; Hafskjold, B.; Smit, B. Effect of surfactant structure on interfacial properties. *Europhysics Letters* **2003**, *63*, 902-907.

(123) Varandaraj, R.; Bock, J.; Zushma, S.; Brons, N.; Colletti, T. Effect of Hydrocarbon Chain Branching on Interfacial Properties of Monodisperse Ethoxylated Alcohol Sufactants. *Journal of Colloid and Interface Science* **1991**, *147*, 387.

(124) La Rosa, M.; Uhlherr, A.; Schiesser, C. H.; Moody, K.; Bohun, R.; Drummond, C. J. A Molecular Dynamics Study of Monolayers of Nonionic Poly(ethylene oxide) Based Surfactants. *Langmuir* **2004**, *20*, 1375-1385.

(125) Eastoe, J.; Paul, A.; Downer, A.; Steytler, D. C.; Rumsey, E. Effects of Fluorocarbon Surfactant Chain Structure on Stability of Water-in-Carbon Dioxide Microemulsions. Links between Aqueous Surface Tension and Microemulsion Stability. *Langmuir* **2002**, *18*, 3014-3017.

(126) Sirard, S. M.; Castellanos, H. J.; Hwang, H. S.; Lim, K.-T.; Johnston, K. P. Steric Stabilization of Silica Colloids in Supercritical Carbon Dioxide. *Industrial & Engineering Chemistry Research* **2004**, *43*, 525-534.

(127) Dickson, J. L.; Ortiz-Estrada, C.; Alvarado, J. F. J.; Hwang, H. S.; Sanchez, I. C.; Luna-Barcenas, G.; Lim, K. T.; Johnston, K. P. Critical flocculation density of dilute water-in-CO2 emulsions stabilized with block copolymers. *Journal of Colloid and Interface Science* **2004**, *272*, 444-456.

(128) Sirard, S. M.; Gupta, R. R.; Russell, T. P.; Watkins, J. J.; Green, P. F.; Johnston, K. P. Structure of End-Grafted Polymer Brushes in Liquid and Supercritical Carbon Dioxide: A Neutron Reflectivity Study. *Macromolecules* **2003**, *36*, 3365-3373.

(129) Melnichenko, Y. B.; Kiran, E.; Heath, K. D.; Salaniwal, S.; Cochran, H. D.; Stamm, M.; Van Hook, W. A.; Wignall, G. D. Comparison of the behaviour of polymers in supercritical fluids and organic solvents via small-angle neutron scattering. *Journal of Applied Crystallography* **2000**, *33*, 682-685.

(130) Luna-Barcenas, G.; Meredith, J. C.; Sanchez, I. C.; Johnston, K. P.; Gromov, D. G.; de Pablo, J. J. Relationship between polymer chain conformation and phase boundaries in a supercritical fluid. *Journal of Chemical Physics* **1997**, *107*, 10782-10792.

(131) Schick, M. J. Physical chemistry of nonionic detergents. *Journal of the American Oil Chemists' Society* **1963**, *40*, 680-687.

(132) Kratzat, K.; Finkelmann, H. Influence of the Molecular Geometry of Nonionic Surfactants on Surface and Micellar Properties in Aqueous Solutions. *Langmuir* **1996**, *12*, 1765-1770.

(133) Johnston, K. P.; Da Rocha, S. *Journal of Supercritical Fluids* **2009**, *(In press)*.

(134) "Enhanced Oil Recovery Scoping Study (TR-113836)," EPRI, Palo Alto, CA, 1999.

(135) da Rocha, S. R. P.; Johnston, K. P. Interfacial Thermodynamics of Surfactants at the CO2-Water Interface. *Langmuir* **2000**, *16*, 3690-3695.

(136) Sagisaka, M.; Fujii, T.; Ozaki, Y.; Yoda, S.; Takebayashi, Y.; Kondo, Y.; Yoshino, N.; Sakai, H.; Abe, M.; Otake, K. Interfacial properties of branch-tailed fluorinated surfactants yielding a water/supercritical CO2 microemulsion. *Langmuir* **2004**, *20*, 2560-2566. .

(137) Psathas, P. A.; da Rocha, S. R. P.; Lee, C. T.; Johnston, K. P.; Lim, K. T.; Webber, S. E. Water-in-Carbon Dioxide Emulsions with PDMS based Block Copolymer Ionomers. *Industrial Engineering and Chemistry Research* **2000**, *39*, 2655-2664.

(138) Johnston, K. P.; Harrison, K.; O'Neill, M.; Yates, M. Emulsions and microemulsions in supercritical fluids. *Book of Abstracts, 211th ACS National Meeting, New Orleans, LA, March 24-28* **1996**, I&EC-093.

(139) McClain, J. B.; Betts, D. E.; Canelas, D. A.; Samulski, E. T.; DeSimone, J. M.; Londono, J. D.; Cochran, H. D.; Wignall, G. D.; Chillura-Martino, D.; Triolo, R. Design of Nonionic Surfactants for Supercritical Carbon Dioxide. *Science* **1996**, *274*, 2049.

(140) Lee, C. T., Jr.; Ryoo, W.; Smith, P. G., Jr.; Arellano, J.; Mitchell, D. R.; Lagow, R. J.; Webber, S. E.; Johnston, K. P. Carbon dioxide-in-water microemulsions. *Journal of the American Chemical Society* **2003**, *125*, 3181-3189.

(141) Danov, K. D. Effect of surfactants on drop stability and thin film drainage. *Courses and Lectures - International Centre for Mechanical Sciences* **2004**, *463*, 1-38.

(142) Edwards, D. A.; Brenner, H.; Wasan, D. T. *Interfacial Transport Processes and Rheology*; Butterworth-Heinemann: Boston, 1991.

(143) Bhakta, A.; Ruckenstein, E. Foams and Concentrated Emulsions: Dynamics and "Phase" Behavior. *Langmuir* **1995**, *11*, 4642-4652.

(144) Joye, J.-L.; Hirasaki, G. J.; Miller, C. A. Asymmetric Drainage in Foam Films. *Langmuir* **1994**, *10*, 3174-3179.

(145) Langevin, D. Influence of interfacial rheology on foam and emulsion properties. *Advances in Colloid and Interface Science* **2000**, *88*, 209-222.

(146) Adkins, S. S.; Chen, X.; Sanders, A.; Nguyen, Q. P.; Johnston, K. P. Comparing the Interfacial Properties of Nonionic Hydrocarbon Surfactants at the Air-Water and Carbon Dioxide-Water Interfaces. *in prep* **2009**.

(147) Guo, X.; Rong, Z.; Ying, X. Calculation of hydrophile-lipophile balance for polyethoxylated surfactants by group contribution method. *Journal of Colloid and Interface Science* **2006**, *298*, 441-450.

(148) da Rocha, S. R. P.; Psathas, P. A.; Klein, E.; Johnston, K. P. Concentrated CO2-in-Water Emulsions with Nonionic Polymeric Surfactants. *Journal of Colloid and Interface Science* **2001**, *239*, 241-253.

(149) Bonfillon-Colin, A.; Langevin, D. Why Do Ethoxylated Nonionic Surfactants Not Foam at High Temperature? *Langmuir* **1997**, *13*, 599-601.

(150) Bancroft, W. D. The Theory of Emulsification. *Journal of Physical Chemistry* **1913**, *17*, 501-520.

(151) Aveyard, R.; Binks, B. P.; Esquena, J.; Fletcher, P. D. I.; Bault, P.; Villa, P. Flocculation Transitions of Weakly Charged Oil-in-Water Emulsions Stabilized by Different Surfactants. *Langmuir* **2002**, *18*, 3487-3494.

(152) Manoj, P.; Watson, A. D.; Hibberd, D. J.; Fillery-Travis, A. J.; Robins, M. M. Characterization of a Depletion-Flocculated Polydisperse Emulsion II. Steady-State Rheological Investigations. *Journal of Colloid and Interface Science* **1998**, *207*, 294-302.

(153) Binks, B. P. In *Modern Aspects of Emulsion Science*; Binks, B. P., Ed.; The Royal Society of Chemistry: Cambridge, 1998.

(154) Lewis, J. E.; Biswas, R.; Robinson, A. G.; Maroncelli, M. Local Density Augmentation in Supercritical Solvents: Electronic Shifts in Anthracene Derivatives. *Journal of Physical Chemistry B* **2001**, *105*, 3306-3318.

(155) Wohlfarth, C.; Wohlfarth, B. In *Group III: Condensed Mater*; Lechner, M. D., Ed.; Springer-Verlag, 1996; Vol. 38B.

(156) Wood, R.; www.robinwood.com; Vol. 2008.

(157) Stubenrauch, C.; von Klitzing, R. Disjoining pressure in thin liquid foam and emulsion films-new concepts and perspectives. *Journal of Physics: Condensed Matter* **2003**, *15*, R1197-R1232.

(158) Karraker, K. A.; Radke, C. J. Disjoining pressures, zeta potentials and surface tensions of aqueous non-ionic surfactant/electrolyte solutions: theory and comparison to experiment. *Advances in Colloid and Interface Science* **2002**, *96*, 231-264.

(159) Ryoo, W.; Dickson, J. L.; Dhanuka, V. V.; Webber, S. E.; Bonnecaze, R. T.; Johnston, K. P. Electrostatic Stabilization of Colloids in Carbon Dioxide: Electrophoresis and Dielectrophoresis. *Langmuir* **2005**, *21*, 5914-5923.

(160) Aronson, A. S.; Bergeron, V.; Fagan, M. E.; Radke, C. J. The influence of disjoining pressure on foam stability and flow in porous media. *Colloids and Surfaces, A: Physicochemical and Engineering Aspects* **1994**, *83*, 109-120.

(161) Sadoc, J. F.; Rivier, N.; Editors *Foams and Emulsions. (Proceedings of the NATO Advanced Study Institute on Foams and Emulsions, Emulsions and Cellular Materials, held 12-24 May 1997, in Cargese, Corsica.) [In: NATO ASI Ser., Ser. E, 1999; 354]*, 1999.

(162) Lucassen-Reynders, E. H.; Cagna, A.; Lucassen, J. Gibbs elasticity, surface dilational modulus and diffusional relaxation in nonionic surfactant monolayers. *Colloids and Surfaces, A: Physicochemical and Engineering Aspects* **2001**, *186*, 63-72.

(163) Bonfillon, A.; Langevin, D. Viscoelasticity of monolayers at oil-water interfaces. *Langmuir* **1993**, *9*, 2172-2177.

(164) Saint-Jalmes, A.; Durian, D.; Weitz, D. In *Kirk-Othmer Encyclopedia of Chemical Technology*; Kroschwitz, J. I., Seidel, A., Eds.; Wiley-Interscience: Hoboken, N.J., 2004; Vol. 12.

(165) Varadaraj, R.; Bock, J.; Valint, P., Jr.; Zushma, S.; Brons, N. Relationship between fundamental interfacial properties and foaming in linear and branched sulfate, ethoxysulfate, and ethoxylate surfactants. *Journal of Colloid and Interface Science* **1990**, *140*, 31-34.

(166) Velev, O. D.; Constantinides, G. N.; Avraam, D. G.; Payatakes, A. C.; Borwankar, R. P. Investigation of thin liquid films of small diameters and high capillary pressures by a miniaturized cell. *Journal of Colloid and Interface Science* **1995**, *175*, 68-76.

(167) Schmitt, V.; Cattelet, C.; Leal-Calderon, F. Coarsening of Alkane-in-Water Emulsions Stabilized by Nonionic Poly(oxyethylene) Surfactants: The Role of Molecular Permeation and Coalescence. *Langmuir* **2004**, *20*, 46-52.

(168) Varadaraj, R.; Bock, J.; Geissler, P.; Zushma, S.; Brons, N.; Colletti, T. Influence of ethoxylate distribution on interfacial properties of linear and branched ethoxylate surfactants. *Journal of Colloid and Interface Science* **1991**, *147*, 396-402.

(169) Lifshitz, I. M.; Slyozov, V. V. *Sov. Phys. JETP* **1959**, *35*, 331.

(170) Wagner, C. Theorie der Alterung von Niederschlagen durch Umlosen. *Z. Elektrochem* **1961**, *65*, 581-594.

(171) Schmitt, V.; Leal-Calderon, F. Measurement of the coalescence frequency in surfactant-stabilized concentrated emulsions. *Europhysics Letters* **2004**, *67*, 662-668.

(172) Marsh, S. P.; Glicksman, M. E. Kinetics of phase coarsening in dense systems. *Acta Materialia* **1996**, *44*, 3761-3771.

(173) Tsau, J.-S.; Heller, J. P. In *Permian Basin Oil and Gas Recovery Conference*; Society of Petroleum Engineers, Inc.: Midland, TX, 1992.

(174) Lee, H. O.; Heller, J. P.; Hoefer, A. M. W. Change in Apparent Viscosity of Carbon Dioxide Foam with Rock Permeability. *SPE Reservoir Engineering* **1991**, 421-428.

(175) Lee, H. O.; Heller, J. P. Laboratory measurements of carbon dioxide foam mobility. *SPE Reservoir Engineering* **1990**, *5*, 193-197.

(176) Yan, W.; Miller, C. A.; Hirasaki, G. J. Foam sweep in fractures for enhanced oil recovery. *Colloids and Surfaces, A: Physicochemical and Engineering Aspects* **2006**, *282-283*, 348-359.

(177) Reidenbach, V. G.; Harris, P. C.; Lee, Y. N.; Lord, D. L. Rheological Study of Foam Fracturing Fluids Using Nitrogen and Carbon Dioxide. *SPE Production Engineering* **1986**, *1*, 31-41.

(178) Hutchins, R. D.; Miller, M. J. A circulating-foam loop for evaluating foam at conditions of use. *SPE Production & Facilities* **2005**, *20*, 286-294.

(179) Smith, D. H.; Johnston, E. L. Viscosities of dispersions of supercritical carbon dioxide in surfactant/carbon dioxide/water/sodium chloride systems. *Journal of Dispersion Science and Technology* **1988**, *9*, 33-59.

(180) Welch, C. F.; Rose, G. D.; Malotky, D.; Eckersley, S. T. Rheology of high internal phase emulsions. *Langmuir* **2006**, *22*, 1544-1550.

(181) Cates, M. E.; Sollich, P. In *Foams and Emulsions*; Sadoc, J. F., Rivier, N., Eds.; Kluwer Academic Publishers: Dordrecht, Netherlands, 1999, pp 207-236.

(182) Princen, H. M.; Kiss, A. D. Rheology of foams and highly concentrated emulsions. IV. An experimental study of the shear viscosity and yield stress of concentrated emulsions. *Journal of Colloid and Interface Science* **1989**, *128*, 176-187.

(183) Kraynik, A. M.; Neilsen, M. K.; Reinelt, D. A.; Warren, W. E. In *Foams and Emulsions*; Sadoc, J. F., Rivier, N., Eds.; Kluwer Academic Publishers: Dordrecht, Netherlands, 1999, pp 259-286.

(184) Verbist, G.; Weaire, D.; Phelan, R. In *Foams and Emulsions*; Sadoc, J. F., Rivier, N., Eds.; Kluwer Academic Publishers: Dordrecht, Netherlands, 1999; Vol. 354, pp 303-314.

(185) Whorlow, R. W. *Rheological Techniques*; second ed.; Ellis Horwood: New York, 1992.

(186) Harris, P. C. Effects of texture on rheology of foam fracturing fluids. *SPE Production Engineering* **1989**, *4*, 249-257.

(187) Bekkour, K.; Scrivener, O. Time-dependent and Flow Properties of Foams. *Mechanics of Time-Dependent Materials* **1998**, *2*, 171-193.

(188) Becher, P., Ed. *Encyclopeida of Emulsion Technology*; Marcel Dekker, Inc.: New York, 1996; Vol. 4.

(189) Patton, J. T.; Holbrook, S. T.; Hsu, W. Rheology of mobility-control foams. *SPEJ, Society of Petroleum Engineers Journal* **1983**, *23*, 456-460.

(190) Enzendorfer, C.; Harris, R. A.; Valko, P.; Economides, M. J.; Fokker, P. A.; Davies, D. D. Pipe viscometry of foams. *Journal of Rheology (New York)* **1995**, *39*, 345-358.

(191) Otsubo, Y.; Prud'homme, R. K. Rheology of oil-in-water emulsions. *Rheologica Acta* **1994**, *33*, 29-37.

(192) Friedmann, F.; Jensen, J. A. In *SPE California Regional Meeting*; Society of Petroleum Engineers, Inc.: Oakland, CA, 1986.

(193) Herzhaft, B.; Kakadjian, S.; Moan, M. Measurement and modeling of the flow behavior of aqueous foams using a recirculating pipe rheometer. *Colloids and Surfaces, A: Physicochemical and Engineering Aspects* **2005**, *263*, 153-164.

(194) McFann, G. J.; Howdle, S. M.; Johnston, K. P. Solubilization in Nonionic Reverse Micelles in Carbon Dioxide. *AIChE* **1994**, *40*, 543.

(195) Fulton, J. L.; Pfund, D. M.; McClain, J. B.; Romack, T. J.; Maury, E. E.; Combes, J. R.; Samulski, E. T.; DeSimone, J. M.; Capel, M. Aggregation of Amphiphilic Molecules in Supercritical Carbon Dioxide: A Small Angle X-ray Scattering Study. *Langmuir* **1995**, *11*, 4241-4249.

(196) Consani, K. A.; Smith, R. D. Observations on the solubility of surfactants and related molecules in carbon dioxide at 50°C. *Journal of Supercritical Fluids* **1990**, *3*, 51-65.

(197) Hoefling, T. A.; Beitle, R. R.; Enick, R. M.; Beckman, E. J. Design and synthesis of highly carbon dioxide-soluble surfactants and chelating agents. *Fluid Phase Equilibria* **1993**, *83*, 203-212.

(198) Dong, X.; Erkey, C.; Dai, H. J.; Li, H. C.; Cochran, H. D.; Lin, J. S. Phase Behavior and Micelle Size of an Aqueous Microdispersion in Supercritical CO2 with a Novel Surfactant. *Industrial & Engineering Chemistry Research* **2002**, *41*, 1038-1042.

(199) Sagisaka, M.; Yoda, S.; Takebayashi, Y.; Otake, K.; Kitiyanan, B.; Kondo, Y.; Yoshino, N.; Takebayashi, K.; Sakai, H.; Abe, M. Preparation of W/scCO2 Microemulsions Using Flourinated Surfactants. *Langmuir* **2003**, *19*, 220-225.

(200) Liu, J.; Han, B.; Li, G.; Zhang, X.; He, J.; Liu, Z. Investigation of Nonionic Surfactant Dynol-604 Based Reverse Microemulsion Formed in Supercritical Carbon Dioxide. *Langmuir* **2001**, *17*, 8040-8043.

(201) Cooper, A. I. Porous Materials and Supercritical Fluids. *Advanced Materials* **2003**, *15*, 1049-1059.

(202) Jacobson, G. B.; Lee, C. T.; Johnston, K. P.; Tumas, W. Enhanced Catalyst Raectivity and Separations Using Water-Carbon Dioxide Emulsions. *Journal of the American Chemical Society* **1999**, *121*, 11902-11903.

(203) Meziani, M. J.; Pathak, P.; Beacham, F.; Allard, L. F.; Sun, Y.-P. Nanoparticle formation in rapid expansion of water-in-supercritical carbon dioxide microemulsion into liquid solution. *Journal of Supercritical Fluids* **2005**, *34*, 91-97.

(204) Wang Joanna, S.; Pan, H.-B.; Wai Chien, M. Deposition of metal nanoparticles on carbon nanotubes via hexane modified water-in-CO2 microemulsion at room temperature. *Journal of nanoscience and nanotechnology* **2006**, *6*, 2025-2030.

(205) Soman, Y. S.; Kuzmenko, T.; Hebb, A.; Kellici, S.; Darr, J. A. Nanograined, hard copper films from "water in CO2" emulsion electrodeposition. *Indian Surface Finishing* **2006**, *3*, 215-221.

(206) Holmes, J. D.; Ziegler, K. J.; Doty, R. C.; Pell, L. E.; Johnston, K. P.; Korgel, B. A. Highly Luminescent Silicon Nanocrystals with Discrete Optical Transitions. *Journal of the American Chemical Society* **2001**, *123*, 3743.

(207) Ohde, H.; Wai, C. M.; Kim, H.; Kim, J.; Ohde, M. Hydrogenation of Olefins in Supercritical CO2 Catalyzed by Palladium Nanoparticles in a Water-in-CO2 Microemulsion. *Journal of the American Chemical Society* **2002**, *124*, 4540-4541.

(208) Keagy, J. A.; Zhang, X.; Johnston, K. P.; Busch, E.; Weber, F.; Wolf, P. J.; Rhoad, T. Cleaning of patterned porous low-k dielectrics with water, carbon dioxide and ambidextrous surfactants. *Journal of Supercritical Fluids* **2006**, *39*, 277-285.

(209) Smith, P. G., Jr.; Ryoo, W.; Johnston, K. P. Electrostatically Stabilized Metal Oxide Particle Dispersions in Carbon Dioxide. *Journal of Physical Chemistry B* **2005**, *109*, 20155-20165.

(210) Melle, S.; Lask, M.; Fuller, G. G. Pickering Emulsions with Controllable Stability. *Langmuir* **2005**, *21*, 2158-2162.

(211) Dai, L. L.; Sharma, R.; Wu, C.-Y. Self-assembled structure of nanoparticles at a liquid-liquid interface. *Langmuir* **2005**, *21*, 2641-2643.

(212) Binks, B. P.; Lumsdon, S. O. Catastrophic Phase Inversion of Water-in-Oil Emulsions Stabilized by Hydrophobic Silica. *Langmuir* **2000**, *16*, 2539-2547.

(213) Binks, B. P.; Lumsdon, S. O. Stability of oil-in-water emulsions stabilised by silica particles. *Physical Chemistry Chemical Physics* **1999**, *1*, 3007-3016.

(214) Dickson, J. L.; Binks, B. P.; Johnston, K. P. Stabilization of Carbon Dioxide-in-Water Emulsions Using Silica Particles. *Langmuir* **2004**, *20*, 7976-7983.

(215) Golomb, D.; Barry, E.; Ryan, D.; Lawton, C.; Swett, P. Limestone-Particle-Stabilized Macroemulsion of Liquid and Supercritical Carbon Dioxide in Water for Ocean Sequestration. *Environmental Science and Technology* **2004**, *38*, 4445-4450.

(216) Golomb, D.; Pennell, S.; Ryan, D.; Barry, E.; Swett, P. Ocean Sequestration of Carbon Dioxide: Modeling the Deep Ocean Release of a Dense Emulsion of Liquid CO2-in-Water Stabilized by Pulverized Limestone Particles. *Environmental Science & Technology* **2007**, ACS ASAP.

(217) Golomb, D.; Barry, E.; Ryan, D.; Swett, P.; Duan, H. Macroemulsions of Liquid and Supercritical CO2-in-Water and Water-in-Liquid CO2 Stabilized by Fine Particles. *Industrial & Engineering Chemistry Research* **2006**, *45*, 2728-2733.

(218) Dickson, J. L.; Adkins, S. S.; Cao, T.; Webber, S. E.; Johnston, K. P. Interactions of Core-Shell Silica Nanoparticles in Liquid Carbon Dioxide Measured by Dynamic Light Scattering. *Industrial & Engineering Chemistry Research* **2006**, *45*, 5603-5613.

(219) Dickson, J. L.; Shah, P. S.; Binks, B. P.; Johnston, K. P. Steric Stabilization of Core-Shell Nanoparticles in Liquid Carbon Dioxide at the Vapor Pressure. *Langmuir* **2004**, *20*, 9380-9387.

(220) Dickson, J. L.; Gupta, G.; Horozov, T. S.; Binks, B. P.; Johnston, K. P. Wetting Phenomena at the CO2/Water/Glass Interface. *Langmuir* **2006**, *22*, 2161-2170.

(221) Binks, B. P.; Lumsdon, S. O. Effects of oil type and aqueous phase composition on oil-water mixtures containing particles of intermediate hydrophobicity. *Physical Chemistry Chemical Physics* **2000**, *2*, 2959-2967.

(222) Binks, B. P. Particles as surfactants - similarities and differences. *Current Opinion in Colloid and Interface Science* **2002**, *7*, 21-41.

(223) Binks, B. P.; Lumsdon, S. O. Influence of Particle Wettability on the Type and Stability of Surfactant-Free Emulsions. *Langmuir* **2000**, *16*, 8622-8631.

(224) Midmore, B. R. Preparation of a novel silica-stabilized oil/water emulsion. *Colloids and Surfaces A: Physiochemical and Engineering Aspects* **1998**, *132*, 257-265.

(225) Tarimala, S.; Wu, C.-y.; Sharma, R.; Dai, L. L. Structure of microparticles and nanoparticles in solid-stabilized emulsions. *AIChE Annual Meeting, Conference Proceedings, Cincinnati, OH, United States, Oct. 30-Nov. 4, 2005* **2004**, 18b/11-18b/16.

(226) Binks, B. P.; Rodrigues, J. A. Enhanced Stabilization of Emulsions Due to Surfactant-Induced Nanoparticle Flocculation. *Langmuir* **2007**, ACS ASAP.

(227) Tripp, C. P.; Combes, J. R. Chemical Modification of Metal Oxide Surfaces in Supercritical CO2: The Interaction of Supercritical CO2 with the Adsorbed Water Layer and the Surface Hydroxyl Groups of a Silica Surface. *Langmuir* **1998**, *14*, 7348-7352.

(228) Binks, B. P.; Whitby, C. P. Nanoparticle silica-stabilized oil-in-water emulsions: improving emulsion stability. *Colloids and Surfaces, A: Physicochemical and Engineering Aspects* **2005**, *253*, 105-115.

(229) Bragg, J. R. In *U.S.*; (Exxon Production Research Company, USA). Us, 1999, pp 21 pp., Cont.-in-part of U.S. Ser. No. 885,507.

(230) Bragg, J. R.; Kaminsky, R. D.; Leonardi, S. A. In *PCT Int. Appl.*; (ExxonMobil Upstream Research Company, USA). Wo, 2007, p 26pp.

(231) Walstra, P.; Smulders, P. E. A. In *Modern Aspects of Emulsion Technology*; Binks, B. P., Ed.; The Royal Society of Chemistry: Cambridge, 1998, pp 56-99.

(232) Lake, L. *Enhanced Oil Recovery*; Prentice Hall: Englewood Cliffs, NJ, 1989.

(233) Rossen, W. R. Theory of mobilization pressure gradient of flowing foams in porous media. III. Asymmetric lamella shapes. *Journal of Colloid and Interface Science* **1990**, *136*, 38-53.

(234) Lee, C. T., Jr.; Johnston, K. P.; Dai, H. J.; Cochran, H. D.; Melnichenko, Y. B.; Wignall, G. D. Droplet Interactions in Water-in-Carbon Dioxide Microemulsions Near the Critical Point: A Small-Angle Neutron Scattering Study. *Journal of Physical Chemistry B* **2001**, *105*, 3540-3548.

(235) Liu, Y.; Kathan, K.; Saad, W.; Prud'homme, R. K. Ostwald Ripening of b-Carotene Nanoparticles. *Physical Review Letters* **2007**, *98*, 036102/036101-036102/036104.

(236) Randolph, T. W.; Blanch, H. W.; Prausnitz, J. M.; Wilke, C. R. Enzymatic Catalysis in a Supercritical Fluid. *Biotechnology Letters* **1985**, *7*, 325-328.

(237) Hobbs, H. R.; Thomas, N. R. Biocatalysis in Supercritical Fluids, Fluorous Solvents and under Solvent-Free Conditions. *Chemical Reviews* **2007**, *107*, 2786-2820.

(238) Al-Duri, B.; Goddard, R.; Bosley, J. Characterisation of a novel support for biocatalysis in supercritical carbon dioxide. *J. Mol Catal. B: Enzym.* **2001**, *11*, 825-834.

(239) Matsuda, T.; Watanabe, K.; Harada, T.; Nakamura, K.; Arita, Y.; Misumi, Y.; Ichikawa, S.; Ikariya, T. High-efficiency and minimum-waste continuous kinetic resolution of racemic alcohols by using lipase in supercritical carbon dioxide. *Chem. Commun.* **2004**, 2286-2287.

(240) Zhang, Z. H.; Tsuyumoto, I.; Kitamori, T.; Sawada, T. Observation of the Dynamic and Collective Behavior of Surfactant Molecules at a Water/Nitrobenzene Interface by a Time-Resolved Quasi-Elastic Laser-Scattering Method. *Journal of Physical Chemistry B* **1998**, *102*, 10284-10287.

(241) Habulin, M.; Knez, Z. Pressure stability of lipases and their use in different systems. *Acta Chimica Slovenica* **2001**, *48*, 521-532.

(242) Dijkstra, Z. J., Weyten, H., Willems, L., Keurentjes, J.T.F. The effect of water concentration on the activity and stability of CLECs in supercritical CO2 in continuous operation. *J. Mol Catal. B: Enzym.* **2006**, *39*, 112-116.

(243) Hobbs, H. R. Biocatalysis in 'Green' Solvents. *Ph.D. Thesis* **2006**, *School of Chemistry*.

(244) Matsuda, T.; Tsuji, K.; Kamitanaka, T.; Harada, T.; Nakamura, K.; Ikariya, T. Rate enhancement of lipase-catalyzed reaction in supercritical carbon dioxide. *Chem. Lett.* **2005**, *34*, 1102-1103.

(245) Kane, M. A.; Baker, G. A.; Pandey, S.; Bright, F. V. Performance of cholesterol oxidase sequestered within reverse micelles formed in supercritical carbon dioxide. *Langmuir* **2000**, *16*, 4901-4905.

(246) Matsuda, T.; Ohashi, Y.; Harada, T.; Yanagihara, R.; Nagasawa, T.; Nakamura, K. Conversion of pyrrole to pyrrole-2-carboxylate by cells of Bacillus megaterium in supercritical CO2. *Chem. Commun.* **2001**, 2194-2195.

(247) Hobbs, H. R.; Kirke, H. M.; Poliakoff, M.; Thomas, N. R. Homogeneous Biocatalysis in both Fluorous Biphasic and Supercritical Carbon Dioxide Systems. *Angewandte Chemie International Edition* **2007 (Ref. anie. 200701488)**.

(248) Adjei, A.; Rao, S.; Garren, J.; Menon, G.; Vadnere, M. Effect of Ion-Pairing on 1-Octanol-Water Partitioning of Peptide Drugs .1. the Nonapeptide Leuprolide Acetate. *International Journal of Pharmaceutics* **1993**, *90*, 141-149.

(249) Matsuura, J.; Powers, M. E.; Manning, M. C.; Shefter, E. Structure and Stability of Insulin Dissolved in 1-Octanol. *Journal of the American Chemical Society* **1993**, *115*, 1261-1264.

(250) Powers, M. E.; Matsuura, J.; Brassell, J.; Manning, M. C.; Shefter, E. Enhanced Solubility of Proteins and Peptides in Nonpolar-Solvents through Hydrophobic Ion-Pairing. *Biopolymers* **1993**, *33*, 927-932.

(251) Paradkar, V. M.; Dordick, J. S. Aqueous-Like Activity of Alpha-Chymotrypsin Dissolved in Nearly Anhydrous Organic-Solvents. *J. Am. Chem. Soc.* **1994**, *116*, 5009-5010.

(252) Falk, R.; Randolph, T. W.; Meyer, J. D.; Kelly, R. M.; Manning, M. C. Controlled release of ionic compounds from poly (L-lactide) microspheres produced by precipitation with a compressed antisolvent. *Journal of Controlled Release* **1997**, *44*, 77-85.

(253) Kendrick, B. S.; Meyer, J. D.; Matsuura, J. E.; Carpenter, J. F.; Manning, M. C. Hydrophobic ion pairing as a method for enhancing structure and activity of lyophilized subtilisin BPN' suspended in isooctane. *Arch. Biochem. Biophys.* **1997**, *347*, 113-118.

(254) Bindhu, L. V.; Abraham, T. E. Preparation and kinetic studies of surfactant-horseradish peroxidase ion paired complex in organic media. *Biochem. Eng. J.* **2003**, *15*, 47-57.

(255) Wilkins, D. K.; Grimshaw, S. B.; Receveur, V.; Dobson, C. M.; Jones, J. A.; Smith, L. J. Hydrodynamic radii of native and denatured proteins measured by pulse field gradient NMR techniques. *Biochemistry* **1999**, *38*, 16424-16431.

(256) Krigbaum, W. R.; Godwin, R. W. Molecular Conformation of Chymotrypsinogen and Chymotrypsin by Low-Angle X-Ray Diffraction. *Biochemistry* **1968**, *7*, 3126-&.

(257) Akbar, U.; Aschenbrenner, C. D.; Harper, M. R.; Johnson, H. R.; Dordick, J. S.; Clark, D. S. Direct solubilization of enzyme aggregates with enhanced activity in nonaqueous media. *Biotechnology and Bioengineering* **2007**, *96*, 1030-1039.

(258) Meredith, J. C.; Johnston, K. P. In *Supercritical Fluids Fundamentals and Applications*; E. Kiran, P. D., C. Peters, Ed.; Kluwer Acad.: Dordrecht, 2000, pp 211-228.

(259) O'Neill, M. L.; Yates, M. Z.; Harrison, K. L.; Johnston, K. P.; Canelas, D. A.; Betts, D. E.; DeSimone, J. M.; Wilkinson, S. P. Emulsion stabilization and flocculation in CO2. 1. Turbidimetry and tensiometry. *Macromolecules* **1997**, *30*, 5050-5059.

(260) Sagisaka, M.; Koike, D.; Yoda, S.; Takebayashi, Y.; Furuya, T.; Yoshizawa, A.; Sakai, H.; Abe, M.; Otake, K. Optimum Tail Length of Fluorinated Double-Tail Anionic Surfactant for Water/Supercritical CO2 Microemulsion Formation. *Langmuir* **2007**, *23*, 8784-8788.

(261) Saunders, A. E.; Shah, P. S.; Park, E. J.; Lim, K. T.; Johnston, K. P.; Korgel, B. A. Solvent Density-Dependent Steric Stabilization of Perfluoropolyether-Coated Nanocrystals in Supercritical Carbon Dioxide. *Journal of Physical Chemistry B* **2004**, *108*, 15969-15975.

(262) Mukejere, P.; Gumkowski, M. J.; Chan, C. C.; Sharma, R. Determination of critical micellar concentrations of perfluorocarboxylates using ultraviolet spectroscopy: some unusual effects. *Journal of PHysical Chemistry* **1990**, *94*, 8832-8835.

(263) Provencher, S. W. Eigenfunction Expansion Method for Analysis of Exponential Decay Curves. *J. Chem. Phys.* **1976**, *64*, 2773-2777.

(264) *Dispersion Technology Software (Nano series and HPPS)*; Malvern Instruments: Malvern, U.K., 2002 - 2003.

(265) Dahl, K.; Biswas, R.; Maroncelli, M. The photophysics and dynamics of diphenylbutadiene in alkane and perfluoroalkane solvents. *Journal of Physical Chemistry B* **2003**, *107*, 7838-7853.

(266) Lide., E.-i.-c. D. R. *CRC handbook of chemistry and physics : a ready-refererence book of chemical and physical data. 85th ed.*; CRC Press: London, 2004.

(267) Licence, P.; Dellar, M. P.; Wilson, R. G. M.; Fields, P. A.; Litchfield, D.; Woods, H. M.; Poliakoff, M.; Howdle, S. M. Large-aperture variable-volume view cell for the determination of phase-equilibria in high pressure systems and supercritical fluids. *Rev. Sci. Instrum.* **2004**, *75*, 3233-3236.

(268) Grochulski, P.; Li, Y.; Schrag, J. D.; Cygler, M. 2 Conformational States of Candida-Rugosa Lipase. *Protein Science* **1994**, *3*, 82-91.

(269) Shah, P. S.; Husain, S.; Johnston, K. P.; Korgel, B. A. Role of Steric Stabilization on the Arrested Growth of Silver Nanocrystals in Supercritical Carbon Dioxide. *Journal of Physical Chemistry B* **2002**, *106*, 12178-12185.

(270) Imura, T.; Gotoh, T.; Otake, K.; Yoda, S.; Takebayashi, Y.; Yokoyama, S.; Takebayashi, H.; Sakai, H.; Yuasa, M.; Abe, M. Control of Physicochemical

Properties of Liposomes Using a Supercritical Reverse Phase Evaporation Method. *Langmuir* **2003**, *19*, 2021-2025.

(271) Leser, M. E.; Luisi, P. L. Application of Reverse Micelles for the Extraction of Amino-Acids and Proteins. *Chimia* **1990**, *44*, 270-282.

(272) Barbaric, S.; Luisi, P. L. Micellar Solubilization of Bio-Polymers in Organic-Solvents .5. Activity and Conformation of Alpha-Chymotrypsin in Isooctane-Aot Reverse Micelles. *J. Am. Chem. Soc.* **1981**, *103*, 4239-4244.

(273) Ghenciu, E. G.; Russell, A. J.; Beckman, E. J.; Steele, L.; Becker, N. T. Solubilization of subtilisin in CO2 using fluoroether- functional amphiphiles. *Biotechnology and Bioengineering* **1998**, *58*, 572-580.

(274) Pich, J.; Friedlander, S. K.; Lai, F. S. The Self-Preserving Particle Size Distribution for Coagulaion by Brownian Motion--III. *Aerosol Science* **1970**, *1*, 115-126.

(275) Shaw, D. J. *Introduction to Colloid and Surface Chemistry*; 4 ed.; Butterworth-Heinemann Ltd.: Boston, 1989.

(276) Okuda, T.; Kidoaki, S.; Ohsaki, M.; Koyama, Y.; Yoshikawa, K.; Niidome, T.; Aoyagi, H. Time-dependent complex formation of dendritic poly(L-lysine) with plasmid DNA and correlation with in vitro transfection efficiencies. *Organic & Biomolecular Chemistry* **2003**, *1*, 1270-1273.

(277) Ju, R. T. C.; Frank, C. W.; Gast, A. P. CONTIN analysis of colloidal aggregates. *Langmuir* **1992**, *8*, 2165-2171.

(278) Kyriakidis, A. S.; Yiantsios, S. G.; Karabelas, A. J. A Study of Colloidal Particle Brownian Aggregation by Light Scattering Tecniques. *Journal of Colloid and Interface Science* **1997**, *195*, 299-306.

(279) Matsoukas, T.; Friedlander, S. K. Dynamics of Aerosol Agglomerate Formation. *Journal of Colloid and Interface Science* **1991**, *146*, 495-506.

(280) Hidy, G. M. On the Theory of the Coagulation on Noninteracting Particles in Brownian Motion. *Journal of Colloid Science* **1965**, *20*, 123-144.

(281) Friedlander, S. K. *Smoke, Dust, and Haze*; John Wiley and Sons: New York, 1977.

(282) Friedlander, S. K.; Wang, C. S. The Self-Preserving Particle Size Distribution for Coagulation by Brownian Motion. *Journal of Colloid and Interface Science* **1966**, *22*, 126-132.

(283) Peck, D. G.; Johnston, K. P. Lattice fluid self-consistent field theory of surfaces with anchored chains. *Macromolecules* **1993**, *26*, 1537-1545.

(284) Meredith, J. C.; Johnston, K. P. Theory of Polymer Adsorption and Colloidal Stabilization in Supercritical Fluids. 2. Copolymer and End-Grafted Stabilizers. *Macromolecules* **1998**, *31*, 5518-5528.

(285) Meredith, J. C.; Johnston, K. P. Density Dependence of Homopolymer Adsorption and Colloidal Interaction Forces in a Supercritical Solvent: Monte Carlo Simulation. *Langmuir* **1999**, *15*, 8037-8044.

(286) Fischer, H.; Polikarpov, I.; Craievich, A. F. Average protein density is a molecular-weight-dependent function. *Protein Science* **2004**, *13*, 2825-2828.

(287) Panza, J. L.; Russell, A. J.; Beckmann, E. J. *ACS Symposium Series* **2002**, *819*, 64-81.